

AD-A015 075

ATMOSPHERIC ABSORPTION APPLIED TO PLUME EMISSION.
EXPERIMENTAL AND ANALYTICAL INVESTIGATIONS OF HOT
GAS EMISSION ATTENUATED BY COLD GASES

G. H. Lindquist, et al

Environmental Research Institute of Michigan

Prepared for:

Air Force Rocket Propulsion Laboratory

August 1975

DISTRIBUTED BY:



National Technical Information Service
U. S. DEPARTMENT OF COMMERCE

**Best
Available
Copy**

276126

AFRPL-TR-75-30

ERIM No. 102700-20-F

ATMOSPHERIC ABSORPTION APPLIED TO PLUME EMISSION

EXPERIMENTAL AND ANALYTICAL INVESTIGATIONS OF HOT GAS
EMISSION ATTENUATED BY COLD GASES

FINAL REPORT

ENVIRONMENTAL RESEARCH INSTITUTE OF MICHIGAN
BOX 618
ANN ARBOR, MICHIGAN 48107

AUTHORS; G. H. LINDQUIST
C. B. ARNOLD
R. L. SPELLICY

AUGUST 1 9 7 5

Approved for Public Release;
Distribution Unlimited

Reproduced by
NATIONAL TECHNICAL
INFORMATION SERVICE
US Department of Commerce
Springfield, VA. 22151

AIR FORCE ROCKET PROPULSION LABORATORY
DIRECTOR OF SCIENCE AND TECHNOLOGY
AIR FORCE SYSTEMS COMMAND
UNITED STATES AIR FORCE
EDWARDS, CALIFORNIA 93523

REF ID: A647145
SEP 23 1975

B

NOTICES

When U. S. Government drawings, specifications, or other data are used for any purpose other than a definitely related Government procurement operation, the Government thereby incurs no responsibility nor any obligation whatsoever, and the fact that the Government may have formulated, furnished, or in any way supplied the said drawings, specifications, or other data, is not to be regarded by implication or otherwise, or in any manner licensing the holder or any other person or corporation, or conveying any rights or permission to manufacture, use, or sell any patented invention that may in any way be related thereto.

FOREWORD

This report was submitted by the Environmental Institute of Michigan (ERIM), Ann Arbor, Michigan, under Contract No. F04611-73-C-0008, Job Order No. 573009DB, with the Air Force Rocket Propulsion Laboratory, Edwards, CA 93523.

This report has been reviewed by the Information Office/DOZ and is releasable to the National Technical Information Service (NTIS). At NTIS it will be available to the general public, including foreign nations.

This report is unclassified and suitable for general public release.


B. DEAN SPIETH, A/C, USAF
Project Engineer

FOR THE COMMANDER


W. S. ANDERSON
Acting Chief, Technology Division


J. DANIEL STEWART
Manager, Plume Technology

ACCESSION FOR	
NTIS	White Section <input type="checkbox"/>
DOC	Offi. Section <input type="checkbox"/>
UNARMED/ARMED	
JUSTIFICATION	
BY	
DISTRIBUTION/AVAILABILITY CODES	
DISL	AVAIL. AND SPECIAL
A	

REPORT DOCUMENTATION PAGE		READ INSTRUCTIONS BEFORE COMPLETING FORM
1. REPORT NUMBER AFRPL-TR-75-30	2. GOVT ACCESSION NO.	3. RECIPIENT'S CATALOG NUMBER
4. TITLE (and Subtitle) ATMOSPHERIC ABSORPTION APPLIED TO PLUME EMISSION: Experimental and Analytical Investigations of Hot Gas Emission Attenuated by Cold Gases		5. TYPE OF REPORT & PERIOD COVERED Final Report 30 March 73 - 15 Oct 74
7. AUTHOR(s) G. H. Lindquist, C. B. Arnold, R. L. Spellacy		6. PERFORMING ORG. REPORT NUMBER 102700-20-F
8. CONTRACT OR GRANT NUMBER(s) F04611-73-C-0008		9. PERFORMING ORGANIZATION NAME AND ADDRESS Environmental Research Institute of Michigan Infrared and Optics Division, P.O. Box 618 Ann Arbor, Michigan 48107
11. CONTROLLING OFFICE NAME AND ADDRESS Air Force Rocket Propulsion Laboratory Edwards, CA 93523		10. PROGRAM ELEMENT, PROJECT, TASK AREA & WORK UNIT NUMBERS Program Element 62302F Work Unit 573009DB
14. MONITORING AGENCY NAME & ADDRESS (if different from Controlling Office)		12. REPORT DATE August 1975
		13. NUMBER OF PAGES 208
16. DISTRIBUTION STATEMENT (of this Report) APPROVED FOR PUBLIC RELEASE; DISTRIBUTION UNLIMITED		15. SECURITY CLASS. (of this report) UNCLASSIFIED
17. DISTRIBUTION STATEMENT (of the abstract entered in Block 20, if different from Report)		
18. SUPPLEMENTARY NOTES		
19. KEY WORDS (Continue on reverse side if necessary and identify by block number) Water Vapor, CO₂ Atmospheric Transmittance, Band Model, Plume Radiance, Hot Cell, Cold Cell, 2.7 μ m, 4.3 μ m.		
20. ABSTRACT (Continue on reverse side if necessary and identify by block number) An investigation of the attenuation of plume radiation was made, emphasizing the effect of possible correlation between plume emission lines and atmospheric absorption lines. The objectives were to determine the magnitude of this correlation and to develop methods whereby these correlation effects could be adequately treated in techniques to calculate plume emission.		

UNCLASSIFIED

SECURITY CLASSIFICATION OF THIS PAGE(When Data Entered)

ABSTRACT (Continued)

Spectra: measurements of the radiance of a hot gas cell, both unattenuated and attenuated by a long simulated atmospheric path, were made to assess line correlation effects. A band model was developed to treat line correlation effects. Comparisons between the measurements, the available emission-absorption parameters, the band model techniques, and the AFCRL line tabulations allowed a number of conclusions to be made.

Correlation effects in the $2.7 \mu m$ bands of both water vapor and CO_2 were severe enough that neglect of correlation effects leads to an error of as great as a factor of about two (dependent on the spectral region and band-pass), and more consistently an error of 50%, at an altitude of 15 km over a 10 to 200 km path. Correlation effects were present throughout the center of the $2.7 \mu m$ band and in the short wavelength wing of the $2.7 \mu m$ band. Correlation effects were minor in the $4.3 \mu m$ CO_2 red spike region for 15 km altitude and $1200^{\circ}K$ source temperatures, and are expected to remain so for lower altitudes and higher temperatures; however, correlation effects are expected to be present at higher altitudes and/or lower temperatures. Neglecting correlation effects near the band head (short wavelength bandwing) leads to about a 20% error over a 10 km path at 15 km altitude. The absorption was too severe to evaluate line correlation effects in the $4.3 \mu m$ CO_2 band center.

The band model developed predicted the line correlation effects better than the other available methods. The emission-absorption parameters tabulated by General Dynamics did not agree well with the CO_2 spectra, and the line tabulation of AFCRL did not agree with any of the hot cell measurements in the band wings, because of the omission of many of the hot lines.

We recommend that (1) the mathematical behavior of the new band model be further investigated and (2) that a new set of emission-absorption parameters be determined by measurements for the $4.3 \mu m$ CO_2 band so that plume radiation in this region can be accurately calculated, and (3) that correlation effects be investigated at lower pressures and temperatures. Some pressure and temperature conditions exist, probably important to low temperature plumes, below which correlation effects in the $4.3 \mu m$ CO_2 band could become important.

PREFACE

This program is the most recent of a long series of hot gas measurements made at ERIM and its predecessor organization, The Willow Run Laboratories of the University of Michigan. Since 1963 measurements of the radiance of hot gases of various types and under various conditions have been measured. Measurements have almost always been made at spectral resolutions appropriate for band model treatment. Water vapor and CO_2 have been measured often and more exotic gases such as HF have been measured on occasion. Most recently measurements were made of non-isothermal paths of hot gases, and it was as a result of this program that we first investigated means whereby the correlation between absorption lines and emission lines could be correctly treated. As a result of that work, some predictions of correlation effects were made but could not be tested against experimental data. We realized that these correlation effects were important to the problem of adjusting the determinations of the radiant intensities of exhaust plumes of various types for atmospheric attenuation and proposed the present work to investigate these effects. This report describes the results and conclusions of that effort. The efforts described in this report were performed in support of Program Element 62302F, under Work Unit 573009DB.

We wish to acknowledge the able assistance of Mr. Quinto Carioti who prepared much of the experimental apparatus used in this work. In addition, we wish to acknowledge the guidance and encouragement of Dr. F. S. Simmons of Aerospace Corporation and Dr. L. P. Quinn of the Rocket Propulsion Laboratory.

CONTENTS

SUMMARY	13
1. INTRODUCTION	15
1.1 Background	15
1.2 Objectives and Approach	18
2. THE DEVELOPMENT OF BAND MODELS TO TREAT CORRELATION EFFECTS AND PATH INHOMOGENEITY.	19
2.1 The Equation of Transfer	20
2.2 Radiance at a Distance Determined by a Multiplicative Transmittance	24
2.3 Application of Equations 5 and 6 to Target Problems of Interest	26
2.4 Prior Efforts to Compute Transmittance Derivatives	26
2.5 Transmittance Derivative for a Band Model	27
2.6 Distribution of Line Strengths	33
2.7 Expression for the Transmittance Derivative	38
2.8 Use of the Band Model	44
3. MEASUREMENTS OF THE HOT WATER VAPOR AND CO₂ RADIANCE AS VIEWED THROUGH COOL WATER VAPOR AND CO₂	48
3.1 Detailed Experiment Description	49
3.2 Hot Cell Construction	51
3.3 Cold Cell Construction	55
3.4 Gas Handling System	57
3.5 The Effect of the Cell Windows on the Measurements	57
3.6 System Checks	61
3.7 Wavelength Calibration	62
3.8 Data Reduction	62
3.9 Results	64
4. COMPARISON OF MEASUREMENTS WITH PREDICTION METHODS	71
4.1 The Measurements Compared to the General Dynamics Parameters	78
4.2 The Measurements Compared to the AFCRL Line Parameter Tabulation in a Band Model	92
4.3 Effect of the Curve of Growth on the Agreement Between the Measurements and the Calculations	103
4.4 Hot-Through-Cold Radiance and the Effect of the Calculational Method	105
4.5 Comparison of Band Model to an Array of Water Vapor Lines	110
5. CONCLUSIONS AND RECOMMENDATIONS	113
5.1 The Presence of Correlation Effects	113
5.2 Conclusions Concerning the Consistency of the Measurements with Band Model Parameters	116
5.3 Conclusions Concerning Calculational Techniques	118
5.4 Recommendations	118
APPENDIX A: EVALUATION OF EQUATION (34)	121
APPENDIX B: COLLECTION OF MEASURED DATA	131
REFERENCES	208

FIGURES

1. Treatment of Plume-Atmosphere Combination by Two Different Calculational Techniques	25
2. Line Strength vs. Lower State Energy for Water Vapor Lines Between 3530 and 3571 cm^{-1}	34
3. Cumulative Probability Distribution for the Strength of Water Vapor Lines Between 3539 and 3571 cm^{-1}	36
4. Dimensionless Average Equivalent Width Derivative vs. Dimensionless Optical Depth for Two Halfwidth Ratios, for Various Temperature Ratios	42
5. Experimental System Used for Radiative Transfer Measurements	50
6. Photographs of Experimental Apparatus	53
7. 5 Meter "White" Cell Eight-Pass Mode Shown	56
8. Notation Used in Deriving the Hot Through Cold Radiance Measurement Expression	59
9. Sample of Analog Chart Recording	63
10. Typical Water Vapor Data	66
11. Typical CO_2 Data	72
12. Comparison of Measured Hot Cell Radiance with Radiance Calculated Using General Dynamics Parameters, Test 8R, 2.7 μm , Water Vapor	80
13. Comparison of Measured Hot Cell Radiance with Radiance Calculated Using General Dynamics Parameters, Test 5, 4.3 μm , CO_2	81
14. Comparison of Measured Hot Cell Radiance with Radiance Calculated Using General Dynamics Parameters, Test 3, 2.7 μm , CO_2	83
15. Comparison of Measured Hot Cell Radiance with Radiance Calculated Using General Dynamics Parameters, Test 17, 4.3 μm , Plume Mixture	84
16. Comparison of Measured Hot Cell Radiance with Radiance Calculated Using General Dynamics Parameters, Test 20, 2.7 μm , Plume Mixture	85
17. Comparison of Measured Cold Cell Transmittance with Transmittance Calculated Using General Dynamics Parameters, Test 20, 2.7 μm , 10 km Path at 15 km Altitude	86
18. Comparison of Measured Cold Cell Transmittance with Transmittance Calculated Using General Dynamics Parameters, Test 19, 2.7 μm , 50 km Path at 15 km Altitude	87
19. Comparison of Measured Cold Cell Transmittance with Transmittance Calculated Using General Dynamics Parameters, Test 18, 2.7 μm , 200 km Path at 15 km Altitude	88
20. Comparison of Measured Cold Cell Transmittance with Transmittance Calculated Using General Dynamics Parameters, Test 17, 4.3 μm , 10 km Path at 15 km Altitude	89

21. Comparison of Measured Cold Cell Transmittance with Transmittance Calculated Using General Dynamics Parameters, Test 16, 4.3 μm , 50 km Path at 15 km Altitude	90
22. Comparison of Measured Cold Cell Transmittance with Transmittance Calculated Using General Dynamics Parameters, Test 15, 4.3 μm , 200 km Path at 15 km Altitude	91
23. Comparison of Measured Hot Cell Radiance with Radiance Calculated Using Parameters Obtained from AFCRL Tabulation, Test 8, 2.7 μm , Water Vapor	94
24. Comparison of Measured Hot Cell Radiance with Radiance Calculated Using Parameters Obtained from AFCRL Tabulation, Test 7, 4.3 μm , CO_2	95
25. Comparison of Measured Hot Cell Radiance with Radiance Calculated Using Parameters Obtained from AFCRL Tabulation, Test 3, 2.7 μm , CO_2	96
26. Comparison of Measured Cold Cell Transmittance with Transmittance Calculated Using Parameters Obtained from AFCRL Tabulation, Test 3, 2.7 μm , CO_2 Only, 10 km Path at 15 km Altitude	97
27. Comparison of Measured Cold Cell Transmittance with Transmittance Calculated Using Parameters Obtained from AFCRL Tabulation, Test 19, 2.7 μm , 50 km Path at 15 km Altitude	98
28. Comparison of Measured Cold Cell Transmittance with Transmittance Calculated Using Parameters Obtained from AFCRL Tabulation, Test 1, 2.7 μm , CO_2 Only, 200 km Path at 15 km Altitude	99
29. Comparison of Measured Cold Cell Transmittance with Transmittance Calculated Using Parameters Obtained from AFCRL Tabulation, Test 17, 4.3 μm , 10 km Path at 15 km Altitude	100
30. Comparison of Measured Cold Cell Transmittance with Transmittance Calculated Using Parameters Obtained from AFCRL Tabulation, Test 16, 4.3 μm , 50 km Path at 15 km Altitude	101
31. Comparison of Measured Cold Cell Transmittance with Transmittance Calculated Using Parameters Obtained from AFCRL Tabulation, Test 15, 4.3 μm , 200 km Path at 15 km Altitude	102
32. Effect of the Curve of Growth on the Computed Hot Cell Radiance in the 2.7 μm Band Test 8	104
33. Comparison of the Hot-Through-Cold Radiance as Measured and as Predicted by 3 Methods for the 2.7 μm Water Vapor Band, Using the General Dynamics Parameters (Test 8)	106
34. Comparison of the Hot-Through-Cold Radiance as Measured and Predicted by 3 Methods for the 2.7 μm Water Band, Using Parameters Obtained from the CRL Tabulation (Test 8)	107
35. Comparison of the Hot-Through-Cold Radiance as Measured and Predicted by 3 Methods for the 4.3 μm CO_2 Band, Using the General Dynamics Parameters (Test 7)	108
36. Comparison of the Hot-Through-Cold Radiance as Measured and Predicted by 3 Methods, for the 4.3 μm CO_2 Band, Using Parameters Obtained from the CRL Tabulation (Test 7)	109
37. Comparison of the Hot-Through-Cold Radiance as Measured and Predicted by 3 Methods, for the 2.7 μm CO_2 Band, Using the General Dynamics Parameters (Test 3)	111

38. Comparison of the Hot-Through-Cold Radiance as Measured and Predicted by 3 Methods, for the $2.7 \mu\text{m}$ CO_2 Band, Using Parameters Obtained from the CRL Tabulation (Test 3)	112
39. Comparison of the Band Model of Section 2, and the Lindquist-Simmons Approximation with Line-by-Line Calculations for Water Vapor at 3550 cm^{-1}	114
A-1. Integrand of Equation $34 \times q/\sqrt{q} \Gamma(q/\sqrt{q})$ for $q/\sqrt{q} = 1/4$, $\gamma/\sqrt{\gamma} = 2$, and for Various Values of u	125
A-2. Dimensionless Equivalent Width Derivative Computed by Various Means	126
A-3. Integrand of Equation $34 \times q/\sqrt{q} \Gamma(q/\sqrt{q})$ for $q/\sqrt{q} = 1/4$, $\gamma/\sqrt{\gamma} = 2$, $u = 1000$, Showing the Effect of Approximations Present in Equations (A14) and (A16)	128
A-4. Contribution from q/\sqrt{q} to the Limits of Equation 34 for Large u	130
B-1. Measurement Results from Test 1	134
B-2. Measurement Results from Test 2	139
B-3. Measurement Results from Test 3	144
B-4. Measurement Results from Test 5	149
B-5. Measurement Results from Test 6	154
B-6. Measurement Results from Test 7	159
B-7. Measurement Results from Test 8R	164
B-8. Measurement Results from Test 9R	169
B-9. Measurement Results from Test 11MR	174
B-10. Measurement Results from Test 15.	179
B-11. Measurement Results from Test 16.	184
B-12. Measurement Results from Test 17.	189
B-13. Measurement Results from Test 18.	194
B-14. Measurement Results from Test 19.	199
B-15. Measurement Results from Test 20.	204

TABLES

1. Coefficients Used in Approximating the Relation of Equation (34)	41
2. Spectrometer Parameters	52
3. Summary of Measurement Conditions	65
B-1. Test-1 Parameters	133
B-2. Test-2 Parameters	138
B-3. Test-3 Parameters	143
B-4. Test-5 Parameters	148
B-5. Test-6 Parameters	153
B-6. Test-7 Parameters	158
B-7. Test-8R Parameters	163
B-8. Test-9R Parameters	168
B-9. Test-11MR Parameters	173
B-10. Test-15 Parameters	178
B-11. Test-16 Parameters	183
B-12. Test-17 Parameters	188
B-13. Test-18 Parameters	193
B-14. Test-19 Parameters	198
B-15. Test-20 Parameters	203

NOMENCLATURE
(units are given in parentheses)

a	path coordinate, amount of absorber per unit cross section (atm-cm, or molecules/cm ²)
a	parameters for function in Table 1
b	
B	beta function (see Reference 11)
c	velocity of light (3×10^{10} cm/sec)
e_v	extinction coefficient at wavenumber $\tilde{\nu}$ in inverse path coordinate units (atm-cm) ⁻¹ or (molecules/cm ²) ⁻¹
E	lower state energy (cm ⁻¹)
E₀	lower state energy at $S_0 = S_e$ (cm ⁻¹)
f(S₀,E),f(S₀)	joint distribution function for line strength and lower state energy, and distribution function for line strength (in inverse strength units)
g	$1/\bar{S} \frac{d\bar{W}}{da}$ (dimensionless)
g_i	degeneracy, Equation 21 only
h	Planck's constant (6.62×10^{-27} erg sec)
h(S₀,E,Δ$\tilde{\nu}$,γ)	product of line shape function and S/\bar{S} , Equations 17 and 18 only
I₀,I₁	Bessel function of the first kind with imaginary argument, zeroth and first order
j	rotational quantum number
J_{tilde}_v	source function in equation of transfer (in radiance units)
K	constant for distribution function (dimensionless)
k	Boltzmann's constant, Equations 13, 21, 24, 44 only (1.38×10^{-16} ergs/K)
k(a)	average line strength-to-spacing ratio, \bar{S}/d (atm-cm) ⁻¹ or (molecules/cm ²) ⁻¹
L_v,L	spectral radiance (W/cm ² -sr-cm ⁻¹)
L_k*	spectral radiance of blackbody at temperature of substance k (W/cm ² -sr-cm ⁻¹)
l_i	physical length of i^{th} element of path of n elements (cm)
m	temperature exponential for strength variation with temperature (dimensionless)
m_j	rotational m-factor, -j for P-branch transitions, j+1 for R-branch transitions
N	number of lines in resolution interval
p_e,p_{e_i}	effective absorbing pressure (atm), of i^{th} species when subscripted
p_b,p_b,p_{b_i}	local and average effective broadening pressure (atm) of i^{th} species when subscripted
Q	parameter, $2uw \frac{T_0/T}{(1 + \nu^2)}$
Q	partition function, Equation 21 only (dimensionless)

\bar{q}, \bar{q}	local and path-averaged value respectively of the temperature ratio T_0/T (dimensionless)
R_{ij}	matrix element of a generalized transition (dimensionless)
S	absorption line strength ($\text{cm}^{-1}/\text{atm}\cdot\text{cm}$)
\bar{S}	line strength averaged over all lines in a spectral resolution interval ($\text{cm}^{-1}/\text{atm}\cdot\text{cm}$)
S_e	line strength value (at T_0) at which assumed dependence of S_0 upon E goes to $E = E_0$
S_0	line strength at temperature T_0 ($\text{cm}^{-1}/\text{atm}\cdot\text{cm}$)
T	temperature (K)
T_0	reference temperature (296K)
(T_0/T)	path-averaged value of the temperature ratio, T_0/T (dimensionless)
u	dimensionless optical depth, defined in Equation 29
v	parameter, $\Delta\tilde{\nu}/\tilde{\gamma}$
W	equivalent width of a line (cm^{-1})
\bar{W}	average equivalent width averaged over all lines in a resolution interval (cm^{-1})
w	parameter S_0/S_e
x	another form of dimensionless optical depth (see first footnote in Section 2.7)
\bar{y}, y	local and average value of second band model parameter defined in Equation 29 (dimensionless)
y_0	value of second bandmodel parameter at STP (dimensionless)
α_{aj}	broadening coefficient for species j with active species a (dimensionless)
α_w, α_g	cell window and sample gas absorptances respectively (dimensionless)
β	second dimensionless band model parameter in another form (see first footnote in Section 2.7)
$\gamma, \bar{\gamma}$	local and average values of the pressure-broadened halfwidths (cm^{-1})
γ^*	normalized incomplete gamma function (see p. 260 of Reference 11)
Γ	gamma function
$\tilde{\nu}$	wavenumber (cm^{-1})
$\Delta\tilde{\nu}$	resolution interval (cm^{-1}) throughout most of the report. Also used as a dummy variable of integration describing spectral distance from line center in Equations 12 through 30
ρ	reflectance of a single solid-air interface of the cell window material (dimensionless)
τ	transmittance (dimensionless)
$\tau_g, \tau_{w/c}$	transmittance of the sample in the white cell, and of the empty white cell respectively (dimensionless)

SUMMARY

An experimental and theoretical study has been made of the atmospheric attenuation of plume radiation. A particular facet of this problem was examined, namely the effect of the correlation of the water vapor and CO_2 emission lines of the plume with the corresponding absorption lines in the atmosphere. These correlations can produce lower effective transmittance of the plume radiation than the usual treatments of atmospheric attenuation predict.

To measure the magnitude of correlation effects, experimental measurements were made of the radiance of a hot cell, filled with mixtures of CO_2 , H_2O , N_2 and other plume gases. These radiances were measured both unattenuated and attenuated by a long cool atmospheric path. A band model method to handle the line correlation effects was also developed.

We were able to conclude that these correlation effects are severe enough in the $2.7 \mu\text{m}$ water vapor- CO_2 band that their neglect can lead to an error of about 50% to a factor of two in computed radiances and radiant intensities for horizontal paths at 15 km altitude. Correlation effects were minor in the $4.3 \mu\text{m}$ band except in the region of the band head where the neglect of correlation leads to about a 20% error in a 10 km path, and in the band center where there was too much absorption to obtain a good signal-to-noise ratio. The measurements did not extend to several higher simulated altitudes. Therefore, it was not possible to make a quantitative statement about the error expected, if correlation effects were neglected, for more realistic situations, such as slant paths to space. However, correlation effects are expected to become more important at lower pressures and temperatures.

We were also able to show that the set of emission-absorption parameters compiled by Ludwig [1] and the most commonly used to compute CO_2 contributions to plume radiances, do not predict the measured emission-absorption spectra very well, while the water predictions showed adequate agreement. In view of the heavy dependence of the CO_2 parameters of Reference 1 on theory, this result is not surprising; it is recommended that a program be conducted to improve the knowledge of the emission-absorption parameters of CO_2 so that accurate plume radiant intensities can be obtained.

The measured emission-absorption spectra were also compared to the extensive line tabulation of McClatchey. The comparison was unsatisfactory in most cases because the line tabulation does not include many of the emission-absorption lines which are important at high temperatures. Because of these missing lines, the line tabulation in its present configuration cannot be expected to accurately predict the emission of hot gases at temperatures over 800-1000°K.

1. C.B. Ludwig, et al., Handbook of Infrared Radiation from Combustion Gases, NASA-SP-3080, Scientific and Technical Information Office, NASA, Washington, District of Columbia, 1973.

Simple band model methods were shown to yield incorrect results when substantial line correlation effects were present. However a band model method was developed which treats these correlation effects in a realistic manner. When compared with a line-by-line calculation for a given realistic random array of lines, this new band model does a much better job of predicting the correlation effect than any of the previously available methods. Its agreement with the measured data is obscured to some extent by the disagreement between the available emission-absorption parameters and the measured spectra. But where good agreement does occur, the new band model predicts the line correlation effects and hence the effect of atmospheric attenuation better than other available methods. The use of this band model, in the form in which it is presented, is not substantially more complicated than the use of others; accordingly we recommend this band model be further investigated before the model is applied to routine plume calculations.

Many important aspects of this problem have yet to be resolved; hence we recommend that the following tasks be undertaken.

- (1) The numerical evaluation of the functions in the model was not completed in this program. It is important that this be done before widespread use is made of the model.
- (2) A better set of emission-absorption parameters is needed, particularly for CO_2 . The need is urgent because there are no existing parameters which accurately treat the emission processes of the "red spike" region of the $4.3 \mu\text{m}$ CO_2 band. The experimental apparatus used for the present program is ideal for the needed measurements.
- (3) Correlation effects in the $4.3 \mu\text{m}$ band will become more important as the plume temperature is reduced from 1200°K and the altitude increased above 15 km. The experimental conditions used in this program did not treat these cases. Hence, line correlation effects in this band should be investigated at lower temperatures (and pressures where possible) in a manner similar to that done for the program.
- (4) High-altitude broadening processes were not treated in the development of the new band model. The band model development should be extended to include these Doppler broadening processes so the techniques can be useful at high altitudes.

INTRODUCTION

Hot gas emission is the primary source of infrared radiation from aircraft and rocket plumes. The vibration-rotation bands of the infrared-active species in the plume (primarily H_2O and CO_2) are the most prominent features of the plume spectrum. The development of means to accurately compute plume emission and irradiance at a sensor are important both for sensor effects and radiation suppression effects. In both these areas, the theory of radiative transfer provides the link between the chemical and aerodynamic processes governing the plume physical properties and the observed emission.

1.1 BACKGROUND

The emission processes from the gaseous species involved have been studied in many contexts in the past. The spectral details of molecular emission (and absorption) at very high spectral resolution have been used to study molecular structure. Meteorologists have long known that the vibration-rotation bands of H_2O and CO_2 molecules play an important role in the environment of our planet. Radiative emission from hot water vapor and CO_2 has also been important in combustion heat transfer studies.

The study of plume emission looks at these emission processes in a way which is different from the disciplines described above, although it has some aspects in common with each. Plume studies require the accurate computation of the magnitude of the radiation from a given "cloud" of water vapor and CO_2 , at some position remote to that "cloud," as a function of wavelength or frequency. The temperatures of these sources of water vapor and CO_2 are usually high with respect to ambient temperature, ranging from a few hundred degrees K to more than 2000^0K . The spectral resolution required of these studies depends upon the device to which the plume emission studies are to be related. A spectral resolution which is fine with respect to the total spectral extent of the vibration-rotation bands, but coarse with respect to the width or spacing of individual lines within those bands, is usually adequate for quantities measurable with field equipment. Thus the presence of great ranges of temperature distinguish plume emission studies from meteorological studies. The expectation that the observation site will be well separated from the cloud of gas means that there will be an intervening path also containing CO_2 and water vapor. This adds a complexity which is not usually present in hot gas radiative transfer studies. The study of plume emission processes is therefore a mixture of the considerations—from meteorological studies—of absorption and emission of atmospheric species (which arise from the intervening atmospheric path) and of the study of the radiative transfer of hot gases.

The required spectral resolution dictates the type of treatment which is appropriate for the spectral character of the radiation. For most plume studies, extremely high spectral resolution is not required. The smallest interval of interest is small with respect to the whole band but large with respect to individual line widths and spacing. This implies a resolution of a few cm^{-1} (say, 5 to 50), whereas the vibration-rotation bands are a few hundred cm^{-1} in width. The two bands of primary interest to plume studies are (a) the $2.7 \mu\text{m}$ H_2O and CO_2 band, which extends roughly from 3200 to 4100 cm^{-1} (2.4 to $3.1 \mu\text{m}$), and (b) the $4.3 \mu\text{m}$ band of CO_2 which extends from about 2150 to 2400 cm^{-1} (4.17 to $4.65 \mu\text{m}$). The $2.7 \mu\text{m}$ H_2O band is a combination of two fundamental bands and an overtone band (ν_1 , ν_3 fundamentals and $2\nu_2$); the $4.3 \mu\text{m}$ CO_2 band is the ν_3 fundamental band. The CO_2 band at $2.7 \mu\text{m}$, in the same region as the water vapor band, is the result of a number of combination bands. The typical width of the lines in these bands, at normal plume temperatures and atmospheric pressures, is of the order of several hundredths of a wavenumber. In the very finest frequency scale, one would expect substantial absorption (and emission) variations over a fraction of the line width. Thus, it would require spectral resolution of the order of 0.01 cm^{-1} to see these variations. (This resolution is beyond the capability of all but the largest of laboratory instruments.)

The average spacing of the lines in these bands is of the order of a wavenumber if only the strongest lines are considered, and substantially less if the weak lines are included. For example, the very complete tabulation of atmospheric absorption lines prepared by McClatchey et al.,^[2] contains about 250 water vapor lines in a 40 cm^{-1} wide interval centered about 3550 cm^{-1} ($2.82 \mu\text{m}$).

Thus a treatment of the spectral dependence in which any given resolution interval is assumed to contain the integrated effect of a large number of lines is appropriate. Any single resolution interval will contain many lines, and the total effect of any given line is largely concentrated within the resolution element in which it falls. Treatment of the frequency dependence in this manner is called a "band model" treatment. Band model techniques have been developed as a means of averaging over the very finest spectral structure of absorption and emission. Band model treatment of the plume emission is employed throughout this study.

Several good surveys of band model techniques for use with gases near ambient temperature are available. Goody^[3] provides a fundamental description of the processes of gaseous emission and absorption leading to the development of band models. Anding^[4] presents a

2. R.A. McClatchey, et al., AFCRL Atmospheric Absorption Line Parameters Compilation, AFCRL-TR-73-006, Air Force Cambridge Research Laboratories, Bedford, Massachusetts, January 1973.
3. R.M. Goody, Atmospheric Radiation I: Theoretical Basis, Clarendon Press, Oxford, England, 1964.
4. D. Anding, Band Model Methods for Computing Atmospheric Slant-Path Molecular Absorption, Report No. 7142-21-T, Willow Run Laboratories, Ann Arbor, Michigan, February 1967.

detailed comparison of various band models with available experimental data. These two references show that there are a number of available band model techniques which predict the transmittance of water vapor and CO_2 paths near atmospheric temperature and pressure quite well.

Band models have also been developed specifically for the treatment of hot gas radiation. Penner^[5] provides a well-known introduction to high temperature gas emission in which techniques closely related to band models are used. Ludwig^[1] provides a more recent treatment in which sufficient numerical values are included so that reasonably accurate hot gas emission calculations can be made without reference to further numerical data. The numerical values included in Reference 1 provide the data base for much of the numerical calculations made on this program.

Neither the atmospheric band models nor the hot gas band models, when taken alone, provide an adequate treatment of plume emission problems in the presence of an intervening atmosphere. The reason for this is that transmittance calculations, for which the atmospheric band models are well suited, assume that the source of radiation is spectrally continuous. That is, the spectral distribution of the source radiation is assumed to be uniform over a spectral interval at least as wide as the spectral resolution of the band model. This approximation is well satisfied for most opaque thermal emitters, such as the terrain features which are the most significant source of thermal radiation in the spectral region beyond 3 μm .

In contrast, the emission from plume gases, being largely due to the same vibration-rotation bands which give rise to atmospheric absorption, are (spectrally) highly discontinuous and consist of spectral line emission—in many cases, the same lines in which atmospheric absorption occurs. The emission lines are thus correlated with the absorption lines in many instances. A band model treatment, by definition, averages over the fine line structure. Hence, it is important that any band model procedure which treats a situation in which the emission and absorption lines are correlated be structured to carry out this averaging after the whole path is treated. In particular, procedures which average over the line structure of the source alone and then over the structure of the atmospheric absorption alone, without any consideration of the effects of these correlations, will yield questionable results where line correlation effects are known to be present.

These line correlation effects are the primary phenomenon investigated in the present program. Although correlation effects are well known, they are often overlooked in many computations of plume emission. The reason is that there has been no definitive treatment

5. S.S. Penner, Quantitative Molecular Spectroscopy and Gas Emissivities, Addison-Wesley, Reading, Massachusetts, 1959.

of their magnitude. Burch et al.,^[6] made limited measurements, but provided insufficient information by which the importance of the demonstrated effects could be judged.

Calculations have been made which attempt to estimate correlation effects in the atmospheric attenuation of hot gas emission. At least for water vapor the predicted effects were large. In 1970, band-model calculations were made^[7] with a conscious effort to include the atmospheric path together with a path through a plume as one long, non-isothermal path. The objective was to avoid averaging over the line structure until after the attenuation of the atmospheric path had been included. This model contained the implicit assumption that the lines were perfectly correlated and, hence, that the attenuation produced by the atmospheric path was much more severe than the attenuation of continuum or greybody emission. Subsequently, a band model treatment was developed^[8] in which the non-homogeneous character of the non-isothermal path was considered but in which the lines were still assumed to be completely correlated. Young extended these ideas^[9] but still did not account for partial correlation. The results from these efforts indicate severe correlation effects. At the time that the work reported in References 7 and 8 was performed, it was not apparent to the authors that the assumption of complete correlation had been made. During the course of the present analysis it became clear, however, that complete correlation was indeed inadvertently assumed in the above-mentioned work.

There is no reason to believe that the source emission lines and atmospheric absorption lines are completely correlated. At high temperatures energy states above the ground state become populated, leading to many lines in emission which are not significantly present in the absorbing gas. No work had been performed to assess the degree to which the emission and absorption lines correlate. No significant measurements of gas emission as viewed through a cool path have been previously made.

1.2 OBJECTIVES AND APPROACH

The objectives were to determine the magnitude of spectral correlation between a target plume and the atmosphere, as well as to develop methods whereby atmospheric absorption, including correlation effects, could be adequately treated in techniques to compute plume radiant emission. Such methods should be useful to calculate the irradiance at a sensor,

6. D.E. Burch and D.A. Gryvnak, Infrared Radiation Emitted by Hot Gases and Its Transmission through Synthetic Atmospheres, Report No. U-1929, Research Laboratory, Aeromutronic Division, Ford Motor Company, Newport Beach, California, October 1962.
7. F.S. Simmons, et al., "Calculation of Radiation from Hot H₂O and CO₂ Viewed Through a Cool Intervening Atmosphere," Applied Optics, Vol. 9, p. 2792f (1970).
8. G.H. Lindquist and F.S. Simmons, "A Band Model for Very Non-Uniform Paths," JQSRT, Vol. 12, p. 807f (1972).
9. S.J. Young, Band Model Formulation for Inhomogeneous Paths, SAMSO-TR-74-255, The Aerospace Corporation, El Segundo, California, December 1974.

after the target radiation has been modified by the atmosphere. The following three tasks were undertaken to satisfy this objective.

Task I. Band models were developed to treat the nonhomogeneities present in the plume-atmospheric path combination and to represent line correlation effects in the hot and cold gases.

Task II. Measurements were made which provided a characterization of the correlation effects and, hence, could be used to assess the accuracy of the band models developed under Task I, as well as that of the older band model techniques. The emission of a small hot cell filled with mixtures of hot water and CO_2 was measured both unattenuated and attenuated by a long cell filled with cool atmospheric gas. The path conditions were chosen to represent paths corresponding to realistic plume observations. These measurements were made in both the $\text{H}_2\text{O}-\text{CO}_2$ band at $2.7 \mu\text{m}$ and the CO_2 band at $4.3 \mu\text{m}$. The resolution of the spectral apparatus was chosen to be appropriate for band model methods.

Task III. The measurements made in Task II were compared to the available predictions. Comparisons were made to the band models derived in Task I, to previously developed band models, and to line-by-line calculations based on the tabulation of atmospheric absorption lines of Reference 1.

2

THE DEVELOPMENT OF BAND MODELS TO TREAT CORRELATION EFFECTS AND PATH INHOMOGENEITIES

The band model development described here is patterned after the treatment of atmospheric band models by Goody.^[3] It is the result of a great deal of thought as to how to best treat line correlation effects. It was originally hoped that an entirely different type of statistical treatment of line correlation effects would be useful, but after several unfruitful efforts, the ideas described here were pursued. They lead to a realistic means for the treatment of correlation effects and are sufficiently general so that a large set of physical conditions can be treated provided suitable extensions to the model are derived. Only one band model is developed. It is a random line model in that the lines are assumed to be randomly positioned.

We originally planned to develop a model specifically for regularly spaced lines. But after preliminary efforts, we were convinced that no physical situation was present where a regular band model would offer significant advantages over a random model. Our original plan for a regular model was based on the fact that lines in individual bands of CO_2 are nearly regularly spaced. Nevertheless, the presence of many individual CO_2 bands, particularly at higher temperatures, means that the emission spectrum is a superposition of a large number of bands with nearly regularly spaced lines. Line spacings vary among the bands. Each of

these bands is nearly randomly spaced with respect to every other. Since the result is a random array of lines in some sense, one would expect that a random model would accurately treat this situation also, particularly since many lines are included in an averaging interval (i.e., in a single spectral resolution element). Furthermore, as the results of Task II show, there were only minor line correlation effects present in CO_2 under the conditions of this experiment. This means that it would be impossible to distinguish between the performance of the random model and that of a regular model in predicting line correlation effects. We did not consider a regular model for use with water vapor because of the demonstrated randomness of the water vapor band (see Reference 3 and the following sections).

The development given here is restricted to collision-broadened lines. Collision broadening is dominant in low altitude plumes viewed through paths which do not extend above several tens of kilometers in altitude. Furthermore, the experimental apparatus used in Task II was not sensitive enough to allow the hot cell pressures to be low enough such that collision broadening was not significant.* Thus, the treatment here is limited to collision-broadened lines. The following sections give the detailed development of a random band model which includes the effect of line correlation and which can treat path inhomogeneities.

2.1 THE EQUATION OF TRANSFER

Elementary considerations of the interactions of radiation with matter lead to the so-called equation of transfer (see Reference 3, p. 25), which treats all interaction processes as either extinction or absorption and which can be written in the following form:

$$dL_{\tilde{\nu}} = (-L_{\tilde{\nu}} e_{\tilde{\nu}} + J_{\tilde{\nu}}) da \quad (1)$$

Here $L_{\tilde{\nu}}$ is the spectral radiance (called intensity by Goody and other astrophysicists). Spectral radiance is the power emitted (or exiting) from a surface per unit cross-section per unit solid angle, per unit spectral interval; for wavenumber units, it is commonly specified in watts/($\text{cm}^2 \cdot \text{sr} \cdot \text{cm}^{-1}$). The quantity $e_{\tilde{\nu}}$ is the extinction coefficient and $J_{\tilde{\nu}}$ is called the source function. The increment da , is the amount of matter in an element of path of unit cross-section along which radiation is transferred, and $\tilde{\nu}$ is the optical wavenumber (or alternatively, frequency or wavelength).

The first (extinction) term assumes Lambert's law of extinction, namely that the amount of extinction is linear with both radiance and with the amount of absorbing matter in the path. (Radiation processes which are nonlinear in nature are important in many current problems,

*Actually, Doppler and collision-broadened halfwidths were of the same order in the measurements. Because of the great difficulty of developing a model to treat mixed broadening, and because the collision effects still dominate when the widths are of the same order, the development of a model for collision-broadened lines as opposed to Doppler-broadened lines is appropriate.

but the flux required is very much larger than the fluxes to be expected from thermal targets of a few thousand degrees Kelvin such as aircraft and rocket plumes.) The form of the second (emission) term also reflects such an assumption of linearity and can be considered as the definition of the source function.

As Goody^[3] states, this equation sets the pattern for all formalisms used in the solution of radiative transfer problems, although its physical content is slight. The physical interpretation of the meaning of the equation is as follows: $L_{\tilde{\nu}}$ is the spectral radiance along the line of sight and in Equation (1) can be considered to be a function of the path coordinate a . The quantities $e_{\tilde{\nu}}$ and $J_{\tilde{\nu}}$ can also be considered functions of the variable a . Note that the subscript implies a wavenumber dependence as well. The variable a can be taken as the path coordinate since it is defined as the amount of absorbing matter per unit path cross section between some point on the path (the point of observation) and a general physical point along the line of sight. Thus, the variable a serves as a line of sight variable. Equation (1) governs the variation in radiance along the line of sight defined by values of a . In order to determine the radiant intensity of a non-homogeneous source such as a plume, at an observer some distance from the plume, it is necessary to solve Equation (1) for all lines of sight from the observer passing through the plume and to then integrate the results over the apparent cross section of the plume.

In order to facilitate the solution of Equation (1), the following algebraic manipulations are often made. We set $a = 0$ at the observer and express the transmittance from the observer to the point "a" as

$$\tau(\tilde{\nu}, a) = \exp \left(- \int_0^a e_{\tilde{\nu}}(\tilde{\nu}, a') da' \right) \quad (2)$$

Note that, because of the assumed linear relationship between extinction and radiance and amount of matter, this is indeed the transmittance of energy emitted at the point "a" to the observer, at wavenumber $\tilde{\nu}$. After a derivative is taken, this definition can be introduced into the equation of transfer. The sign of the variable a in Equation (1) must be reversed to correspond to the definition of τ in Equation (2). In Equation (2), the variable a increases along the line of sight going away from the observer —i.e., in the direction of increasing radiance when no source is present ($J_{\tilde{\nu}} = 0$); whereas in Equation (1), a increases in the direction of decreasing radiance when $J_{\tilde{\nu}} = 0$. The substitution of (2) into (1) yields

$$\tau(\tilde{\nu}, a) dL_{\tilde{\nu}}(a) = -L_{\tilde{\nu}}(a) \frac{\partial \tau(\tilde{\nu}, a)}{\partial a} da + J_{\tilde{\nu}}(a) \frac{\partial \tau(\tilde{\nu}, a)}{\partial a} da$$

If $d[\tau(\tilde{\nu}, a)L_{\tilde{\nu}}(a)]$ is the differential of the product of τ and $L_{\tilde{\nu}}$ along the line of sight, then the above equation can be written

$$d[\tau(\tilde{\nu}, a)L_{\tilde{\nu}}(a)] = J_{\tilde{\nu}}(a) \frac{\partial \tau(\tilde{\nu}, a)}{\partial a} da \quad (3)$$

This can now be integrated over the line of sight from the observer to the far limit of the line of sight. This far limit should extend to some opaque surface; however, in most measurement systems radiation from portions of the path behind the target of interest is either automatically subtracted or otherwise compensated for. Hence, the far limit is usually taken at the far boundary of the target of interest. (For targets immersed in an atmosphere and viewed by relatively wide field instruments, radiation from the path in front of the target is also often automatically compensated for.) Thus Equation (3) can be integrated to yield the quantity

$$\tau(\tilde{\nu}, \text{far limit})L_{\tilde{\nu}}(\text{far limit}) - L_{\tilde{\nu}}(\text{observer}) = \int_{\text{observer}}^{\text{far limit}} J_{\tilde{\nu}}(a) \frac{\partial \tau(\tilde{\nu}, a)}{\partial a} da$$

If the far limit of the path does not yield significant radiances, (i.e., $L_{\tilde{\nu}}(\text{far limit}) = 0$), then the first term can be ignored, leaving the contribution from the gas target alone:

$$L_{\tilde{\nu}}(\text{observer}) = - \int_{\text{observer}}^{\text{far limit}} J_{\tilde{\nu}}(a) \frac{\partial \tau(\tilde{\nu}, a)}{\partial a} da \quad (4)$$

So far, nothing has been said about the source function. Under the conditions of thermodynamic equilibrium, which we expect to hold for rocket and aircraft exhaust plumes at reasonably low altitudes, the source function is the Planck blackbody radiance function, a function of temperature and frequency only.

The treatment so far has assumed that the measurement system to be used to measure these radiances has perfect spectral resolution. But every practical instrument measures an average over a spectral region either by means of its spectral "slit function" if it is a dispersing instrument or by other frequency-selective mechanisms in case of radiometric measurements. The case of most interest to this particular program is that of a detection system with moderate resolution. Such an instrument takes an average over a frequency interval large with respect to individual molecular absorption line spacings but small with respect to the width of a molecular vibration-rotation band. Upon integration of Equation (4) over a frequency band of width $\Delta\tilde{\nu}$, we obtain for the average radiance seen by the observer:

$$\bar{L}_{\tilde{\nu}} = \frac{-1}{\Delta\tilde{\nu}} \int_{\Delta\tilde{\nu}}^{\text{far limit}} \int_{\text{observer}} J_{\tilde{\nu}'}(a) \frac{\partial \tau(\tilde{\nu}', a)}{\partial a} da d\tilde{\nu}'$$

The order of integration can be reversed so that

$$\bar{L}_{\tilde{\nu}} = \frac{-1}{\Delta\tilde{\nu}} \int_{\text{observer}}^{\text{far limit}} \int_{\Delta\tilde{\nu}} J_{\tilde{\nu}'}(a) \frac{\partial \tau(\tilde{\nu}', a)}{\partial a} d\tilde{\nu}' da$$

If the source function can be assumed sensibly constant over $\Delta\tilde{\nu}$, as it can over the spectral widths of 25 cm^{-1} around 4000 cm^{-1} which are of interest here, then $J_{\tilde{\nu}}(a)$ can be removed from the integration over $\Delta\tilde{\nu}$, and we obtain

$$\begin{aligned} \overline{L}_{\tilde{\nu}} &= \underset{\text{observer}}{\text{far limit}} \int J_{\tilde{\nu}}(a) \left[\frac{1}{\Delta\tilde{\nu}} \int_{\Delta\tilde{\nu}} \frac{\partial \tau(\tilde{\nu}', a)}{\partial a} d\tilde{\nu}' \right] da \\ &= \underset{\text{observer}}{\text{far limit}} \int J_{\tilde{\nu}}(a) \frac{\partial \tau(\tilde{\nu}_c, a)}{\partial a} da \end{aligned} \quad (5)$$

Equation (5) is similar to (4) except that the transmittance derivative involved is now the spectral average of the transmittance derivative at perfect resolution. ($\tilde{\nu}_c$ is the frequency at the center of $\Delta\tilde{\nu}$.) The integration of Equation (4) or (5) is often mapped into an integration over τ or $\bar{\tau}$. Thus,

$$\overline{L}_{\tilde{\nu}} = \underset{\text{observer}}{\text{far limit}} \int J_{\tilde{\nu}}(\bar{\tau}) d\bar{\tau} \quad (6)$$

or

$$\overline{L}_{\tilde{\nu}} = \underset{\text{observer}}{\text{far limit}} \int J_{\tilde{\nu}}(\tau) d\tau \quad (7)$$

All of the above manipulation has been carried out independent of the character of the emitting matter. The only restrictions involved are

- (1) Only linear processes are involved in the extinction and emission processes. This also implies that the perfectly resolved transmittances will obey Beer's law (Equation 2). But the average transmittances are not thus restricted. An average of a number of exponentials like Equation (2), each of different $e_{\tilde{\nu}}$, does not necessarily lead to another exponential. In fact, most band model expressions for spectrally averaged τ are not exponentials.
- (2) The conditions of thermodynamic equilibrium are satisfied everywhere along the path of interest.
- (3) If Equation (5) or (6) is to be used, the Planck blackbody function must be essentially constant over the spectral region $\Delta\tilde{\nu}$.

The above Equations (4), (5), (6), and (7) are therefore valid for a wide variety of situations in which the radiance seen at some observing position, due to sources distributed along the line of sight, is to be calculated. The remainder of this section applies these particular

equations to calculations of gas radiation in the molecular vibration-rotation bands of CO_2 and H_2O which are of primary interest to this program.

2.2 RADIANCE AT A DISTANCE DETERMINED BY A MULTIPLICATIVE TRANSMITTANCE

In many situations of this type, the radiance at a distance (through an atmospheric path) is computed by first computing the radiance of the gaseous target alone and then multiplying this by the transmittance of the atmospheric path. Such a process decouples the gas radiation from the atmospheric transmittance. It is useful at this point to compare this procedure with the result of Equations (4) through (7). Consider the line of sight shown in Figure 1(a). The segment from 0 to a_p is the atmospheric path and that from a_p to a_{p+t} the hot gas of interest. Assume that the radiance contribution from the atmospheric path (from 0 to a_p) is either small or compensated for by the detection system. The target contribution given by Equation (5) is thus

$$\bar{L}_{\bar{\nu}} = - \int_{a_p}^{a_{p+t}} J_{\bar{\nu}}(a') \frac{d\bar{\tau}(a')}{da'} da' \quad (8a)$$

The decoupled procedure mentioned above corresponds to the evaluation of Equation (5) with the observer placed at the boundary of target, as in Figure 1(b). The result is multiplied by the transmittance from 0 to a_p . For this case,

$$\bar{L}_{\bar{\nu}} = \bar{\tau}(0 \text{ to } a_p) \cdot \int_0^{a_t} J_{\bar{\nu}}(a') \frac{d\bar{\tau}(a')}{da'} da' \quad (8b)$$

Assuming that the target is essentially isothermal, the radiances of Equations (8a) and (8b) are equal only if

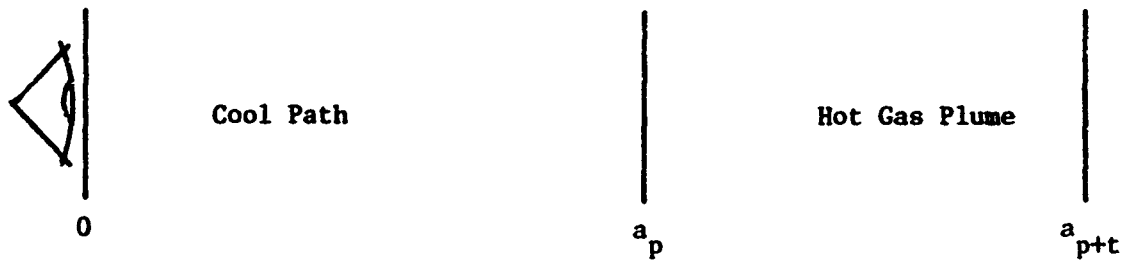
$$\bar{\tau}(0 \text{ to } a_p) \cdot [1 - \bar{\tau}(0 \text{ to } a_t)] = \bar{\tau}(0 \text{ to } a_p) - \bar{\tau}(0 \text{ to } a_{p+t})$$

or

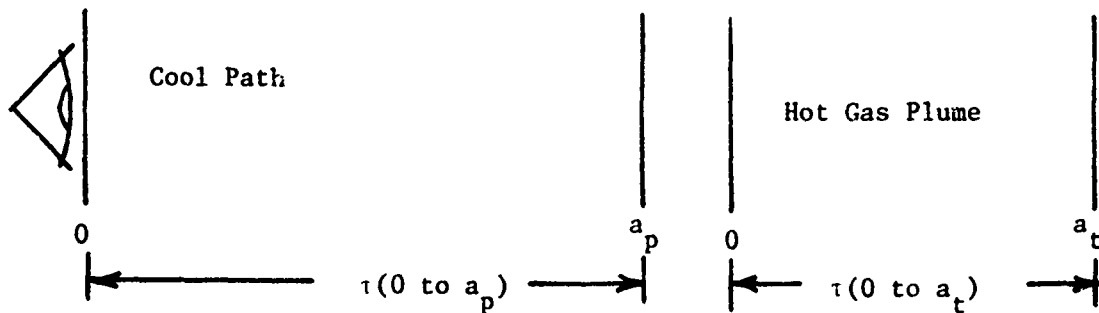
$$\bar{\tau}(0 \text{ to } a_t) \cdot \bar{\tau}(0 \text{ to } a_p) = \bar{\tau}(0 \text{ to } a_{p+t}) \quad (9)$$

The transmittance of the whole path (target plus atmosphere) must equal the product of the transmittance of the atmosphere alone and the transmittance of the target alone.

There are only a limited number of situations where this can be true. For instance, if the transmittances are given by simple exponentials of an optical depth, relation (9) is easily shown to hold. But the averaged transmittances given by band model expressions rarely are represented by such exponentials. Yet, there are other cases where relation (9) holds. The transmittances are each averaged over many lines. If the lines in one portion of the path



(a) Cool Absorbing Path and Hot Gas Plume Treated as a Single Non-Isothermal Path



(b) Cool Absorbing Path and Hot Gas Plume Treated as Separate Decoupled Paths

FIGURE 1. TREATMENT OF PLUME-ATMOSPHERE COMBINATION BY TWO DIFFERENT CALCULATIONAL TECHNIQUES

(atmosphere) are on the average uncorrelated with those in the other portion (target), then the average of the product of two transmittances will equal the product of the averages. This situation can be expected to hold when the atmospheric species producing the absorption are not the same as the emitting species of the plume and when the numbers of target lines and of atmosphere lines in a resolution interval are large. The transmittances of different gases, averaged over many lines, can be multiplied because the correlation between any group of lines of the two molecules will be small.

Relation (9) also holds when either or both of the transmittances is sensibly constant over the integration interval. These transmittances of continuum emitter-absorbers can always be safely multiplied by other transmittances.

Despite the many cases where relation (9) holds, it cannot hold where the absorbing and emitting species are identical and where the band model relations for the average transmittances deviate from simple exponentials. Such is certainly the case for water vapor; less so for CO_2 .

Nor can relation (9) hold when the resolution interval is so small that it includes only a few lines from either the emitting gas or the atmospheric absorbing gases. Thus the product rule cannot be expected to hold for a spectral interval which includes only a few lines from a species like HF (whose lines are widely separated), even when there are many atmospheric lines in the interval.

2.3 APPLICATION OF EQUATIONS 5 AND 6 TO TARGET PROBLEMS OF INTEREST

The procedure discussed in the previous section, in which the target emission and the atmospheric attenuation are decoupled, is incorrect in general and, although it is still commonly used, it will not be considered further in this section. Comparisons of experimental measurements and calculations made using this assumption will be discussed in a later section. The primary consideration of the present section will be to lay out the means to be used to evaluate Equations (5) and (6) which correctly represent moderate resolution radiances of gaseous targets at a distance. The quantity in these equations which must be determined is the transmittance derivative along the path in the case of Equation (5) and the essentially equivalent transmittance differential in Equation (6).

2.4 PRIOR EFFORTS TO COMPUTE TRANSMITTANCE DERIVATIVES

Equation (6) is used in many existing computer programs, which take first differences of successive transmittance calculations, each made for a path from the observer to a general point in the line sight. Generally the Curtis-Godson approximation is used to account for path non-homogeneities. Lindquist and Simmons^[8] and Young^[9] show that the effective transmittance derivative obtained by this procedure leads to incorrect and even physically unreasonable results in some cases. Lindquist and Simmons also determined a more accurate transmittance

derivative in which the Curtis-Godson approximation was applied to the transmittance derivative rather than to the transmittance itself. A heuristic extension to a random model was also made. Young further extended this formulation to several distributions of line strengths but did not account for the fact that different lines change strength with temperature (and hence along the path) in different ways.

It became apparent early in the experimental portion of this contract that the Lindquist-Simmons approximation does not do substantially better at predicting hot gas radiance through a cool path than does the very naive approximation described earlier (hot gas radiance multiplied by cool gas transmittance). Therefore, development of an expression for the spectrally averaged transmittance derivative was undertaken using band model procedures. The results of this effort came too late to allow complete comparisons to be made of the resulting mathematical formulations with the experimental results. Section 4 describes those comparisons which were made. The following section describes the formulation.

2.5 TRANSMITTANCE DERIVATIVE FOR A BAND MODEL

In all of the molecular vibration-rotation bands of interest here, and in particular in the $2.7 \mu\text{m}$ bands of H_2O and CO_2 and the $4.3 \mu\text{m}$ band of CO_2 , each band consists of a very large number of emission-absorption lines. As the temperature increases, the population of vibrational states above the ground state increases. This fact causes so called "hot bands" to become important. These hot bands are bands which involve the same change in vibrational state as the nominal ground state band but which have an initial vibrational level above the ground vibrational state. (The $2.7 \mu\text{m}$ water band results from the ν_1 and ν_3 fundamental ($\Delta v = 1$) vibrational transition, as well as the first overtone ($\Delta v = 2$) of ν_2 transitions of water vapor; the $4.3 \mu\text{m}$ band of CO_2 is the ν_3 fundamental.) In addition, higher temperatures result in the population of more rotational levels, which in turn causes more lines of each vibration-rotation band to have significant strength.

Though "hot bands" occur in the same nominal spectral position as the ground state bands, there is no reason to expect the lines of the hot bands and ground state bands to exactly coincide in position. Thus the physical picture of a vibration-rotation band presented by any molecule, at temperatures substantially above ambient, is that of a number of arrays of lines, one for each band and all essentially uncorrelated with each other. In the case of water vapor, the lines in each band are essentially randomly distributed. This results from the very complicated nature of the rotational structure of this molecule. Each band for CO_2 consists of approximately equally spaced lines. Using this picture, a general expression for the transmittance derivative will be derived. Because the different bands are essentially uncorrelated with each other, random distributions of lines result for both molecules.

The following picture is suitable for water vapor. Consider a spectral interval $\Delta\tilde{\nu}$ having within it N lines of varying strength and randomly positioned. Let us assume that each of

these lines is one member of a random array of equal strength lines of average spacing $\Delta\tilde{\nu}$. The superposition of an appropriate N of these arrays yields the arrangement of lines in $\Delta\tilde{\nu}$ described above. The average spacing of these lines is

$$\delta = \frac{\Delta\tilde{\nu}}{N}$$

Goody derives the transmittance of such an arrangement of lines to be

$$\bar{\tau} = \exp \left[-\frac{1}{N\delta} \sum_{i=1}^N W_i \right] \quad (10)$$

where W_i is the equivalent width (in the appropriate wavenumber or frequency unit) of the i th line in $\Delta\tilde{\nu}$. The derivative of this expression with respect to the path variable a is

$$\begin{aligned} \frac{d\bar{\tau}}{da} &= \frac{d\bar{\tau}}{da} \\ &= -\bar{\tau} \left(\frac{1}{N\delta} \sum_{i=1}^N \frac{dW_i}{da} \right) \\ &= -\frac{1}{\delta} \frac{dW}{da} \\ &= -\frac{\bar{\tau}}{\delta} \frac{dW}{da} \end{aligned} \quad (11)$$

Note that the first equality arises because the derivative of an average with respect to an independent variable is always the average of the derivative. Thus it is now necessary to find an expression for the average derivative of the equivalent width of the lines in $\Delta\tilde{\nu}$.

At this point it is necessary to consider the type of broadening to be expected. Since the experiments were done in a region where pressure broadening is most important, corresponding to targets below about 20 km altitude, Lorentz line profiles will be assumed throughout.

From Reference 7,

$$\frac{dW_i}{da} = \frac{1}{\pi} S_i(a) \gamma_i(a) \int_{-\infty}^{\infty} \frac{1}{\gamma_i^2(a) + \Delta\tilde{\nu}^2} \exp \left[\frac{-1}{\pi} \int_0^a \frac{S_i(a') \gamma_i(a')}{\gamma_i^2(a') + \Delta\tilde{\nu}^2} da' \right] d(\Delta\tilde{\nu}) \quad (12)$$

where S_i and γ_i are the absorption strength and the width of the i^{th} line. The absorption strength is given in terms of the appropriate wavenumber units over optical pathlength, $\text{cm}^{-1}/(\text{molecule}/\text{cm}^2)$. The halfwidth is given in wavenumber units. From this point, since we have no further need for a mathematical symbol for the resolution interval, $\Delta\tilde{\nu}$ will be used as a dummy variable to represent the spectral distance to line center.

An average for this expression must now be obtained over the N lines in the interval. (Note that we have assumed that all of the equivalent width is sensibly included in the resolution interval; since line widths less than 0.1 cm^{-1} are expected in an interval of about 10 to 30 cm^{-1} , this assumption will be satisfied for almost all lines.) Young^[9] has obtained the required average by applying the Curtis-Godson approximation to the exponential argument (attenuation term) so that for each line two strengths appear, the local strength $S_i(a)$ and the average strength $S_{ei}(a)$. He has assumed all S_i and S_{ei} to vary with temperature in identical fashion and has averaged over Equation (12) using different line strength distributions. In this effort we would like to account for the fact that the strengths of the different lines in the interval grow in different ways with temperature, depending on their lower state energy.

The growth of the strength of a line with temperature is due solely to the change in equilibrium populations of the upper and lower states involved. This growth is given by the following expression:

$$S(T) = S_0 \left(\frac{T_0}{T} \right)^m \exp \left[\frac{E}{k} \left(\frac{1}{T_0} - \frac{1}{T} \right) \right] \quad (13)$$

where S_0 is the strength at T_0 , E is the lower state energy in the appropriate units, m is a quantity depending on the rotational degeneracy of the molecule involved, and k is Boltzmann's constant. For H_2O , $m = 3/2$; for CO_2 , $m = 1$.*

It is also necessary to consider the Lorentz halfwidths of the lines involved, their distribution, and the degree to which they are dependent or independent of the strengths of the lines. In this report, the halfwidths will all be assumed identical. This is commonly done in band model treatments, and the introduction of varying line widths would greatly complicate the formulations.

The line widths in a given band vary slowly across the band. Thus, for any single band, the assumption of constant line width in any resolution interval is reasonable. It becomes more difficult to justify the use of constant line width when many hot bands become important. In a later section of the derivation, the absorption in the square root limit is set equal to the correct square root limit, in which the effects of variable line width are accounted for. Thus the effects of line width variation are limited to the transition between linear and square root growth. This transition region is also sensitive to a number of other assumptions of the band model; and since line width variations (to the extent that they are known) are less than a factor of 3 in the wing of the $2.7 \mu\text{m}$ band, it seems reasonable to neglect these variations. Existing band model formulations for isothermal transmittance almost always ignore these variations without compromising their prediction capability. However, to make the same statement

*The vibrational partition function has been neglected in this expression. Its inclusion does not change the resulting formulations.

for the present formulation would require further testing. For the present, we assume identical halfwidths for all the lines in the interval but allow them to vary according to the temperature and pressure variation encountered along the line of sight.

Rather than substitute the complicated form of Equation (13) into the expression for the average equivalent width derivative at this point, we will only note the functional dependencies of Equation (13):

$$\frac{d\bar{W}}{da} = \iint f(S_o, E) \frac{dW(S_o, E)}{da} dS_o dE \quad (14)$$

S_o and E are now the randomly varying parameters associated with the N lines in a given resolution interval. The function $f(S_o, E)$ is a joint probability density function for S_o and E . Note also that, in this expression, the line positions are assumed to be independent of S_o and E , an assumption which seems reasonable considering the physical picture described earlier. Inserting Equation (12) into Equation (14) yields

$$\begin{aligned} \frac{d\bar{W}}{da} = \frac{1}{\pi} \iint_{S_o, E} S(a, S_o, E) \gamma(a) \int_{-\infty}^{\infty} \frac{1}{\gamma^2(a) + \Delta\tilde{\nu}^2} \\ \cdot \exp \left[-\frac{1}{\pi} \int_0^a \frac{S(S_o, E, a') \gamma(a')}{\gamma^2(a') + \Delta\tilde{\nu}^2} da' \right] f(S_o, E) d(\Delta\tilde{\nu}) dS_o dE \end{aligned} \quad (15)$$

In general the integrations over S_o , E , and $\Delta\nu$ can be interchanged at will, but the integration over a' is within the exponential and cannot be interchanged. However, it is this integral which we would like to perform last. In other words, we seek a formulation in which the integrations over $\Delta\nu$, S_o , and E can be performed once for all, so that integrations over different physical paths can be performed at will and without requiring separate integrations over $\Delta\tilde{\nu}$, S_o , and E . This has been the function of the Curtis-Godson approximation in calculations of transmittance. Armstrong has provided a general treatment of this approximation^[10]; and because S_o , E , and γ all appear in the integral, a somewhat more complicated approximation to the integral than discussed by Armstrong must be made. The Curtis-Godson approximation had been intuitively derived in the past; Armstrong showed that it could be derived by expanding the integrand within the integral in a Taylor series about an appropriate variable and defining an average for that variable such that the second term in the expansion is zero. We are going to require averages of two variables in order to perform the desired integration

10. B.H. Armstrong, "Analysis of the Curtis-Godson Approximation and Radiation Transmission through Inhomogeneous Atmospheres," Journal of the Atmospheric Sciences, Vol. 25, p. 312f (1968).

and will use an extension of the treatment by Armstrong to determine these average values. We will expand the integral in a two-dimensional Taylor series about the two appropriate variables and define the two averages so that terms linear in the differences of the two variables are both zero. We will also introduce the average line strength over the resolution interval \bar{S} at any given temperature into the formulation. This will make it easier to relate the results to previous band model formulations and make it possible to use the results with a minimum of changes to previous methods. The argument of the exponential in Equation (15) becomes:

$$-\frac{1}{\pi} \int_0^a \frac{S(S_0, E, a') \gamma(a')}{\gamma^2(a') + \Delta\tilde{\nu}^2} da' = -\frac{1}{\pi} \int_0^a \frac{\bar{S}(S_0, E, a') \gamma(a')}{\bar{S}(a') \gamma^2(a') + \Delta\tilde{\nu}^2} da' \quad (16)$$

In order to obtain a form of the Curtis-Godson approximation similar to that used in the past, all of the integrand save the $\bar{S}(a')$ term will be expanded in a Taylor series as follows:

$$\begin{aligned} \frac{\bar{S}(S_0, E, a') \gamma(a')}{\gamma^2(a') + \Delta\tilde{\nu}^2} &= h\left(S_0, E, \Delta\tilde{\nu}, \frac{T_0}{T}(a'), \gamma(a')\right) \\ &\approx h\left(S_0, E, \Delta\tilde{\nu}, \frac{T_0}{T}, \bar{\gamma}\right) + \frac{\partial h}{\partial \gamma} \Bigg|_{\bar{\gamma}} [\gamma(a') - \bar{\gamma}] + \frac{\partial h}{\partial \left(\frac{T_0}{T}\right)} \Bigg|_{\left(\frac{T_0}{T}\right)} \cdot \left[\frac{T_0}{T}(a') - \frac{T_0}{T}\right] + \dots \quad (17) \end{aligned}$$

Note that S/\bar{S} is now treated as a parameter dependent on S_0 , E , and a' resulting from the combined dependences of S and \bar{S} . The three terms shown are now used as an approximation to the function h and substituted into Equation (16) to yield

$$\begin{aligned} -\frac{1}{\pi} \int_0^a \frac{\bar{S}(S_0, E, a') \bar{S}(a') \gamma(a')}{\gamma^2(a') + \Delta\tilde{\nu}^2} da' \\ = -\frac{1}{\pi} \int_0^a \bar{S}(a') \left\{ h\left(S_0, E, \frac{T_0}{T}, \bar{\gamma}\right) + \left[\frac{\partial h}{\partial \gamma} \Bigg|_{\bar{\gamma}} \cdot (\gamma(a') - \bar{\gamma}) \right] + \left[\frac{\partial h}{\partial \left(\frac{T_0}{T}\right)} \Bigg|_{\left(\frac{T_0}{T}\right)} \cdot \left(\frac{T_0}{T}(a') - \frac{T_0}{T}\right) \right] \right\} da' \quad (18) \end{aligned}$$

We are now free to choose $\bar{\gamma}$ and \bar{T}_0/T to minimize the error in the integrated expression. In particular we can choose $\bar{\gamma}$ and \bar{T}_0/T so that when the integration is performed the terms in the first derivatives vanish. This choice requires that $\bar{\gamma}$ and \bar{T}_0/T be given by

$$\bar{\gamma} = \frac{\int_0^a \bar{S}(a') \gamma(a') da'}{\int_0^a \bar{S}(a') da'} \quad (19)$$

and

$$\frac{\bar{T}_0}{T} = \frac{\int_0^a \bar{S}(a') \frac{T_0}{T}(a') da'}{\int_0^a \bar{S}(a') da'} \quad (19)$$

With the foregoing expressions for $\bar{\gamma}$ and \bar{T}_0/T , Equation (18) becomes

$$\begin{aligned} & -\frac{1}{\pi} \int_0^a \frac{\bar{S}(S_0, E, a') \bar{S}(a') \gamma(a')}{\gamma^2(a') + \Delta\tilde{\nu}^2} da' \\ & \approx -\frac{1}{\pi} \frac{\bar{S}(S_0, E, \frac{\bar{T}_0}{T}) \bar{\gamma}}{\bar{\gamma}^2 + \Delta\tilde{\nu}^2} \int_0^a \bar{S}(a') da' \end{aligned} \quad (20)$$

The error involved in this approximation can be evaluated for any particular path of interest by evaluating the higher order terms of the Taylor series. The magnitudes of the higher order terms compared to Equation (20) are a measure of the accuracy of this approximation. Equation (20) is a Curtis-Godson type of approximation for the formulation used here. Note that no approximation is needed for the emission portion of Equation (15); the purpose of introducing the approximation is only to allow the order of integration over a to be changed, so that it can be performed last rather than first as required by Equation (15).

It is also worthwhile to note that the variables about which the integrand was expanded are rather arbitrary; we chose γ and T_0/T because the choice of γ leads to a familiar form of the Curtis-Godson approximation and also because it and T_0/T are natural variables about which to perform this expansion. Armstrong expanded the line shape function about the broadening pressure to yield the Curtis-Godson approximation in terms of an average pressure. In cases of interest here, however, the large temperature variations will also have some effect on

the Lorentz line width so that expansion about the width itself seems more natural. One cannot determine, for general paths, that expansion variable (or variables) about which the expansion would be optimum (that is, which would lead to minimum error in the path integral). It can easily be shown that expansions about variables which are linear combinations of each other are equivalent; but, except for this, different expansions are not easily compared without introducing specific path examples.

2.6 DISTRIBUTION OF LINE STRENGTHS

It is now necessary to consider suitable forms for the joint distribution $f(S_0, E)$ defined in Equation (14). To begin with, it will not do to assume S_0 independent of E . Comparatively weak lines almost always are weak because their lower states are comparatively less populated, indicating a higher lower state energy. In simple approximations, in fact, the matrix element of all transitions within a band are identical; the variations in strength of the lines in such a band are due solely to variations in lower state populations and hence to changes in E . In such a case S_0 and E are completely correlated. The $2.7 \mu\text{m}$ H_2O band is made up of a number of different vibrational transitions. In addition, the hot bands for each of these transitions become important at the higher temperatures. Since lines for all vibrational transitions appear throughout the $2.7 \mu\text{m}$ spectral region, every $\Delta\tilde{\nu}$ will contain lines from all bands. Since band strengths and lower states for each of these bands are different, one would not expect the individual line strengths and lower state energies in a given $\Delta\tilde{\nu}$ to be completely correlated. To visualize this effect, we have in Figure 2 plotted S_0 , the strength at 296°K , versus the lower state energy E for all the water vapor lines in the 40 cm^{-1} interval between 3530 cm^{-1} and 3570 cm^{-1} contained in the AFCRL line tabulation of McClatchey et al. (see Reference 1). There are about 260 lines in this interval; only the 160 lines having strengths S_0 greater than $10^{-24} \text{ cm}^{-1}/\text{mol}\cdot\text{cm}^{-2}$ are plotted. The density of points at a given S_0 and E value is representative of the value of $f(S_0, E)$ at that point. If S_0 and E were completely correlated, the points would all lie on a single curve. They do not, but the points do lie in a crudely straight band running roughly from upper left to lower right. The relation for the strength of an absorption line at temperature T_0 , in terms of the matrix element of the transition associated with that line, is — see Reference 2 —

$$S(T_0) = \frac{m_j(2j+1)}{g_i Q(T_0)} e^{-E/kT_0} \cdot \frac{8\pi\tilde{\nu} |R_{ij}|^2}{3hc} \quad (21)$$

The quantities in this expression that vary from line to line in any given $\Delta\tilde{\nu}$ are the matrix element R_{ij} , the lower state energy E , the wavenumber of the transition $\tilde{\nu}$, and the rotation-quantum-number-dependent quantities $m_j(2j+1)/g_i$. $\Delta\tilde{\nu}$ is small enough (of the order of 10 cm^{-1}) compared to the wavenumber of the bands of interest here ($\sim 3000 \text{ cm}^{-1}$) so that the wavenumber in the numerator can be considered sensibly constant for all the lines in $\Delta\tilde{\nu}$. If

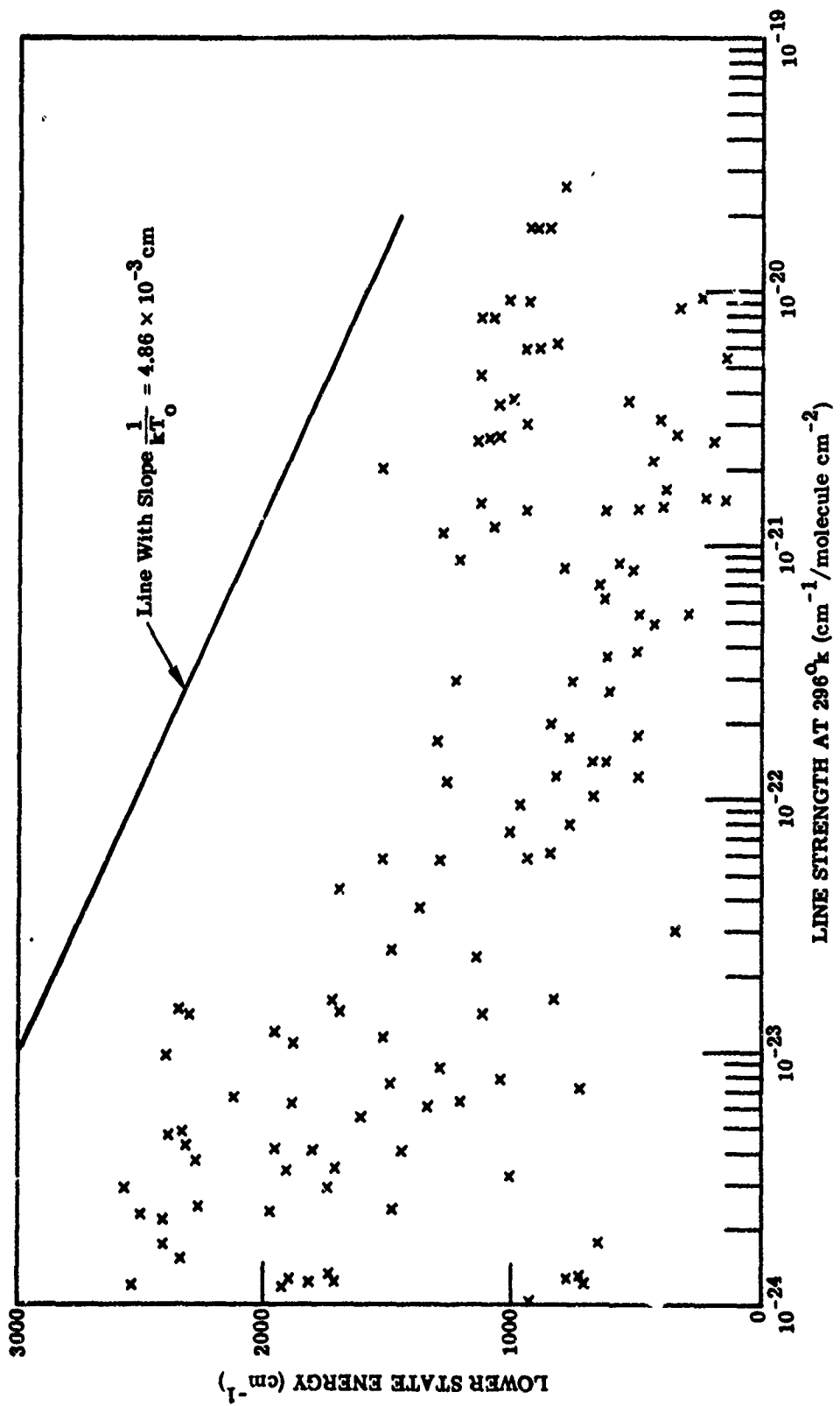


FIGURE 2. LINE STRENGTH VERSUS LOWER STATE ENERGY FOR WATER VAPOR LINES BETWEEN 3530 AND 3571 cm⁻¹

the product of the quantities $m_j(2j + 1)/g_j$ and the matrix elements were identical for all lines in $\Delta\nu$, then S_0 would be related to E by a fixed exponential relation, a straight line on the semi-log plot of Figure 2. The spread of the points indicates of course that the above mentioned product is not identical for all lines, but nevertheless, the grouping of the lines in a region of Figure 2 indicates a limited variation in this quantity. We have tried representing the density of points in this figure by uniform distributions over limited ranges of E and S_0 to try to approximate the grouping of the points. The formulations became very complex, however, and we decided to approximate the distribution of points on Figure 2 by a single straight line. This leads to a formulation which is workable, which represents at least the spirit of the relationship of Equation (21), and which can be chosen to represent the mean of the points of Figure 2. It should also provide a great improvement over previously made assumptions in which all lines are assumed to grow with temperature according to a common multiplicative function. The line chosen should have a slope close to that of Equation (21), namely $1/kT_0 = 4.86 \times 10^{-3}$ cm. A line of this slope is shown on Figure 2 also. It can be seen the lines are grouped roughly according to this slope. We will use this slope without further justification.

We have decided to assume S_0 and E completely correlated as described above; we must then choose a distribution for S_0 . Using the same set of lines as used for Figure 2, the cumulative distributions of S_0 were computed and plotted on Figure 3 in semi-log coordinates. This presentation is similar to that of Figure 4.6 in Reference 2. A straight line in these coordinates represents an inverse intensity distribution of line strengths. The points on this figure indicate that the choice of an inverse intensity distribution would represent the data points rather well. On the other hand, the assumption of an exponential distribution of line strengths leads, in the case of transmittance formulations (as opposed to the transmittance derivative formulation sought here), to simpler formulations. But the points shown on Figure 3 do not lend themselves at all to representation by an exponential distribution. This figure shows many more weak lines than an exponential distribution would predict. Therefore, to preserve some correspondence to reality for water vapor, we will use an inverse-strength distribution of the form

$$f(S_0) = \frac{K}{S_0} \quad (22)$$

for some range of strengths S_m to S_e where K is a constant of the distribution, S_m is a minimum line strength and S_e is the line strength when E is the lowest possible vibration-rotation energy E_0 . To summarize, then, we have assumed the lower state energy to be completely correlated to the line strength S_0 (S_0 is the line strength at temperature T_0) and the strengths to be distributed according to the inverse of the strength. The integrals over E in the preceding expressions will thus disappear.

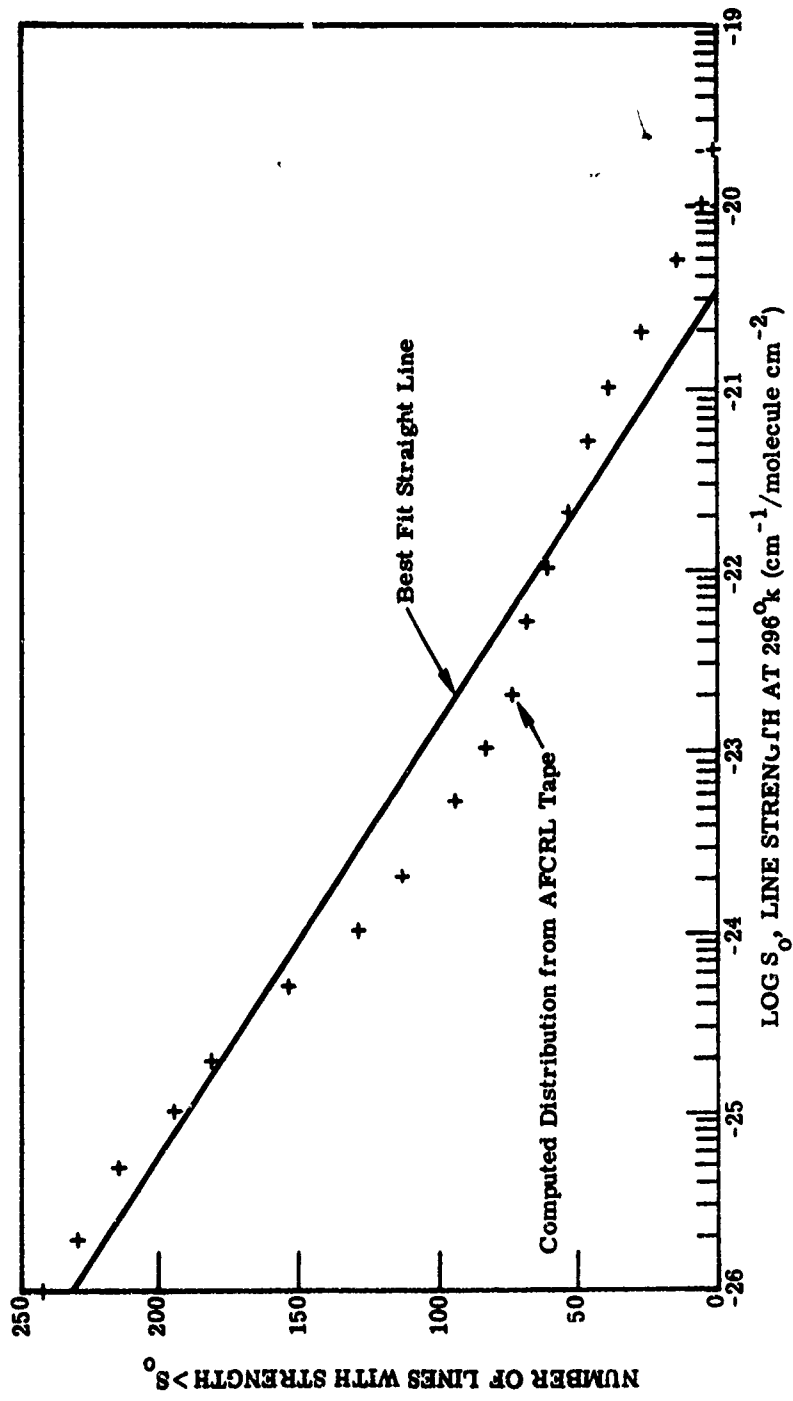


FIGURE 3. CUMULATIVE PROBABILITY DISTRIBUTION FOR THE STRENGTH OF WATER VAPOR LINES
BETWEEN 3530 AND 3571 cm^{-1}

Average Strength at Temperature T

Using the distribution described above, it will be necessary to determine the average line strength as a function of temperature in terms of the parameters of the distribution. This will be necessary not only because we will have to evaluate these parameters from experimental absorption coefficient data (which are often presented in terms of average line strength), but also because we have introduced this quantity into the path integral in Equation (20).

The average strength at any temperature is given by

$$\bar{S}(T) = \int S(S_0, E, T) f(S_0) dS_0 \quad (23)$$

where $f(S_0)$ is to be taken from Equation (22). As discussed in the previous paragraph, S_0 will be assumed to be completely correlated with E according to the relation

$$S_0 = S_e \exp [-(E - E_0)/kT_0],$$

where S_e is the strength at which the lower state energy reaches E_0 . It is not necessary at this point to determine a value for S_e . Inversion of this equation yields E in terms of S_0 as follows:

$$E(S_0) = -kT_0 \ln \frac{S_0}{S_e} + E_0 \quad (24)$$

Substitution of Equation (24) into the expression for strength, Equation (13), yields

$$S(S_0, \frac{T_0}{T}) = S_e \left(\frac{T_0}{T}\right)^m \left(\frac{S_0}{S_e}\right)^{T_0/T} \exp \left[\frac{E_0}{k} \left(\frac{1}{T_0} - \frac{1}{T} \right) \right] \quad (25)$$

Further substitution of Equations (22) and (25) into Equation (23) gives

$$\begin{aligned} \bar{S}(T) &= \int_{S_m}^{S_e} \left(\frac{T_0}{T}\right)^m \left(\frac{S_0}{S_e}\right)^{(T_0/T)-1} \exp \left[\frac{E_0}{k} \left(\frac{1}{T_0} - \frac{1}{T} \right) \right] K dS_0 \\ &= \left(\frac{T_0}{T}\right)^m S_e K \frac{1 - \left(\frac{S_m}{S_e}\right)^{T_0/T}}{\frac{T_0}{T}} \exp \left[\frac{E_0}{k} \left(\frac{1}{T_0} - \frac{1}{T} \right) \right] \end{aligned}$$

Since the range of strengths to be encountered is very large, $S_m/S_e \approx 0$, so that

$$\bar{S}(T) \approx \left(\frac{T_o}{T}\right)^{m-1} S_e K \exp \left[\frac{E_o}{k} \left(\frac{1}{T_o} - \frac{1}{T} \right) \right] \quad (26)$$

In order to evaluate Equation (20) we need S/\bar{S} . From Equations (25) and (26),

$$\frac{S}{\bar{S}} \left(S_o, \frac{T_o}{T} \right) = \frac{T_c/T}{K} \left(\frac{S_o}{S_e} \right)^{T_o/T} \quad (27)$$

Substituting Equation (27) into Equation (20) gives

$$-\frac{1}{\pi} \frac{S}{\bar{S}} \left(S_o, E, \frac{T_o}{T} \right) \frac{\bar{\gamma}}{\bar{\gamma}^2 + \Delta \tilde{\nu}^2} \int_0^a \bar{S}(a') da' = -\frac{1}{\pi} \frac{\left(\frac{T_o}{T} \right)}{K} \left(\frac{S_o}{S_e} \right)^{T_o/T} \frac{\bar{\gamma}}{\bar{\gamma}^2 + \Delta \tilde{\nu}^2} \int_0^a \bar{S}(a') da' \quad (28)$$

2.7 EXPRESSION FOR THE TRANSMITTANCE DERIVATIVE

At this point, we are ready to construct the final expression which represents the transmittance derivative. It is appropriate first to introduce the usual band model parameters. Except for the variation of E with S_o , the band model up to this point is identical with that developed by Goody for an inverse-strength distribution of lines (see Reference 2, pp. 130-136). To facilitate comparisons with our model, it is convenient to use the same variables and nomenclature used by Goody. Thus we define

$$\bar{y} = \frac{K}{\delta} \frac{\bar{\gamma}}{\left(\frac{T_o}{T} \right)}$$

and

$$u = \frac{\int_0^a \bar{S}(a') da'}{2\pi \bar{y} \delta} \quad (29)$$

$$= \frac{\int_0^a k(a') da'}{2\pi y}$$

The only difference between these variables and those of Goody is the inclusion of the factor (T_o/T) , the average inverse temperature ratio, in y . This factor, of course, does not appear on Goody's treatment since it arises from our relation between E and S_o . It is included in y to provide exact correspondence between the transmittance relation obtained here and

Equation (4.37) in Goody's transmittance.* Note that $k(a')$ is the strength-to-spacing ratio evaluated at the temperature at a' , which appears in all band model treatments. Equation (28), the argument for the exponential for Equation (15), now becomes

$$-\frac{1}{\pi} \frac{\left(\frac{T_o}{T}\right) \left(\frac{S_o}{S_e}\right)^{\frac{T_o}{T}}}{K} \int_0^a \frac{\gamma}{\gamma^2 + \Delta\tilde{\nu}^2} \bar{S}(a') da' = -2 \frac{u}{\left(1 + \frac{\Delta\tilde{\nu}^2}{\gamma^2}\right)} \left(\frac{S_o}{S_e}\right)^{\frac{T_o}{T}} \quad (30)$$

This relation, Equation (27) for S in terms of \bar{S} and T_o/T , and Equation (22) can be substituted into Equation (15) for $d\bar{W}/da$ to give

$$\frac{d\bar{W}}{da} = \frac{1}{\pi} \bar{S}(a) \frac{T_o}{T} \int_{S_m}^{S_e} \left(\frac{S_o}{S_e}\right)^{\frac{T_o}{T}} \int_{-\infty}^{\infty} \frac{\gamma(a)}{\gamma^2(a) + \Delta\tilde{\nu}^2} \exp \left[-\frac{2u}{1 + \left(\frac{\Delta\tilde{\nu}}{\gamma}\right)^2} \left(\frac{S_o}{S_e}\right)^{\frac{T_o}{T}} \right] \frac{1}{S_o} d\Delta\tilde{\nu} dS_o \quad (31)$$

By making the following changes of variables,

$$w = \frac{S_o}{S_e}$$

and

$$v = \frac{\Delta\tilde{\nu}}{\gamma}$$

the following expression is obtained :

$$\frac{d\bar{W}}{da} \frac{1}{\bar{S}(a)} = \frac{T_o}{T} \frac{\gamma}{\pi} \int_{-\infty}^{\infty} \frac{1}{\left(\frac{\gamma}{v}\right)^2 + v^2} \int_0^1 w^{\frac{T_o}{T} - 1} \exp \left[-\frac{2u}{1 + v^2} w^{\frac{T_o}{T}} \right] dw dv \quad (32)$$

The ratio S_m/S_e has been assumed to be zero. A further substitution of

*The variables u and y are very simply related to the corresponding variables x and β used in Reference 7 and in earlier band-model treatments by Simmons. They are $u = 4x$, $y = \beta/8\pi$.

$$Q = \frac{2uw}{1+v^2} \frac{T_o/T}{T_o}$$

along with $q(a) = T_o/T(a)$ and $\bar{q}(a) = \bar{T}_o/T(a)$ yields

$$\frac{dW}{da} \frac{1}{S(a)} = \frac{q \gamma}{q \gamma \pi} \int_{-\infty}^{\infty} \frac{1}{\left(\frac{\gamma}{\bar{\gamma}}\right)^2 + v^2} \cdot \left\{ \left(\frac{1+v^2}{2u} \right)^{q/\bar{q}} \int_0^{2u/1+v^2} Q^{q/\bar{q}-1} \exp(-Q) dQ dv \right\} \quad (33)$$

Note now that the expression depends only on the normalized optical depth u , the ratio between the local and the average inverse temperature q/\bar{q} , and the ratio of the local and average half-widths $\gamma/\bar{\gamma}$. This corresponding expression in the Lindquist-Simmons approximation depended on only the normalized optical depth and the halfwidth ratio. The portion of Equation (33) enclosed in curly brackets can be replaced by a normalized incomplete gamma function, γ^* (see Abramovitz and Stegun, [11], p. 260) as follows:

$$\frac{dW}{da} \frac{1}{S(a)} = \frac{1}{\pi} \frac{\gamma}{\bar{\gamma}} \frac{q}{q} \Gamma\left(\frac{q}{\bar{q}}\right) \int_{-\infty}^{\infty} \frac{\gamma^*\left(\frac{q}{\bar{q}}, \frac{2u}{1+v^2}\right)}{\left(\frac{\gamma}{\bar{\gamma}}\right)^2 + v^2} dv \quad (34)$$

A general solution for this integral for a large range of values of u , q/\bar{q} , and $\gamma/\bar{\gamma}$ could not be found. Extensive numerical evaluations have not yet been made but enough evaluations and asymptotic limits were found to obtain expressions which seem to approximate the function quite well. Appendix A describes the evaluations made for this work.

The Interpretation of Equation (34)

An expression which seems to approximate Equation (34) very well is an expression of the form

$$\frac{1}{\sqrt{1 + (au)^b}}$$

where a and b are dependent on q/\bar{q} and $\gamma/\bar{\gamma}$. It is surprising that this simple expression seems to approximate Equation (34) as well as it does. Table 1 gives values for a and b which seem to work well for $q/\bar{q} < 1$ and $\gamma/\bar{\gamma}$ in the vicinity of 0.1 to 10. Figure 4 shows plots of the

11. M. Abramovitz and I.A. Stegun, Handbook of Mathematical Functions, AMS-55, National Bureau of Standards, Washington, District of Columbia, 1964.

TABLE 1. COEFFICIENTS USED IN APPROXIMATING
THE RELATION OF EQUATION (34)*

$$\frac{dW}{da} \frac{1}{S} = f\left(u, \frac{\gamma}{\bar{\gamma}}, \frac{q}{\bar{q}}\right)$$

$$\approx \frac{1}{\sqrt{1 + (au)^b}}$$

where

$$a = \frac{1}{(\gamma/\bar{\gamma})^2} \text{ for } q/\bar{q} < 1/2$$

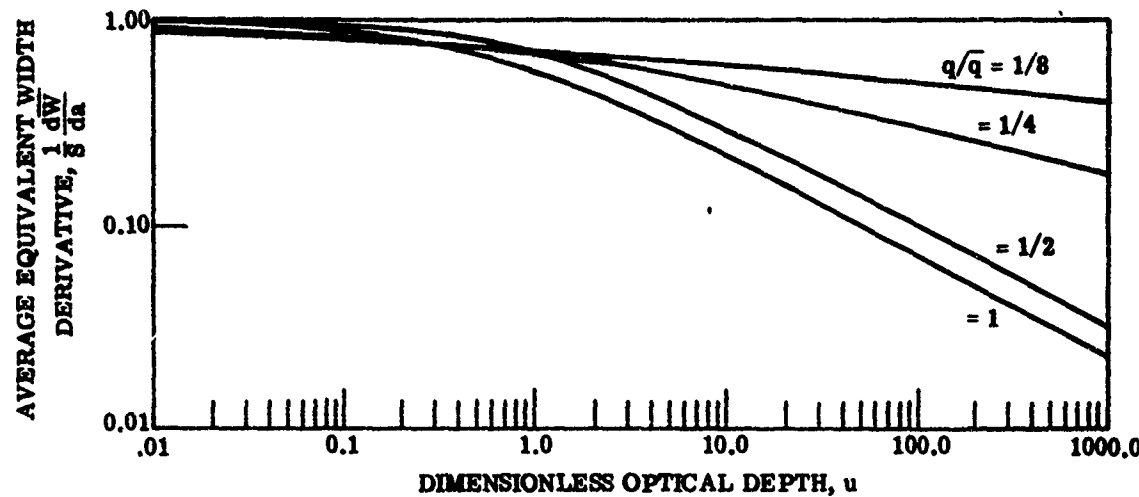
$$a = \frac{2(q/\bar{q})}{(\gamma/\bar{\gamma})^2} \text{ for } 1 > q/\bar{q} > 1/2$$

and

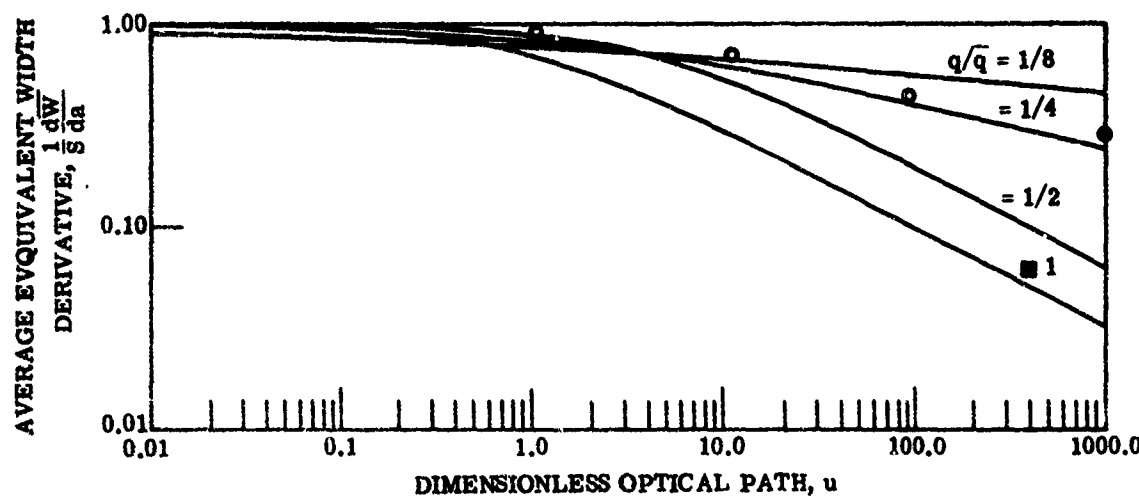
$$b = 2(q/\bar{q}) \text{ for } q/\bar{q} < 1/2$$

$$b = 1 \text{ for } q/\bar{q} > 1/2$$

*See Figure 4.



(a) Halfwidth Ratio, $\gamma/\bar{\gamma} = 1$



(b) Halfwidth Ratio, $\gamma/\bar{\gamma} = 2$

FIGURE 4. DIMENSIONLESS AVERAGE EQUIVALENT WIDTH DERIVATIVE VERSUS DIMENSIONLESS OPTICAL DEPTH FOR TWO HALFWIDTH RATIOS, FOR VARIOUS TEMPERATURE RATIOS

approximation for $\gamma/\bar{\gamma} = 1.0$ and 2.0, for various values of q/\bar{q} . Figure 4(b) also shows several computed values of the complete function of Equation (34). Since these values were calculated numerically by hand, they are of unknown accuracy. Agreement with the approximation seems to be of the order of 5%. Appendix A discusses the means used to obtain the approximations. It would have been desirable to perform extensive tests of this approximation compared to Equation (34), but time and funds were not available to do so. The result is important enough to be presented as we have, with minimal confirmation, since (as discussed in Section 4) it forms the basis of a much improved ability to predict plume radiation through an atmospheric path.

The range of parameters which are important for plume calculation is as follows. The parameter q/\bar{q} is the ratio between the inverse of the local temperature to the average inverse temperature. For the experiments presented in this work

$$\frac{q}{\bar{q}} \approx \frac{1/1200}{1/300} = 0.25$$

This is the reason for the use of $q/\bar{q} = 0.25$ in Figure 4. For a plume submerged in an atmosphere at 250°K , q/\bar{q} could be expected to vary between, say,

$$\frac{1/600}{1/250} = 0.42 \text{ and } \frac{1/1600}{1/250} = 0.16$$

Values of $q/\bar{q} > 1$ correspond to targets cooler than ambient, not an interesting case for plume studies. As the path progresses from the near boundary of the target to the far boundary, the value of q/\bar{q} approaches unity. In the experiments described in Section 3, the value of q/\bar{q} went from 0.25 at the near boundary at all frequencies and increased to about 0.3 at the far boundary in the band center. At the edges of the band, where there is a great difference between the values for \bar{S}/δ at ambient temperature and at 1200°K , the value of q/\bar{q} at the far boundary became somewhat greater than 0.4.

$\gamma/\bar{\gamma}$ has a rather special interpretation in this model. If this ratio is interpreted strictly as a ratio of halfwidths, it should be a function only of the local pressure and temperature and the average pressure and temperature. But earlier in the development the variables K and $\bar{\gamma}$ were lumped together into the variable y . This variable controls the approach of the transmittance curve-of-growth to the square-root region; to ensure correspondence with reality, its value is either taken from experimental data or computed using the special strength weighting given by Goody (Reference 3, Equation (4.41)). In the same fashion, the parameter $\gamma/\bar{\gamma}$ controls the approach of the transmittance derivative into the region that corresponds to the square-root-region for transmittance. Hence, the parameter $\gamma/\bar{\gamma}$ must also be taken from the variable y . Using the definition given in Equation (29),

$$y = \frac{Ky}{\delta q}$$

$$\bar{y} = \frac{K\bar{y}}{\delta q}$$

Note that K is a fixed quantity for the whole path since it is a parameter of the distribution for S_0 . Also δ is invariant over the path; since the model assumes that all lines are present at all path conditions, only their strengths vary. Thus $\gamma/\bar{\gamma}$ should be taken as

$$\frac{\gamma}{\bar{\gamma}} = \frac{y q}{\bar{y} \bar{q}}$$

This will ensure proper correspondence with the square-root region. This ratio corresponds directly to the ratio β/β_e in the Lindquist-Simmons approximation except for the temperature factor.

Young^[12] indicates that values of $y/\bar{\gamma}$ ranging from 10^{-7} to 200 can be expected in plume calculations. Thus the investigation of Equation (34) given here is nowhere near complete. We have investigated the behavior of Equation (34) only for values of $\gamma/\bar{\gamma}$ of 1 and 2. A great deal of effort remains to be accomplished before the behavior of Equation (34) can be said to be well known.

A strange feature of Equation (34) is that, for $q/\bar{q} < 1/2$, $d\bar{W}/da$ $1/\bar{S}$ does not go as $u^{-1/2}$ for larger u , but rather goes as $u^{-q/\bar{q}}$. This is apparent in the approximations given in Table 1 and in the values calculated. This behavior is puzzling and contrary to what one would expect. It means that so many weak lines become strong that square-root growth can not be achieved. This is another facet of Equation (34) that requires further investigation.

From the evaluations and analysis that were done of Equation (34), it is apparent that the character of the function changes greatly at $q/\bar{q} = 1/2$. Unfortunately, we have not yet done any careful evaluations at $q/\bar{q} = 1/2$ in order to uncover exactly why the function changes behavior at this value. Further investigation of this problem should be undertaken before extensive use is made of Equation (34).

2.8 USE OF THE BAND MODEL

We have incorporated the bandmodel represented of the preceding sections into our calculation procedures. Much of the procedure is similar to that used previously; only those portions dealing with the evaluation of the transmittance derivative have been modified. This routine performs a numerical evaluation of Equation (5), using Equation (11) to obtain values for $d\bar{\tau}/da$. Since Equation (11) and all subsequent equations through Equation (34) assume a fixed frequency interval, the derivative in Equation (11) corresponds exactly to the partial derivative given in Equation (5). By means of Equation (11) it is easy to evaluate $d\bar{\tau}/da$ once Equation (34) has been evaluated:

12. S.J. Young, Band Model Calculations of Atmospheric Transmittance for Hot Gas Line Emission Sources, SAMSO-TR-74-248, The Aerospace Corporation, El Segundo, California, December 1974.

$$\frac{d\bar{\tau}}{da} = \frac{\bar{\tau}}{\delta} \frac{dW}{da} = \frac{\bar{\tau}}{\delta} \left[\frac{1}{\bar{S}} \frac{dW}{da} \right] \quad (35)$$

where the quantity in the brackets is the quantity given by Equation (34) and \bar{S}/δ is the strength-to-spacing ratio. Thus at any position a in the path, an expression for $d\bar{\tau}/da$ can be obtained if band model parameters along the whole path are available. The band model parameters required are $k = \bar{S}/\delta$ and y as a function of temperature (and frequency).

The computational procedure used here operates as follows. Given a non-isothermal, non-isobaric path of known temperature and composition, it is first divided into a number of segments, each of which can be considered sensibly isothermal. The number of integrals into which a path must be broken for accurate representation, which has been investigated by Young^[12], depends on the path composition. In our routine, this break-up can be performed either automatically or manually.

Once the path is broken up into n segments, the following variables are determined for each:

$$y_i = y_0(T_i) \cdot p_{bi} \quad (36)$$

$$\Delta a_i = p_{ei} \cdot l_i$$

$$\Delta(ak)_i = k(T_i) \cdot p_{ei} \cdot l_i$$

where k is the average strength-to-spacing ratio for temperature T_i , p_{ei} is the effective absorbing pressure of the active gas (either CO_2 or H_2O) in atmospheres at STP, and l_i is the length of the segment. The variable y is dimensionless; furthermore, the reference pressure for the value of γ in y is one atmosphere — so that the pressure in atmospheres can be used to preserve the dimensionless character of y . To retain identity with previous work, we have used optical path length in atmosphere-cm. Thus,

$$p_{ei} = p_{ia} \cdot \frac{273.15}{T_i}$$

where p_{ia} is the actual partial pressure of the active gas in segment i . This temperature adjustment on the pressure is required to insure correspondence between the optical path length in atm-cm and the number of absorbing molecules in a unit cross-section of path. The above definition for p_{ei} allows easy comparison with the AFCRL line tabulation^[2]. Since the variable k is the strength-to-spacing ratio, it will have the units of the reciprocal of the optical path. (Strength has the units of wavenumber per optical path unit; spacing is in units of wavenumber.) Thus the products $\Delta(ak)_i$ are unitless.

p_{bi} , which is the broadening pressure, is given by

$$p_{bi} = p_{ai} + \sum_j \alpha_{aj} p_{ij}$$

where the sum over j is a sum over all the other species present and α_{aj} is the broadening coefficient for species j with the active species a . p_{ij} is the pressure of species j in path segment i . Since few accurate values for such broadening coefficients are actually available, we assume that all other species broaden like air and use the values for H_2O and CO_2 valid for air-broadening

$$\alpha(H_2O, \text{air}) = 0.2$$

$$\alpha(CO_2, \text{air}) = 0.77$$

$y_0(T_i)$ is the 2nd band-model parameter at one atmosphere pressure and temperature T_i obtained from band-model tabulations.

From the optical depth, we take an average value \bar{y} and define a dimensionless quantity u :

$$\bar{y}_i = \frac{\sum_{j=1}^i \Delta(ak)_j \cdot y_j}{\sum_{j=1}^i \Delta(ak)_j} \quad (37)$$

$$u_i = \frac{\sum_{j=1}^i \Delta(ak)_j}{2\pi\bar{y}_i}$$

The average inverse temperature is also calculated:

$$\bar{q}_i = \frac{\sum_{j=1}^i \Delta(ak)_j \cdot \frac{1}{T_j}}{\sum_{j=1}^i \Delta(ak)_j} \quad (38)$$

$$\text{where } q_j = \frac{1}{T_j}.$$

The transmittance derivative is now computed at both ends of every path segment. This is accomplished from Equation (35):

$$\frac{d\bar{\tau}}{da} = \bar{\tau} \cdot \frac{\bar{S}}{S} \cdot \left(\frac{1}{S} \frac{dW}{da} \right) = \bar{\tau}(a)k(a)f\left(u, \frac{\alpha}{\bar{\alpha}}, \frac{q}{\bar{q}}\right)$$

At the near edge of segment i ,

$$u_{near,i} = u_{i-1}$$

$$\frac{\alpha}{\bar{\alpha}}_{near,i} = \frac{y_i}{\bar{y}_{i-1}} \frac{q_i}{\bar{q}_{i-1}}$$

$$\frac{q}{\bar{q}}_{near,i} = \frac{q_i}{\bar{q}_{i-1}}$$

and

$$\frac{d\bar{\tau}}{da}_{near,i} = \bar{\tau}_{i-1} k_i f \left[u_{i-1}; \frac{\alpha}{\bar{\alpha}}_{near,i}; \frac{q}{\bar{q}}_{near,i} \right]$$

For the far boundary of each segment, the corresponding values are

$$u_{far,i} = u_i$$

$$\frac{\alpha}{\bar{\alpha}}_{far,i} = \frac{y_i}{\bar{y}_i} \frac{q_i}{\bar{q}_i}$$

and

$$\frac{d\bar{\tau}}{da}_{far,i} = \bar{\tau}_i k_i f \left[u_i; \frac{\alpha}{\bar{\alpha}}_{far,i}; \frac{q}{\bar{q}}_{far,i} \right]$$

The transmittances $\bar{\tau}$ used in these expressions were obtained from the curve-of-growth for this band model. This expression has been shown to be identical to that given by Goody for an inverse strength distribution of lines (see Reference 3, Equation 4.37).

$$\bar{\tau}_i = 2\pi y_i \left[e^{-u_i} I_0(u_i) + 2u_i e^{-u_i} (I_0(u_i) + I_1(u_i)) - 1 \right] \quad (39)$$

I_0 and I_1 are Bessel functions of the first kind with imaginary arguments. Values for I_0 and I_1 were taken from [11].

The effective transmittance derivative for a given segment is taken to be the average of the near and far values for that segment:

$$\Delta\bar{\tau}_i = \frac{d\bar{\tau}}{da} \Big|_i \cdot \Delta a_i = \frac{1}{2} \left[\frac{d\bar{\tau}}{da} \Big|_{far,i} + \frac{d\bar{\tau}}{da} \Big|_{near,i} \right] \Delta a_i$$

In order to ensure consistency between these derivatives and the $\bar{\tau}$ values used for farther segments, the transmittance at the far boundary of each segment is modified, after the transmittance derivative calculations, to be equal to the transmittance at the near boundary of that segment minus the transmittance change determined for that segment:

$$\bar{\tau}_i = \bar{\tau}_{i-1} - \Delta\bar{\tau}_i$$

Thus, only $\bar{\tau}_1$ remains unchanged from its value obtained directly by Equation (39).

The values of $\Delta\bar{\tau}_i$ are then used directly in a form analogous to Equation (6) to obtain the radiance

$$\bar{L}_\nu = \sum_{i=1}^n L_\nu^*(\tau_i) \cdot \Delta\bar{\tau}_i$$

These procedures provide means by which the band model developed here is used to compute radiances of non-isothermal paths.

It is not clear how the number of segments into which the path is divided affects the results of the calculation. This is the most important aspect yet to be analyzed in the calculations themselves. It is not sufficient to divide the path into segments of the order of the temperature-scale-length because more variables than temperature are involved. Since $d\bar{\tau}/da$ is not constant within a segment even though the segment is isothermal, it appears that a careful treatment of the number of segments is required. Young states that, for near homogeneous paths, the Lindquist-Simmons approximation requires a larger number of segments. The process described here provides a treatment for the first path element which is identical to that provided by an isothermal treatment and, hence, should do a good job for the first segment. On the other hand, when the second and third and subsequent segments are of similar composition to the first, the treatment of their elements by the present procedure is not so easily examined. These unknown properties of the current calculation procedures should be carefully examined.

3

MEASUREMENTS OF THE HOT WATER VAPOR AND CO₂ RADIANCE AS VIEWED THROUGH COOL WATER VAPOR AND CO₂

No definitive set of measurements existed which accurately characterizes the amount of correlation actually present between hot and cold water vapor and CO₂ lines in the bands of interest for plume measurements. Burch^[1] made several measurements which served only to demonstrate the effect. We are aware of no other controlled measurements of this correlation. Therefore a portion of the present program was devoted to the measurement of the radiance of hot water and CO₂ as viewed through cool mixtures of the same gases. These measurements can be looked upon as measurements of the degree to which the product rule discussed in Section 2 holds, or as measurements of the transmittance derivative, or they can be compared directly to band model techniques of various types.

We originally planned to measure the transmittance derivative directly. The measurements were to involve the radiance of a very short isothermal hot cell viewed through a long cold cell. This situation would closely approximate a measurement of the integrand of Equation (5). Actually, however, a hot cell 60 cm long was required to obtain a large enough radiance signal to be measured accurately. In the frequency bands of interest, at conditions applicable to plume studies, this cell length produces optical paths extending into the square root region at many wavelengths. The measurements are valid measurements of the effect of line correlation, but band model calculations are required to extract transmittance derivatives from them.

The measurements are of emission-absorption spectra of a two-element optical path. The two elements consist of (a) a heated cell filled with a mixture of CO_2 , H_2O , and nitrogen (and, in a few cases, other gases to simulate the combustion products present in a rocket exhaust) and (b) a long cell at ambient temperature filled with mixtures of H_2O , CO_2 , and nitrogen to simulate atmospheric paths. The cool cell is a multiple pass evacuable cell capable of operation at a variable number of path lengths. The two paths were arranged in series so that the instruments viewed the hot cell through the cool cell.

The detection apparatus consisted of a commercial grating monochromator and detector set up to give spectral resolution appropriate to band model methods. A heated blackbody source was used for the absorption measurements. The instrument was always operated as a dual-beam instrument in that the measurements were always referred to identical measurements made through a nitrogen-flushed reference beam. The latter was identical in configuration to the sample beam except that a long cool cell was present only in the sample beam. Every spectral scan was taken as the ratio of the energy in the sample beam to the energy received in the reference beam. This served to compensate for source variations and for residual ambient atmospheric absorption not eliminated in the system by other means.

3.1 DETAILED EXPERIMENT DESCRIPTION

Hot-through-cold radiative transfer measurements were performed with the experimental system shown schematically in Figure 5. The hot gas sample was placed in a 60 cm alumina cell with sapphire windows (H/C) and maintained at the desired temperature by an electrically heated oven (0). The long ambient-temperature absorbing path was obtained using a multiple pass White cell (W/C) capable of path lengths up to 200 meters^[13]. The White cell could be put in or out of the optical path by means of a sliding carriage on which mirrors F_1 , F_2 , and F_3 were mounted. Spherical mirrors S_1 and S_2 were used in conjunction with flats F_1 , F_4 and F_2 , F_3 respectively to match the F-number of the White cell with that of the optical system.

13. G.H. Lindquist, et al., Investigations of Chemical Laser Processes, Report No. 191300-1-P, Environmental Research Institute of Michigan, Ann Arbor, Michigan, February 1973.

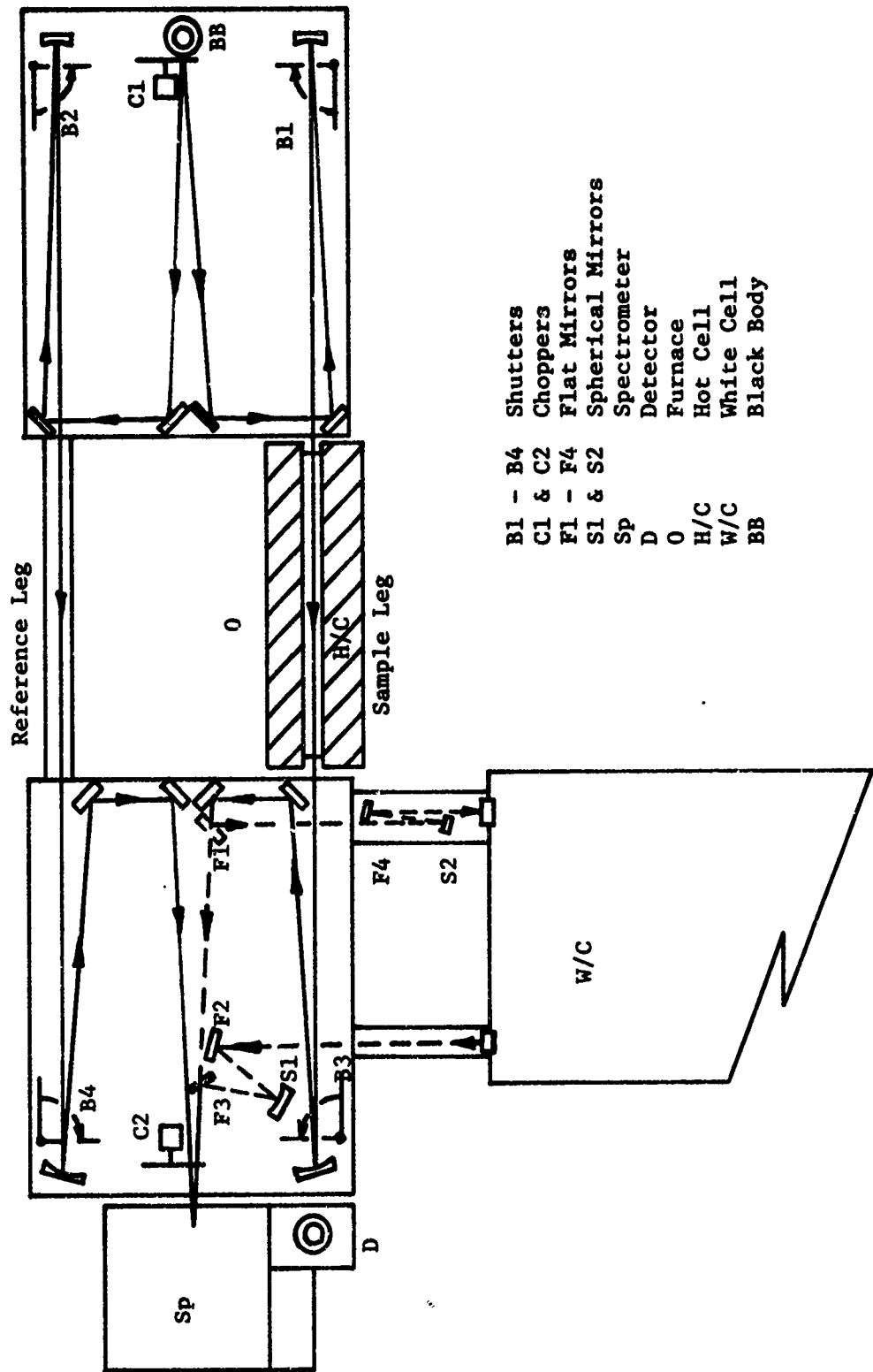


FIGURE 5. EXPERIMENTAL SYSTEM USED FOR RADIATIVE TRANSFER MEASUREMENTS

Radiation from the blackbody source (BB) was split into two beams: a reference beam chopped at 420 Hz and a sample beam chopped at 780 Hz. After passing through separate legs of the system, these beams were recombined at a Perkin-Elmer Model 99G spectrometer (Sp), detected with a single nitrogen-cooled detector (D), and synchronously amplified using two lock-in amplifiers operating at 420 and 780 Hz respectively. Signals from these amplifiers were digitized and ratioed using a Hewlett-Packard digital voltmeter. They were then punched on computer cards for data reduction. Background atmospheric absorption in the paths traversed by both beams was minimized by flushing the entire system with dry nitrogen obtained from the boil-off of a liquid nitrogen tank. Figure 6(a) shows an overall view of the measurement system.

Both emission and absorption scans were performed with the same system. For an absorption measurement all shutters (B_1 , B_2 , B_3 , B_4) were left open and chopper C_1 was operated with chopper C_2 stationary. In this configuration any radiation emitted by the hot gas was unchopped and would not be detected. For an emission scan, shutter B_1 was closed and chopper C_2 operated with chopper C_1 stationary. This eliminated blackbody radiation from the sample side of the system and chopped all emitted radiation. As will be seen below, both absorption and emission scans are required to characterize the emission and absorption of the path in the system.

Measurements were made both on the $2.7 \mu\text{m}$ water vapor- CO_2 band and the $4.3 \mu\text{m}$ CO_2 band. The system configuration was somewhat different for each of the two spectral bands. Table 2 summarizes these differences.

The line correlation effect to be observed is temperature dependent; hence, measurements at a variety of hot cell temperatures would be desirable. However, a temperature near 1200°K was required to obtain the necessary signal levels. This temperature was very close to the highest which the cell could sustain without softening of the window seals. Because of these two considerations the measurements were limited to 1200°K .

To ensure even heat distribution, a 60 cm alumina hot cell was enclosed in a Monel tube which, in turn, was surrounded by seven individually controllable furnace elements. The alumina hot cell is shown in Figure 6(b). The thermocouples placed along the Monel tube monitored the cell temperature. The furnace elements were adjusted manually to achieve isothermal conditions along the hot cell.

3.2 HOT CELL CONSTRUCTION

The construction of the hot cell posed substantial problems. A fused quartz cell was available for this program which would sustain the high temperatures required. It was used for preliminary measurements at $2.7 \mu\text{m}$, but did not transmit beyond about $3 \mu\text{m}$. Sapphire appeared to be the only window material capable of both withstanding the high temperatures

TABLE 2. SPECTROMETER PARAMETERS

	<u>2.7 μm Measurements</u>	<u>4.3 μm Measurements</u>
Detector	Cooled PbS	Cooled InSb
Grating	64 mm \times 64 mm Bausch & Lomb replica 100 grooves/mm, 5.18 μ m blaze	
Slit Width	500 μ m	150 μ m
Spectral Resolution	14 cm^{-1}	3.2 cm^{-1}

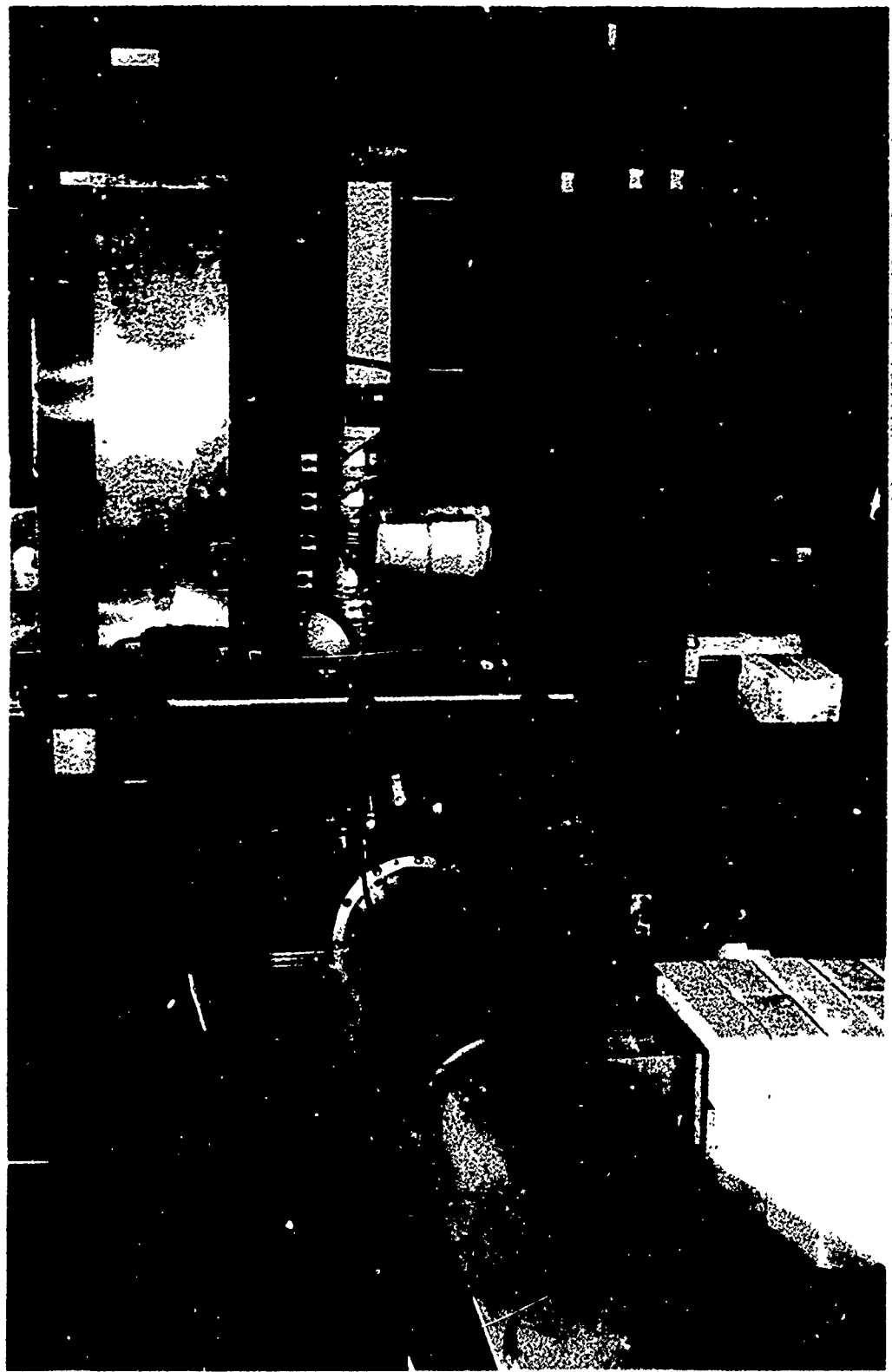


FIGURE 6. PHOTOGRAPHS OF EXPERIMENTAL APPARATUS
(a) Overall



(b) Alumina Hot Cell

FIGURE 6. PHOTOGRAPHS OF EXPERIMENTAL APPARATUS

and of transmitting beyond $3 \mu\text{m}$. However, in previous programs we had never succeeded in maintaining a seal between a sapphire window and a cell material at temperatures near 1200°K .

At the beginning of the program we obtained information about a sealing process, from National Beryllia Corporation, which was demonstrated to maintain a vacuum-tight seal between sapphire and alumina. It was our plan to purchase a custom-made cell from National Beryllia consisting of a 60-cm long, 1-inch diameter alumina tube with sapphire windows sealed to it with the National Beryllia process. However, a furnace capable of firing such a long cell was not available.

A number of unsuccessful attempts were made to seal the windows to the cell by obtaining optical contact between sapphire windows and the ends of an alumina tube. We did succeed in making seals at room temperature with such a technique; but when the cell was heated, differential thermal expansion of the alumina tube always caused the seal to fail over at least a portion of the seal.

A sample of the frit used in the National Beryllia sealing process had been obtained earlier along with instructions for its use. After several unsuccessful attempts to find furnaces capable of performing the required firings, we finally built a simple propane-gas-fired brick kiln of the appropriate dimensions to enclose the cell. The sapphire windows were successfully fired onto the cell with this kiln using the National Beryllia frit. An NBS-calibrated optical pyrometer was used to measure the critical firing temperatures. The windows were held to the alumina tube during firing by applying a very slight vacuum to the fill tube which had been previously fired to the alumina tube.

This process was ultimately successful in obtaining a rugged gas-tight cell with sapphire windows capable of withstanding temperatures of 1200°K - see Figure 6(b). We consider the successful construction of this cell to be a significant technological accomplishment, particularly in view of the many previously unsuccessful attempts to construct such a cell, both on this and several previous contracts.

3.3 COLD CELL CONSTRUCTION

The cold cell was an evacuable 5 meter-long multiple-pass White cell constructed for this effort. In a cell of this type the energy entering the cell at the entrance slit, where the incoming energy is focussed, is reimaged by a spherical mirror at the far end of the cell onto a second spherical mirror at the near end of the cell. This mirror directs the energy onto a second spherical mirror at the far end of the cell which, in turn, redirects the energy back to another position on the front mirror. This process continues, alternating between the two spherical mirrors at the far end of the cell until the energy focussed back on the front mirror coincides with the position of the exit slit. Figure 7 is a schematic of the cell showing the light path.

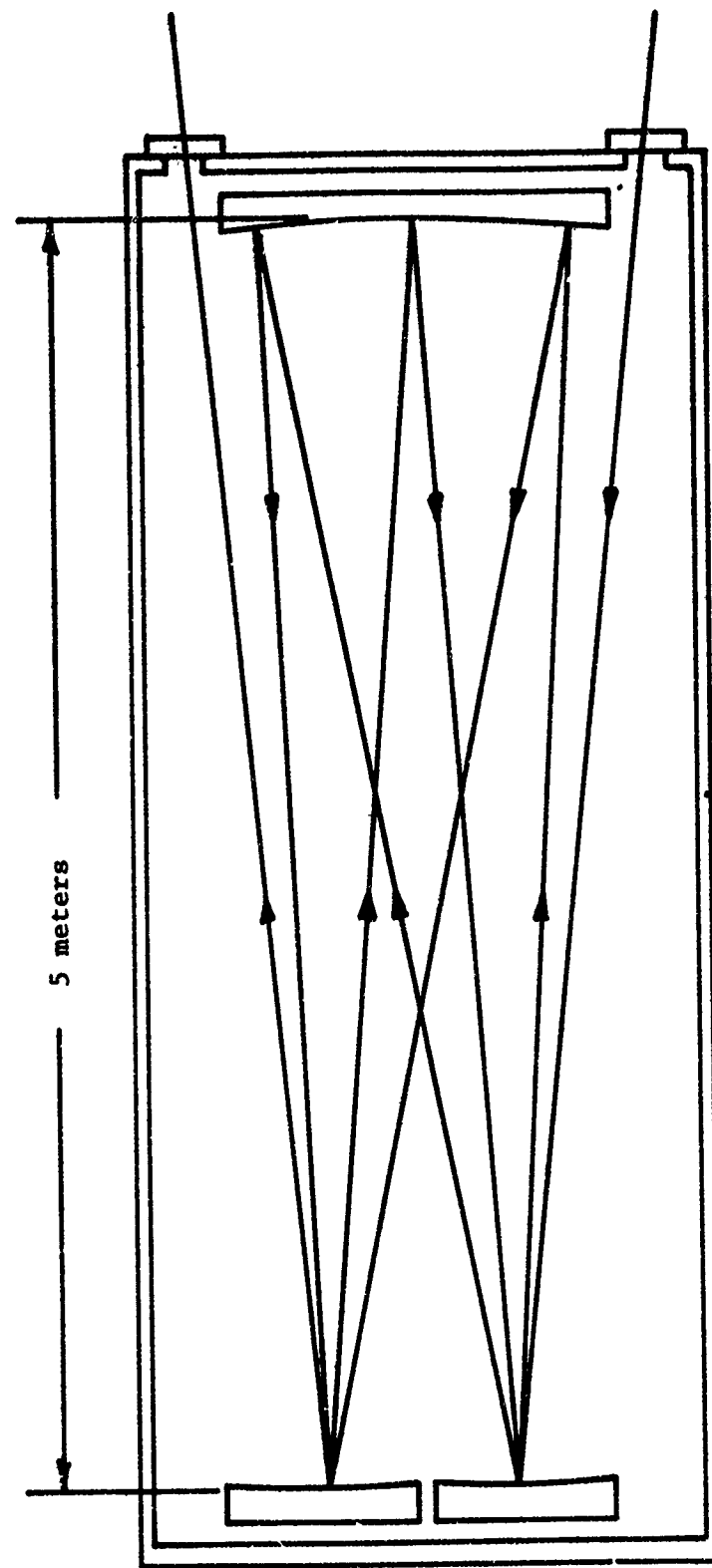


FIGURE 7. 5 METER "WHITE" CELL EIGHT-PASS MODE SHOWN

The cell was made of thick wall hard aluminum tubing. The mirror mounts were designed to be as immune as possible to vibration. Vibration effects become significant at total path lengths near 200 m (40 passes). Most measurements were made at a 100 m path length (20 passes).

3.4 GAS HANDLING SYSTEM

Since measurements were to be made on mixtures of a number of gases, a manifold system was constructed whereby any desired mixtures of gases could be applied to the cold cell and the hot cell individually. The basic pressure measurements for the filling process were made using a capacitance manometer capable of reading from 0.01 to 100 mm of Hg. Higher pressures were measured with a Wallace and Tiernan high accuracy pressure gauge in the case of the hot cell, and a mercury manometer in the case of the cold cell. The water vapor was obtained from a constant temperature bath of distilled water, which also served as a check on the accuracy of the capacitance manometer.

The filling process for either cell was carried out by first filling the cell with the gas to be present at the lowest partial pressure. Subsequent gases were added in the order of increasing desired partial pressures. This procedure, in addition to the excellent reproducibility and accuracy of the capacitance manometer, made accurate fills possible.

Adsorption effects were noted for water vapor, particularly in the hot cell. The account for these effects, the water vapor pressure was allowed to equilibrate until the pressure read on the capacitance manometer agreed with the equilibrium vapor pressure of the water bath. Additional gases were added to the hot cell only after this equilibration process was complete. No adsorption effects were observed for any of the other gases used. As a result of this observation, the assumption was made that the presence of the other gases did not alter the equilibrium between the water vapor in the cell and the water adsorbed on the cell walls.

Based on the published accuracy of the capacitance manometer system and on calibrations made with constant temperature baths, and considering our attempts to assure cell equilibrium, it is our opinion that the cell fills are accurate to within several percent.

3.5 THE EFFECT OF THE CELL WINDOWS ON THE MEASUREMENTS

Since the hot gas cell is maintained at an elevated temperature the emissions of the cell windows, as well as their absorption and reflection, must be accounted for if a true gas emission is to be determined. For an optically thick material it may be shown that the emission at a given wavenumber $\tilde{\nu}$ is given by

$$L_{\tilde{\nu}} = L_{\tilde{\nu}}^* \alpha_{\tilde{\nu}} \quad (40)$$

where $L_{\tilde{\nu}}$ is the spectral radiance of the material, α its absorptance and $L_{\tilde{\nu}}^*$ the spectral radiance of a blackbody at the same temperature. For a thin optically transparent material

like the windows of the cell used here, multiple reflections must be taken into account. In this case the spectral radiance is given by

$$L_{\nu} = L_{\nu}^* \rho(\alpha - \alpha^2) + \alpha / [1 - \rho^2(1 - \alpha)^2]$$

or

$$L_{\nu} = L_{\nu}^* \alpha / [1 - \rho(1 - \alpha)] \quad (41)$$

Here α and ρ are the hot cell window absorptance and reflectance. For simplicity, the spectral dependences of α and ρ are ignored.

At 1200°K, for the sapphire windows used, $\alpha \sim 0.18$ and $\rho \sim 0.07$ in the $4.3 \mu\text{m}$ band, and $\alpha \sim 0.02$ and $\rho \sim 0.07$ at $2.7 \mu\text{m}$. Although this implies an error of

$$\frac{1}{1 - \rho(1 - \alpha)} = \begin{cases} 1.061 & \text{at } 4.3 \mu\text{m} \\ 1.074 & \text{at } 2.7 \mu\text{m} \end{cases}$$

if multiple reflections are ignored, it may be shown that the correction to the hot gas radiance or hot-through-cold radiance is given by

$$(1 - \alpha) / \left\{ 1 - \frac{\alpha}{[1 - \rho(1 - \alpha)]} \right\}$$

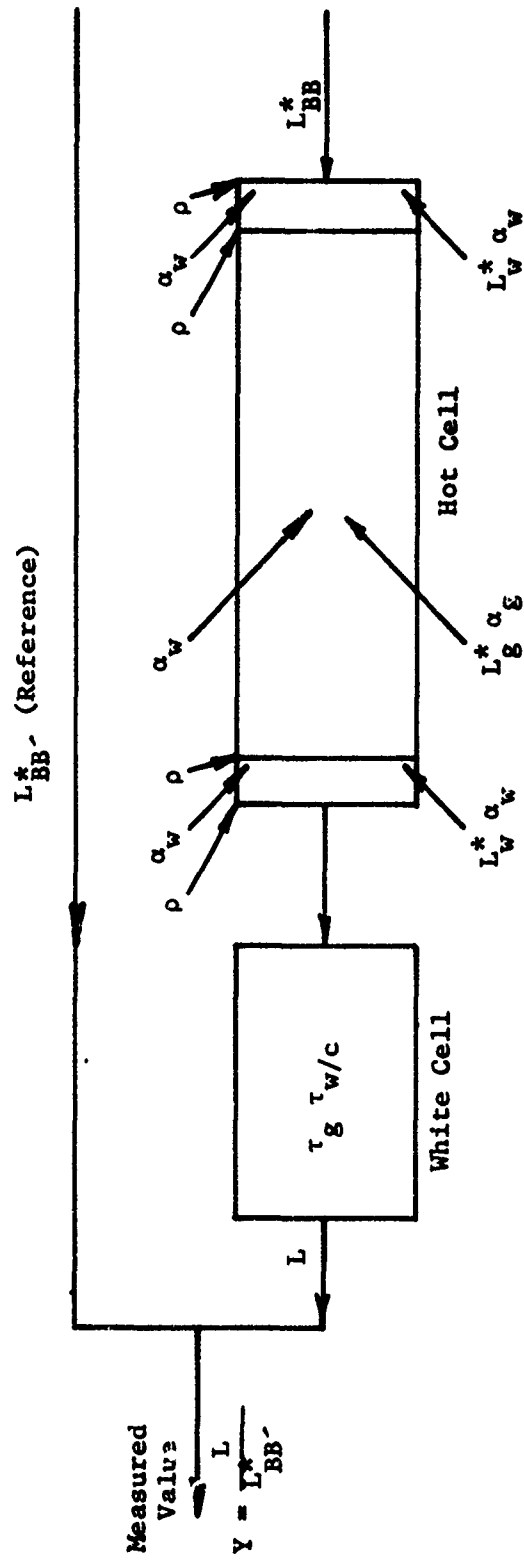
Therefore, neglecting multiple reflections introduces an error of $\sim 1\%$ at $4.3 \mu\text{m}$ and $\sim 0.1\%$ at $2.7 \mu\text{m}$. Because of the added complexity in accounting for the multiple reflections, and because we do not expect accuracies better than about 5% from the system as a whole, multiple reflections have been ignored.

As a result of the complications introduced by the alumina cell, measured radiances do not give the derived hot through cold radiance directly. This may be appreciated by writing an explicit expression for the observed radiance in terms of the optical parameters of the experimental system. Using the notation of Figure 8, and assuming that the hot cell is isothermal throughout, we can set

$$L_w^* = L_g^* = L^*$$

Again, the spectral dependence is suppressed for simplicity. The measured radiance Y of the hot cell and its gas sample as seen through the long cold path is, therefore,

$$Y = \frac{L^*}{L_{BB}^*} \alpha_g \tau_{w/c} \tau_g (1 - \rho)^2 (1 - \alpha_w) [1 - (1 - \rho) \alpha_w] + \frac{L^*}{L_{BB}^*} (1 - \rho) \alpha_w \tau_{w/c} \tau_g [1 + (1 - \rho)^2 (1 - \alpha_w)] \quad (42)$$



ρ = Window Reflectance
 α_w = Window Absorptance
 α_g = Gas Absorptance
 τ_g = Transmittance of Gas
 in White Cell
 $\tau_{w/c}$ = Transmittance of Empty
 White Cell

$L^*_{BB'}$ = Blackbody Radiance
 Sample Side
 $L^*_{BB'}$ = Blackbody Radiance
 Reference Side
 L^*_{k} = Blackbody Radiance at
 Temperature of Material - k
 L = Total Radiance
 Sample Side

FIGURE 8. NOTATION USED IN DERIVING THE HOT THROUGH COLD RADIANCE MEASUREMENT EXPRESSION

again ignoring multiple reflections within the cell windows. This equation was obtained by summing the contributions from the rear window, the gas in the cell, and the front window, and then separating out those terms containing α_g .

The desired output is the radiance of the hot gas as viewed through the White cell. In terms of the variables of Figure 8, this is given by inversion of Equation (42) as

$$L^* \alpha_g \tau_g = \frac{Y - \frac{L^*}{L_{BB}^*} (1 - \rho) \alpha_w \tau_w \tau_{w/c} \left[1 + (1 - \rho)^2 (1 - \alpha_w) \right]}{(1 - \rho)^2 (1 - \alpha_w)^2 \left[1 + \frac{\rho \alpha_w}{(1 - \alpha_w)} \right] \tau_{w/c}} L_{BB}^* \quad (43)$$

Since the bracketed term in the denominator is on the order of 1.01 with sapphire windows at the experimental conditions used, it may be taken equal to unity with negligible error. Additional measurements are necessary in order to account for the terms $(1 - \rho) \alpha_w \tau_{w/c} \left[1 + (1 - \rho)^2 (1 - \alpha_w) \right]$ and $(1 - \rho)^2 (1 - \alpha_w)^2$. The following measurements are convenient for this: an emission measurement with the White cell and hot cell empty ($\alpha_g = 0$, $\tau_g = 1$), which we call a "cell" scan, given by

$$\text{Cell} = \frac{L^*}{L_{BB}^*} (1 - \rho) \alpha_w \left[1 + (1 - \rho)^2 (1 - \alpha_w) \right] \tau_{w/c}$$

and another emission measurement similar to the "cell" scan except with the blackbody shutter B1 open to the sample side of the system ("Beam" scan)

$$\text{Beam} = \left\{ \frac{L_{BB}^*}{L_{BB}^*} (1 - \rho)^4 (1 - \alpha_w)^2 \right\} \tau_{w/c} + \text{cell}$$

In terms of these measurements, the hot through cold radiance is

$$L_g \tau_g = L^* \alpha_g \tau_g = \left[\frac{Y - \text{cell} \tau_g}{\text{Beam} - \text{cell}} \right] L_{BB}^* (1 - \rho)^2 \quad (44)$$

The blackbody radiance L_{BB}^* may be calculated using the Planck function once its temperature is determined with an optical pyrometer and the hot cell window reflectance ρ is calculated from refractive index data. Consequently, the only unknown in this equation is the transmission of the cold gas sample in the White cell (τ_g). This parameter may be evaluated using the "Beam" scan above and an identical scan made with the White cell filled. In this case,

$$\tau_g = \frac{\text{Beam (White cell filled)}}{\text{Beam (White cell empty)}} \quad (45)$$

where it is assumed that, because there is no correlation between the transmission of the White cell itself and the cold gas sample, the total transmission of this system is $\tau_g \tau_{w/c}$.

Determination of hot through cold radiance therefore requires four individual scans:

Y = emission measurement of hot cell and hot gas viewed through a long cold path

Cell = emission measurement of empty hot cell

Beam (White cell empty) = emission measurement of empty hot cell with blackbody radiation background, White cell empty

Beam (White cell filled) = emission measurement of empty hot cell with blackbody radiation background, White cell filled

3.6 SYSTEM CHECKS

During data taking the oven temperature was continuously monitored with ten thermocouples placed along the length of the alumina cell. The internal consistency of the data can be tested by calculating an apparent temperature for the emitting gas and comparing this value with the oven thermocouple temperatures. The radiance and the absorption of the hot cell alone (cold cell evacuated) as measured by the system is used in the inverse Planck function to determine an apparent temperature T^* .

$$T^* = \frac{hc\tilde{\nu}}{k} \left/ \log_e \left[\frac{2hc^2\tilde{\nu}^3\alpha_g}{L_g} + 1 \right] \right. \quad (46)$$

where L_g is the measured gas spectral radiance obtained from the scans of Equation (42) with the cool cell empty, h is Planck's constant, c the speed of light, $\tilde{\nu}$ the spectral position in cm^{-1} , and α_g the absorption of the gas at wavenumber $\tilde{\nu}$.

Two additional scans are required to evaluate α_g independent of L_g : (a) an absorption scan (ABSO) with the hot cell filled and the cold cell empty and (b) an absorption background scan (ABSB) identical to the absorption scan but with both cells empty. From these two scans the hot gas absorption, α_g can be obtained:

$$\alpha_g = \frac{\text{ABSB-ABSO}}{\text{AESB}} \quad (47)$$

and consequently T^* evaluated. The discrepancy between T^* and the oven temperature determined from the thermocouple readings is indicative of errors in the data taking or reduction procedures. These checks were performed on all measurements.

A second check was performed several times during the program to verify the pyrometric temperature reading of the blackbody. In this case the hot cell is filled with a gas sample which is opaque in the spectral region of interest ($\alpha_g = 1$). An emission scan made with this gas fill may then be used to determine the blackbody radiance as

$$L_{BB}^* = \frac{L_{T_0}^* \alpha_g}{\left[\frac{Y\text{-cell}}{\text{Beam-cell}} \right] (1 - \rho)^2} \quad (48)$$

where $L_{T_0}^*$ is the Planck function evaluated at the temperature of the oven; Y, "beam," and "cell" are the data scans mentioned earlier; and ρ is again the reflection loss at a single sapphire-air boundary. Once this spectral radiance is known, the blackbody temperature may be calculated from the inverse Planck function as in Equation (5), and compared with the pyrometric temperature measurement.

3.7 WAVELENGTH CALIBRATION

Wavelength calibration was performed in the $2.7 \mu\text{m}$ region by use of a small burner placed in the reference beam, which burned SF_6 and H_2 . HF, a primary combustion product of this reaction, has an absorption band in this region. The HF line positions are well known and the lines well isolated so that an accurate wavelength calibration was easily obtained.

In the $4.3 \mu\text{m}$ region, the calibration was performed by observing the CO fundamental at 2147 cm^{-1} ($4.66 \mu\text{m}$) using the cold cell and a path length of 100 meters. The CO lines are well separated and their positions well known so a calibration could be easily established.

Constants relating the optical frequency to the spectrometer drum-number were used in the data reduction program to relate the digitized experimental data to the optical frequency. Data were collected at equal drum-number increments so that knowledge of the beginning drum-number of each scan completely defined the optical frequency.

3.8 DATA REDUCTION

In addition to the digitally collected data, analog chart recordings were made as well. These were used as preliminary data checks to see that the system was operating as expected. They were particularly useful in noting drift in the system. A sample analog chart is shown in Figure 9.

The data scans were first examined for drift. Once noted, the data reduction program automatically applied drift corrections based on the noted drift punched on a header card. The initial drum-number of the scan was also punched on a header card; subsequent drum-number changes were checked by coding one data point every drum revolution.

The appropriate data scans—CELL, BEAM, ABSB, ABSO, Y (hot through cold), Y (hot alone), and BEAM (cold cell filled)—were read into the University of Michigan's 360 system and edited where necessary.

The data reduction program then matched all scans for drum-number and computed the required results using Equations (44) through (47). Results were obtained for: (a) hot cell

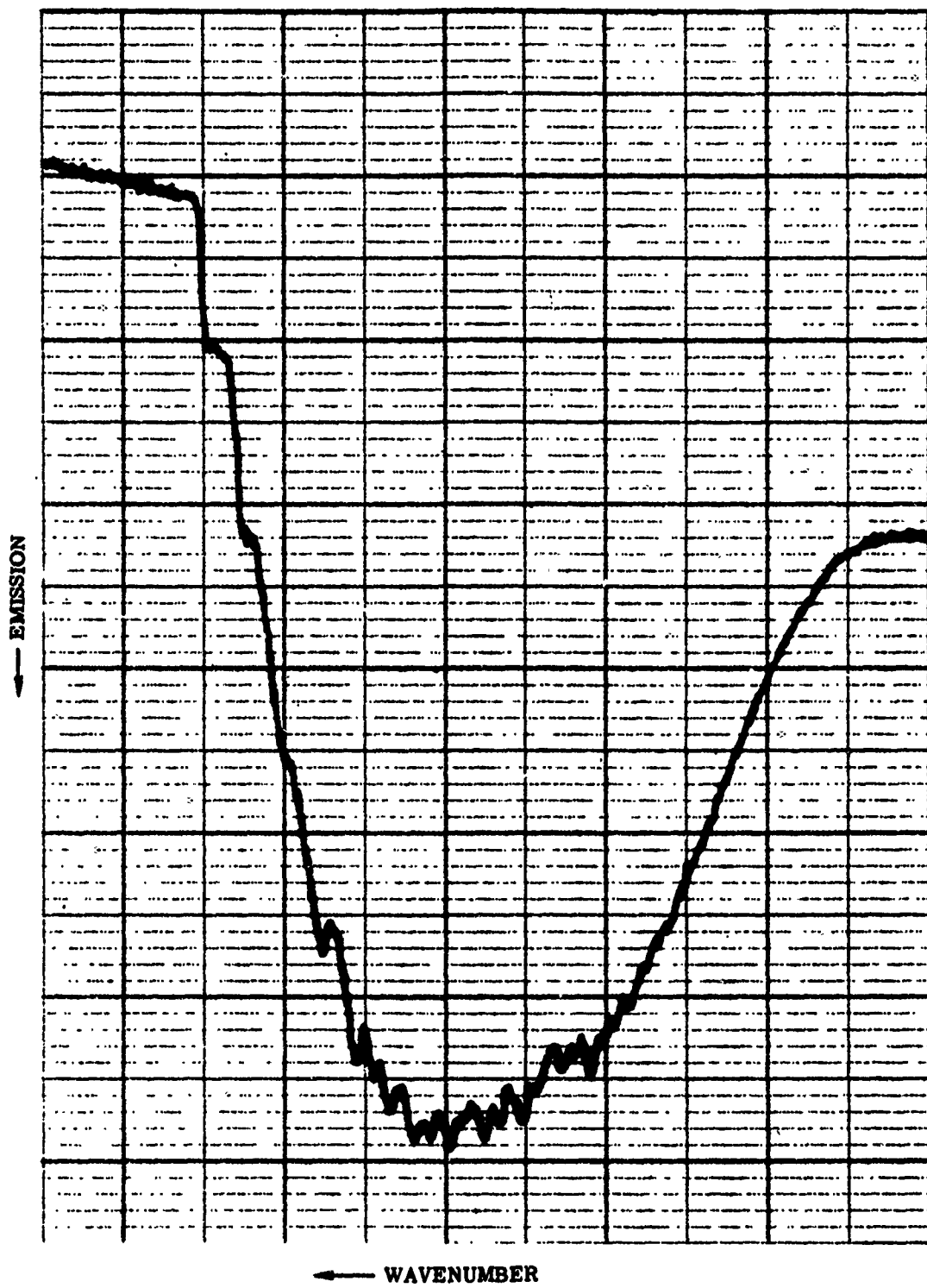


FIGURE 9. SAMPLE OF ANALOG CHART RECORDING (4.3 μm HOT CELL RADIANCE SHOWN)

radiance, (b) cold cell transmittance, (c) hot cell radiance as viewed through the cold cell, (d) hot cell absorptance, and (e) hot cell apparent temperature. Both data input and data output have been saved on tape. The outputs were automatically plotted on the plotting system at the University of Michigan Computing Center.

The apparent temperature plot was checked for consistency with the thermocouple readings. When apparent temperatures fell within about 25°C of the thermocouple temperature in the middle of the band (indicating radiance errors of less than 7%) and remained fairly uniform across the band (although showing deviations at both band edges), the data were assumed to be internally consistent. When these conditions did not exist, the raw data were re-examined for unnoticed drifts, and appropriate changes were made. If the data could not be made to satisfy these consistency criteria, the run was rejected and the tests repeated.

Note that while these consistency checks verify that measured emission values, absorption values, and temperature values all make sense, they have no bearing at all on the accuracy of the cell fill. The consistency checks monitor the radiometric accuracy of the measurements, but the manometer system is relied upon for the accuracy of the cell filling procedures.

3.9 RESULTS

During the program, tests were made with many different cell fills and the results of 15 tests are included in this report. Table 3 describes these tests. After successful operation has been confirmed using typical water vapor-nitrogen fills (Tests 8, 9, and 11), priorities for other mixtures were assigned by mutual agreement between ERIM and the Air Force, and subsequent runs were made in the order of these priorities. There were insufficient funds to obtain good data on all of the tests planned. Those placed at the top of the priority lists simulated real amine-fuel rocket exhausts (Tests 15 through 20). They were mixtures of water vapor, CO_2 , CO , H_2 , and N_2 at a total pressure of 0.1 atmosphere. Measurements were made at both $2.7 \mu\text{m}$ and $4.3 \mu\text{m}$ for 3 different atmospheric paths. Subsequent measurements were made of pure water vapor at $2.7 \mu\text{m}$, and pure CO_2 at $2.7 \mu\text{m}$ and $4.3 \mu\text{m}$. Detailed test conditions are shown with the data in Appendix B. The lack of funds eliminated some water vapor data with longer hot cell optical paths (Tests 12 through 14). In addition, tests to check the assumption that the correlation between lines of different absorbing gases is zero (Tests 4 and 10) were planned but not completed.

The results obtained from a typical water vapor run at $2.7 \mu\text{m}$ are shown in Figure 10(a-e). Five plots are shown. The first (a) is a plot of apparent temperature (T^*) versus frequency. It can be seen that the apparent temperature was within about $\pm 15^{\circ}\text{K}$ of the hot cell temperature (1202°K) over all of the band where significant absorption occurred; and at the ends of the band, where the cell began to become transparent, the apparent temperature makes large excursions to either side of the cell temperature. This is the proper appearance for these T^* determinations. The temperature deviation of $\pm 15^{\circ}\text{K}$ represents a radiance uncertainty of $\pm 5.6\%$, which is a reasonable accuracy for measurements of this type.

TABLE 3. SUMMARY OF MEASUREMENT CONDITIONS
(See Appendix B for detailed physical parameters)

Test No.	Priority No.	Spectral Region (μm)	Mixture	Hot Cell Pressure (Atm)	Optical Path (0.6 m long, 1200° K) (Atm-cm)	Path Simulated by Cold Cell (100 m long, 300° K) (length in km @ altitude in km)	
						200 @ 15	200 @ 15
1	7	2.7	CO_2/N_2	0.1	3	50 @ 15	50 @ 15
2	8	2.7	CO_2/N_2	0.1	3	10 @ 15	10 @ 15
3	9	2.7	CO_2/N_2	0.1	3	typical	typical
4*	14	2.7	--	typical	$\text{H}_2\text{O}/\text{N}_2$ fill	CO_2/N_2 fill	$\text{H}_2\text{O}/\text{N}_2$ fill
5	10	4.3	CO_2/N_2	0.1	3	200 @ 15	200 @ 15
6	11	4.3	CO_2/N_2	0.1	3	50 @ 15	50 @ 15
7	12	4.3	CO_2/N_2	0.1	3	10 @ 15	10 @ 15
8	--**	2.7	$\text{H}_2\text{O}/\text{N}_2$	0.1	3	86 @ 18	86 @ 18
9	--**	2.7	$\text{H}_2\text{O}/\text{N}_2$	0.1	3	28.8 @ 18	28.8 @ 18
10*	13	2.7	--	typical	CO_2/N_2 fill	CO_2/N_2 fill	$\text{H}_2\text{O}/\text{N}_2$ fill
11	--**	2.7	$\text{H}_2\text{O}/\text{N}_2$	0.1	3	288 @ 18	288 @ 18
12*	15	2.7	$\text{H}_2\text{O}/\text{N}_2$	0.3	9	200 @ 15	200 @ 15
13*	16	2.7	$\text{H}_2\text{O}/\text{N}_2$	0.3	9	50 @ 15	50 @ 15
14*	17	2.7	$\text{H}_2\text{O}/\text{N}_2$	0.3	9	10 @ 15	10 @ 15
15	6	4.3	Plume Mixture	0.1	--***	200 @ 15	200 @ 15
16	5	4.3	Plume Mixture	0.1	--***	50 @ 15	50 @ 15
17	4	4.3	Plume Mixture	0.1	--***	10 @ 15	10 @ 15
18	3	2.7	Plume Mixture	0.1	--***	200 @ 15	200 @ 15
19	2	2.7	Plume Mixture	0.1	--***	50 @ 15	50 @ 15
20	1	2.7	Plume Mixture	0.1	--***	10 @ 15	10 @ 15

*Not completed because of time and funding limitations.

**Completed before priority assignment.

***See tables in Appendix B.

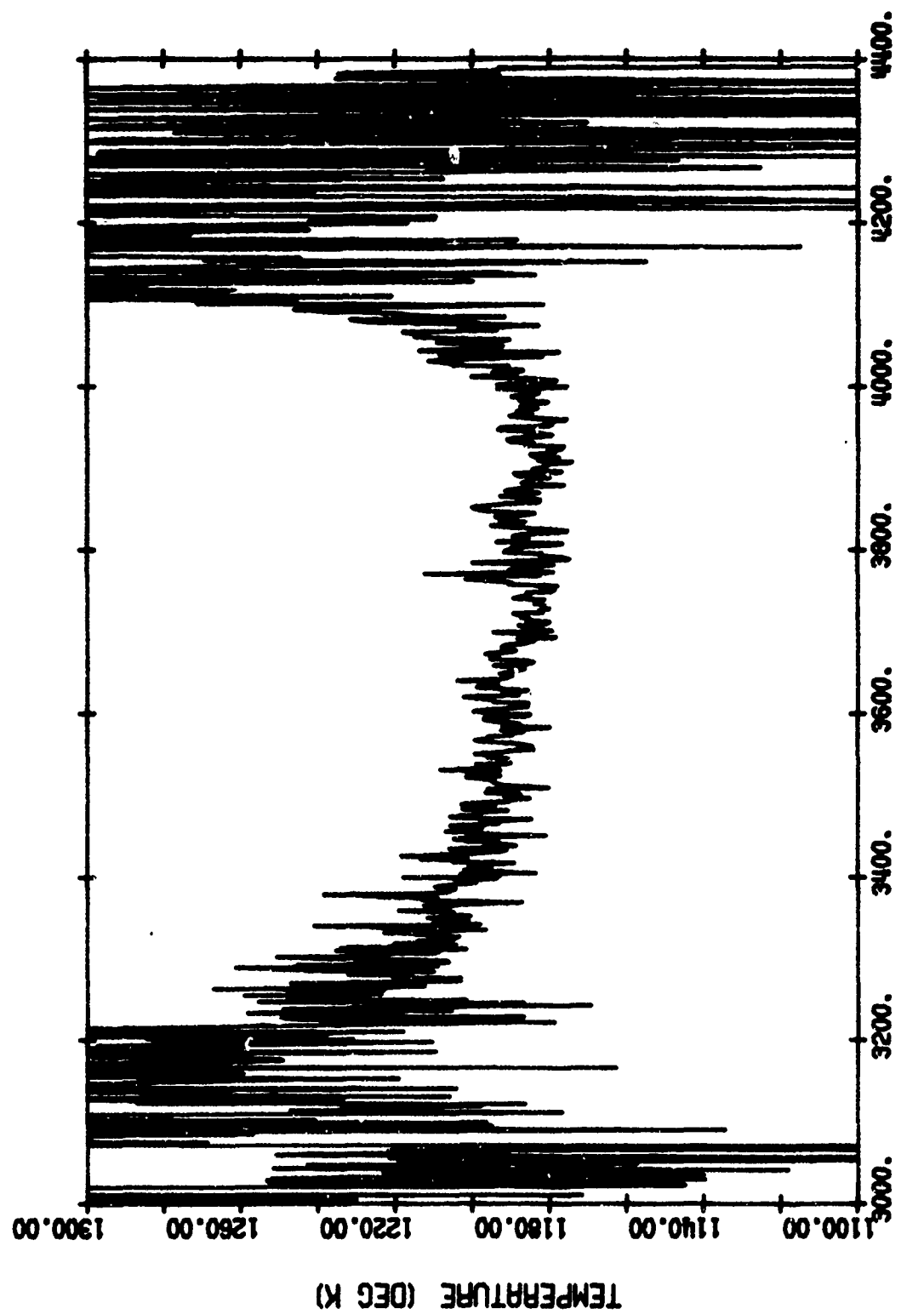
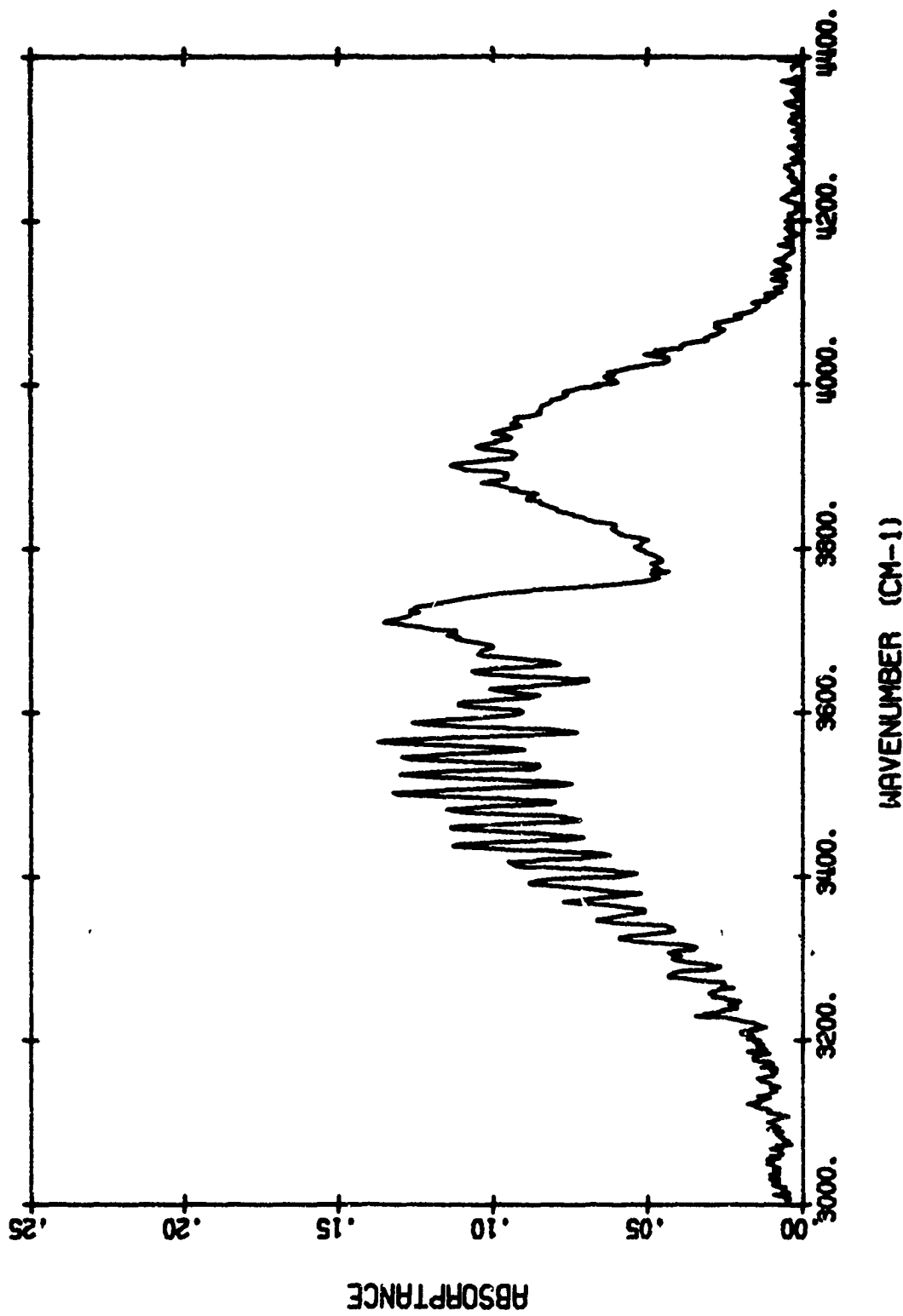


FIGURE 10. TYPICAL WATER VAPOR DATA (Continued)
(a) Measured Apparent Temperature



(b) Measured Hot Cell Absorptance

FIGURE 10. TYPICAL WATER VAPOR DATA (Continued)

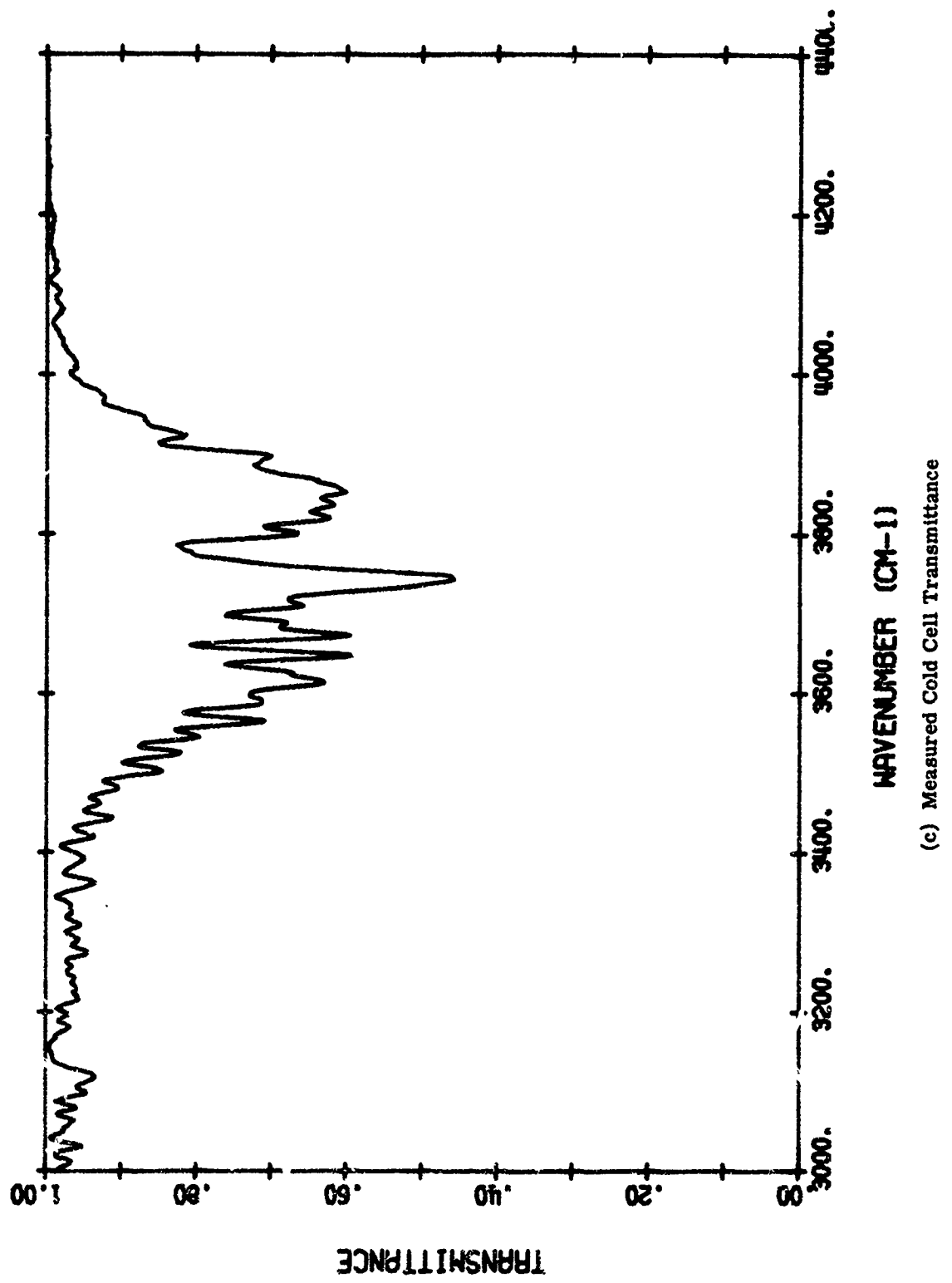
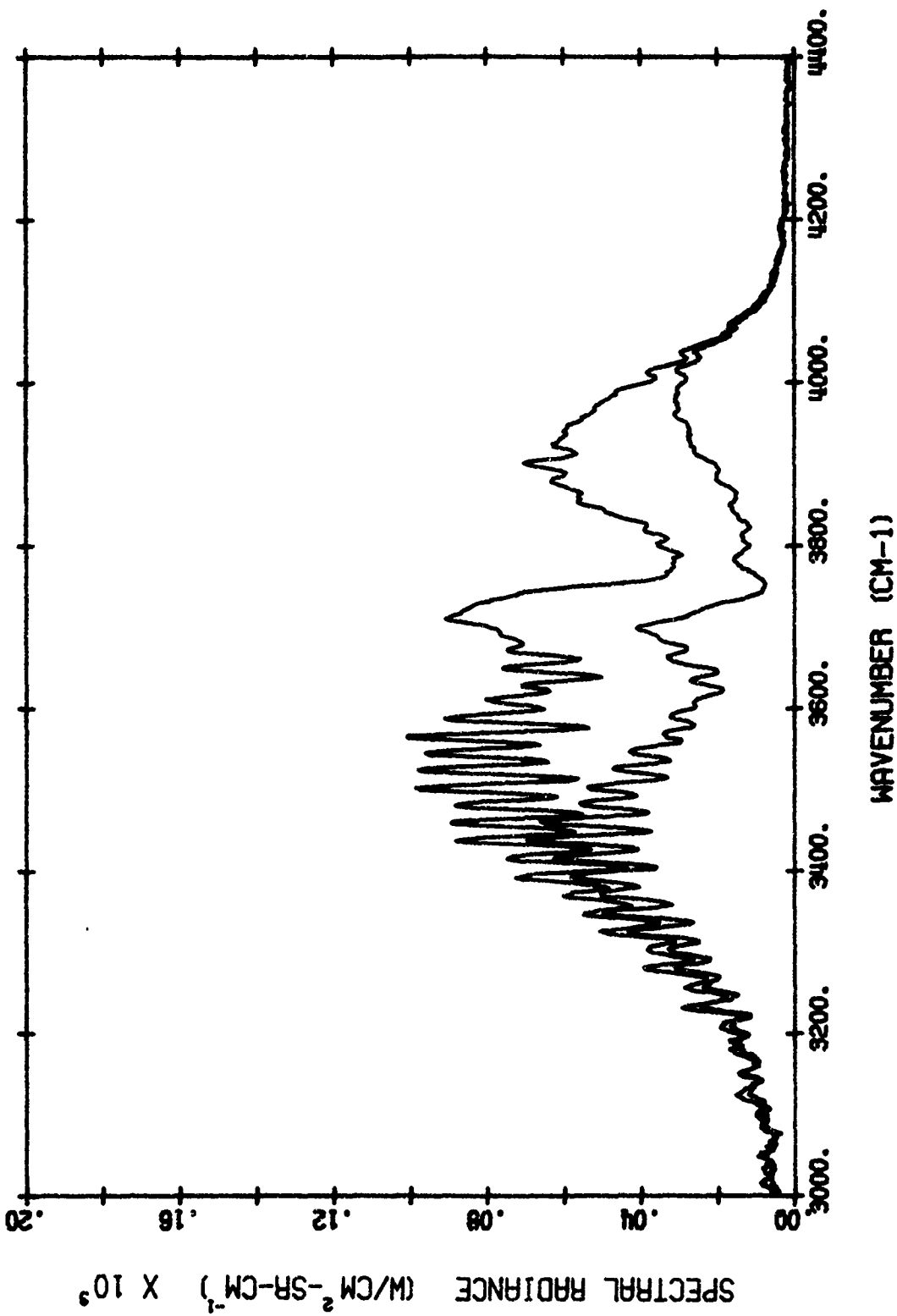
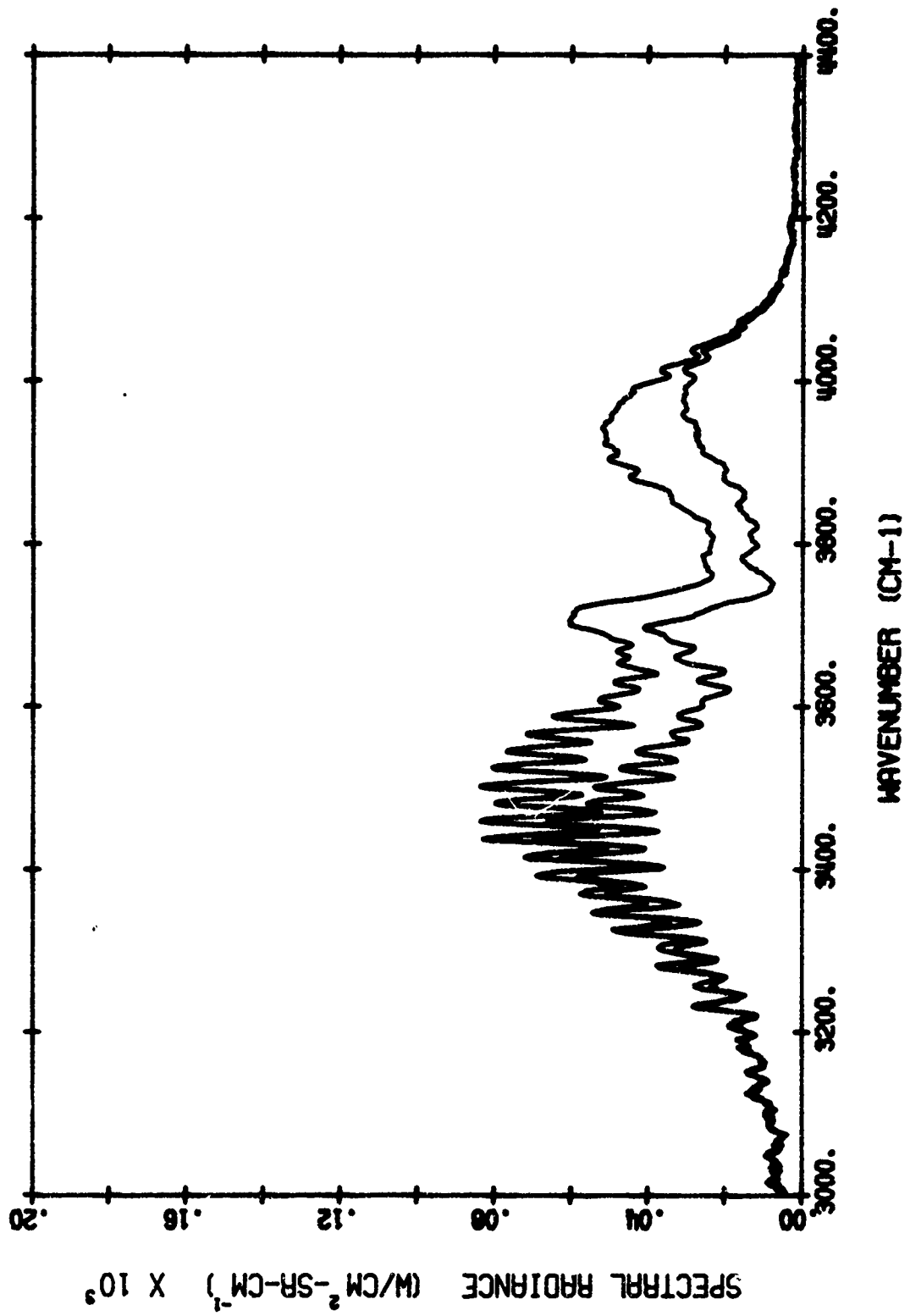


FIGURE 10. TYPICAL WATER VAPOR DATA (Continued)



(d) Measured Hot Cell Radiance (Upper) and Hot-Through-Cold Radiance (Lower)

FIGURE 10. TYPICAL WATER VAPOR DATA (Continued)



(e) Measured Hot-Through-Cold Radiance (Lower) and Product of Hot Cell Radiance and Cold Cell Transmittance (Upper)

FIGURE 10. TYPICAL WATER VAPOR DATA (Concluded)

The second (b) and third (c) curves show the hot cell absorptance and the cold cell transmittance. The fourth curve (d) shows the measured hot cell radiance (the cold cell evacuated) on the upper curve, as well as the hot cell radiance as viewed through the cold cell (lower curve). This plot demonstrates the attenuation produced by the cold cell. The fifth plot (e) demonstrates the degree to which the water vapor lines in the hot and cold cells are indeed correlated. The upper curve is the product, wavenumber by wavenumber, of the measured hot-cell radiance—upper curve on (d)—and the cold cell transmittance (c). The lower curve, which is the measured hot cell radiance as viewed through the cold cell, is the same as the lower curve in (d). The difference between these two curves shows the degree to which the multiplicative transmittance approach fails. In the center of the band the correlation effect produces a radiance which is lower by a factor of as much as two compared to what one would expect using the multiplicative property. Detailed discussion of these effects is delayed until Section 4 where comparison of various computation techniques is made.

Figure 11(a-e) show typical CO_2 data at $4.3 \mu\text{m}$ in the same five types of curves. The apparent temperature curve (a) has a behavior similar to that for water vapor except that it does not show the fluctuations at the edge of the band. This is expected because of the generally smoother character of the spectra in this region. Figure 11(b) through (d) shows the hot cell absorptance (b), the cold cell transmittance (c), as well as the hot cell radiance (d, upper) and the observed hot cell through cold cell radiance (d, lower). Figure 11(e) again shows the degree to which line correlation effects occur. One of the primary features of this and all the $4.3 \mu\text{m}$ CO_2 spectra is that the multiplicative transmittance approach seems to work well for most of the band wings. The large amount of absorption in the simulated paths precludes judgments concerning band center. The product of the hot-cell radiance and the cold cell transmittance agrees very well with the hot cell through cold cell radiance except for a very small region on the long wavelength side of the "blue spike" at 2390 cm^{-1} . Thus, it appears that correlation effects can indeed be ignored for the $\text{CO}_2 4.3 \mu\text{m}$ band. This does not hold for the $2.7 \mu\text{m}$ CO_2 band, however. The correlation effects observed in this band are midway between those observed for water vapor and those observed for CO_2 at $4.3 \mu\text{m}$. Again, detailed discussion of the data is deferred to Section 4.

Appendix B contains plots of all of the data taken on this program for use in future comparisons with calculation techniques. In addition, the results have been saved on computer tape for future use.

COMPARISON OF MEASUREMENTS WITH PREDICTION METHODS

In order to judge the ability of plume calculation methods to predict the line correlation effects that are present (or not present) in the measured hot-through-cold radiances, it is

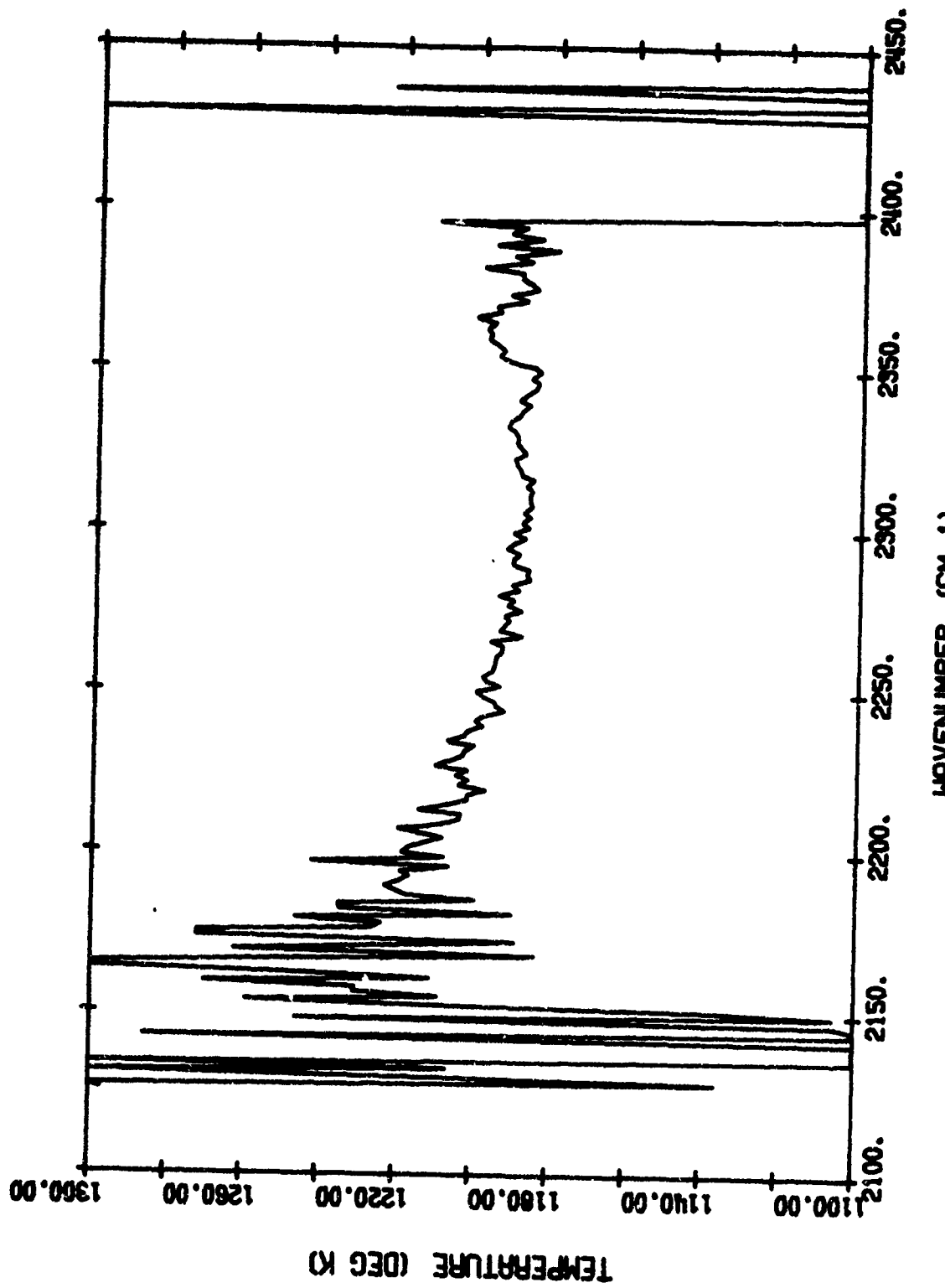
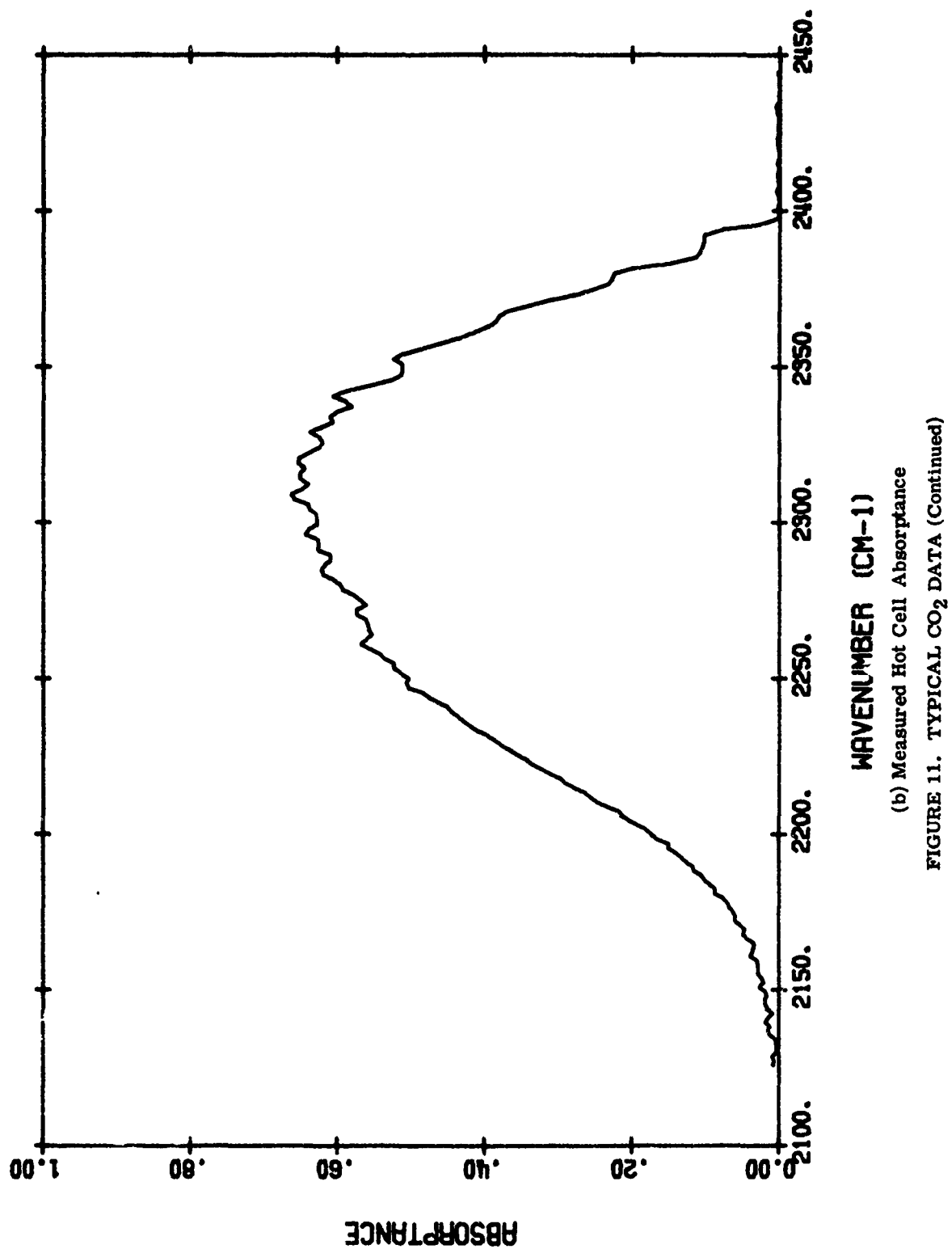
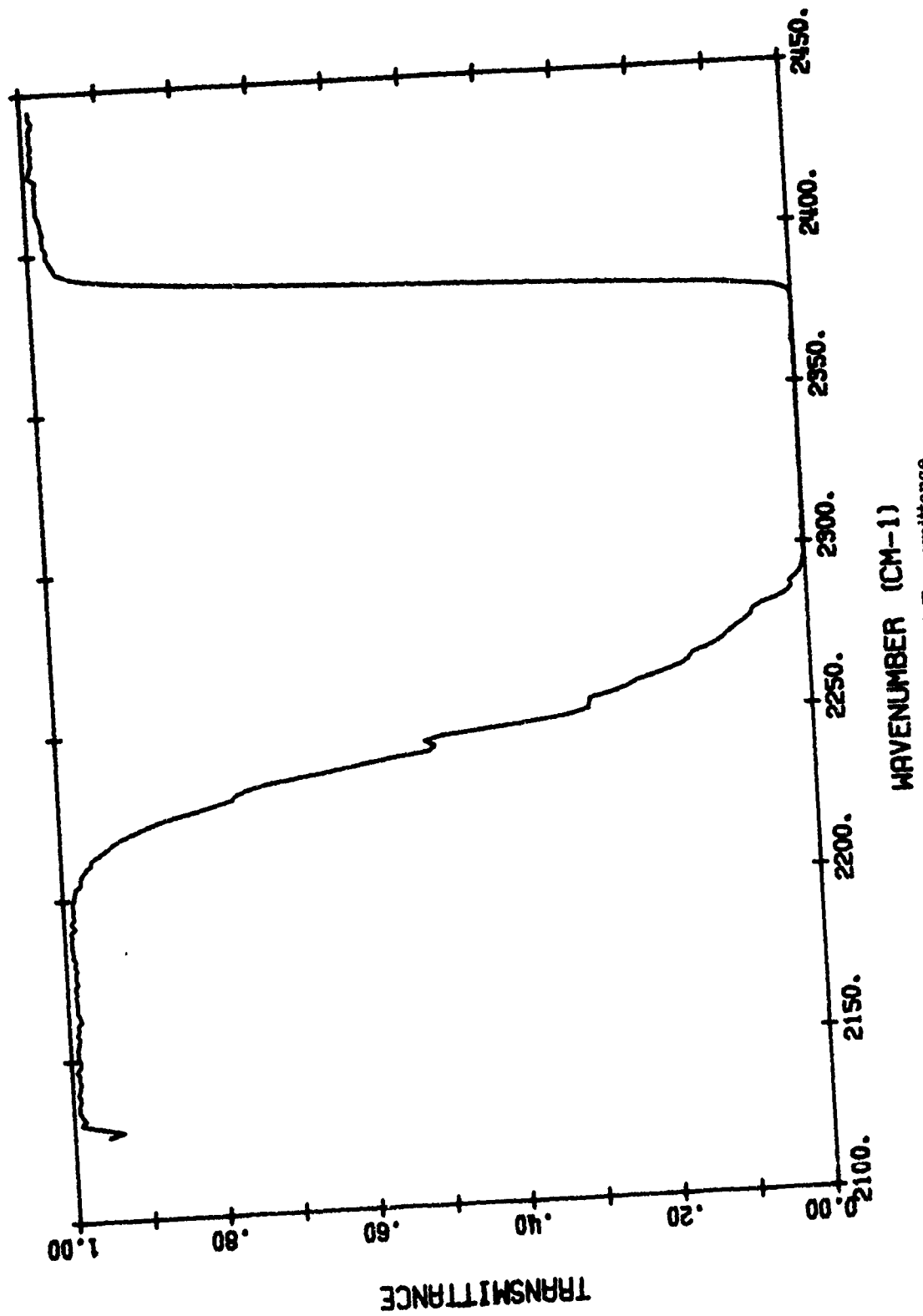


FIGURE 11. TYPICAL CO_2 DATA (Continued)
(a) Measured Apparent Temperature



(b) Measured Hot Cell Absorbance
FIGURE 11. TYPICAL CO_2 DATA (Continued)



(c) Measured Cold Cell Transmittance
FIGURE 11. TYPICAL CO₂ DATA (Continued)

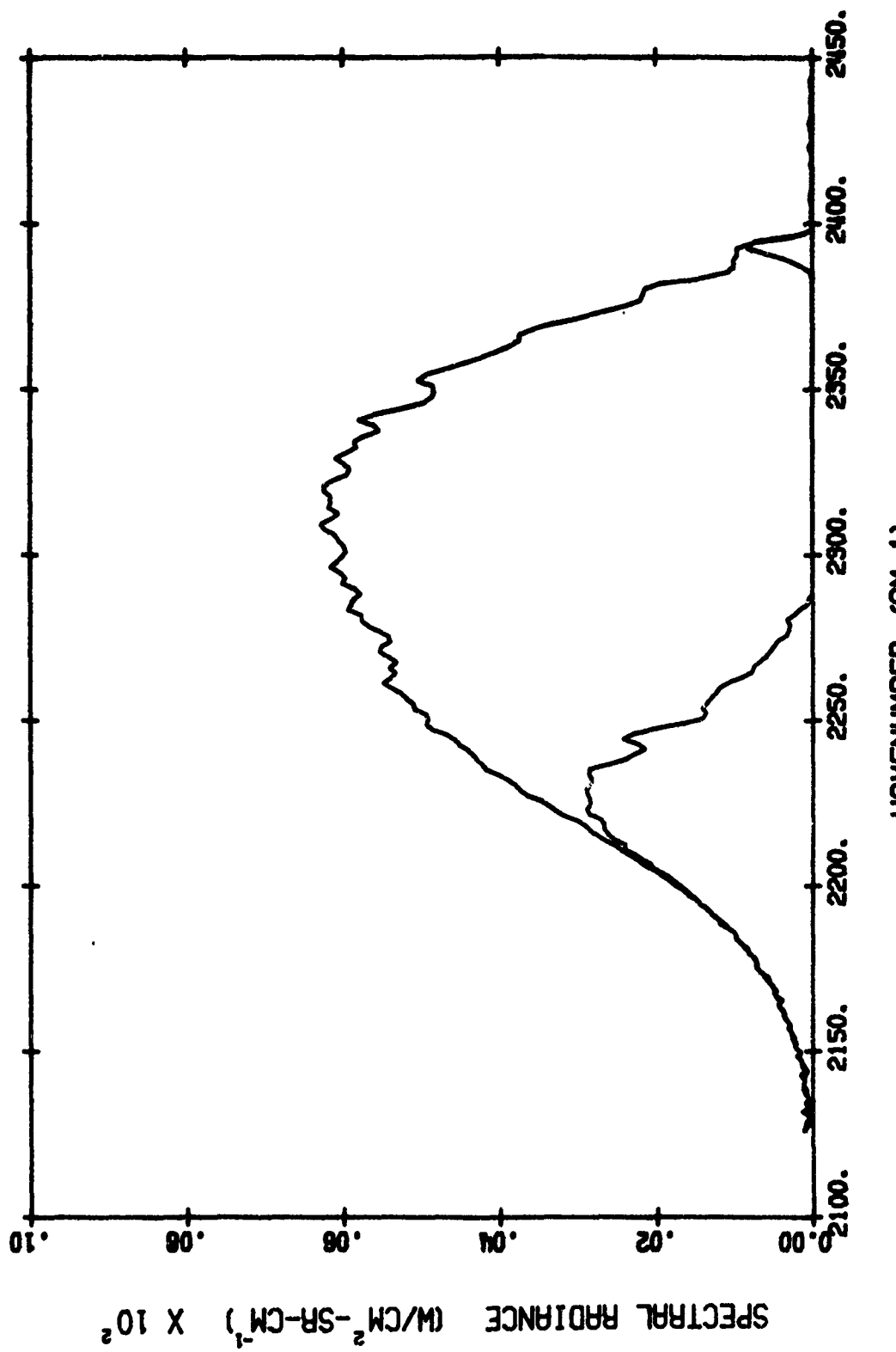
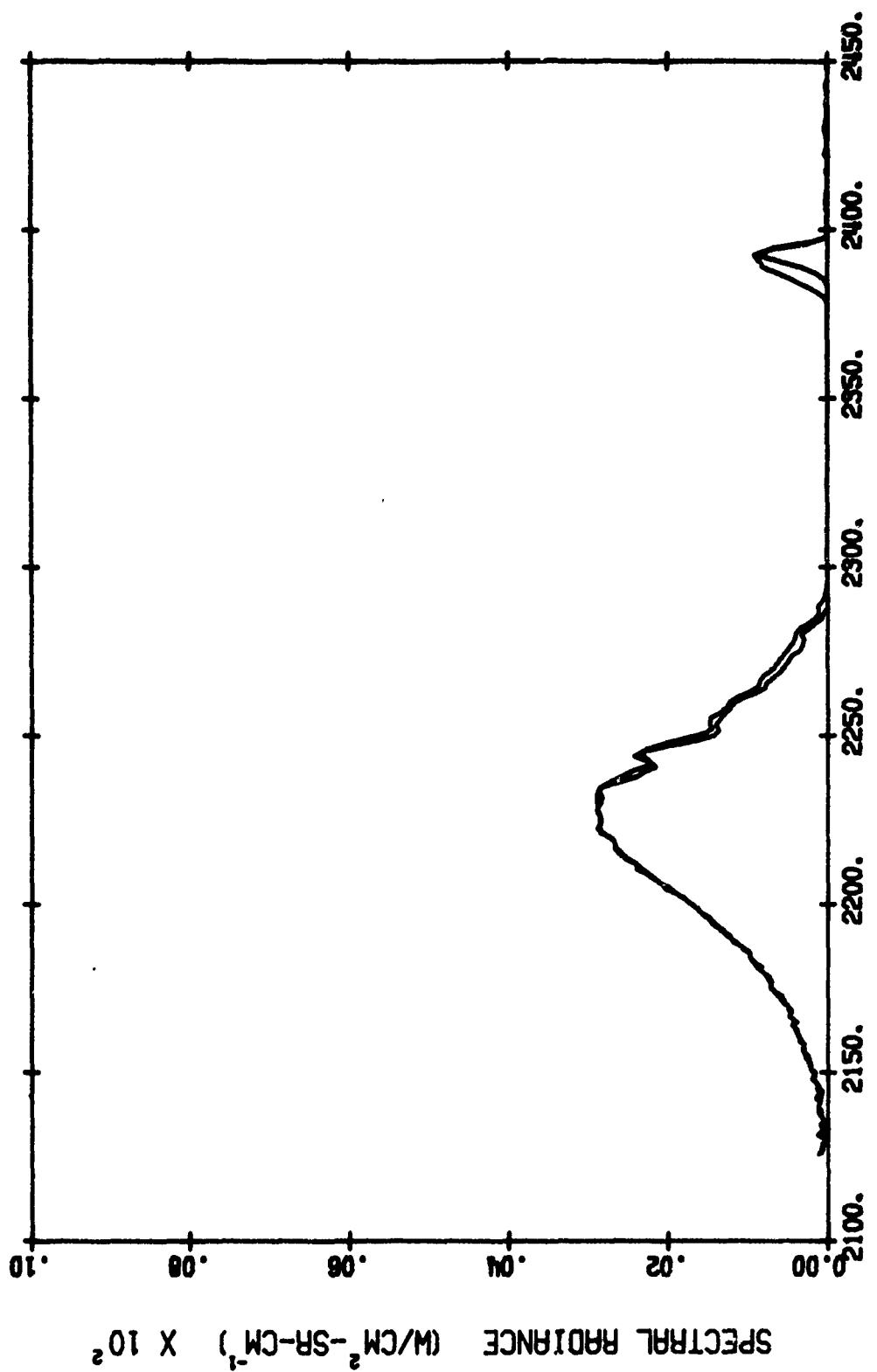


FIGURE 11. TYPICAL CO_2 DATA (Continued)



(e) Measured Hot-Through-Cold Radiance (Lower) and Product of Hot Cell Radiance and Cold Cell Transmittance (Upper)

FIGURE 11. TYPICAL CO₂ DATA (Concluded)

worthwhile to compare the measurements made to the band model development of Section 2 and to other information available for computing these effects.

It would, of course, be most desirable if there were a single computational scheme which, though difficult, could be relied upon to give absolutely correct results. Although the line tabulation of McClatchey might appear to provide the basis for such a technique, it has been shown to lack many lines whose states are important at high temperatures^[14]. Therefore, for the time being the tabulation is considered only as an additional basis of calculations.

We had also planned to compare each of the measurement data sets to individual line-by-line calculations using the McClatchey parameters. These calculations represent a substantial expenditure of funds, and when it appeared that they could not be considered to provide definitive results, we sought another less expensive means of comparing the measurements to the line tabulation.

The method chosen was to construct a band model from the line tabulation. Goldman and Kyle^[15] state that such a model fits the line-by-line calculation to within 5%. This is within the accuracy to be expected from the measurements themselves. The band model parameters were computed for the random model with an inverse-strength distribution of line strengths, as is used in Section 2. These band model parameters were then checked with line-by-line calculations over a single small spectral interval for one of the water vapor cases.

The other set of emission-absorption information with which the data are compared consists of model calculations based on an extensive tabulation of band model parameters developed by Ludwig, et al. and most recently tabulated in Reference 1.

In addition to the emission-absorption parameters, there is an additional variable which affected the agreement of calculation and experiment. This is the curve-of-growth used with the various calculational techniques. Since the curve-of-growth to be used is a direct outcome of the band model to be used (e.g., Equation (39) of Section 2), one would not expect it to be an independent variable. We consider it as such since it affects the fit between the calculated and measured hot cell radiance substantially.

There are three ways in which the two sets of parameters may be used in computational schemes for non-isothermal paths. The first means is, of course, the band model scheme developed in Section 2. The second is the Lindquist-Simmons approximation developed in the past^[8]. The third is the multiplicative-transmittance approach described in the early portion

14. G.H. Lindquist, "High Resolution Measurements of Water Vapor Spectrum," ongoing contract on ARPA Order 2656, Environmental Research Institute of Michigan, Ann Arbor, Michigan, April 1974-August 1975.

15. A. Goldman and T.G. Kyle, "A Comparison Between a Statistical Model and Line-by-Line Calculations with Application to the 9.6 μ m Ozone and the 2.7 μ m Water Vapor Bands," Applied Optics, Vol. 7, p. 1167f (1968).

of Section 2 in which the radiance of the hot gas source is simply multiplied by the cool path transmittance over small wavenumber intervals. The measurements show that this latter technique is not adequate for water vapor if a factor-of-2 error is unacceptable. On the other hand, the measurements show the technique to be satisfactory for the CO_2 wings at $4.3 \mu\text{m}$.

An additional comparison which should be made is one in which the statistical treatment of Section 2 is compared with a realistic ensemble of lines. In this case, of course, line-by-line calculations are necessary. Here the line tabulation serves as a realistic array of varying strength, width, position, and temperature dependence, all falling in a narrow frequency interval. The statistical treatment of Section 2, used in obtaining a transmittance derivative for this array of lines, can be compared to the true transmittance derivative calculated using a line-by-line procedure.

The following sections describe the comparisons which we performed using these variables. Because of the large number of variables, we did not obtain all possible comparisons but tried to obtain enough of them to ascertain the degree to which band model calculations could be used to reproduce the measurements.

4.1 THE MEASUREMENTS COMPARED TO THE GENERAL DYNAMICS PARAMETERS

The parameters are most easily checked with respect to emission and absorption data by comparing measured and computed hot cell radiance values and cold cell transmittance values. Each path (hot and cold) alone represents an isothermal path whose emission or absorption depends only on the parameters used.

The band model tabulations of General Dynamics^[1] are designed for use in band model calculations of hot gases. For CO_2 these tabulations are the result of theoretical calculations which used the known spectroscopic constants for CO_2 (to give accurate band positions) but used harmonic oscillator approximations to obtain hot band strengths from the experimentally determined strengths of the ground state bands. These tabulations are generally assumed to be accurate for CO_2 .

For water vapor, parameter tabulations were determined experimentally. A substantial number of measurements of the isothermal absorption of hot water vapor were made using a variable length strip-burner as the source of water vapor. These provided absorption data above 1200°K . Data below this temperature were based both on extrapolation and comparison with other low temperature measurements. Values as published did not fit the extension ambient temperature band model tabulation of Anding, but under a later effort the 300°K values were modified to agree with the model of Anding. The modification was not entirely successful, as will be seen by comparison with the cold cell measurements.

The General Dynamics tabulation contains values of the average strength-to-spacing ratio and, as the second band model parameter, the average line spacing which could be

combined with the average line width to give a second parameter. The line strength-to-spacing ratio is the first band model parameter in most band model formulations, including the one developed in Section 2 and the one which we have commonly used prior to this work. Under previous efforts, the average line spacing information had been combined with average half widths to obtain the dimensionless parameter β :

$$\beta = \frac{2\pi\gamma}{\delta}$$

where the parameter $1/\delta$ was obtained from the GD tabulations. The parameter γ used in Section 2 is related by β by

$$\gamma = \frac{\beta}{8\pi}$$

General Dynamics extracted a value of $1/\delta$ from calculations and absorption measurements using a curve of growth of a form equivalent to

$$W/\delta = \beta \frac{x}{\sqrt{1 + \frac{\pi}{2}x}}$$

where x is defined as $\int k da/\beta$. Values of k and β were used directly in the comparison of the data with the General Dynamics tabulations. Some dependence on the curve-of-growth was apparent, as will be discussed in Section 4.3.

During the measurement program, only three different hot cell fills were used: (1) a 0.1 atmosphere, 50-50 mixture of water vapor and nitrogen, (2) a 0.1 atmosphere, 50-50 mixture of CO_2 and nitrogen, and (3) a 0.1 atmosphere mixture simulating a rocket exhaust. Comparison of these hot cell radiances with computed values using the General Dynamics parameters are shown for typical tests in the upper curves of Figures 12 through 16. Comparisons for additional tests would only yield information on measurement reproducibility, which was found to be quite good.

Figure 12 compares radiances resulting from the General Dynamics parameters to the measurements made on pure water vapor at $2.7 \mu\text{m}$. In general, prediction by these parameters is very good at 1200°K . The predicted radiance is slightly low, but the choice of a curve of growth affects these values greatly because the optical depths near band center fall intermediate between the linear and square root region, where the different curves of growth have their greatest variability. (See Section 4.3 for an explanation of the curves of growth used.)

Figure 13 shows the hot cell radiance measured for a $\text{CO}_2\text{-N}_2$ mixture at $4.3 \mu\text{m}$ compared to the predicted results using the General Dynamics parameters for Test 5. Although the shape of the observed spectrum agrees with the predicted shape, the observed radiance at the peak of the band is substantially less than the predicted radiance. The observed and

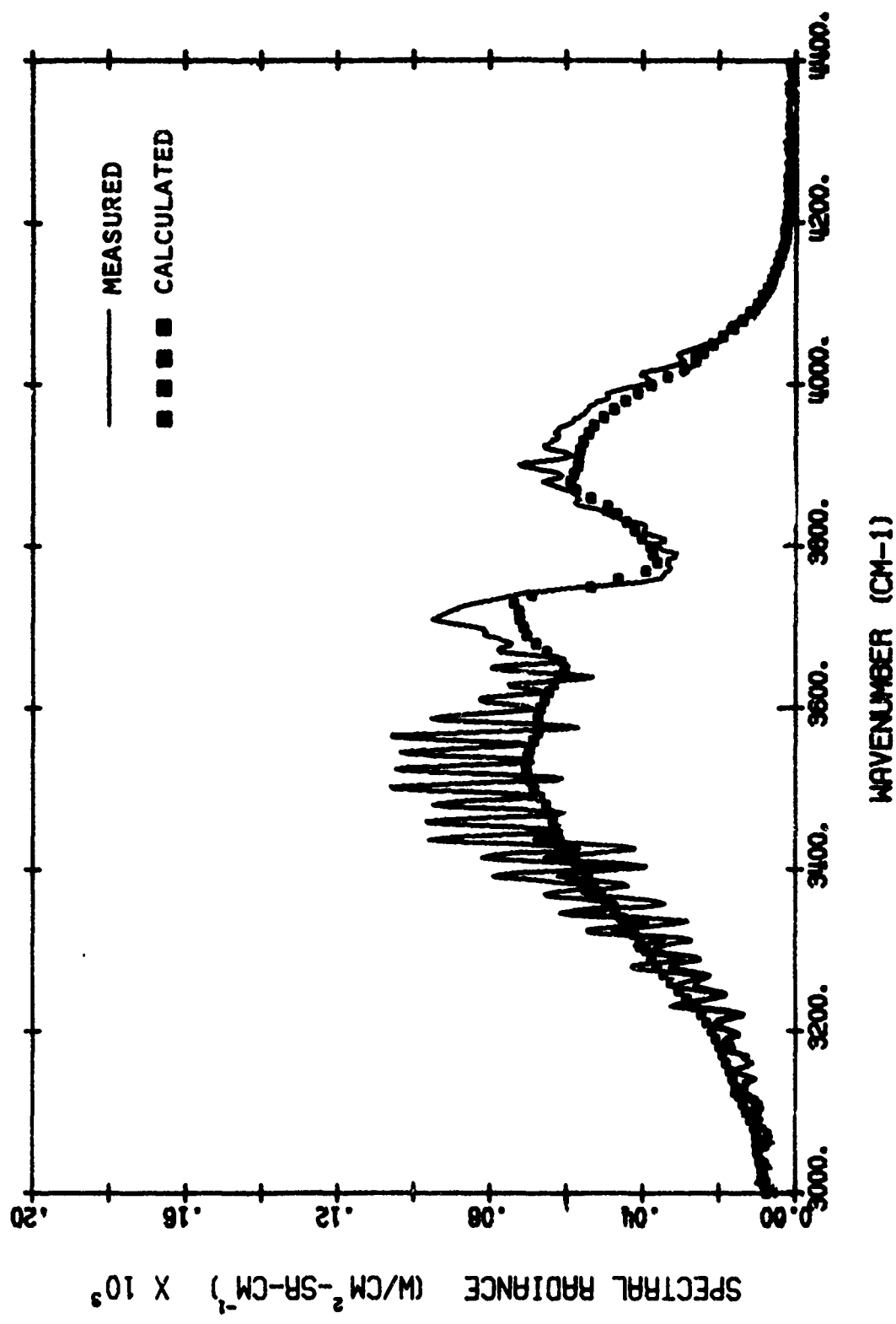


FIGURE 12. COMPARISON OF MEASURED HOT CELL RADIANCE WITH RADIANCE CALCULATED USING GENERAL DYNAMICS PARAMETERS, TEST 8R, 2.7 μ m WATER VAPOR

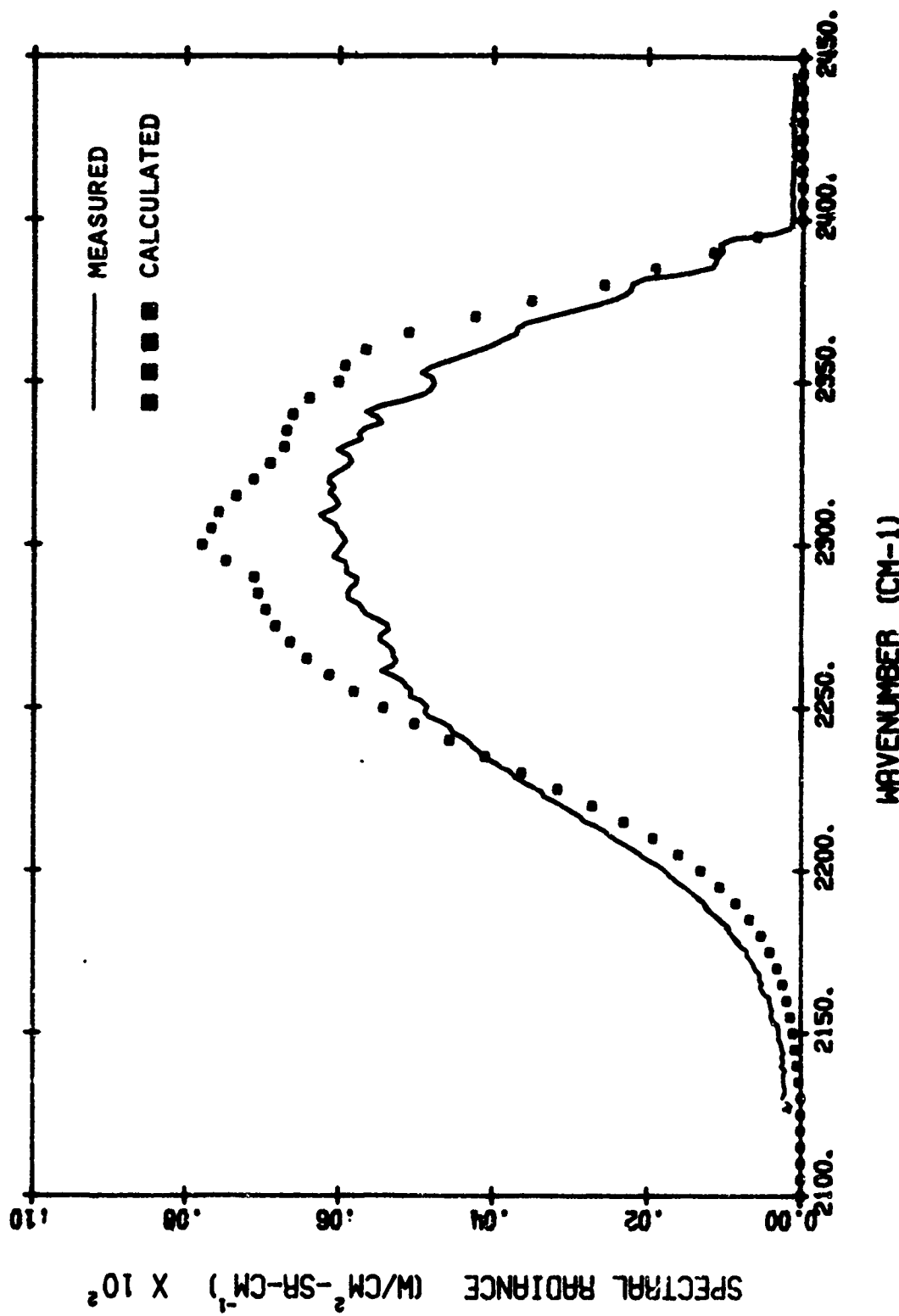


FIGURE 13. COMPARISON OF MEASURED HOT CELL RADIANCE WITH RADIANCE CALCULATED USING GENERAL DYNAMICS PARAMETERS, TEST 5, 4.3 μ m, CO_2

predicted curves cross in the long wavelength wing so that the far wing is underpredicted rather than overpredicted. This latter feature produces severe disagreement between the observed and predicted hot-through-cold radiance using these parameters. It is apparent that the General Dynamics parameters for the CO_2 region, although producing gross agreement with experiment, give substantial variances in the detailed shape of the band, so much that the red spike region is distorted. This is surely the result of the very heavy dependence on theory in obtaining these parameters.

Figure 14 shows the hot cell radiance measured for a $\text{CO}_2\text{-N}_2$ mixture at $2.7 \mu\text{m}$ compared to predicted results using the GD tabulation for Test 3. It can be seen that the General Dynamics tabulation predicts the observed hot cell radiances very poorly. Reasons for this are not known except that perhaps they are again the result of the heavy dependence upon theory in obtaining the parameters. The shape of the spectra are well predicted, but the absolute values are not. We believe that the observed spectra accurately characterize the true gas radiance.

Figures 15 and 16 show comparisons for the hot cell fill simulating a rocket plume. At $4.3 \mu\text{m}$ (see Figure 15) the prediction is within 25% on the long wavelength side of the band, but the agreement at band center is much better than was observed for the $\text{CO}_2\text{-N}_2$ runs. This would appear to indicate that the treatment of broadening is not correct in our calculation procedure. The broadening coefficients are poorly known for N_2 and essentially unknown for water vapor and hydrogen, and it is difficult to identify the reason for the band center disagreement between Figures 13 and 15 without making measurements on pure CO_2 . Such measurements are necessary to separate errors in the treatment of foreign gas broadening from errors in the band model parameters themselves. It appears that a study of foreign gas broadening of CO_2 is needed, as well as a better determination set of band model parameters, if the agreement in the $4.3 \mu\text{m}$ band is to be improved.

The comparison for the simulated rocket plume mixture at $2.7 \mu\text{m}$ is shown in Figure 16. The water vapor features of the band are reasonably well treated, commensurate with the results for water vapor- N_2 . The CO_2 features are also reasonably well predicted. That we can make this statement is very surprising in view of the very poor agreement observed in the $\text{CO}_2\text{-N}_2$ runs. Again this indicates that the broadening of CO_2 is poorly treated using the available broadening coefficients.

Three basic atmospheric paths were used in the program simulating 10, 50, and 200 km paths at 15 km altitude. Figures 17 through 22 show the measured cold cell transmittances compared to GD predictions. From Figures 17 and 22, it can be seen that predictions for water vapor are reasonably good, perhaps underestimating the absorption slightly. On the other hand, the results for CO_2 are not very good at all. The band appears slightly shifted in some cases, and at intermediate optical depths substantial disagreement is apparent. Because

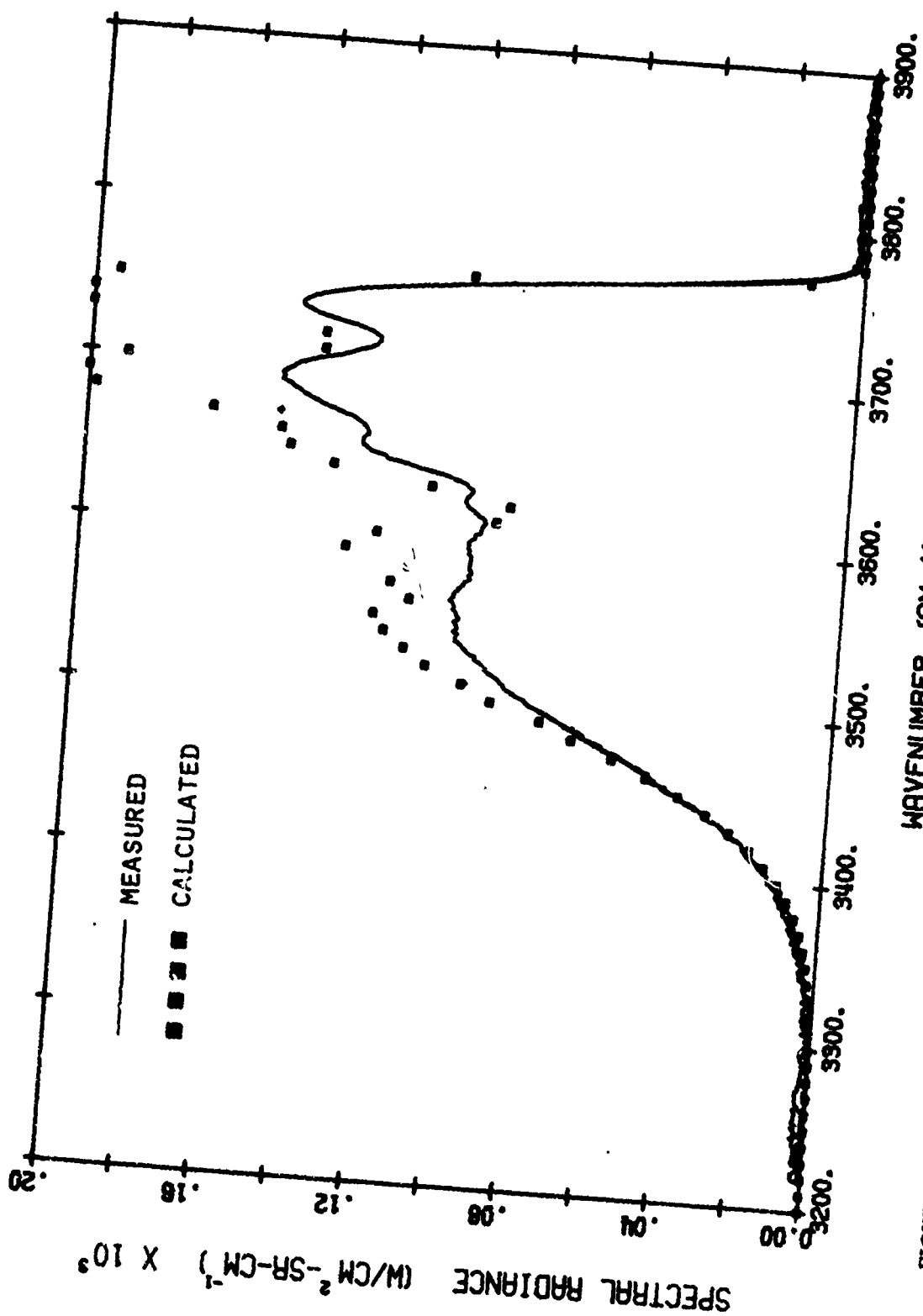


FIGURE 14. COMPARISON OF MEASURED HOT CELL RADIANCE WITH RADIANCE CALCULATED USING GENERAL DYNAMICS PARAMETERS, TEST 3, $2.7 \mu\text{m}$, CO_2

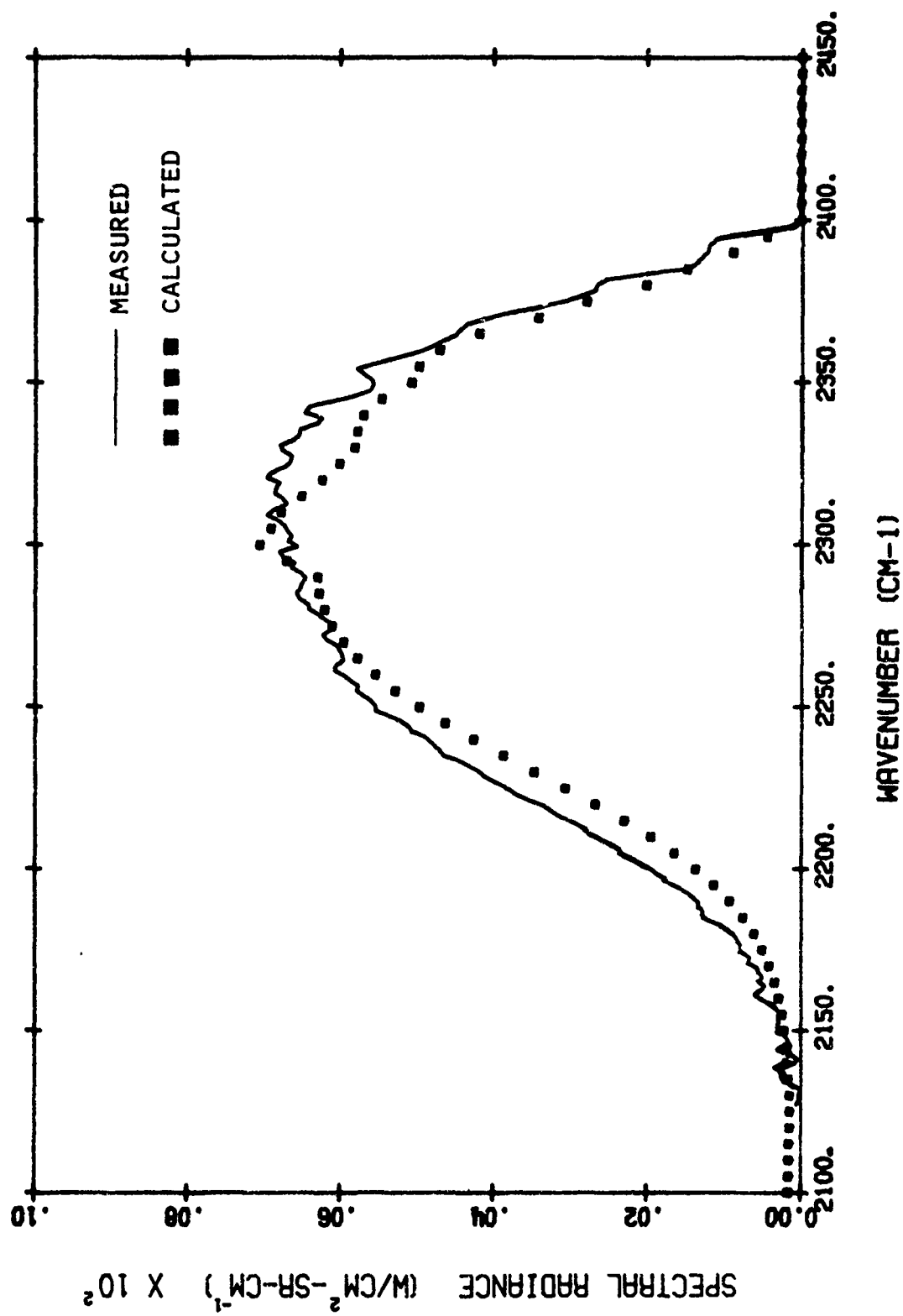


FIGURE 15. COMPARISON OF MEASURED HOT CELL RADIANCE WITH RADIANCE CALCULATED USING GENERAL DYNAMICS PARAMETERS, TEST 17, 4.3 μ m, PLUME MIXTURE

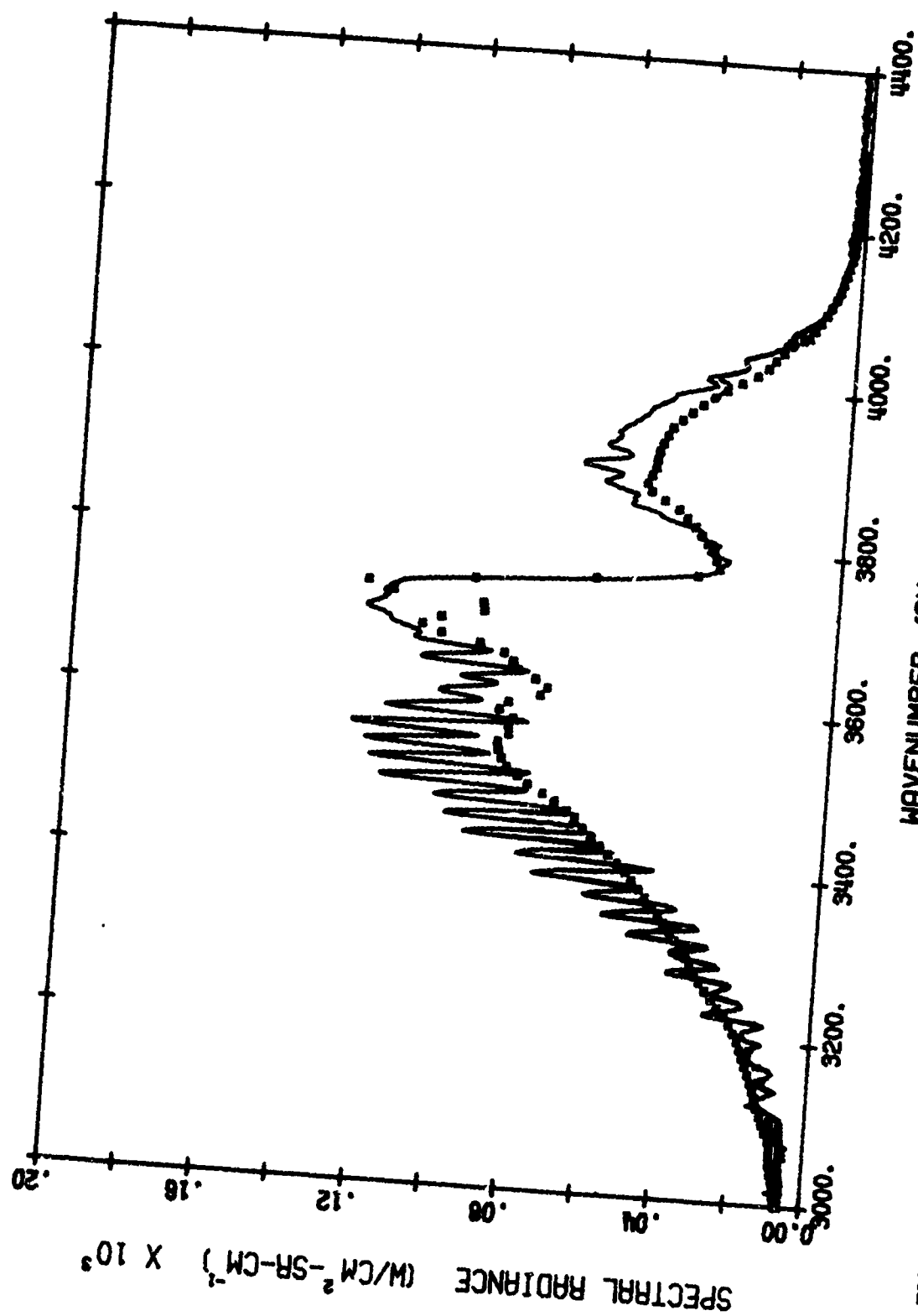


FIGURE 16. COMPARISON OF MEASURED HOT CELL RADIANCE WITH RADIANCE CALCULATED USING GENERAL DYNAMICS PARAMETERS, TEST 20, 2.7 μ m, PLUME MIXTURE

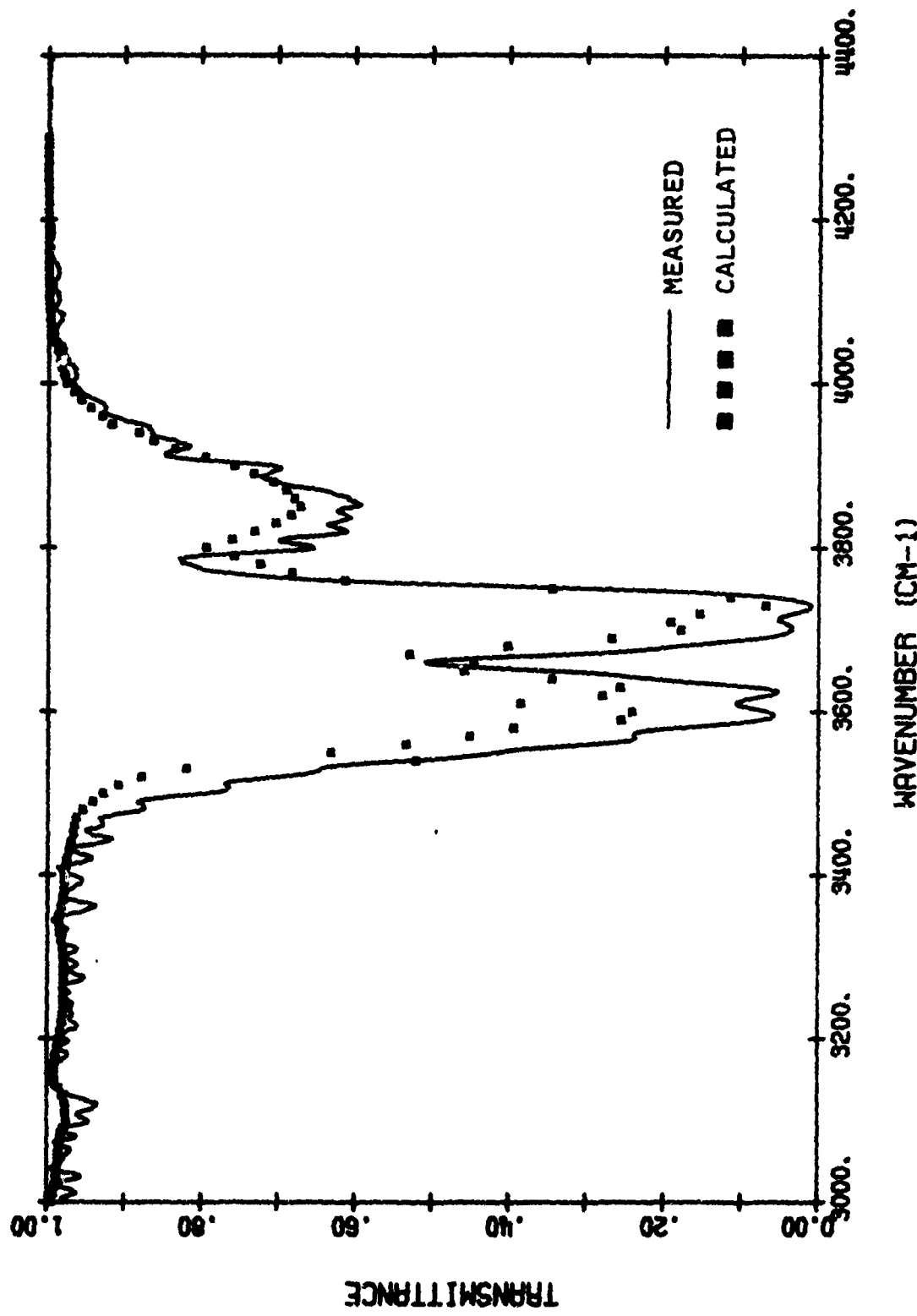


FIGURE 17. COMPARISON OF MEASURED COLD CELL TRANSMITTANCE WITH TRANSMITTANCE CALCULATED USING GENERAL DYNAMICS PARAMETERS, TEST 20, 2.7 μ m, 10 km PATH AT 15 km ALTITUDE

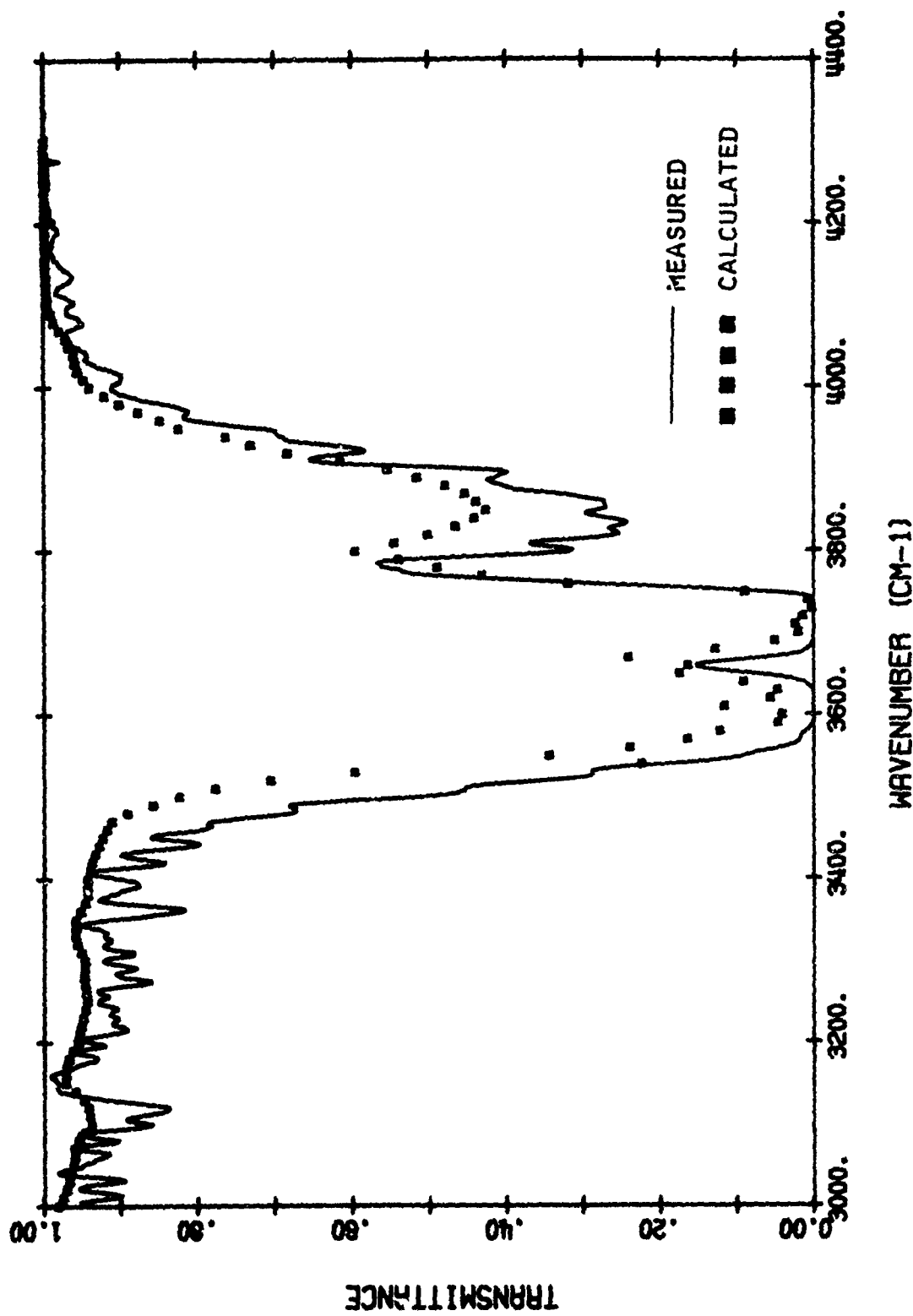


FIGURE 18. COMPARISON OF MEASURED COLD CELL TRANSMITTANCE WITH TRANSMITTANCE CALCULATED USING GENERAL DYNAMICS PARAMETERS, TEST 19, 2.7 μ m, 50 km PATH AT 15 km ALTITUDE

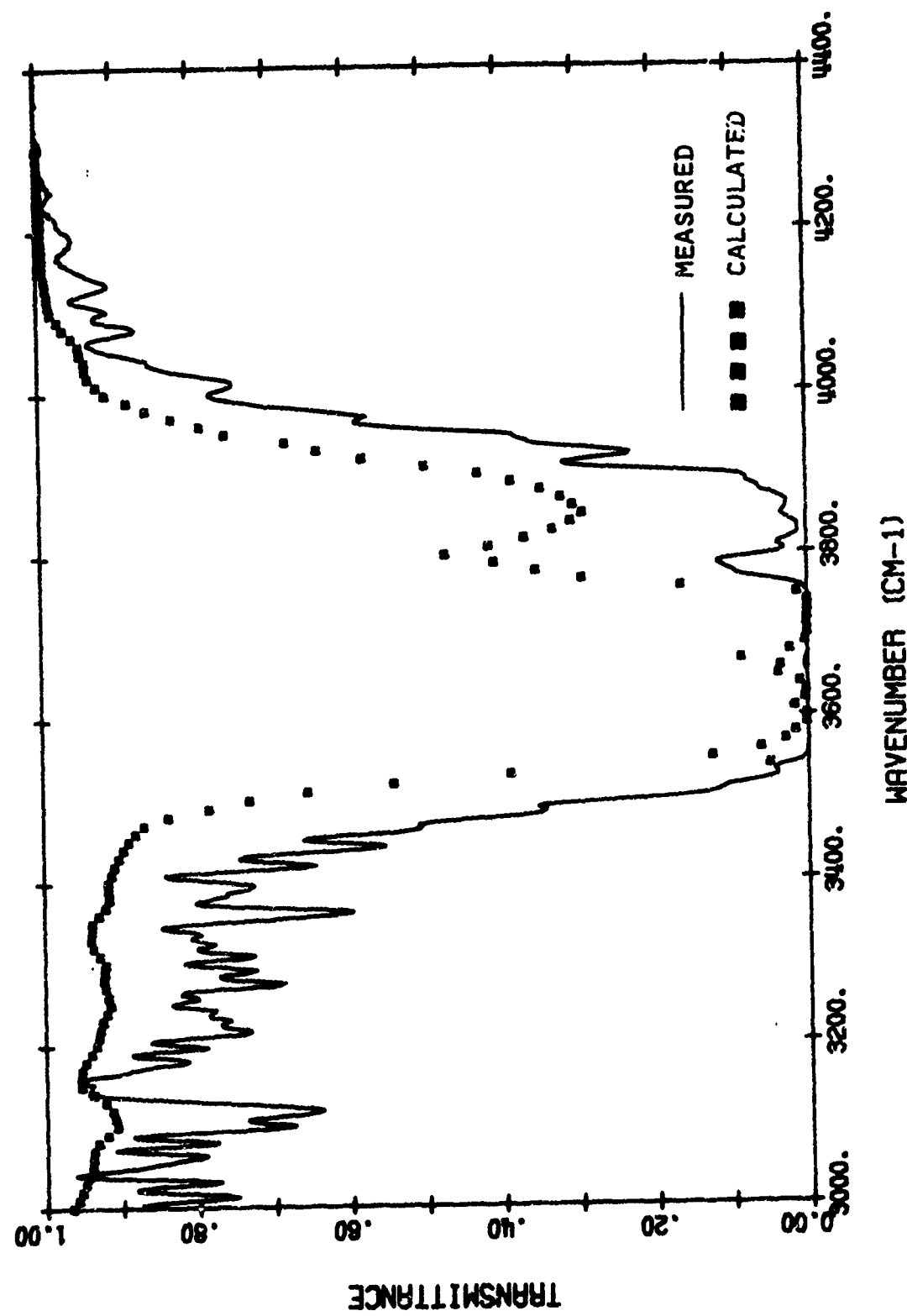


FIGURE 19. COMPARISON OF MEASURED COLD CELL TRANSMITTANCE WITH TRANSMITTANCE CALCULATED USING GENERAL DYNAMICS PARAMETERS, TEST 18, 2.7 μ m, 200 km PATH AT 15 km ALTITUDE

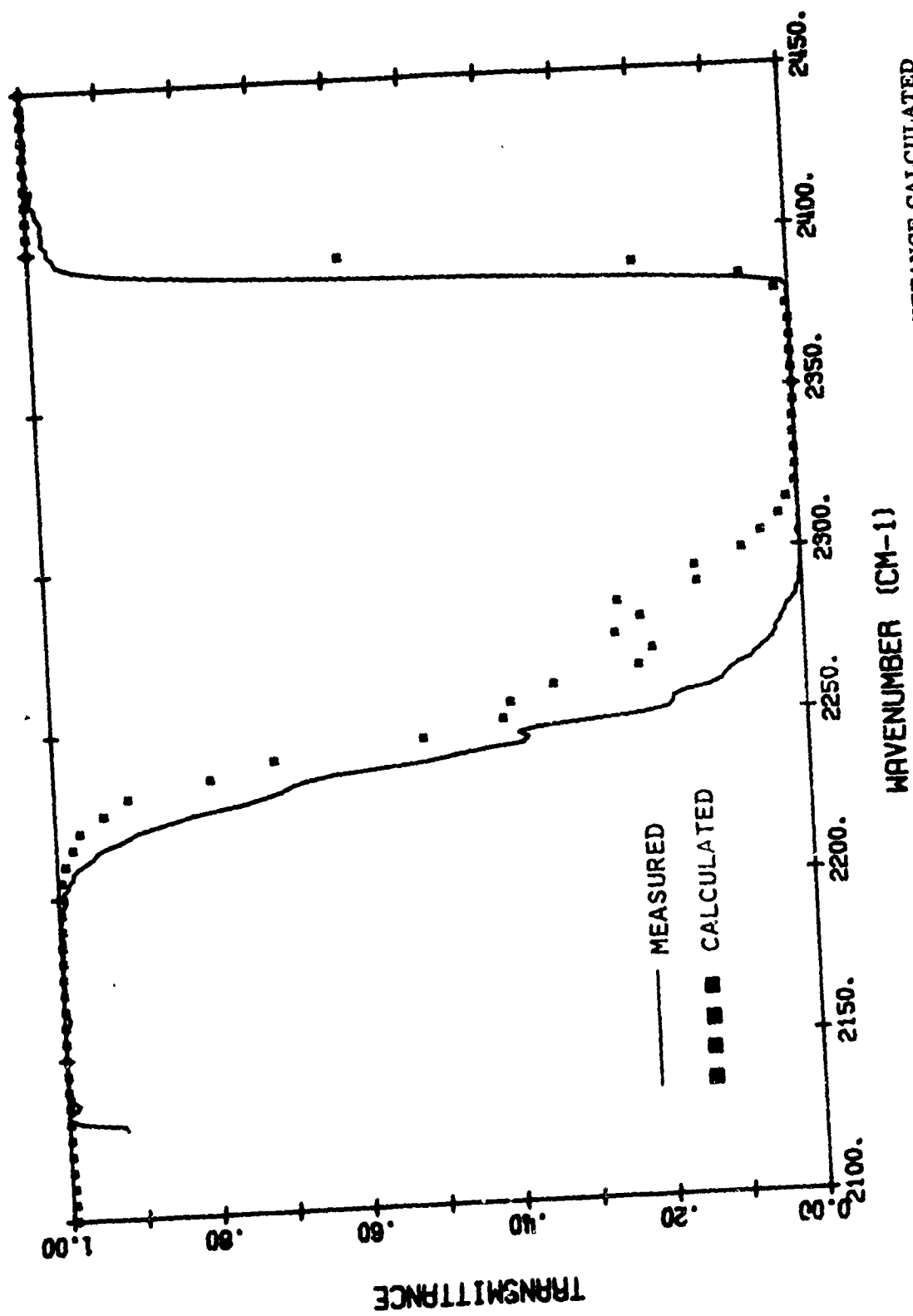


FIGURE 20. COMPARISON OF MEASURED COLD CELL TRANSMITTANCE WITH TRANSMITTANCE CALCULATED USING GENERAL DYNAMICS PARAMETERS, TEST 17, 4.3 μ m, 10 km PATH AT 15 km ALTITUDE

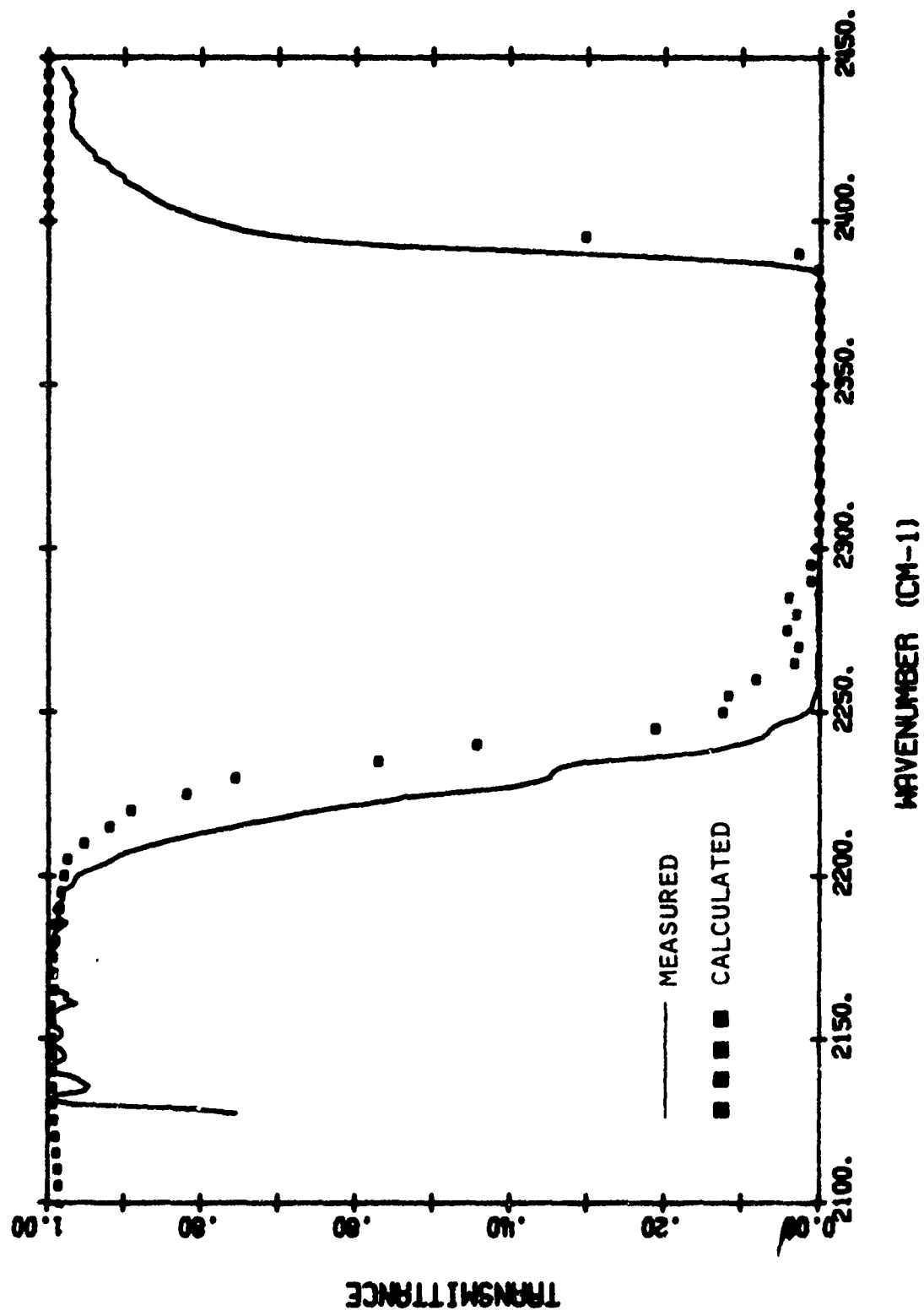


FIGURE 21. COMPARISON OF MEASURED COLD CELL TRANSMITTANCE WITH TRANSMITTANCE CALCULATED USING GENERAL DYNAMICS PARAMETERS, TEST 16, 4.3 μ m, 50 km PATH AT 15 km ALTITUDE

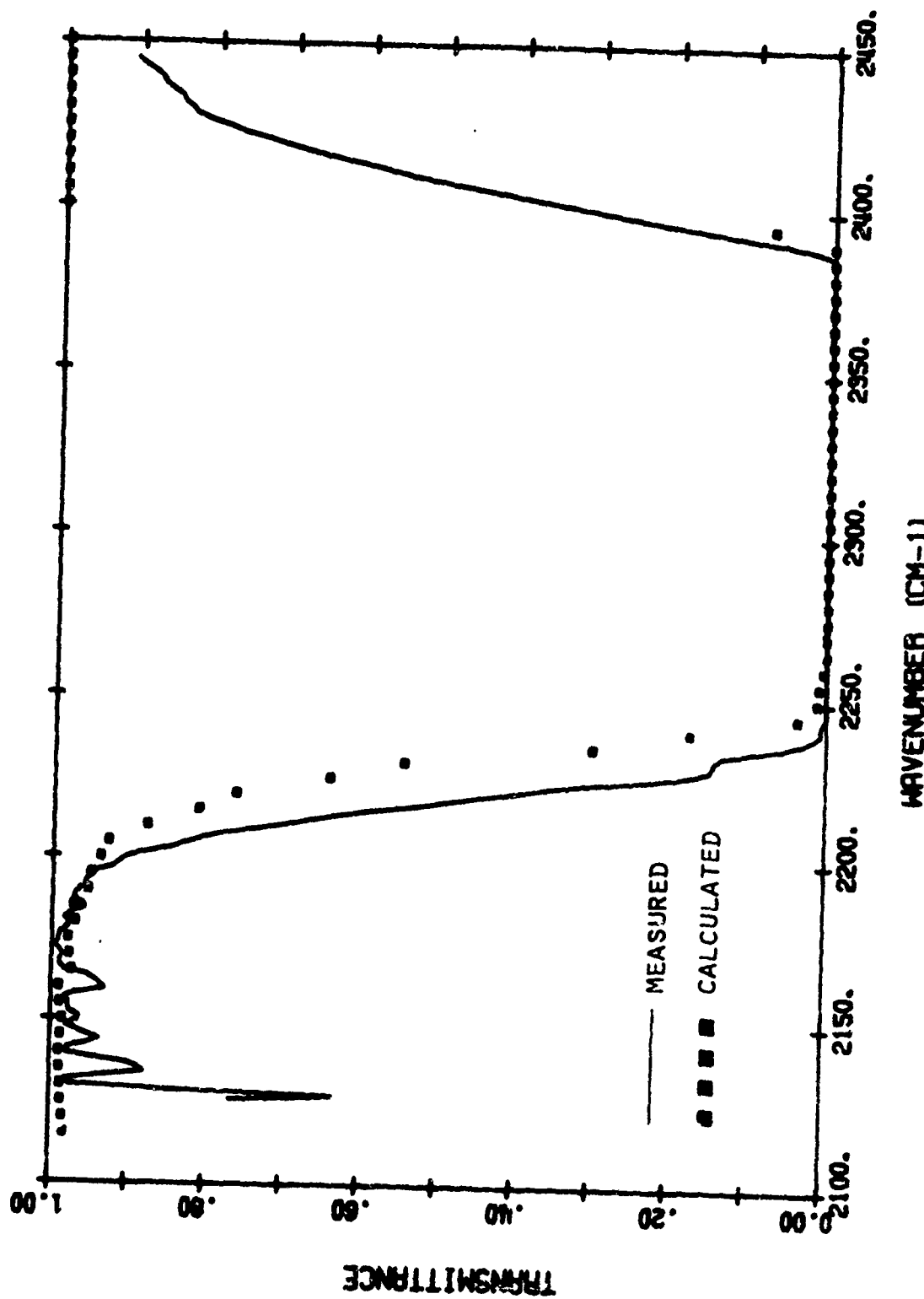


FIGURE 22. COMPARISON OF MEASURED COLD CELL TRANSMITTANCE WITH TRANSMITTANCE CALCULATED USING GENERAL DYNAMICS PARAMETERS, TEST 15. 4.3 μ m, 200 km PATH AT 15 km ALTITUDE

the GD parameters for water vapor at these low temperatures are to some extent extrapolations while for CO_2 they are based primarily on theoretical calculations, poor agreement at low temperatures may not be surprising.

4.2 THE MEASUREMENTS COMPARED TO THE AFCRL LINE PARAMETER TABULATION IN A BAND MODEL

In order to facilitate the comparison between the line tabulation of AFCRL and the measurements of Section 3, a band model was developed from the line tabulation using the techniques described in [4]. The band model was developed for use with a curve of growth like

$$\frac{W}{d} = \beta \frac{x}{\sqrt{1 + \frac{\pi}{2}x}} \quad (49)$$

where again $x = \int k da/\beta$. (See footnote p. 39.) The parameters k and β were determined as a function of temperature and for one atmosphere pressure of pure absorber using the following relations:

$$k(T) = \frac{\sum_{i=1}^N S_i(T)}{Nd} \quad (50)$$

$$= \frac{\sum_{i=1}^N S_i(T)}{\Delta \tilde{\nu}}$$

where $\Delta \tilde{\nu}$ is the spectral resolution used for the band model. A value of 25 cm^{-1} was used for $\Delta \tilde{\nu}$ in the $2.7 \mu\text{m}$ region and 10 cm^{-1} was used in the $4.3 \mu\text{m}$ region. In order to determine the strengths as a function of temperature, a harmonic oscillator vibrational partition function was used in addition to the rotational partition function given in Reference 2. This proved to be quite important in obtaining reasonable results, especially for CO_2 which has a rather low-frequency bending vibration.

The second parameter β was determined using the relation

$$\beta_0(T) = \frac{2\pi}{\Delta \nu} \frac{\left(\sum_{i=1}^N \sqrt{S_i(T)} \gamma_{0i}(T) \right)^2}{\sum_{i=1}^N S_i(T)} \quad (51)$$

where β_0 and γ_0 signify values at one atmosphere pressure. $\gamma_{0i}(T)$, which is the halfwidth for pure-gas broadening has an inverse square root temperature dependence. Values were obtained from the air-broadened halfwidths contained in the AFCRL tabulation by division by

the appropriate broadening coefficient — 0.2 in the case of water vapor and 0.77 for CO_2 . The coefficient 2π in Equation (51) differs from the coefficient of 1/4 given in Reference 3, Equation (4.41), in order that the proper square root limit is approached using the curve of growth in Equation (49).

Comparisons of the hot cell radiance using these band model parameters are shown in Figures 23 through 25. In the $2.7 \mu\text{m}$ water vapor region, (see Figure 23) the agreement with hot cell radiance measurements is reasonably good near band center, except near 3700 cm^{-1} where the line parameters predict substantially more radiance than observed. In the wings of the band, however, the agreement is not so good. In the long wavelength wing between 3000 and 3300 cm^{-1} agreement is poor. Presumably this is because the line tabulation has not been carried out to high enough rotational quantum numbers for the 1200^0K cell temperature. The agreement at band center is particularly satisfying, however, and is better at some frequencies than that obtained using the GD parameters.

The band model parameters obtained from the line tabulation yield good results at the short wavelength side of the $4.3 \mu\text{m}$ CO_2 band (see Figure 24) but do very poorly at predicting the middle and long-wavelength portions of the band. This again is probably due to the omission from the tabulation of many lines which are important at temperatures near 1200^0K .

Throughout the $2.7 \mu\text{m}$ band of CO_2 (see Figure 25) agreement is poor. Radiance is underpredicted on the basis of the line tabulation to about the same degree as it is overpredicted based on the GD parameters. The large amount of disagreement in this band is surprising and unexplainable at present.

The agreement of the band model parameters from the CRL tabulation with the cool cell transmittance values is basically good, as one would expect. Figures 26 through 31 demonstrate this. Several features of the comparison are puzzling however. First, in the $2.7 \mu\text{m}$ CO_2 band the cold cell transmittance, like the hot cell radiance, is not accurately predicted. Again, measurements on pure CO_2 paths are needed to sort out these uncertainties. Second, as seen in Figure 27, a portion of the water vapor band is not well predicted, also for unknown reasons. Third, the measured short wavelength shoulder of the $4.3 \mu\text{m}$ CO_2 band shows substantial absorption below the shortest wavelength band head at 2300 cm^{-1} . The calculations show an abrupt end to the absorption at this wavelength. The observed absorption could be produced by the integrated effect of the line wings of the strong lines in the band. Band model methods do not easily treat these effects, except in an empirical fashion; neither will line-by-line calculations treat them unless the far line shapes are accurately known. Thus we accept them as real, unaccounted-for effects for which an empirical correction must be added over long atmospheric paths.

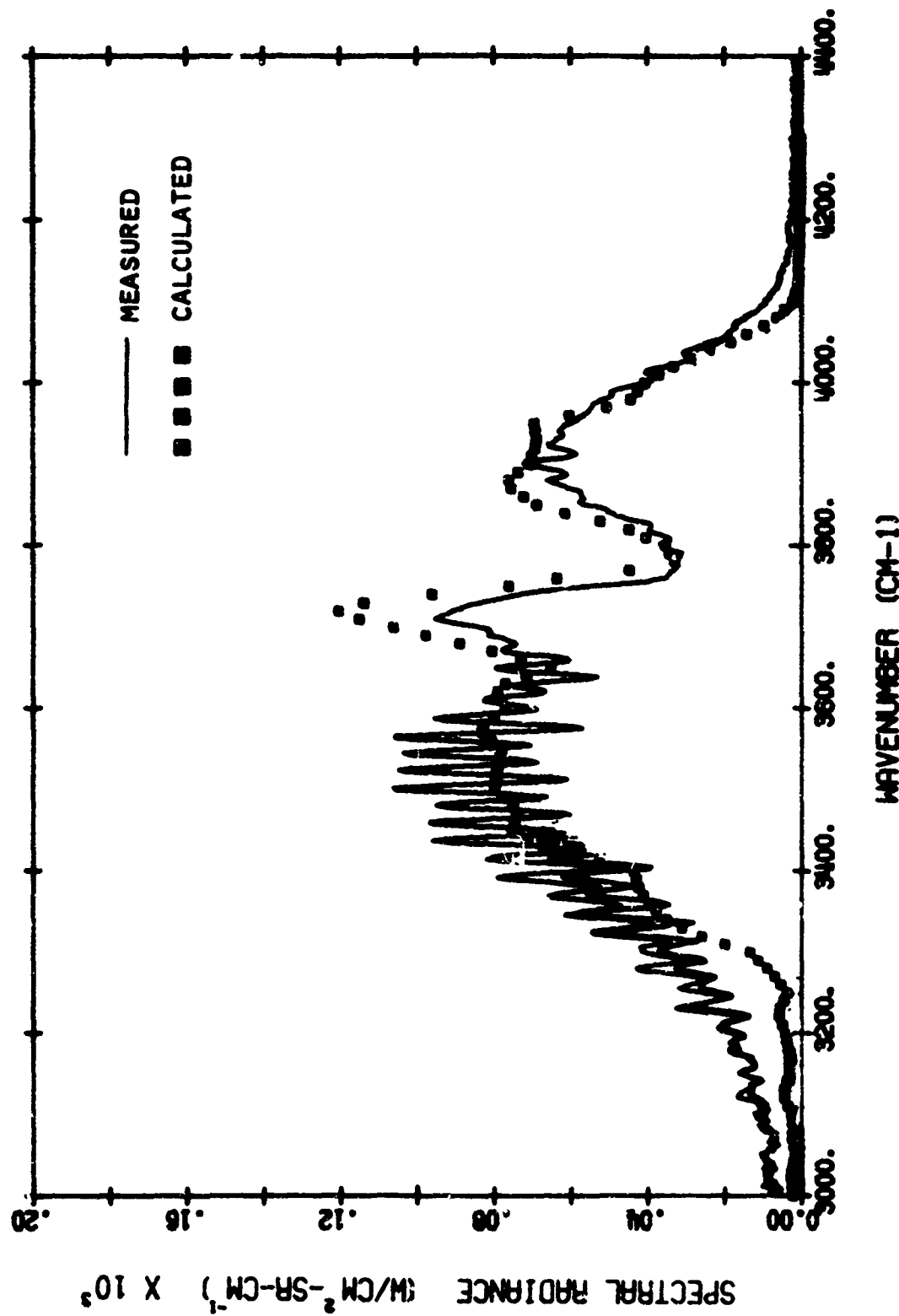


FIGURE 23. COMPARISON OF MEASURED HOT CELL RADIANCE WITH RADIANCE CALCULATED USING PARAMETERS OBTAINED FROM AFCRL TABULATION, TEST 8, 2.7 μ m, WATER VAPOR

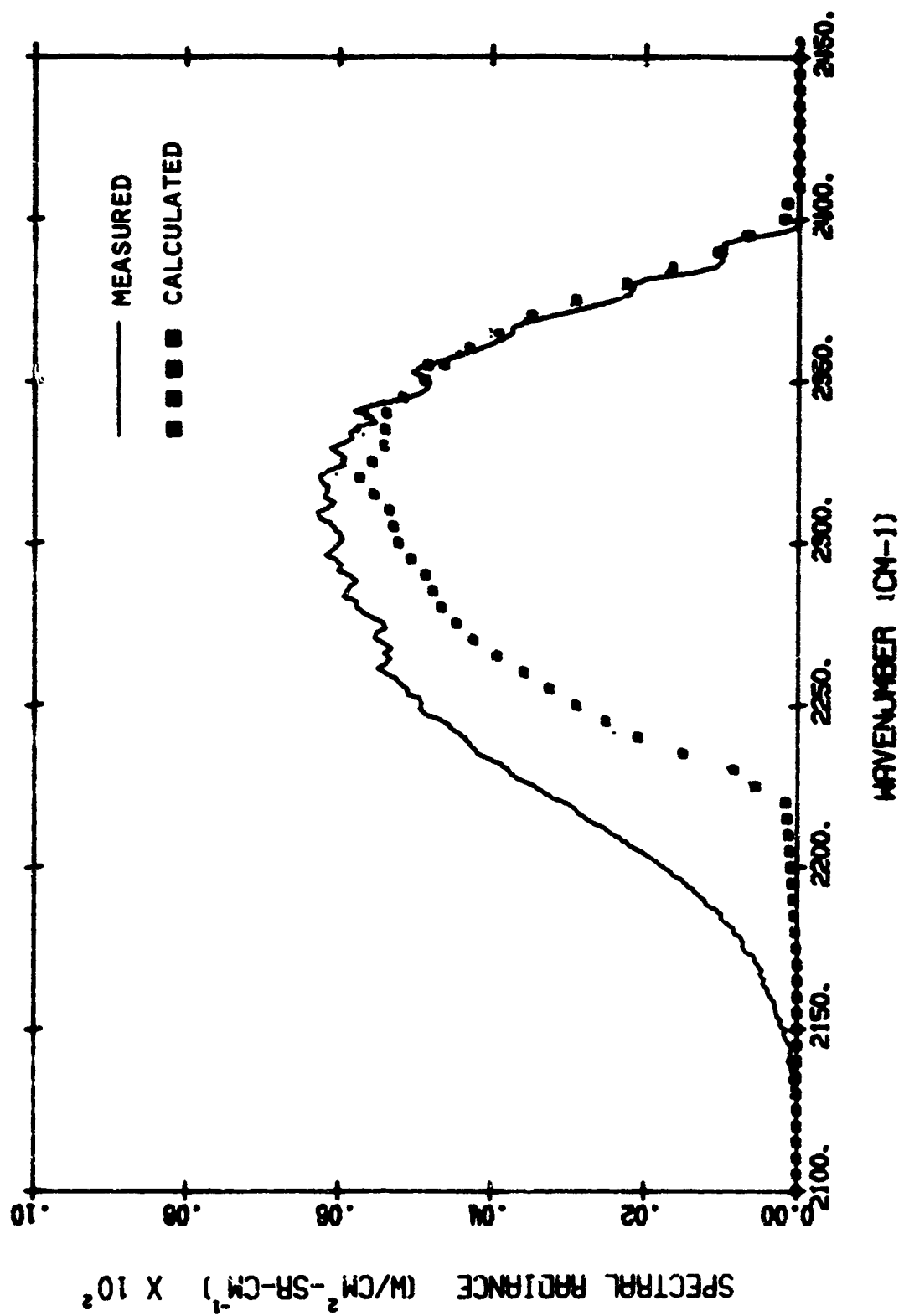


FIGURE 24. COMPARISON OF MEASURED HOT CELL RADIANCE WITH RADIANCE CALCULATED USING PARAMETERS OBTAINED FROM AFCRL TABULATION TEST 7, 4.3 μm , CO_2

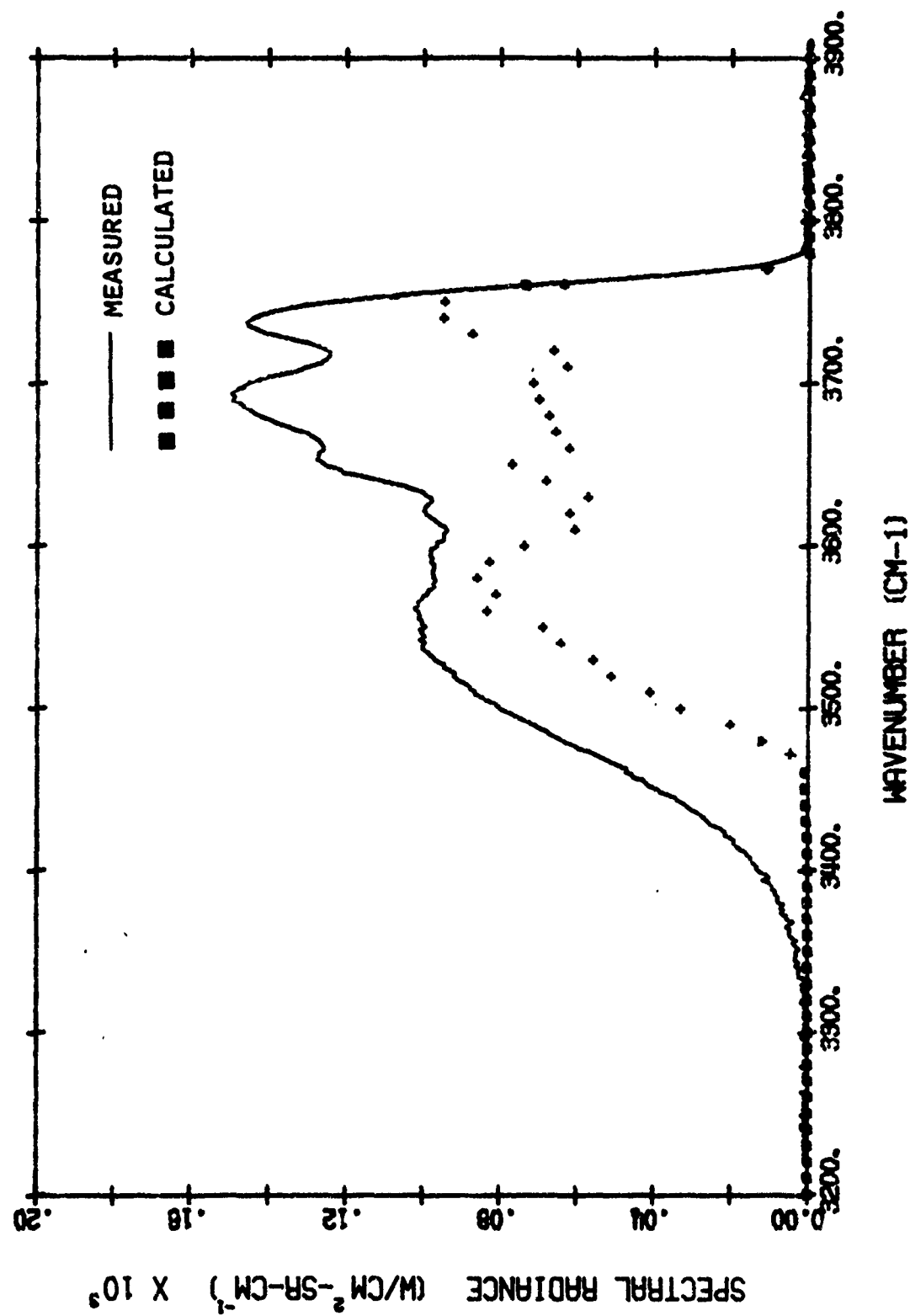


FIGURE 25. COMPARISON OF MEASURED HOT CELL RADIANCE WITH RADIANCE CALCULATED USING PARAMETERS OBTAINED FROM AFCRL TABULATION TEST 3, 2.7 μ m, CO₂

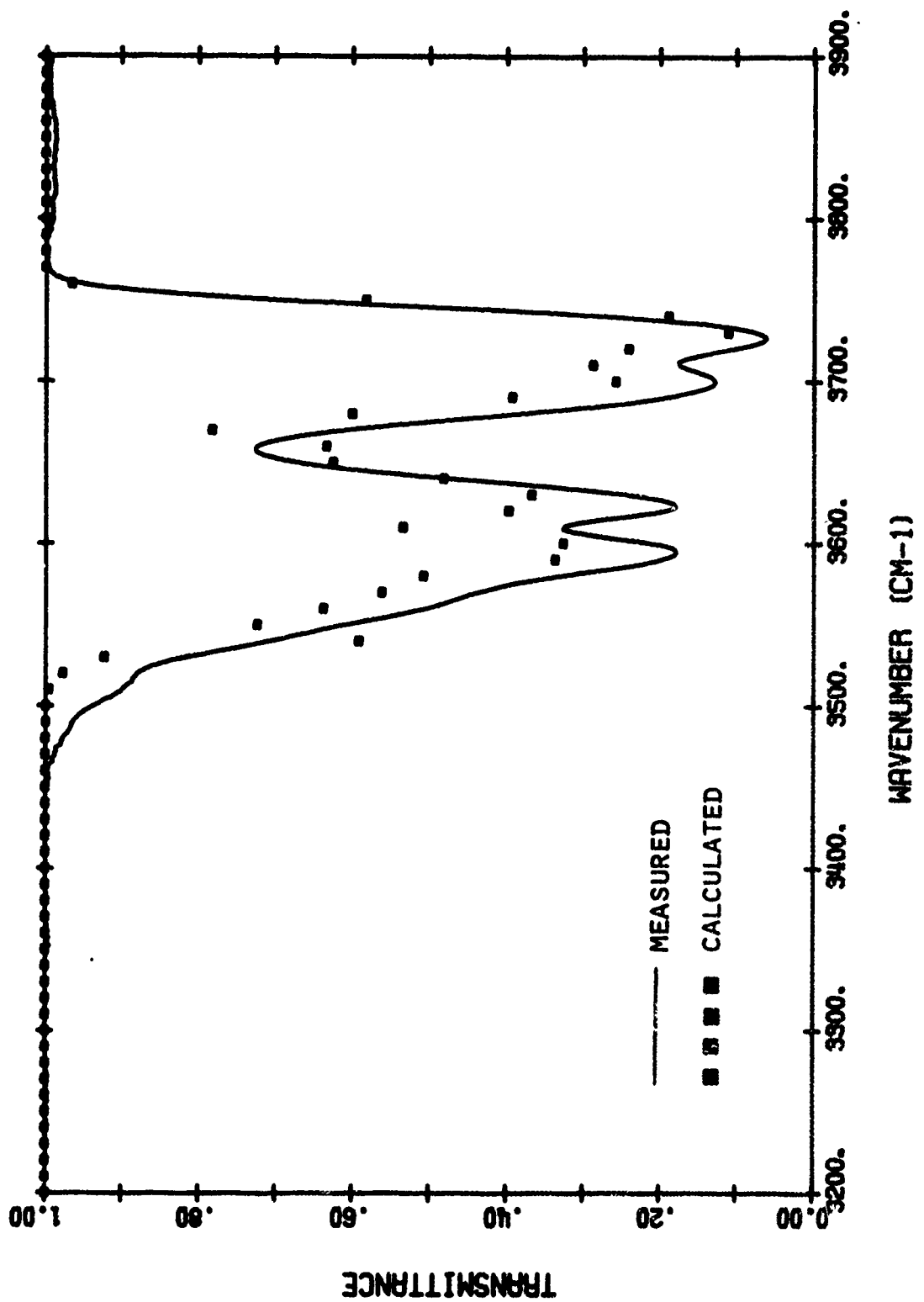


FIGURE 26. COMPARISON OF MEASURED COLD CELL TRANSMITTANCE WITH TRANSMITTANCE CALCULATED USING PARAMETERS OBTAINED FROM AFTRL TABULATION, TEST 3, 2.7 μ m, CO₂ ONLY, 10 km PATH AT 15 km ALTITUDE

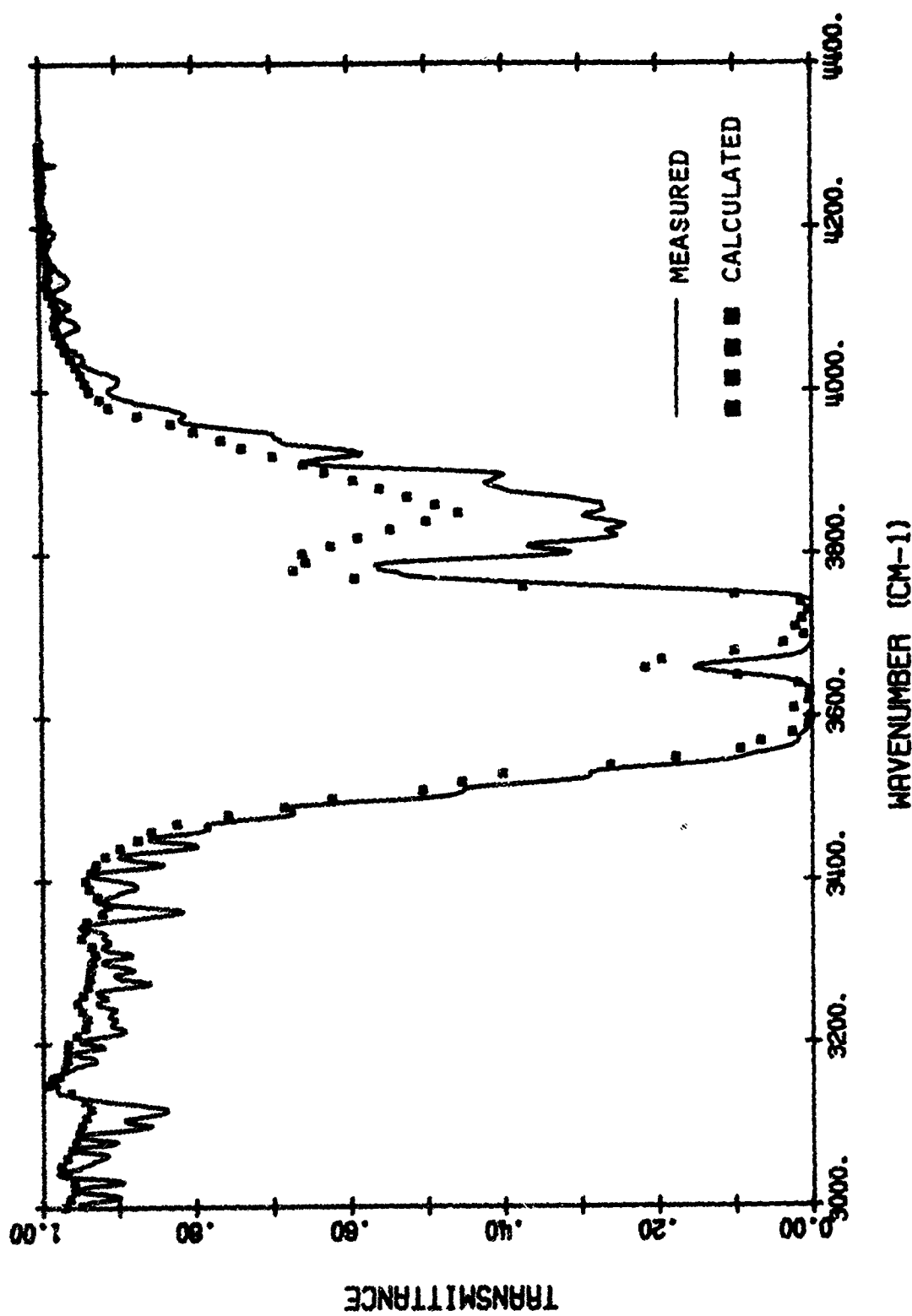


FIGURE 27. COMPARISON OF MEASURED COLD CELL TRANSMITTANCE WITH TRANSMITTANCE CALCULATED USING PARAMETERS OBTAINED FROM AFCRI TABULATION, TEST 19, 2.7 μ m, 50 km PATH AT 15 km ALTITUDE

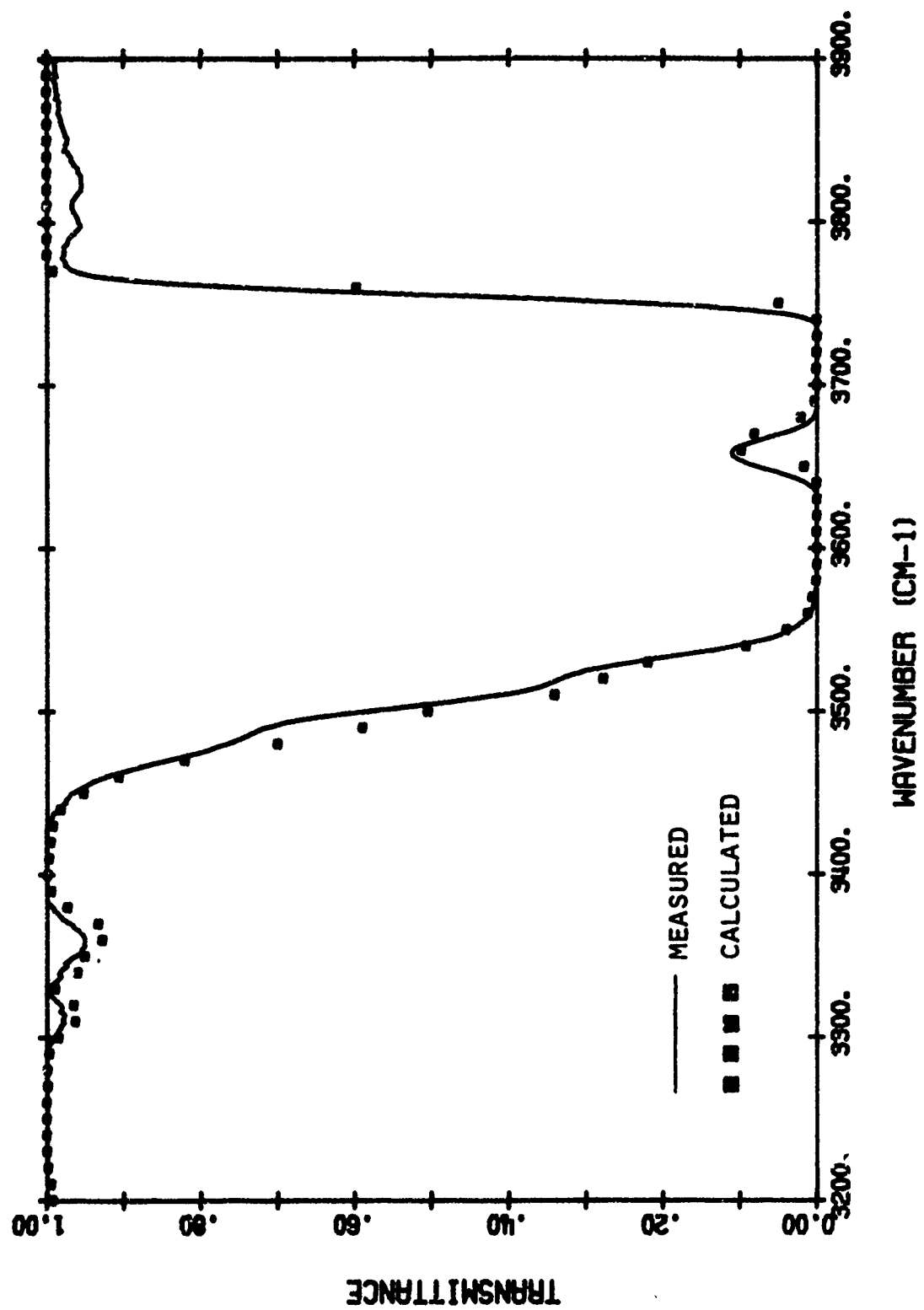


FIGURE 28. COMPARISON OF MEASURED COLD CELL TRANSMITTANCE WITH TRANSMITTANCE CALCULATED USING PARAMETERS OBTAINED FROM AFCRL TABULATION TEST 1, 2.7 μ m, CO₂ ONLY, 200 km PATH AT 15 km

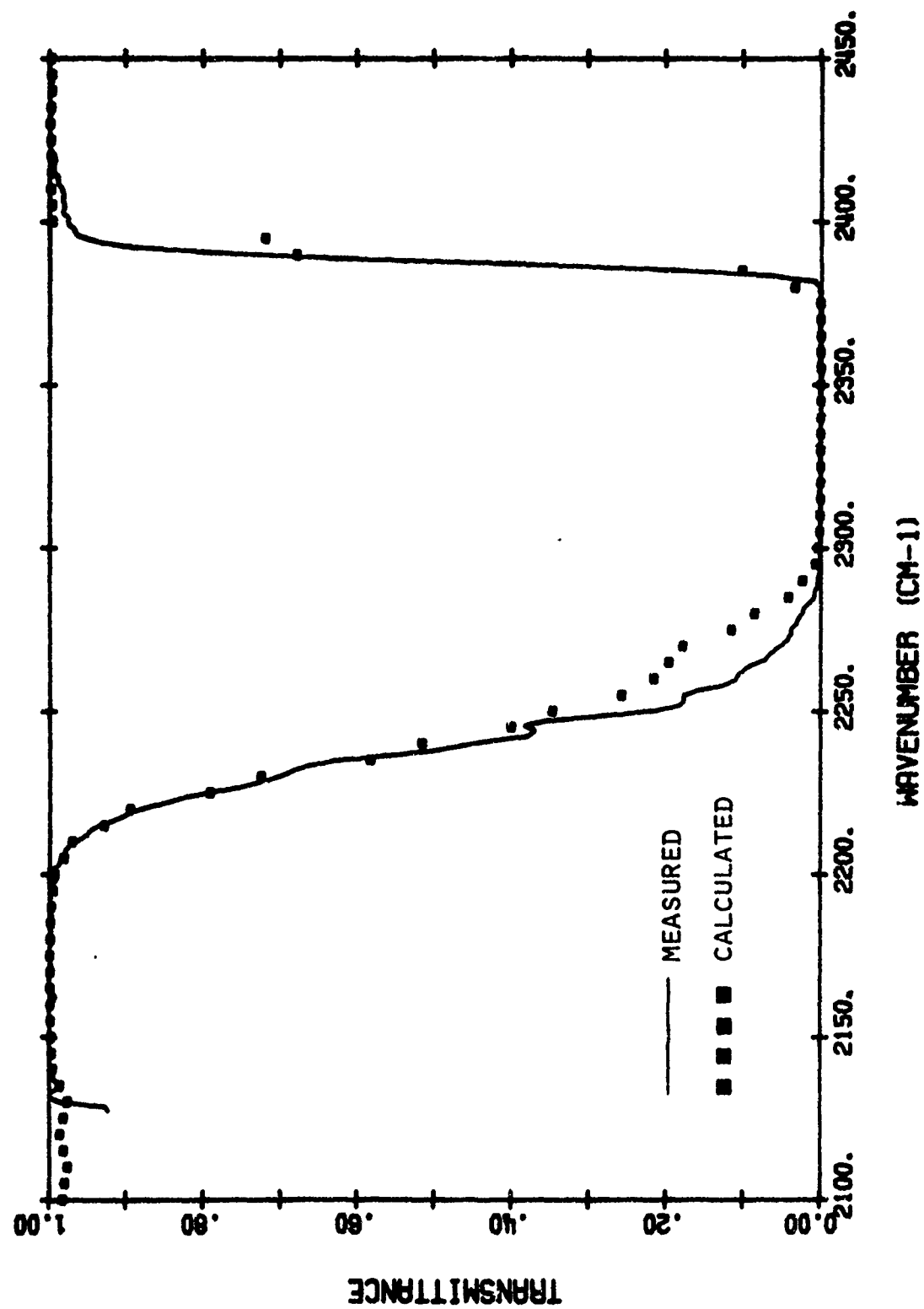


FIGURE 29. COMPARISON OF MEASURED COLD CELL TRANSMITTANCE WITH TRANSMITTANCE CALCULATED USING PARAMETERS OBTAINED FROM AFCRL TABULATION TEST 17, 4.3 μ m, 10 km PATH AT 15 km ALTITUDE

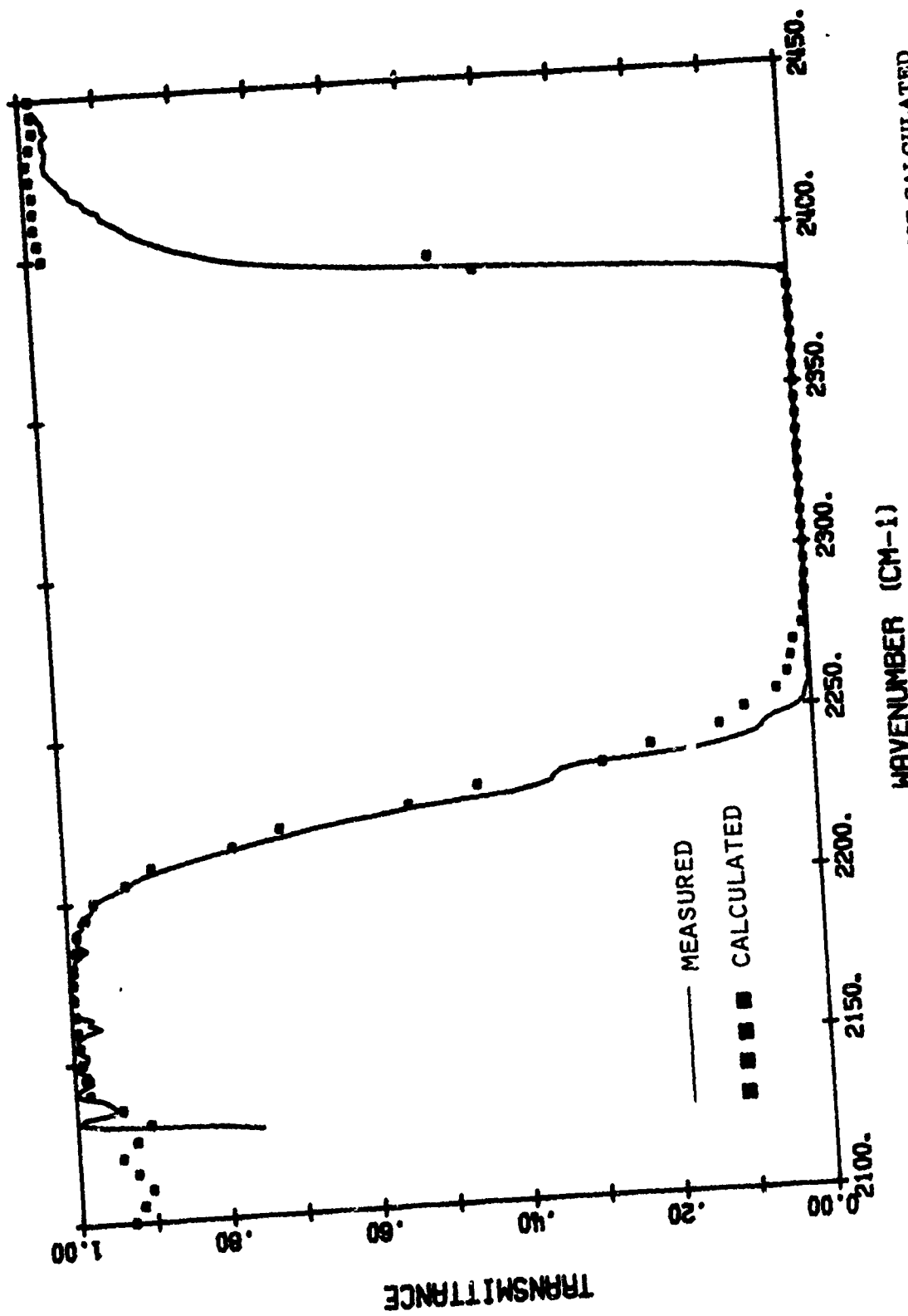


FIGURE 30. COMPARISON OF MEASURED COLD CELL TRANSMITTANCE WITH TRANSMITTANCE CALCULATED USING PARAMETERS OBTAINED FROM AFTRL TABULATION TEST 16, 4.3 μ m, 50 km PATH AT 15 km ALTITUDE

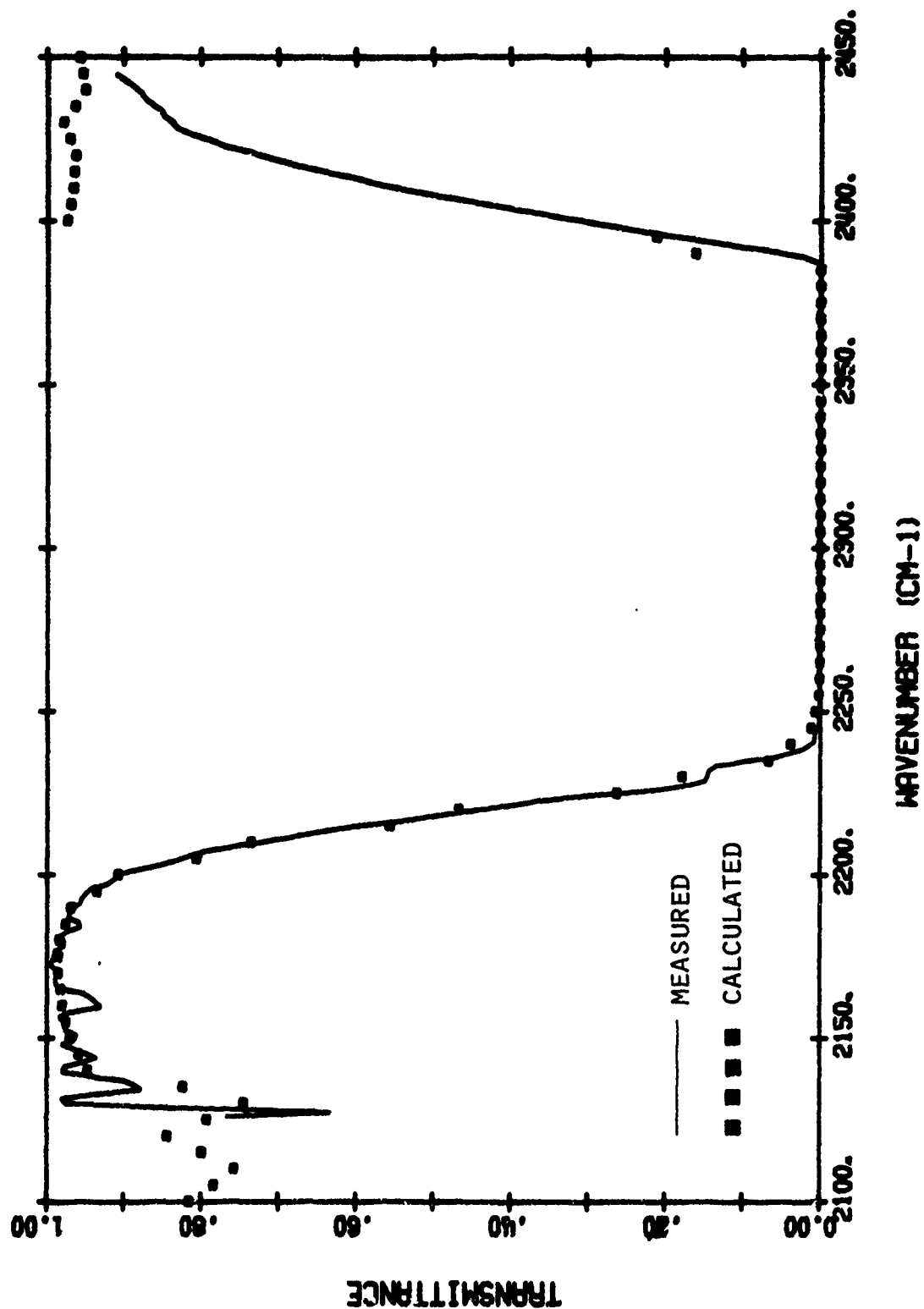


FIGURE 31. COMPARISON OF MEASURED COLD CELL TRANSMITTANCE WITH TRANSMITTANCE CALCULATED USING PARAMETERS OBTAINED FROM AFCRL TABULATION TEST 15, 4.3 μ m, 200 km PATH AT 15 km ALTITUDE

4.3 EFFECT OF THE CURVE OF GROWTH ON THE AGREEMENT BETWEEN THE MEASUREMENTS AND THE CALCULATIONS

We did not expect the calculations to be greatly dependent on the curve of growth. However, the hot cell radiances fell in regions of the curve of growth intermediate between the linear and square root regions at many of the frequencies. Where this was the case the computed results were affected by the curve of growth used. For the General Dynamics comparison shown in Figures 12 through 22 the curve of growth of Equation (49) was used. This curve of growth, which is valid for a random model with an exponential distribution of lines, is the form used to obtain the General Dynamics parameters from experimental data in the first place. Other curves of growth that could have been used are (a) the function valid for an inverse-strength distribution, Equation (39), and (b) the Ladenburg-Reiche function, valid for band of lines of equal strengths. The curve of growth of Equation (49) produces the best fit between the General Dynamics parameters and the measured data. On the one hand, this is not surprising because of its use by GD in fitting the data. On the other hand, if General Dynamics were indeed able to accurately determine the square root limit for each frequency, then the GD parameter determination should have been independent of the curve of growth, in which case the best-fit curve of growth for these measurements should be that which describes the line distribution best. Figure 3 showed that, for water at 3550 cm^{-1} at least, the line strength distribution is well represented by an inverse-intensity function. As a result, one would expect that Equation (39) would provide the best curve of growth. Since it does not, it can only be surmised that GD was not able to determine the actual square root limit for water vapor but only approximated it by extrapolation using the curve of growth of Equation (49).

The parameters obtained from the AFCRL tabulation do include the proper square root limit by definition, provided that the line strengths and widths are complete and accurate. (They appear to be accurate near band center.) Hence we would expect the best curve-of-growth to be that which corresponds most closely to the true statistical character of the band, again that of Equation (39). This curve-of-growth is indeed best for some portions of the band, but not for others. Figure 32 presents predictions, using parameters obtained from the AFCRL tabulations and based on the curves of growth of both Equations (39) and (49), compared to measured data.

The discussion here only serves to point out the problems involved in the choice of a curve-of-growth. It is not possible to separate the effects of possible failure of the assumptions of the band model (e.g., non-random spacing, coincidental line occurrences, etc.) with the possible effects of missing lines in the case of the AFCRL tabulation or with effects of errors in parameter determination in the case of the General Dynamics parameters.

Thus, the conclusion to be made from these sections, at least for isothermal paths, is that set of parameters and curve-of-growth should be used which give the best agreement with measurement.

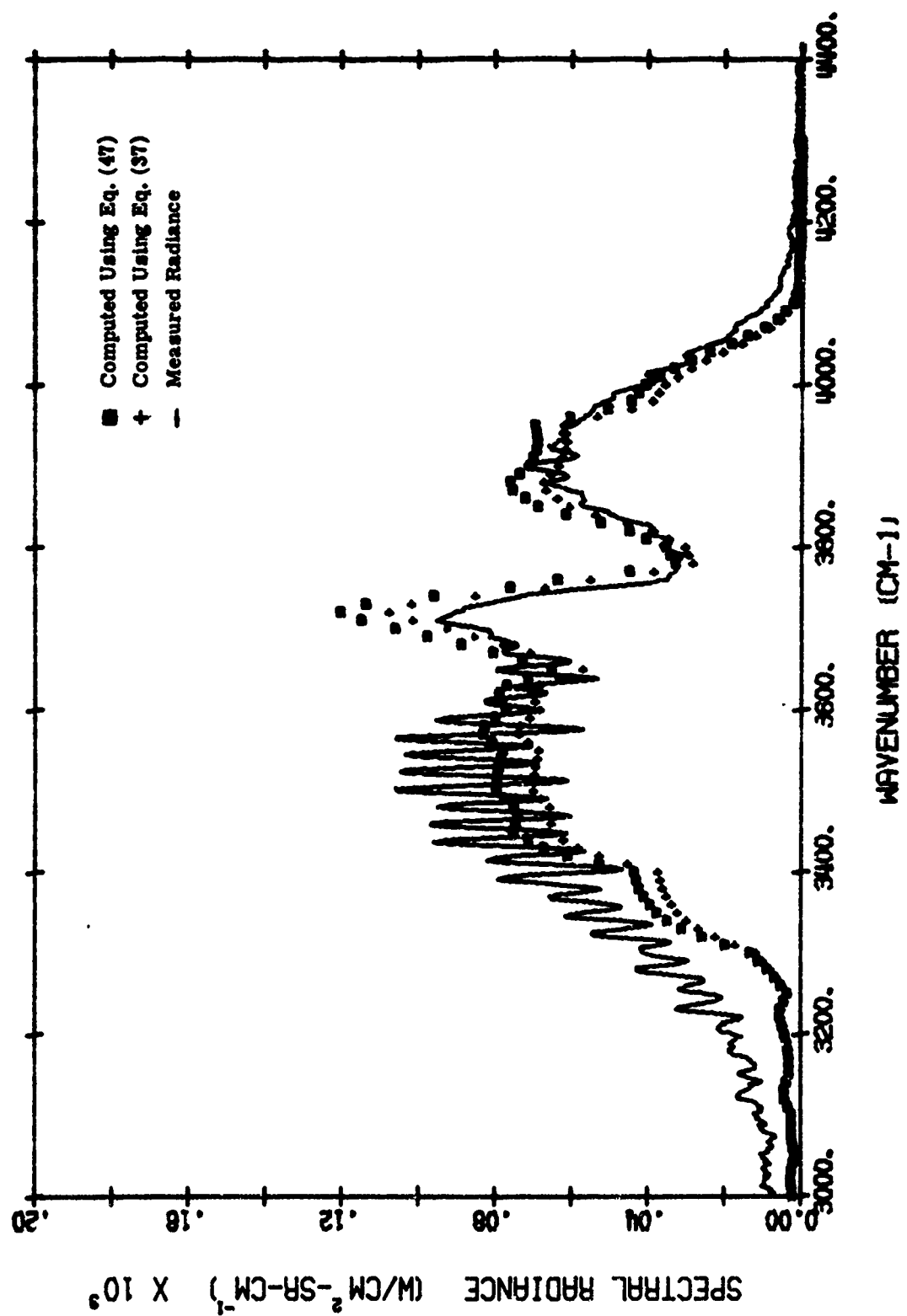


FIGURE 32. EFFECT OF THE CURVE OF GROWTH ON THE COMPUTED HCl CELL RADIANCE IN THE 2.7 μ m BAND (TEST 8)

4.4 HOT-THROUGH-COLD RADIANCE AND THE EFFECT OF THE CALCULATIONAL METHOD

In Section 2 a band model was developed specifically to handle the very non-isothermal conditions expected in computing the hot gas radiance as viewed through cold gases. A previous model^[8] was also developed to treat such cases, but it was never tested on real situations. In this section the two calculation techniques will be compared to experimental data for hot-through-cold radiances. We had hoped to make this comparison independent of the choice of spectroscopic parameters (GD parameters or AFCRL line tabulation), but there was enough variability in the degree to which these parameters fit the hot cell radiance measurements to produce variations in the way the two calculational methods predicted the radiances.

Figure 33 shows comparisons of the Lindquist-Simmons approximations^[8] of bottom data points, the band model of Section 2 (middle data points), and the multiplicative-transmittance approach (upper data points), along with measured hot-through-cold radiances (curve) for a typical water vapor run. The General Dynamics parameters and the curve-of-growth of Equation (49) were used for all of these comparisons (even though the curve-of-growth of Equation (39) applies strictly to the band model of Section 2). The case chosen was that representing the presence of the largest line correlation effects. It can be seen that the band model of Section 2 agrees best with measurements, although the values it produces are systematically low.

Figure 34 presents the same data, but based on the band model parameters obtained from the AFCRL line tabulations. Here, near band center, the band model of Section 2 represents the measured data very closely. Near the band edge none of the computed curves fits the data well, but this is again representative of the line tabulations failure to predict band edges because of the lack of upper state lines.

Figure 35 shows a curve similar to Figure 33 for the $4.3 \mu\text{m}$ CO_2 band. Here, the correlation effect is known to be negligible as discussed in Section 3. The three predictions are similar except for minor variations as might be expected based on the known lack of correlation effects. The results do not agree well with the data however because of the lack of agreement with the GD band model parameters as outlined in Section 4.1.

Figure 36 shows curves similar to Figure 34 for the $4.3 \mu\text{m}$ CO_2 band. Here the AFCRL parameters are used for the predictions. This curve demonstrates how poorly the line tabulation predicts the red spike. The three calculations show some effect of line correlation (the upper set of points is well separated from the lower set of points). This indicates that the lines in the tabulation are not so densely spaced as to eliminate correlation effects at 1200°K , whereas the measurements indicate no correlation effect in these regions of the band. This is further evidence for missing lines. The disagreement between measurement and each of the predictions is large enough that one cannot judge the best calculational technique.

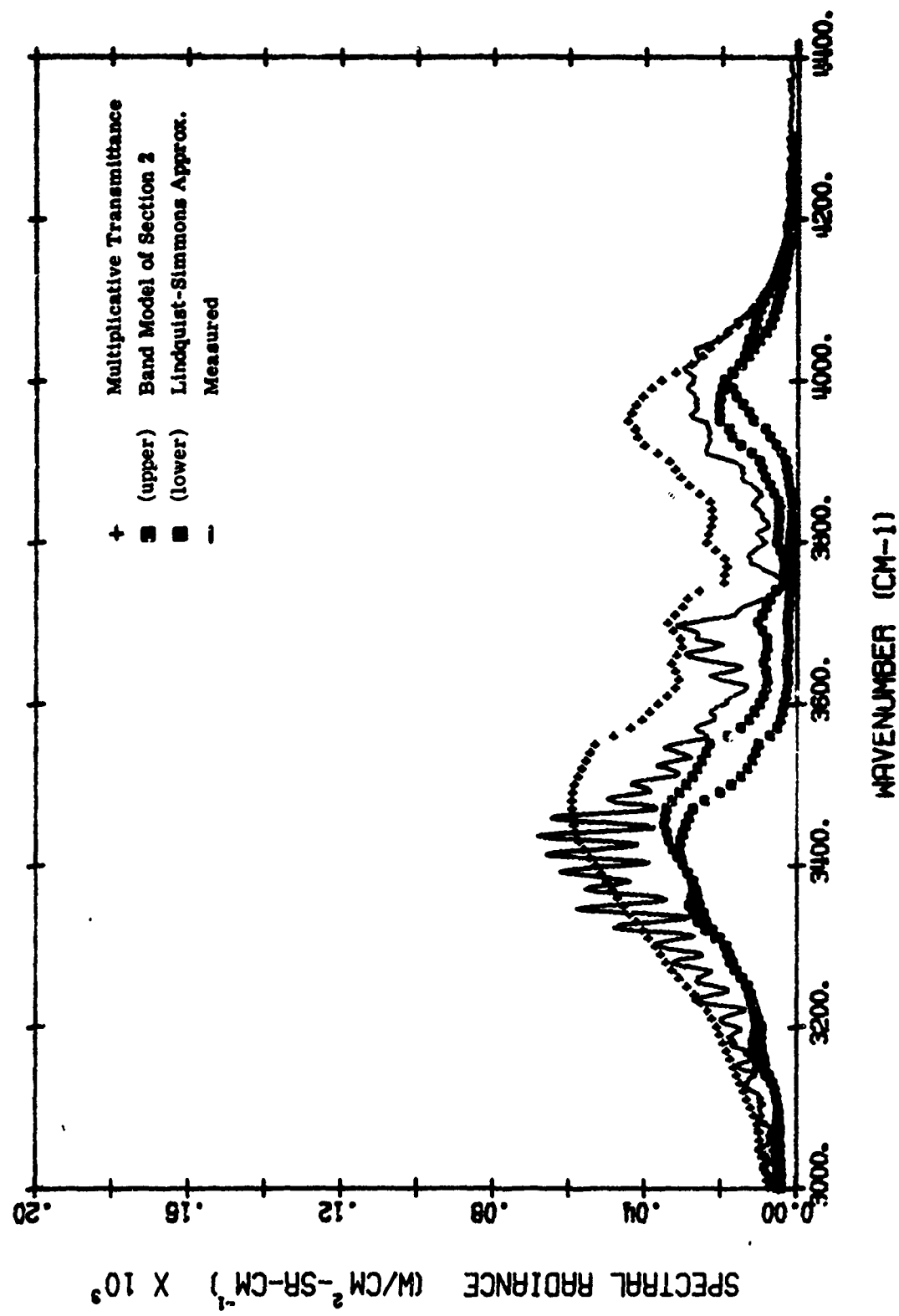


FIGURE 33. COMPARISON OF THE HOT-THROUGH-COLD RADIANCE AS MEASURED AND AS PREDICTED BY 3 METHODS FOR THE 2.7 μm WATER VAPOR BAND, USING THE GENERAL DYNAMICS PARAMETERS (TEST 8)

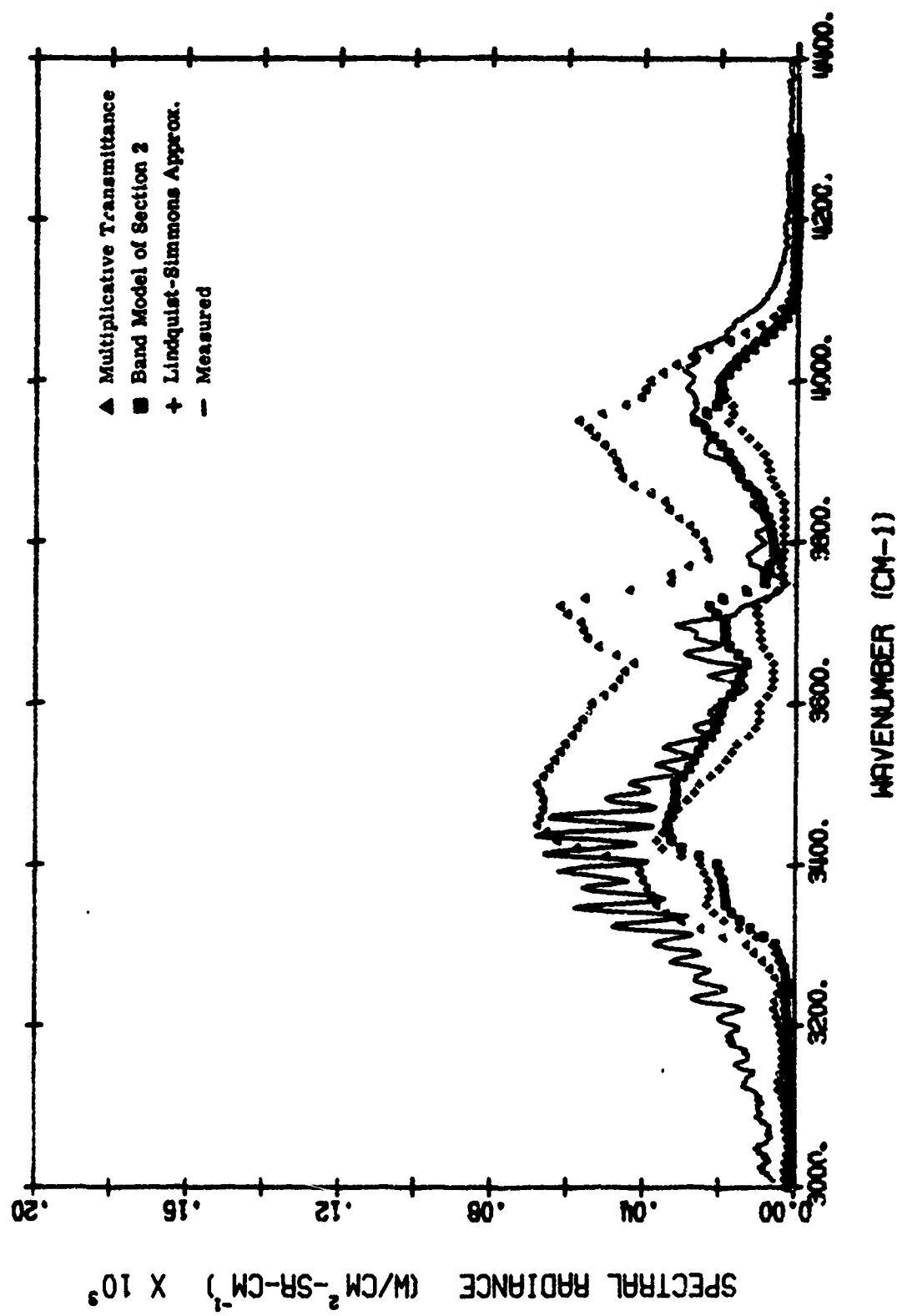


FIGURE 34. COMPARISON OF THE HOT-THROUGH-COLD RADIANCE AS MEASURED AND PREDICTED BY 3 METHODS FOR THE $2.7 \mu m$ WATER BAND, USING PARAMETERS OBTAINED FROM THE CRL TABULATION (TEST 8)

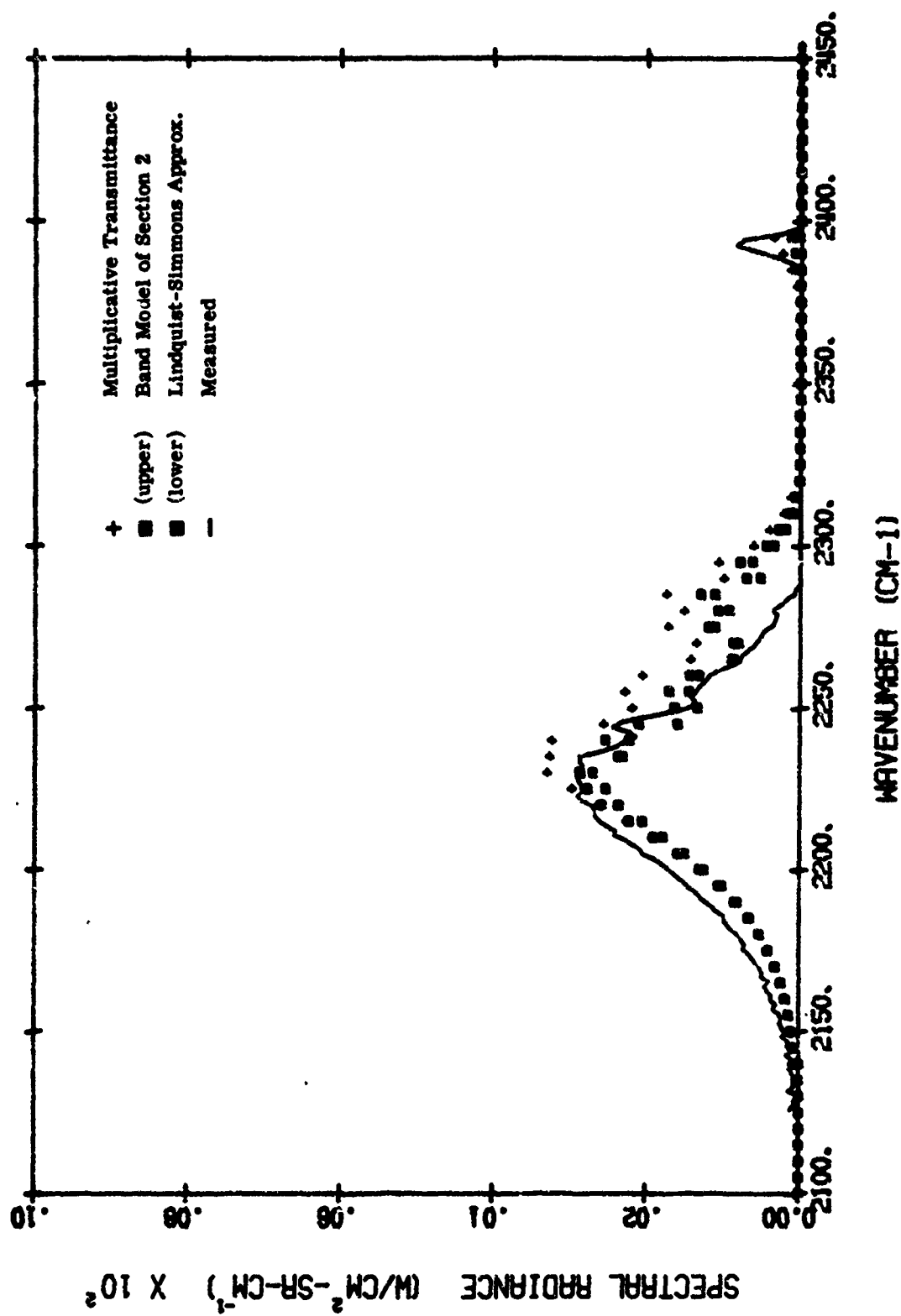


FIGURE 35. COMPARISON OF THE HOT-THROUGH-COLD RADIANCE AS MEASURED AND PREDICTED BY 3 METHODS FOR THE $4.3 \mu\text{m}$ CO_2 BAND, USING THE GENERAL DYNAMICS PARAMETERS (TEST 7)

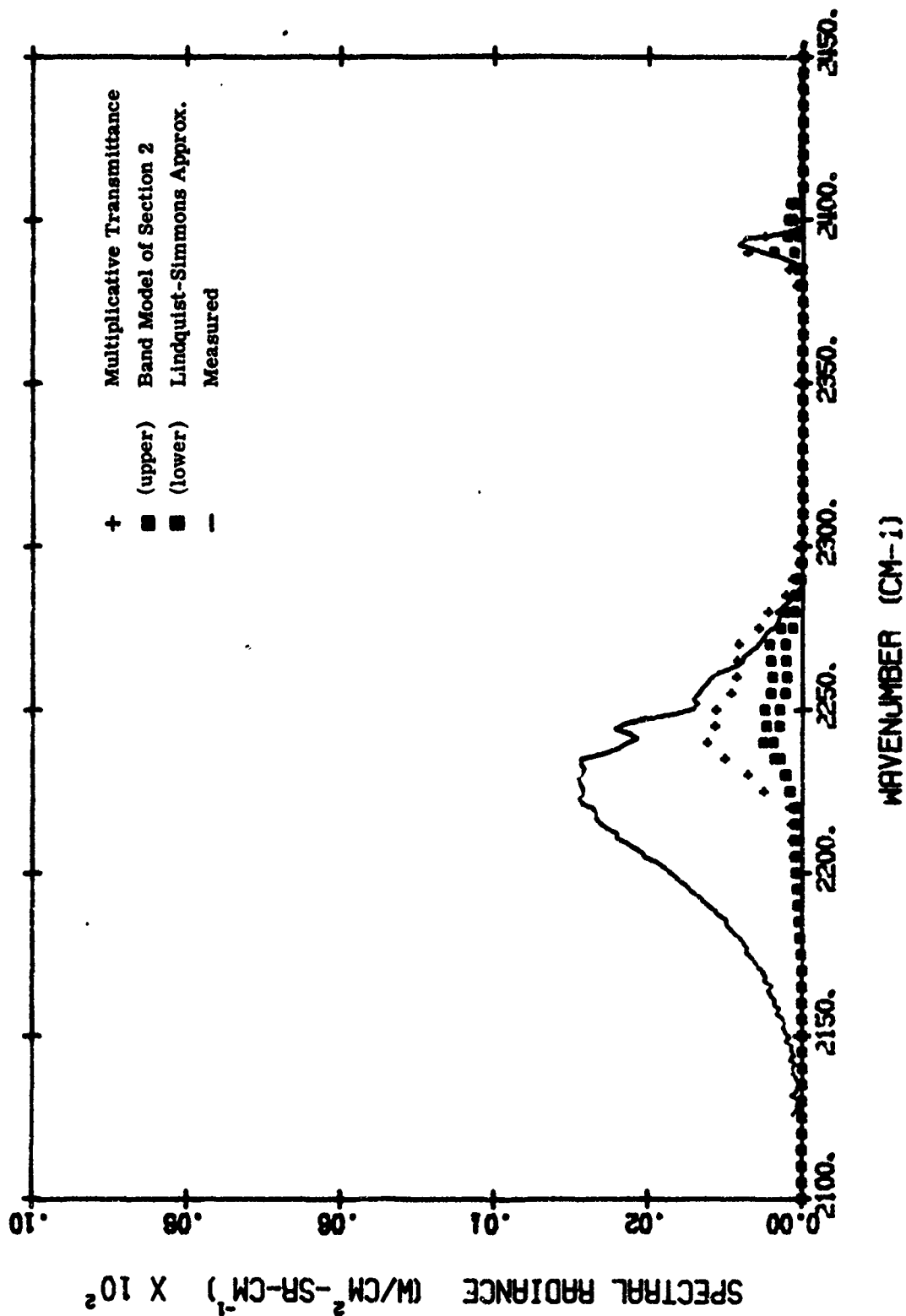


FIGURE 36. COMPARISON OF THE HOT-THROUGH-COLD RADIANCE AS MEASURED AND PREDICTED BY 3 METHODS, FOR THE $4.3 \mu\text{m}$ CO_2 BAND, USING PARAMETERS OBTAINED FROM THE CRL TABULATION (TEST 7)

Figures 37 and 38 show curves for the $2.7 \mu\text{m}$ CO_2 band. Since correlation effects are important here, the three predictions again give different results. Here again, the disagreement between the measurements and the available parameters is so great that a judgment concerning the calculational techniques cannot be made.

From the foregoing figures it can be seen that the water vapor region at $2.7 \mu\text{m}$ is the only region where both (1) the band model parameters are consistent with the data, and (2) where correlation effects are present. It is only under these conditions that the three calculational techniques (the band model of Section 2, the Lindquist-Simmons approximation, and the multiplicative transmittance approach) can be fairly compared. In this region the band model of Section 2 does indeed do a better job of prediction than the other two methods. However, the agreement between this new method and the experimental data is not as good as it might be. We currently attribute this uncertainty to the uncertainties in the emission-absorption parameters compared to the measured hot gas radiance values.

4.5 COMPARISON OF BAND MODEL TO AN ARRAY OF WATER VAPOR LINES

A much more satisfying way of evaluating the band model of Section 2 would be to compare it to a specific array of absorption lines. Such an array need not correspond exactly to a real band in order to provide a test of the model. We have performed such an evaluation for a spectral resolution element 25 cm^{-1} wide centered at 3550 cm^{-1} .

It was done by computing the transmittance derivative with infinitely fine resolution using the AFCRL line tabulation, smoothing the result to 25 cm^{-1} , and comparing the result to the transmittance derivative of Equation (34), which was evaluated using the band model parameters determined from the line tabulation.

The line-by-line calculations of the transmittance derivative were made using the same homogeneous path approximations as were made in the development of Section 2. This procedure made the comparisons free of any effects introduced by non-homogeneous paths and limited the comparison to the statistical properties of the arrangement of the array of lines. The following equation was used in the line-by-line calculation of the transmittance derivative.

$$\frac{d\tau}{da}(\tilde{\nu}) = \sum_{i=1}^N \frac{S_i(T)\gamma_i(T,p)}{\gamma_i^2(T,p) + (\tilde{\nu} - \tilde{\nu}_{o_i})^2} \exp \left[\frac{S_i(\bar{T})\gamma_i(\bar{T},\bar{p})a}{\gamma_i^2(\bar{T},\bar{p}) + (\tilde{\nu} - \tilde{\nu}_{o_i})^2} \right] \quad (52)$$

where \bar{T}, \bar{p} are the temperature and broadening pressure of the isothermal cool path, and a is its absorbing length. T, p are the local temperature and broadening pressure of the hot emitting path.

Equation (52) was used to compute the transmittance derivative for several cases representing different optical path lengths corresponding to several values of the quantity u , as well as for a single combination of $T = 1200$, $\bar{T} = 300$, $P = 0.0379$ atmosphere of water vapor,

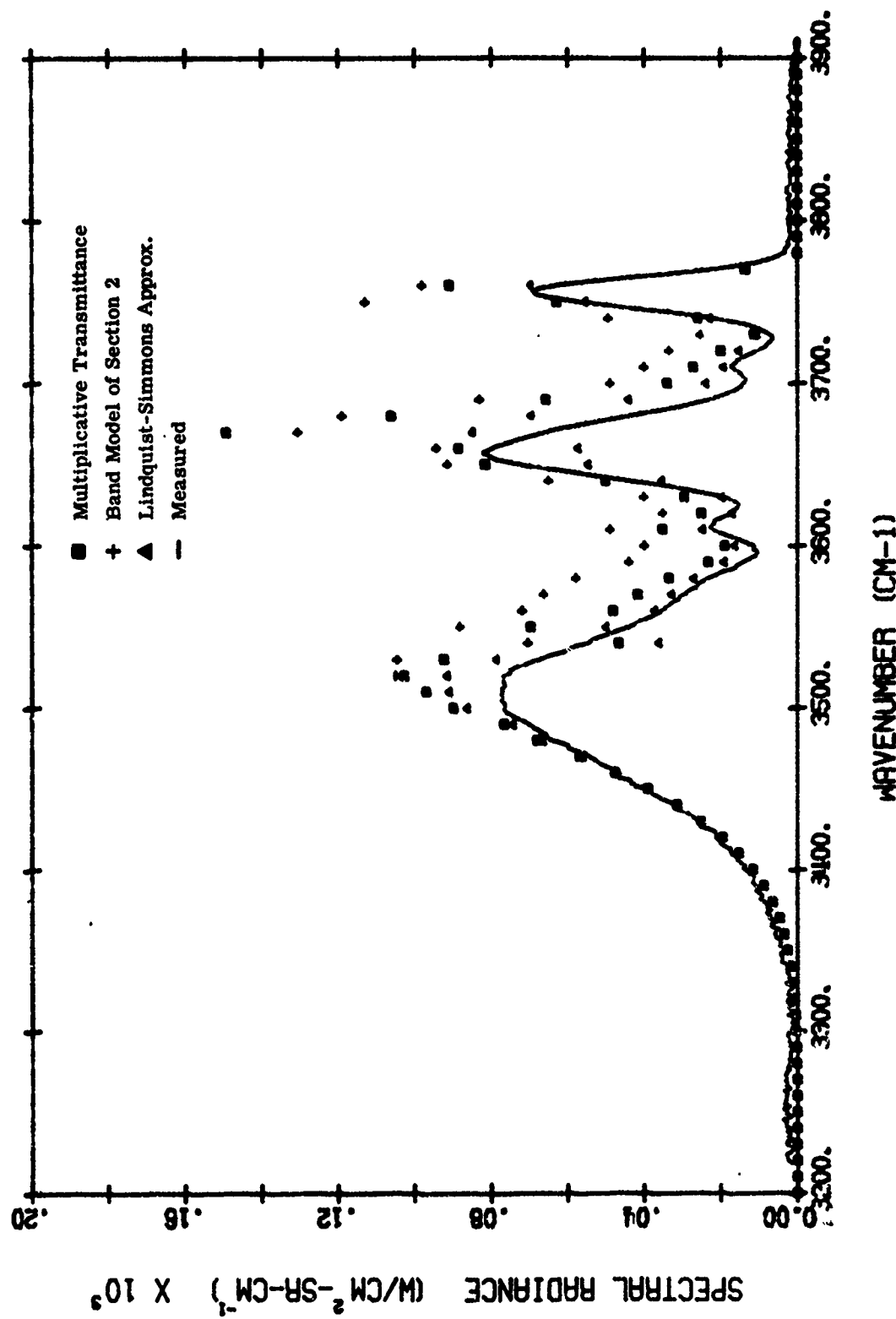


FIGURE 37. COMPARISON OF THE HOT-THROUGH-COLD RADIANCE AS MEASURED AND PREDICTED BY 3 METHODS, FOR THE $2.7 \mu\text{m}$ CO_2 BAND, USING THE GENERAL DYNAMICS PARAMETERS (TEST 3)

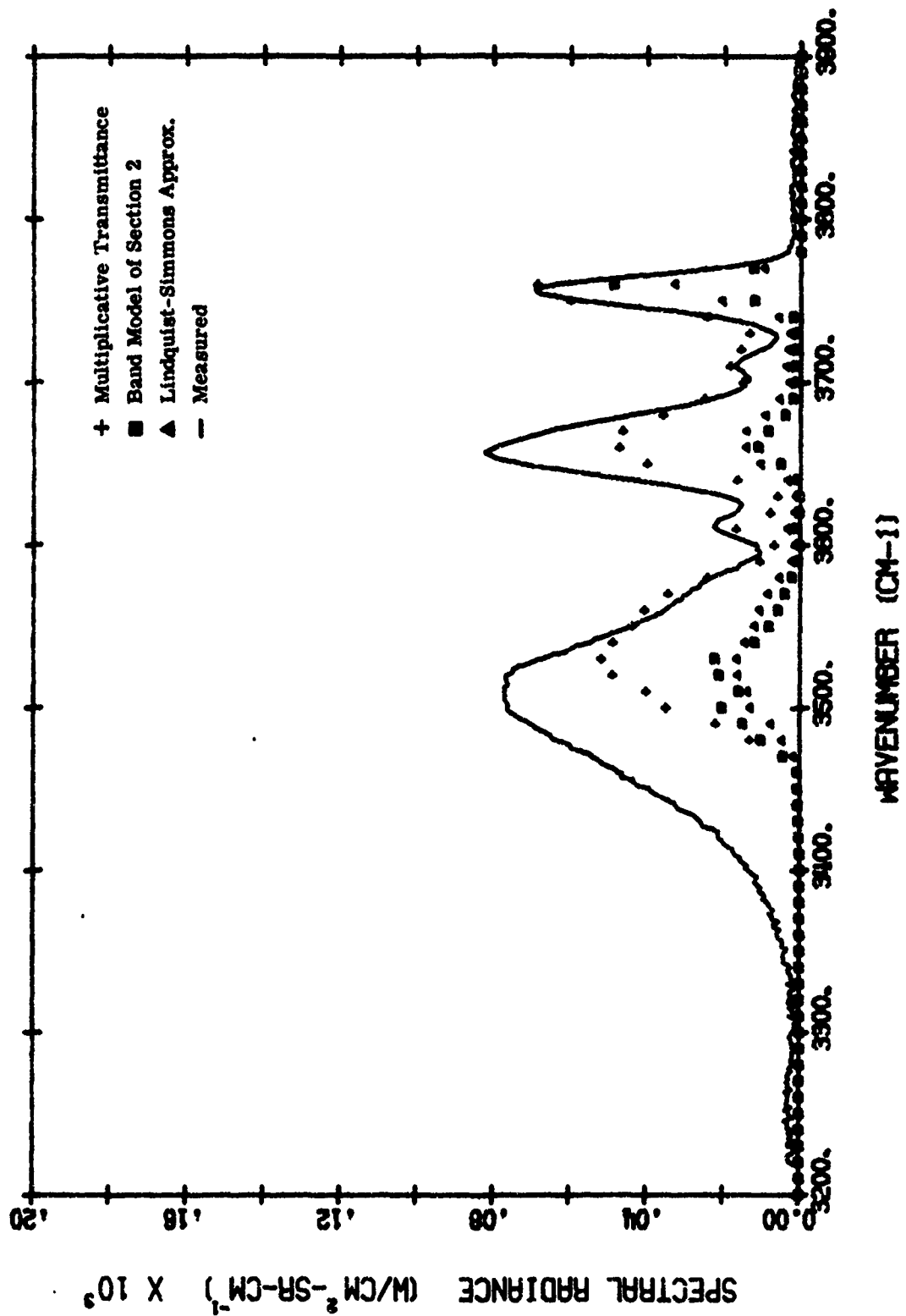


FIGURE 38. COMPARISON OF THE HOT-THROUGH-COLD RADIANCE AS MEASURED AND PREDICTED BY 3 METHODS, FOR THE $2.7 \mu\text{m}$ CO_2 BAND, USING PARAMETERS OBTAINED FROM THE CRL TABULATION (TEST 3)

and $\bar{P} = 0.003$ atmosphere of water vapor. No foreign gas broadening was used in the calculation. This gave the conditions $q/\bar{q} = 1/4$, $y/\bar{y} = 8$ so that $\gamma/\bar{\gamma} = 2$ in the band model of Section 2. The transmittance derivative computed by Equation (52) was smoothed with a square slit function 25 cm^{-1} wide to correspond to the averaging width used to compute band model parameters from the AFCRL tabulation.

Figure 39 shows the average equivalent width derivative as predicted by the Lindquist-Simmons approximation, the band model of Section 2, and these line-by-line calculations. The results from the line-by-line calculations fall between the two band-model calculation methods, and they are a result of the fact that neither set of assumptions is completely satisfied by the group of lines contributing to the line-by-line calculations. Calculations at additional frequencies are sure to give different results, and more extensive comparisons are needed before judgments are made. (Because the development of Section 2 was not completed until the very end of the effort, comparisons could not be exhaustive.) Any substantial disagreement between the band model of Section 2 and the line-by-line calculations which persist is most probably the result of the assumed relationship between E and S_o . This relationship could be adjusted to provide optimum agreement with line-by-line calculations once a definitive comparison is made. Such a task should receive high priority in future work.

5

CONCLUSIONS AND RECOMMENDATIONS

Because there was a mixture of experimental and theoretical efforts in this work, there are a great many conclusions.

The evidence for these conclusions is not complete in some cases, but several significant statements can be made concerning plume calculation techniques. We have organized these conclusions into four categories.

5.1 THE PRESENCE OF CORRELATION EFFECTS

It is concluded from the experimental results that in the $2.7 \mu\text{m}$ water bands, the accurate calculation of plume radiation at a distance requires that line correlation effects be accounted for if errors of the order of a factor of 2 are to be avoided. Based on these measurements, we expect that line correlation effects will be important for this band independent of the optical path involved. Therefore, the calculation techniques used should be able to treat these effects. Although its accuracy has not been completely verified during this program, the band model of Section 2 does appear to do a creditable job of handling correlation effects.

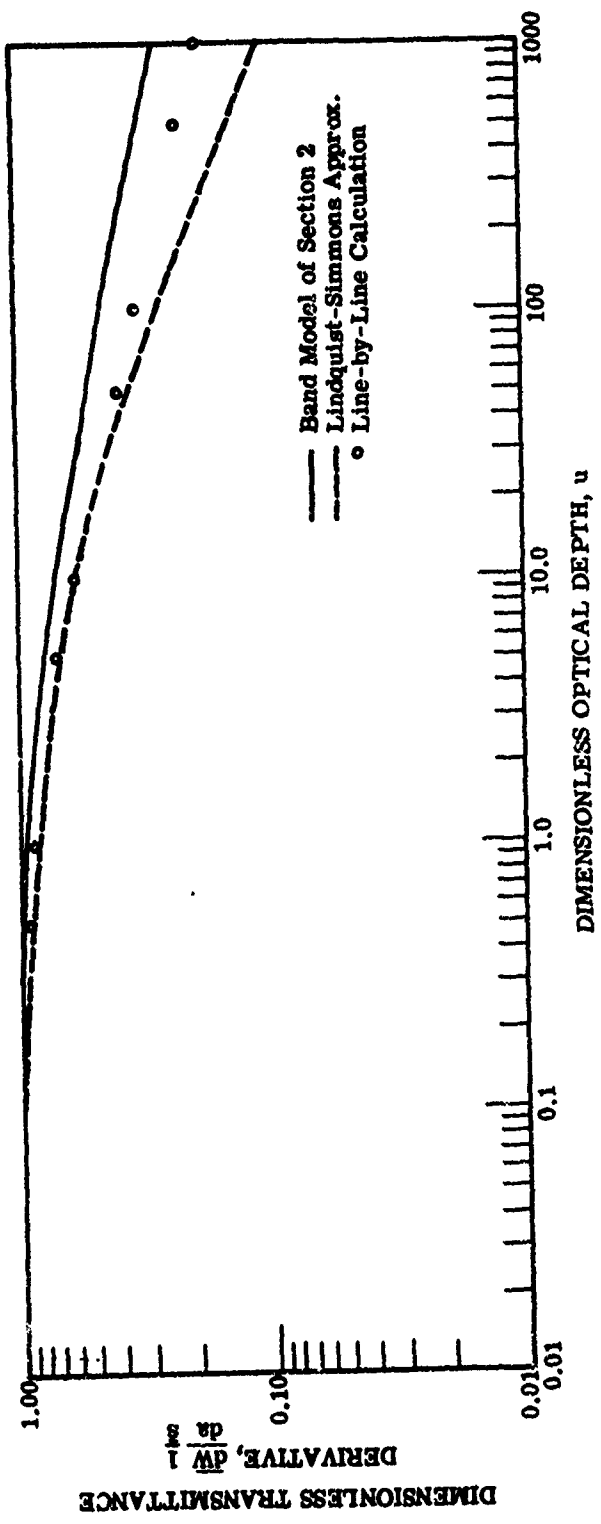


FIGURE 39. COMPARISON OF THE BAND MODEL OF SECTION 2, AND THE LINDQUIST-SIMMONS APPROXIMATION WITH LINE-BY-LINE CALCULATIONS FOR WATER VAPOR AT 3550 cm^{-1}

The CO_2 band at $4.3 \mu\text{m}$ is not so easily dismissed. At the moderate altitude conditions used in this program (about 0.1 atmosphere) it should be valid to ignore line correlation effects in the long wavelength wing. The measurements confirm this and the band model parameters predict it. Thus at 0.1 atmospheres or more, even the multiplicative-transmittance approach provides realistic results for plume radiation through an atmospheric path. The reason for this cannot be that the emission and absorption lines are uncorrelated. Rather, it must be that the lines are wide enough and/or so densely spaced that either the emission or absorption spectrum (or both) takes on a continuous appearance. That this is almost certainly the case can be assessed from the band model parameter β (or equivalently y), which is a measure of approach to square-root growth where line overlap is important. The General Dynamics tabulations for the $4.3 \mu\text{m}$ CO_2 band indicate values for β of the order of 30 to 50 at 1200°K and 100 or larger at higher temperatures. The fact that these values are so large implies line overlapping. At temperatures below 1200°K the values are not large and are generally less than 10 at sea level pressure. Thus, as temperature and pressure are decreased, the GD parameters predict that correlation effects will become more important. The current measurements, limited in temperature and pressure by the sensitivity of the system as it was operated during this program, were not able to include hot-through-cold radiance measurements at lower temperatures than 1200°K , nor at optical depths smaller than that produced by 60 cm of CO_2 at a 0.05 atmosphere pressure. Thus, the possible correlation effects in the $4.3 \mu\text{m}$ band occur at lower temperatures (and pressures) than could be produced in these experiments and remain essentially unexplored. Measurements specifically aimed at the conditions where correlation effects might be important could be made with the instrumentation used in this program, with addition of a grating which gives optimum dispersion around $4.3 \mu\text{m}$ and by sacrificing some of the spectral resolution. (The 4 cm^{-1} spectral resolution used in this region is finer than needed.)

Since the band model parameters extracted from the line tabulation do not predict the observed hot-through-cold radiances well in the $4.3 \mu\text{m}$ region, they are probably not useful for predicting when high temperature correlation effects will be important. This is most likely the result of omission of most of the "hot" lines from the AFCRL tabulation. At lower temperatures, where the tabulation should be valid, the AFCRL tabulation predicts β values at only 2 to 3, even at mid-band, so that one would indeed expect correlation effects under these conditions.

The short wavelength wing of the $4.3 \mu\text{m}$ CO_2 band consists primarily of the higher rotational lines of the ν_3 fundamental band, the so-called "blue spike." One would expect correlation effects to be important here except right at the band head, and the measurements do indeed show this.

Measurements in the $2.7 \mu\text{m}$ CO_2 band show moderate line correlation effects, but the poor agreement of both sets of band model parameters with the measurements makes it

difficult to assess the degree to which these effects can be handled using present calculation techniques. One would expect, however, that the development of a set of parameters which adequately treats this band is the primary missing link; the calculation techniques which work for the $2.7 \mu\text{m}$ water band and the $4.3 \mu\text{m}$ CO_2 band should also be suitable for treating correlation effects in the $2.7 \mu\text{m}$ CO_2 band.

To summarize, correlation effects are important in the $2.7 \mu\text{m}$ water band. They are observed in all the measurements throughout the band. Therefore, special attention should be given to plume calculation techniques to be sure that correlation effects are included, as in the model of Section 2. Correlation effects were observed only in the "blue spike" region of the $4.3 \mu\text{m}$ CO_2 band, but parameter values indicate that correlation techniques could be important throughout the band at lower temperatures and pressures. Correlation effects were observed throughout the $2.7 \mu\text{m}$ CO_2 band, but they were less severe than those observed in water vapor.

5.2 CONCLUSIONS CONCERNING THE CONSISTENCY OF THE MEASUREMENTS WITH BAND MODEL PARAMETERS

The band model parameters of General Dynamics do reasonably well in calculating the radiance expected from the isothermal hot cell alone. The agreement for water vapor is reasonably good throughout the band.

For the $4.3 \mu\text{m}$ CO_2 band, the long wavelength wing is not as well predicted as the remainder of the band; this effect produces substantial disagreement in the prediction of hot-through-cold radiances in this portion of the band.

The band model tabulations for the $2.7 \mu\text{m}$ CO_2 band produce radiance predictions substantially different from those observed. These disagreements appear to be real and substantial, particularly when the tabulations are used to compute radiances of hot targets viewed through cool atmospheric paths. Therefore, it appears that a series of isothermal measurements are needed to resolve the deficiencies both in the long wavelength wing of the $4.3 \mu\text{m}$ band and throughout the $2.7 \mu\text{m}$ band. It appears that the calculations made by Malkmus, from which the existing General Dynamics CO_2 parameters were obtained, are quite consistent with existing measurements, but differ enough in the details of the long wavelength wing to produce non-negligible inaccuracies in hot-through-cold radiances.

The General Dynamics parameters do not predict the cold cell transmittances well. This is probably the result of the fact that they were obtained primarily by extrapolation from high temperature measurements.

The band model parameters derived from the AFCRL line tabulation^[2] do an adequate job of predicting the measurements only when all lines which are significant at the temperatures involved are included in the tabulation. This is the case for the cold cell transmittances

and, it appears, for regions in the center of the water vapor band at $2.7 \mu\text{m}$. At the edges of the $2.7 \mu\text{m}$ band, however, the parameters from the AFCRL tabulation do not predict the observed absorption accurately. That the band center is well treated while the band edges are poorly treated indicates that lines are missing mostly from the band edges. This, in turn, probably indicates that important higher level rotational lines are missing. For CO_2 , the CRL line parameters agree well on the short wavelength side but poorly on the long wavelength side. The short wavelength wings contain the band heads of all the R-branches of the bands; if the tabulation extends to the band heads or nearly so, this could be the reason for the good agreement in the R-branch. Missing rotational lines might then be the reason for the poor agreement in the long wavelength wing (P-branches).

We have not examined the line tabulation in order to sort out the reasons for this lack of agreement, except to note that the tabulation of the $\tilde{\nu}_3$ fundamental extends out nearly to the $\tilde{\nu}_3$ fundamental band head which produces the "blue spike" at $4.17 \mu\text{m}$. The tabulation ends only several lines short of this band head.

At its present state, the AFCRL line tabulation is surely not adequate to accurately predict plume radiation above temperatures of 1200°K . The reasons for the disagreement between the line tabulation and the measurements made in the program need to be determined, and the important missing lines added to the tabulation where possible. This task is now underway, but the substantial disagreement between the line tabulation and the measurements described herein indicates that there is much to be done.

Previous discussion has dealt mostly with comparisons of the hot cell radiance measurements with band-model calculation results using different sets of parameters. Since measurements were made with rather short high temperature optical paths, the comparisons apply more to the first band model parameter (the line-strength-to-spacing ratio) rather than the second (which governs the approach to the square-root region). But the hot-through-cold radiance measurements, having been made through long cold paths, depend heavily on the ratio of a local value of the 2nd band model parameter in the hot path to its average value up to the hot path. This dependence is demonstrated in both the Lindquist-Simmons approximation and the band model developed in Section 2 by the importance of the variable, $\gamma/\bar{\gamma}$. Agreement of either of these methods with the observed data depends heavily upon the accuracy of the second band model parameter, thus creating a problem which is illustrated by the wings of the $2.7 \mu\text{m}$ water vapor band.

The extreme wings of this band in the hot cell radiance are not significantly attenuated by the cold cell, as shown by the measured hot-through-cold radiance data and by cold cell transmittance measurements. Yet both the Lindquist-Simmons and the band-model of Section 2 predict substantial attenuation in these wings and produce much poorer percentage agreement with measurements in this region than in any other. Since the hot cell radiance is

correctly predicted, this poor agreement is either due to a gross departure of the wing of the $2.7 \mu\text{m}$ band from the band model assumptions or to errors in the second-band-model parameter in the hot cell. It appears that values for the second parameter in these wings are the result of an extrapolation in the General Dynamics work^[16], perhaps because in their measurements the square root region could not be approached. This could easily account for the observed disagreement. The accurate calculation of plume radiances through cool atmospheric paths thus requires accurate values for the second band model parameter in the hot path. It is possible that a formulation could be found which would allow the determination of the second band model parameter in a hot path from a hot-through-cold radiance measurement. Such a technique would be very useful in eliminating uncertainties in these parameter values. It is much easier to produce experimentally a long, cool path having a short hot segment at one end than a long, hot isothermal path.

5.3 CONCLUSIONS CONCERNING CALCULATIONAL TECHNIQUES

Several different techniques for calculating the radiance of a plume through a cool atmosphere have been discussed. First, the band model of Section 2 has been developed and a method described for its use. Second, the naive assumption that the plume radiance, calculated without accounting for the atmosphere, can be corrected for atmospheric attenuation by multiplication by the atmospheric transmittance has been discussed. Third, comparisons have been made using the Lindquist-Simmons approximation and two other methods. The band model developed in Section 2 represents the line arrangement within the plume and atmosphere more accurately than the other two; and, because a simple approximation to the average equivalent width derivative was found, it is simple to use. However, the degree to which this band model agrees with the measurements is obscured by the disagreement between calculations based on the available band model parameters and the measured radiance values. Furthermore, the difficulty of evaluating the expression for the average equivalent width derivative — Equation (34), made it necessary to use an approximation without adequate evaluation of the regions of validity of the approximation or of the error involved in it.

5.4 RECOMMENDATIONS

Based on the foregoing conclusions, a number of recommendations for necessary additional work can be made.

- (1) The function described in Equation (34) must be carefully evaluated and appropriate approximations determined, including regions of validity and errors involved. The departure from inverse square-root limit for high temperature targets should also be examined.

16. C.B. Ludwig, "Measurements of the Curves-of-Growth of Hot Water Vapor," Applied Optics, Vol. 10, p. 1057f (1971).

- (2) Similar band models for other distributions of line strengths (exponential, exponentially tailed inverse, and uniform) should be evaluated in order to examine the effect of curve of growth on the band model.
- (3) The effect of path segment size on the error involved in making plume radiance calculations should be carefully investigated for this new model.
- (4) From the GD and the AFCRL tabulations, a new set of band-model parameters should be developed which will provide the low temperature accuracy of the AFCRL tabulation and the high temperature accuracy of the GD tabulation.
- (5) Work should begin on a program to determine a new set of band model parameters for the $2.7 \mu\text{m}$ CO_2 band and the long-wavelength wing (the "red spike") of the $4.3 \mu\text{m}$ CO_2 band. This program should receive high priority since none of the available parameters predict the $2.7 \mu\text{m}$ CO_2 radiances accurately enough for useful model comparisons. The same statement is true to a lesser extent in the red spike region. The apparatus used for the current measurements would be ideal for such a program.
- (6) The calculation method developed in Section 2 should be extended to include Doppler broadening, and, following that, mixed Lorentz and Doppler broadening. This will extend the usefulness of these calculation techniques to higher altitude cases. Correlation effects are likely to become more important as the pressure is reduced so that the availability of calculational techniques which adequately treat line correlation effects becomes particularly important as altitude is increased.
- (7) Only minimal line correlation effects were observed in the $4.3 \mu\text{m}$ CO_2 "red spike" region at the conditions under which measurements were made (1200°K , 15 km simulated altitude). Correlation effects are expected to become more important as temperature is reduced. (Many plumes of interest are at lower temperature.) Thus, hot-through-cold measurements should be made at lower temperatures than 1200°K to investigate the correlation effects expected. These measurements can be performed with existing facilities by using a different grating with dispersion optimized for the $4.3 \mu\text{m}$ region and by degrading the spectral resolution to an appropriate value of 10 cm^{-1} . (The present program utilized a 4 cm^{-1} resolution.)
- (8) The degree to which the lines of different gases are truly uncorrelated remains to be explored. Some measurements of these effects between H_2O and CO_2 should be made in the $2.7 \mu\text{m}$ region, if for no other reason than to check for non-correlation. Further, for gases having widely spaced lines, such as HF, the assumption that lines of different gases are uncorrelated could prove to be invalid for certain narrow spectral intervals. If such gases are important plume species, measurements or calculations to assess these effects should be undertaken.

Appendix A

EVALUATION OF EQUATION (34)

In order to be able to use the results of the band model development of Section 2, it is necessary to evaluate the expression of Equation (34), namely

$$\begin{aligned} \frac{d\bar{W}}{da} \frac{1}{S(a)} &= g\left(u, \frac{\gamma}{\gamma}, q/\bar{q}\right) \\ &= \frac{1}{\pi} \frac{\gamma}{\gamma} \frac{q}{\bar{q}} \Gamma(q/\bar{q}) \int_{-\infty}^{\infty} \frac{\gamma^* \left(\frac{q/\bar{q}}{1+v^2}, \frac{du}{1+v^2} \right)}{\left(\frac{q/\bar{q}}{1+v^2} \right)^2 + v^2} dv \end{aligned}$$

Values of g are needed for the following ranges of variables:

$$0.001 < 1000.$$

$$0.2 \times 10^{-7} < \gamma/\bar{\gamma} < 200.$$

$$0.16 < q/\bar{q} < 1.0.$$

Several approaches were used in obtaining the approximations for g given in Table 1.

Evaluation by Series

Initial efforts to evaluate this function centered around a series approximation* to the normalized gamma function, γ^* . From Reference 11,

$$\gamma^*(a, x) = \frac{1}{\Gamma(a)} \sum_{n=0}^{\infty} \frac{(-x)^n}{(a+n)n!} \quad (53)$$

so that

$$g(u, \gamma/\bar{\gamma}, q/\bar{q}) = \frac{1}{\pi} \frac{\gamma}{\gamma} \frac{q}{\bar{q}} \sum_{n=0}^{\infty} \frac{(-2u)^n}{(q/\bar{q} + n)n!} \int_{-\infty}^{\infty} \frac{dv}{\left[\left(\frac{q/\bar{q}}{1+v^2} \right)^2 + v^2 \right] \left[1 + v^2 \right]^n} \quad (54)$$

The integral can now be performed using the formula 3.259.3 of Gradshteyn and Ryzhik^[17] to yield the following two equivalent expressions.

*We wish to acknowledge the contributions of B.D. Spieth of AFRPL to this portion of the evaluation.

17. I.S. Gradshteyn and I.W. Ryzhik, Table of Integrals, Series and Products, Academic Press, New York, New York, 1965.

$$\int_{-\infty}^{\infty} \frac{dv}{[(\gamma/\bar{\gamma})^2 + v^2](1 + v^2)^n} = \frac{1}{(\gamma/\bar{\gamma})^2} B\left(\frac{1}{2}, n + \frac{1}{2}\right) {}_2F_1\left[1, \frac{1}{2}; n + 1; 1 - \frac{1}{(\gamma/\bar{\gamma})^2}\right] \quad (55)$$

$$= \frac{1}{\gamma/\bar{\gamma}} B\left(\frac{1}{2}, n + \frac{1}{2}\right) {}_2F_1\left[n, \frac{1}{2}; n + 1; 1 - (\gamma/\bar{\gamma})^2\right] \quad (56)$$

where B is the beta function^[11]

$$B(a, b) = \frac{\Gamma(a)\Gamma(b)}{\Gamma(a+b)}$$

and ${}_2F_1$ is the hypergeometric function^[11,17]

$${}_2F_1(a, b; c; x) = \frac{T(c)}{T(b)T(a)} \sum_{m=0}^{\infty} \frac{T(a+m)T(b+m)}{T(c+m)} \frac{x^m}{m!}$$

The two expressions (55) and (56) are advantageous for different situations. Since the hypergeometric series in Equation (55) is a power series in $[1 - 1/(\gamma/\bar{\gamma})^2]$ it will converge more rapidly than (56) when $\gamma/\bar{\gamma} > 1$. Conversely, Equation (56) will converge more rapidly than (55) when $\gamma/\bar{\gamma} < 1$. Using this rationale, after writing out and simplifying the appropriate series for each $\gamma/\bar{\gamma}$ regime, we get the following.* For $\gamma/\bar{\gamma} < 1$:

$$g(u, \gamma/\bar{\gamma}, q/\bar{q}) = q/\bar{q} \sum_{n=0}^{\infty} \frac{(-1)^n 2^n u^n}{n!} \left(\frac{1}{q/\bar{q} + n} \right) \frac{(2n-1)!!}{(2n)!!} \cdot n \left\{ \sum_{m=0}^{\infty} \frac{(2m-1)!!}{2^m (m+n)m!} [1 - (\gamma/\bar{\gamma})^2] \right\}^m \quad (57)$$

For $\gamma/\bar{\gamma} > 1$:

$$q(u, \gamma/\bar{\gamma}, q/\bar{q}) = \frac{q/\bar{q}}{\gamma/\bar{\gamma}} \sum_{n=0}^{\infty} \frac{(-1)^n 2^n u^n}{q/\bar{q} + n} \frac{(2n-1)!!}{2n!!} \cdot \left\{ \sum_{m=0}^{\infty} \frac{(2m-1)!!}{2^m (m+n)!} \left[1 - \frac{1}{(\gamma/\bar{\gamma})^2} \right]^m \right\} \quad (58)$$

For an isothermal path ($q/\bar{q} = \gamma/\bar{\gamma} = 1$), the integral reduces to the following:

*The notation of Gradshteyn and Ryzhik^[17] has been used, i.e.,

$(2n-1)!! = 1 \cdot 3 \cdot 5 \cdot 7 \dots 2n-1$

and

$$(2n)!! = 2 \cdot 4 \cdot 6 \cdot 8 \dots 2n = 2^n \cdot n!$$

$$g(u, 1, 1) = \sum_{n=0}^{\infty} \frac{(-1)^n 2^n u^n}{(n+1)!} \frac{(2n-1)!!}{(2n)!!} \quad (59)$$

This series should be identical to the derivative of the curve-of-growth of Equation (39) since the band model is identical to that leading to Equation (39) for an isothermal path. This is shown to be true in the following way.

$$\begin{aligned} g(u, 1, 1) &= \frac{1}{\bar{S}(a)} \frac{d\bar{W}}{da} \\ &= \frac{\delta}{\bar{S}(a)} \frac{d(\bar{W}/\delta)}{du} \frac{du}{da} \end{aligned}$$

From Equation (39),

$$\frac{\bar{W}}{\delta} = 2\pi y \left[e^{-u} I_0(u) + 2u e^{-u} [I_0(u) + I_1(u)] - 1 \right]$$

and, from Equation (29), $du/da = \bar{S}/2\pi y \delta$ so that

$$\begin{aligned} g(u, 1, 1) &= \frac{d}{du} \left\{ e^{-u} I_0(u) + 2u e^{-u} [I_0(u) + I_1(u)] - 1 \right\} \\ &= e^{-u} [I_0(u) + I_1(u)] \end{aligned} \quad (60)$$

Although we did not show the equivalence of Equations (59) and (60) analytically, we did determine that they were numerically identical for $u < 1$.

It was at this point that difficulties were encountered. As $u \rightarrow 0$, $g \rightarrow 1$ regardless of the value of $\gamma/\bar{\gamma}$ or q/\bar{q} . The value of g begins to depart substantially from unity for u greater than 1, so that large values of u are of primary interest. The alternating series representations developed above satisfy the convergence tests for all u . The inner series in $(\gamma/\bar{\gamma})^2$ converges easily since the term in $(\gamma/\bar{\gamma})^2$ never exceeds unity. But the outer series involves powers of u , and although the terms of this series eventually approach zero, they increase in magnitude (although they alternate in sign) for the first few terms. For $u = 10$, these terms become so large ($\sim 10^{20}$) before they decrease that there is no hope of evaluating the series on the available computer system without severe round-off error. Furthermore, we are most interested in the asymptotic behavior of g for large u . Thus, a series representation of the type developed above is not very useful for present purposes.

We then sought a series representation for g valid for large u . However, since the argument of the normalized gamma function in Equation (34) takes on all values between 0 and u during the integration, a series representation for γ^* valid only for large arguments will not suffice. More analytical effort is required here.

Numerical Evaluation

In order to obtain a limited set of values for the function of Equation (34), the function was evaluated numerically after first making the following transformation:

$$v = \tan \phi/2 \quad (61)$$

Then

$$g(u, \gamma/\bar{\gamma}, q/\bar{q}) = \frac{2}{\pi} \gamma/\bar{\gamma} q/\bar{q} \Gamma(q/\bar{q}) \int_0^{\pi} \frac{\gamma^* [q/\bar{q}, u(1 + \cos \phi)] d\phi}{\cos \phi [(\gamma/\bar{\gamma})^2 - 1] + (\gamma/\bar{\gamma})^2 + 1} \quad (62)$$

This function was evaluated graphically after plotting the integrand. Values of γ^* were computed from expressions 6.5.29 and 6.5.32 in Reference 11. Values were computed for $q/\bar{q} = 1/4$ (corresponding to the value encountered in the measurements) and for $\gamma/\bar{\gamma} = 1.8$ and 2.0 . These corresponded to the values needed at 3550 cm^{-1} in order to compare with the measurements. Values were computed for $u = 1, 10, 100, \text{ and } 1000$. The product of $q/\bar{q} \Gamma(q/\bar{q})$ and the integrand of Equation (62) is plotted in Figure A-1 for the four u values, from which results the graphical integrations were performed. Figure A-2 shows the computed values. These evaluations provided some idea of the behavior of the function.

Asymptotic Values

In order to investigate the behavior of the function it is necessary to know its behavior at various limits. At $u = 0$, the function is easily shown to be unity. For the isothermal case, ($\gamma/\bar{\gamma} = q/\bar{q} = 1$), the asymptotic values can be found from Equation (60).

$$\lim_{u \rightarrow \infty} [g(u, 1, 1)] = \sqrt{\frac{2}{\pi u}} \quad (63)$$

For the Lindquist-Simmons approximation, the limit is shown to be (see Reference 9)

$$\lim_{u \rightarrow \infty} g_{LS}(u, \gamma/\bar{\gamma}) = \frac{\gamma}{\bar{\gamma}} \sqrt{\frac{2}{\pi u}} \quad (64)$$

Thus inverse square root behavior for large u might be expected as all of the lines approach the square root region.

A similar asymptotic limit for Equation (34) was obtained by operating on Equation (15) in Section 2 (i.e., before the reduction in terms of the incomplete gamma function). A term of unity was neglected in comparison to v^2 in both the denominator of the integrand and the denominator of the exponential. Then the expression $(\gamma/\bar{\gamma})^2 - 1/v^2$ was assumed to be small for all v so that

$$1 - \frac{(\gamma/\bar{\gamma})^2 - 1}{v^2} \approx \exp \left[-\frac{(\gamma/\bar{\gamma})^2 - 1}{v^2} \right]$$

We obtained the result:

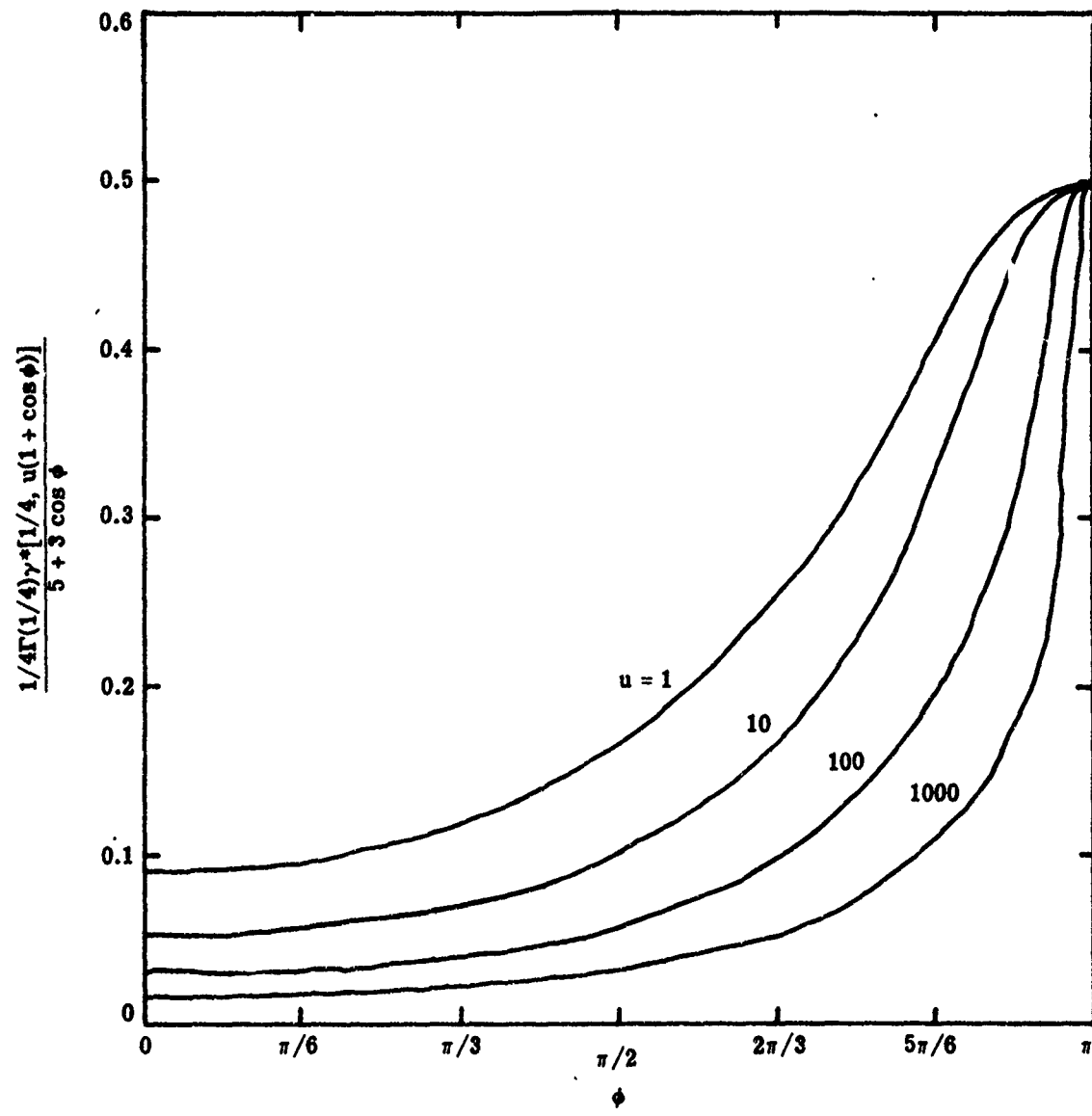


FIGURE A1. INTEGRAND OF EQUATION $34 \times q/\bar{q} \Gamma(q/\bar{q})$ FOR $q/\bar{q} = 1/4$, $\gamma/\bar{\gamma} = 2$, FOR VARIOUS VALUES OF u

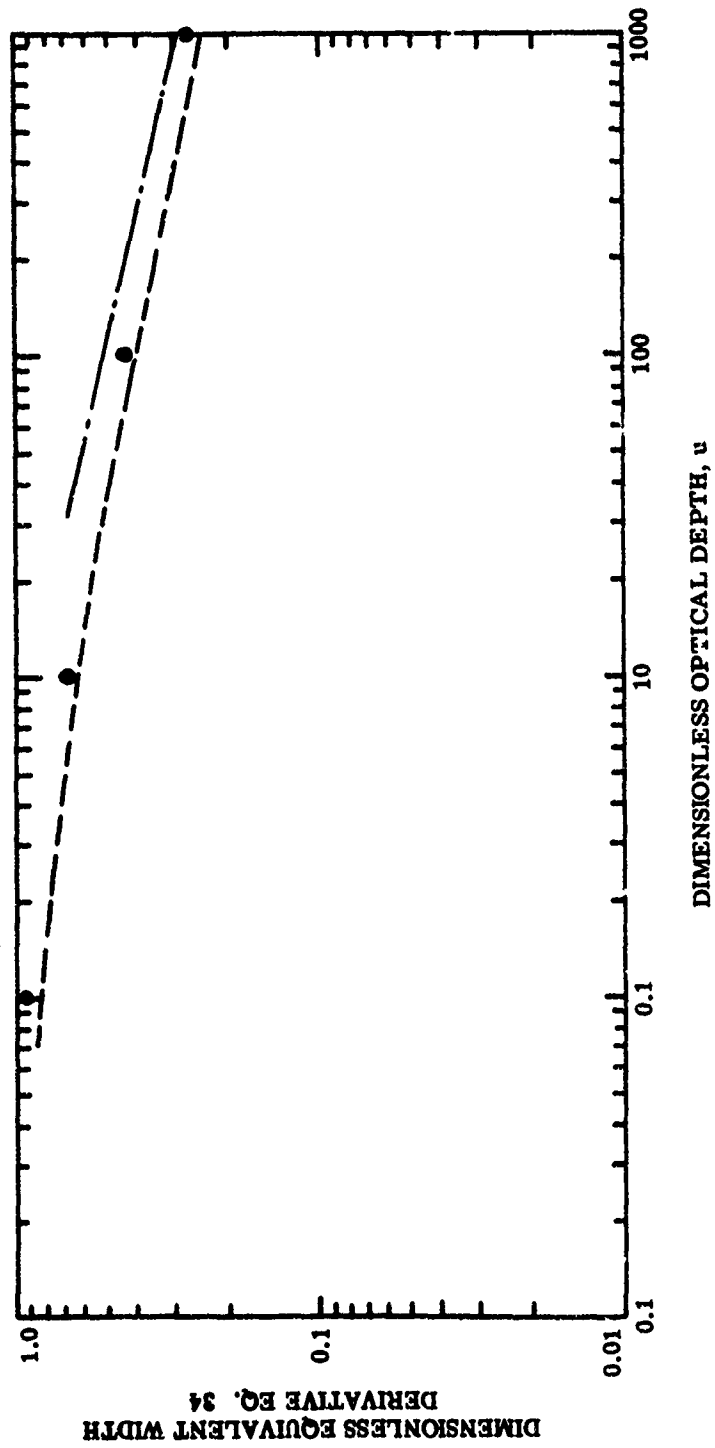


FIGURE A2. DIMENSIONLESS EQUIVALENT WIDTH DERIVATIVE COMPUTED BY VARIOUS MEANS. $q/\bar{q} = 1/4$, $\gamma/\bar{\gamma} = 2$.

- Computed Numerically
- — Approximation of Table 1
- · · · Limit for Large u of Equation 70

$$\lim_{u \rightarrow \infty} g(u, \gamma/\bar{\gamma}, q/\bar{q}) = \frac{1}{\sqrt{\pi}} \frac{\gamma}{\bar{\gamma}} \frac{q}{\bar{q}} \frac{\int_0^{2u} \frac{u^{q/\bar{q}-1} du}{[u' + (\gamma/\bar{\gamma})^2 - 1]}^{1/2}}{(2u)^{q/\bar{q}}} \quad (65)$$

This could be evaluated only for integer q/\bar{q} to yield

$$\lim_{u \rightarrow \infty} g(u, \gamma/\bar{\gamma}, q/\bar{q}) = \frac{1}{\sqrt{\pi}} \frac{\gamma}{\bar{\gamma}} \frac{q}{\bar{q}} \frac{1}{\sqrt{2u(q/\bar{q} - 1/2)}} \quad (66)$$

for large u . This expression has a singularity at $q/\bar{q} = 1/2$. Although the expression was strictly valid for integer q/\bar{q} , it appears to be useful for non-integer values larger than 1 as well (although these values are not of significant interest). The integral of Equation (65) was evaluated for $q/\bar{q} = 1/2$ to yield

$$\lim_{u \rightarrow \infty} g(u, \gamma/\bar{\gamma}, 1/2) = \frac{1}{\sqrt{\pi}} \frac{\gamma}{\bar{\gamma}} (1/2) \frac{\log_e \left(\frac{8u}{\gamma/\bar{\gamma}^2 - 1} \right)}{(2u)^{1/2}} \quad (67)$$

In order to obtain corresponding relations for $q/\bar{q} < 1/2$, it became apparent during the numerical integration that for almost all of the range of important values, as well as for small q/\bar{q}

$$\gamma^* \left(q/\bar{q}, \frac{2u}{1 + v^2} \right) \approx \left(\frac{2u}{1 + v^2} \right)^{-q/\bar{q}}$$

We introduce this to obtain

$$g(u, \gamma/\bar{\gamma}, q/\bar{q}) \approx \frac{2}{\pi} \frac{\gamma}{\bar{\gamma}} \frac{q}{\bar{q}} \Gamma\left(\frac{q}{\bar{q}}\right) (2u)^{-q/\bar{q}} \int_0^{\infty} \frac{(1 + v^2)^{q/\bar{q}}}{\gamma/\bar{\gamma}^2 + v^2} dv \quad (68)$$

The product of the integrand of this function and $q/\bar{q} \Gamma(q/\bar{q})$ is plotted in Figure A-5 after transformation into the variable ϕ , along with the exact function for $u = 1000$, $q/\bar{q} = 1/4$, and $\gamma/\bar{\gamma} = 2$. It can be seen that the approximation agrees well with the exact representation of Equation (34) except near $\phi = \pi$ and should not contribute substantial error to the integral. This agreement is expected to remain true for small q/\bar{q} and large u . It can be seen from Equation (68) that, where the approximation holds, the transmittance derivative will follow a $u^{-q/\bar{q}}$ dependence. This somewhat surprising result indicates that square root growth is never fully achieved for some lines and may be the result of allowing the integration over strength S_0 (i.e., w) to extend completely to zero, whereas the inverse strength distribution cannot be normalized when this occurs. The integral in Equation (68) cannot be performed in closed form except for some special cases. For $\gamma/\bar{\gamma} = 1$, $q/\bar{q} < 1/2$,

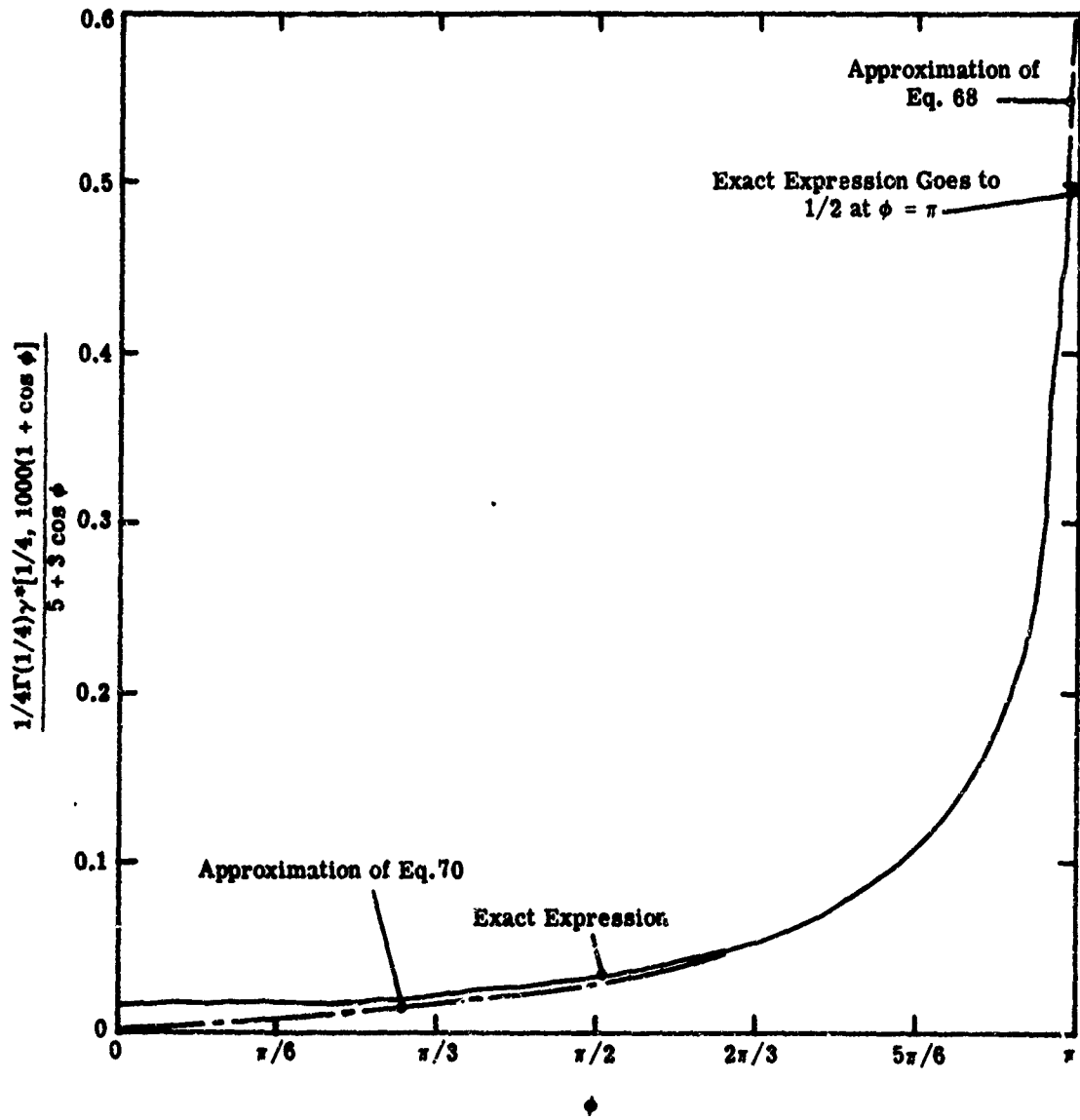


FIGURE A3. INTEGRAND OF EQUATION 34 $\times q/\bar{q} \Gamma(q/\bar{q})$ FOR $q/\bar{q} = 1/4$, $\gamma/\bar{\gamma} = 2$, FOR VARIOUS VALUES OF u .

$$\lim_{u \rightarrow \infty} g(u, 1, q/\bar{q}) \approx \frac{q}{\bar{q}} \Gamma(q/\bar{q})(2u)^{-q/\bar{q}} \cdot \frac{1}{\sqrt{\pi}} \frac{\Gamma(1/2 - q/\bar{q})}{\Gamma(1 - q/\bar{q})} \quad (69)$$

For $(\gamma/\bar{\gamma})^2$ large enough, unity in the numerator of Equation (68) can be ignored compared to v^2 to yield

$$\lim_{u \rightarrow \infty} g(u, \gamma/\bar{\gamma}, q/\bar{q}) = \frac{q}{\bar{q}} \Gamma\left(\frac{q}{\bar{q}}\right) (2u)^{-q/\bar{q}} \left(\frac{\gamma}{\bar{\gamma}}\right)^{2q/\bar{q}} \operatorname{cosec} \pi(q/\bar{q} + 1/2) \quad (70)$$

The integrand for this additional approximation is also shown in Figure A-3. The approximation becomes more valid as u becomes larger. The limit given by Equation (70) is plotted on Figure A-1 along with the computed values.

The asymptotic limits were compared in order to obtain a simple generalized form which can be useful for representation of a large range of values of q/\bar{q} , which does not have a singularity at $q/\bar{q} = 1/2$. Figure A-4 shows the asymptotic limits of those terms of Equations (66), (69), and (70) governing their behavior with q/\bar{q} . Thus, for Equation (66) we have plotted

$$\frac{1}{\sqrt{\pi}} \frac{q}{\bar{q}} \left(\frac{1}{q/\bar{q} - 1/2} \right)$$

For Equation (69) we have plotted

$$\frac{q}{\bar{q}} \Gamma\left(\frac{q}{\bar{q}}\right) \frac{1}{\sqrt{\pi}} \frac{\Gamma(1/2 - q/\bar{q})}{\Gamma(1/2 - q/\bar{q})}$$

For Equation (70) we have plotted

$$\frac{q}{\bar{q}} \Gamma\left(\frac{q}{\bar{q}}\right) \operatorname{cosec} \pi(q/\bar{q} + 1/2)$$

The approach to the singularity at $q/\bar{q} = 1/2$ is apparent. By examination of this figure, we have chosen unity as being representative of these functions for $q/\bar{q} < 1/2$ without the singularities, and $\sqrt{2/\pi(q/\bar{q})}$ as being representative for $1/2 < q/\bar{q} < 1$. (Values for $q/\bar{q} > 1$ are not required.) These limits are shown on Figure A-4.

As a result of the preceding paragraphs, a set of asymptotic limits which appear to be suitable for most situations that we expect to encounter has been synthesized. To summarize:

$$\begin{aligned} \lim_{u \rightarrow \infty} g(u, \gamma/\bar{\gamma}, q/\bar{q}) &\approx (\gamma/\bar{\gamma})^{2q/\bar{q}} u^{-q/\bar{q}} & \text{for } \frac{q}{\bar{q}} < 1/2 \\ &= (\gamma/\bar{\gamma}) \sqrt{\frac{2}{\pi q/\bar{q}}} u^{-1/2} & \text{for } \frac{q}{\bar{q}} > 1/2 \end{aligned} \quad (71)$$

Approximate Functional Form for Equation (34)

Curves of growth of the type given in Equations (39) and (49) have been represented in the form (see Reference 12)

$$\frac{W}{\delta} = \frac{2\pi y u}{(1 + (au)^b)^c} \quad (72)$$

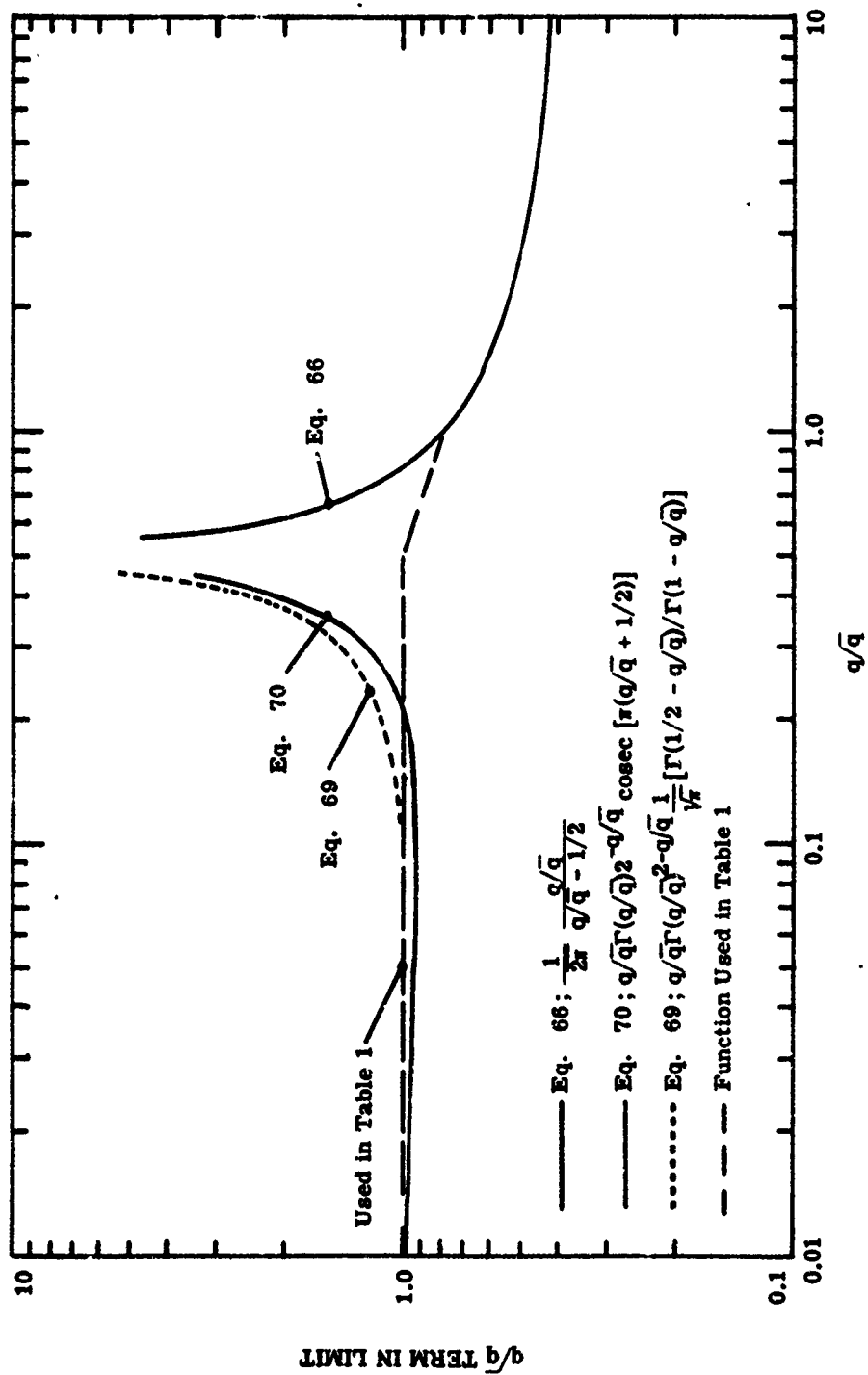


FIGURE A4. q/\sqrt{q} CONTRIBUTION TO THE LIMITS OF EQUATION 34 FOR LARGE u

Since Equation (34) for an isothermal case can easily be shown to follow such a law, we attempted to fit such a function to the points computed for $q/\bar{q} = 1/4$, $\gamma/\bar{\gamma} = 2$ and the asymptotes given in Equation (71). The result, also shown in Figure A-1, agreed quite well with the computed data points. On this basis, and in view of the necessity of approximating Equation (34) without the time or funds to perform a more detailed examination of its properties, this form of expression was used to represent the function for all $q/\bar{q} < 1$ and all $\gamma/\bar{\gamma}$, using the asymptotic limits given in Equation (71). This procedure leads directly to the specifications of Equation (72) given in Table 1 of Section 2.

Discussion

We have evaluated Equation (34) exactly for only a few values of u , q/\bar{q} , and $\gamma/\bar{\gamma}$. Asymptotic limits for large u were examined for most combinations of q/\bar{q} and $\gamma/\bar{\gamma}$. Because of time and budget limitations, the bounds within which these asymptotic forms were valid were not determined carefully. Therefore, the rather simple approximation used may not represent the function well in certain domains. The crossovers of these functional forms (see Figure 4, Section 2) are indications of this. More detailed investigations of the behavior of this function, including bounds for the validity of the approximations as well as approximations for values of u near zero, still need to be investigated. Since the band model of Section 2 is a substantial improvement over previous band models, such additional effort would be worthwhile.

Appendix B COLLECTION OF MEASURED DATA

In order that the data acquired in this program be available to others wishing to test calculation techniques, this appendix includes all of the hot cell radiances, the cold cell transmittances, and the corresponding cell radiances as measured through the cold cell. Curves are also included showing the product of the hot cell radiance and the cold cell transmittance. The difference between this latter function and the measured hot-through-cold radiance shows the degree to which line correlation effects are important.

The organization of the data set for each test is as follows. First a table is shown which gives the detailed physical parameters corresponding to that test. Second, a figure is presented showing two curves, the upper being the measured unattenuated hot cell radiance and the lower the measured hot cell radiance as attenuated by the cold cell. Third, a figure showing the corresponding measured cold cell transmittance is given. Fourth, we present a figure showing the hot cell radiance as measured through the cold cell again (lower curve in every case) and the product of the unattenuated hot cell radiance and the cold cell transmittance (upper curve). The difference between the two curves on this figure demonstrates the degree of line correlation effects present in each case. Last, a plot is presented of the measured

apparent temperature as a function of wavenumber. The degree to which these values deviate from the hot cell temperature given in the table are a measure of the radiometric consistency of the data.

TABLE B-1. TEST-1 PARAMETERS

Spectral Region	2.7 μ m	
Hot Cell	Simulated Altitude: 16 km 3.0 atm-cm CO_2	
	Total Absolute Pressure	76.0 mm
	$P_{\text{H}_2\text{O}}$	0.0 mm
	P_{CO_2}	38.0 mm
	P_{N_2}	38.0 mm
	$L = 0.6$ m	$T = 1202^{\circ}\text{K}$
Cold Cell	Simulated 200-km Path @ 15-km Altitude	
	Total Absolute Pressure	98.0 mm
	$P_{\text{H}_2\text{O}}$	0.0 mm
	P_{CO_2}	88.63 mm
	P_{N_2}	9.37 mm
	$L = 100$ m	$T = 295^{\circ}\text{K}$

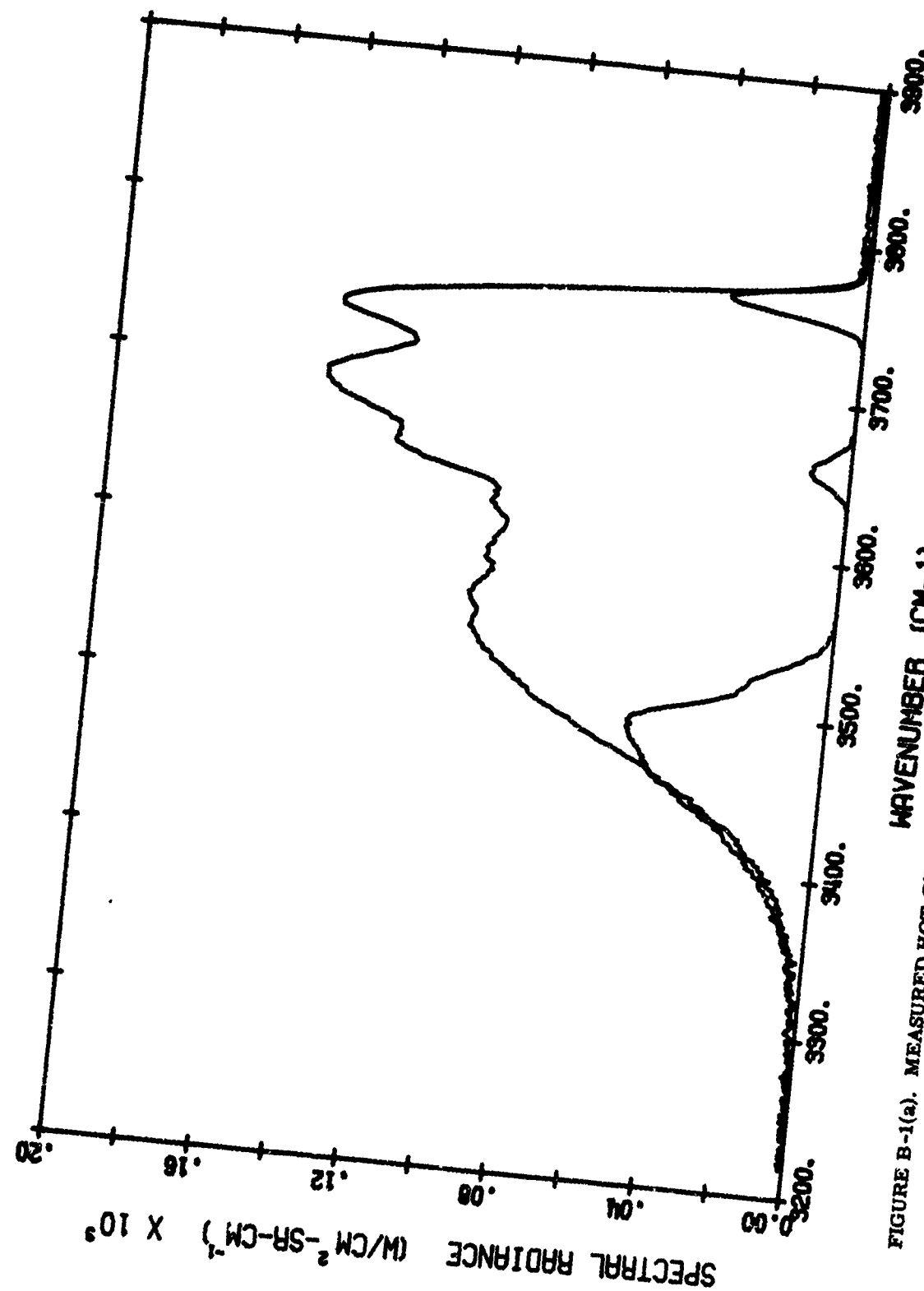
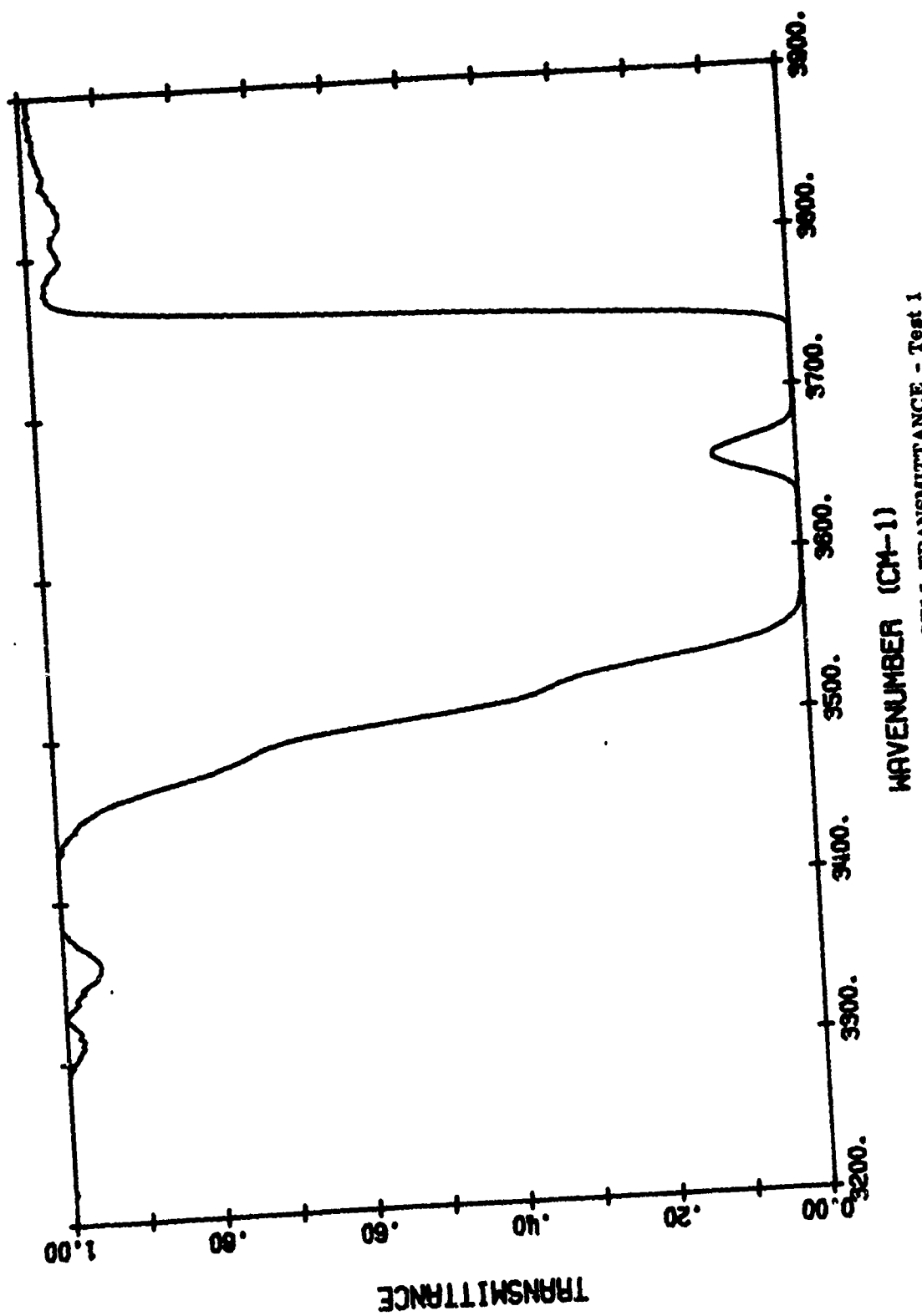


FIGURE B-1(a). MEASURED HOT CELL RADIANCE (UPPER) AND HOT THROUGH COLD RADIANCE (LOWER)
Test 1



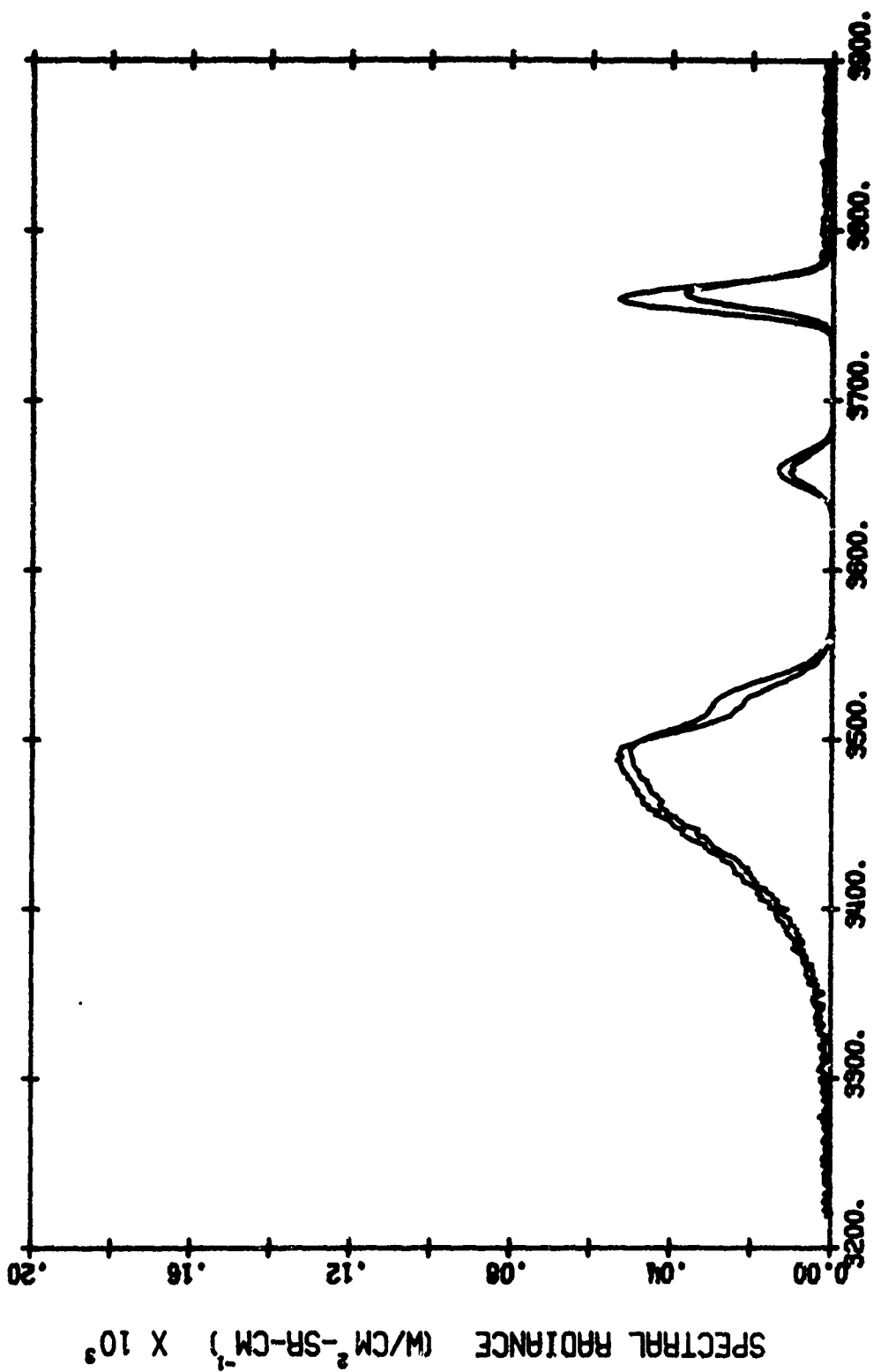


FIGURE B-1(c). MEASURED HOT THROUGH COLD RADIANCE (LOWER) AND PRODUCT OF HOT CELL RADIANCE AND COLD CELL TRANSMITTANCE (UPPER) - Test 1

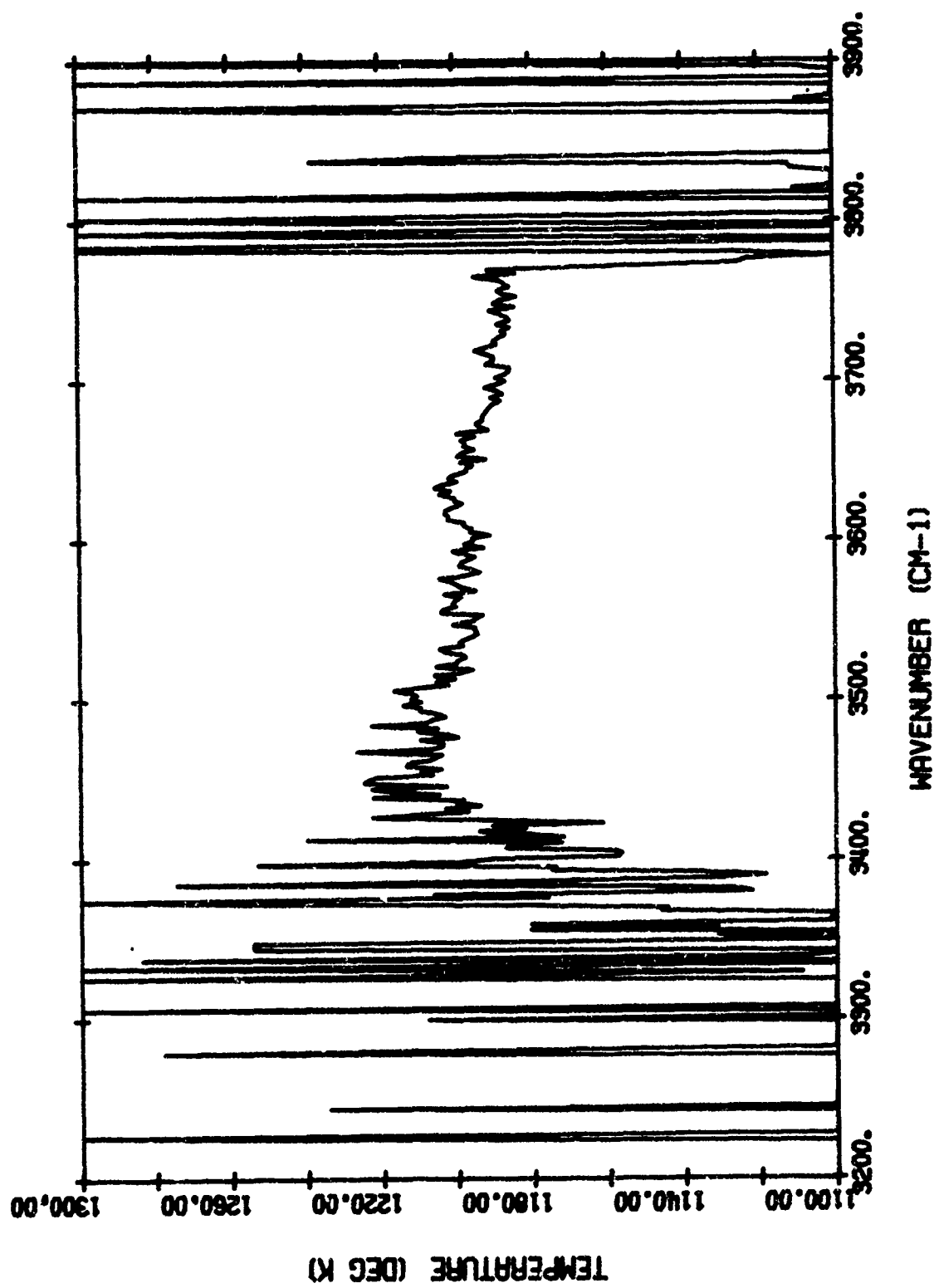


FIGURE B-1(d). MEASURED APPARENT TEMPERATURE - TEST 1

TABLE B-2. TEST-2 PARAMETERS

Spectral Region	2.7 μ m	
Hot Cell	Simulated Altitude: 16 km 3.0 atm-cm CO ₂	
	Total Absolute Pressure	76.0 mm
	P _{H₂O}	0.0 mm
	P _{CO₂}	38.0 mm
	P _{N₂}	38.0 mm
	L = 0.6 m	T = 1202°K
Cold Cell	Simulated 50-km Path @ 15-km Altitude	
	Total Absolute Pressure	98.0 mm
	P _{H₂O}	0.0 mm
	P _{CO₂}	22.15 mm
	P _{N₂}	75.86 mm
	L = 100 m	T = 297°K

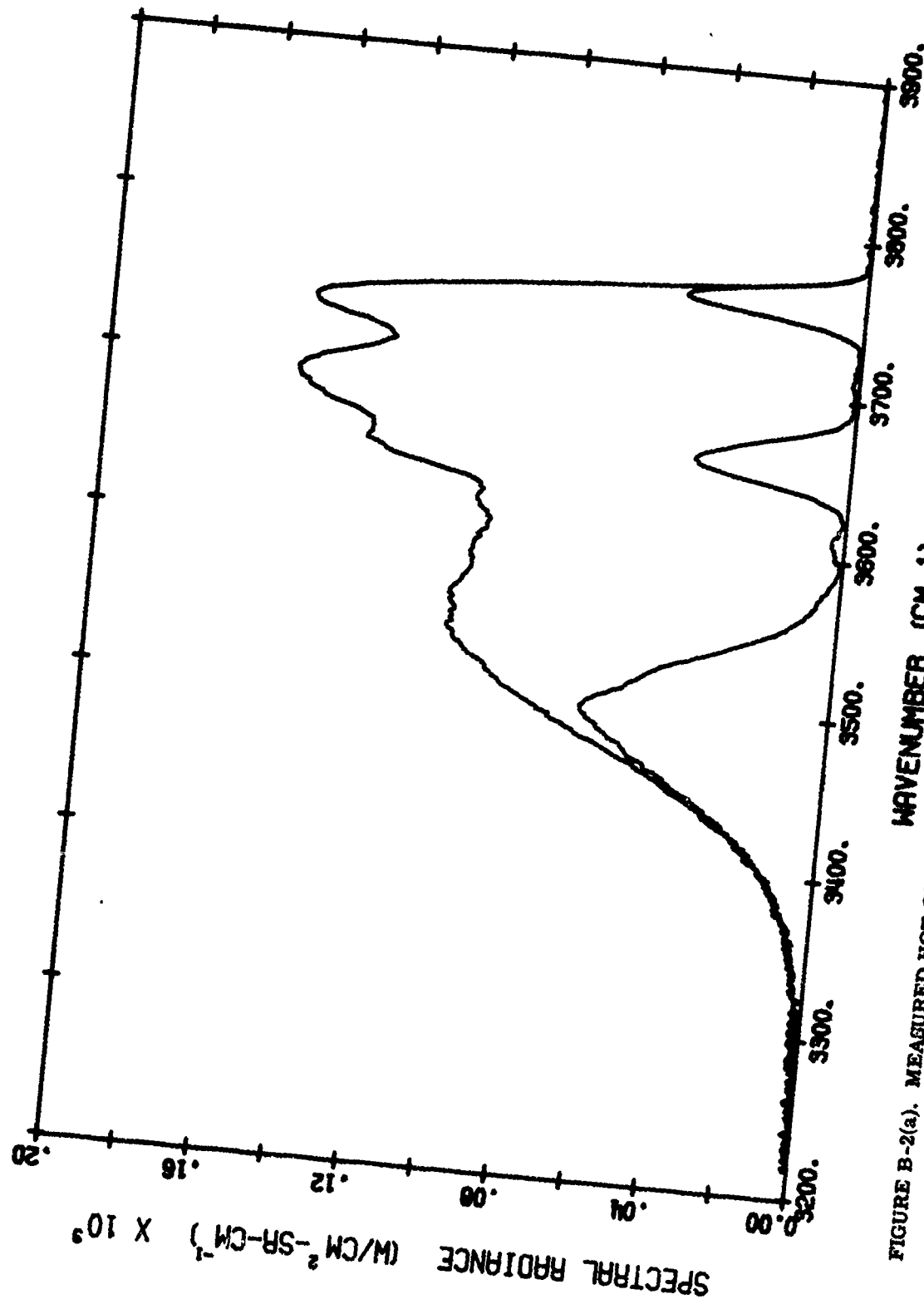


FIGURE B-2(a). MEASURED HOT CELL RADIANCE (UPPER) AND HOT-THROUGH-COLD RADIANCE (LOWER)
Test 2

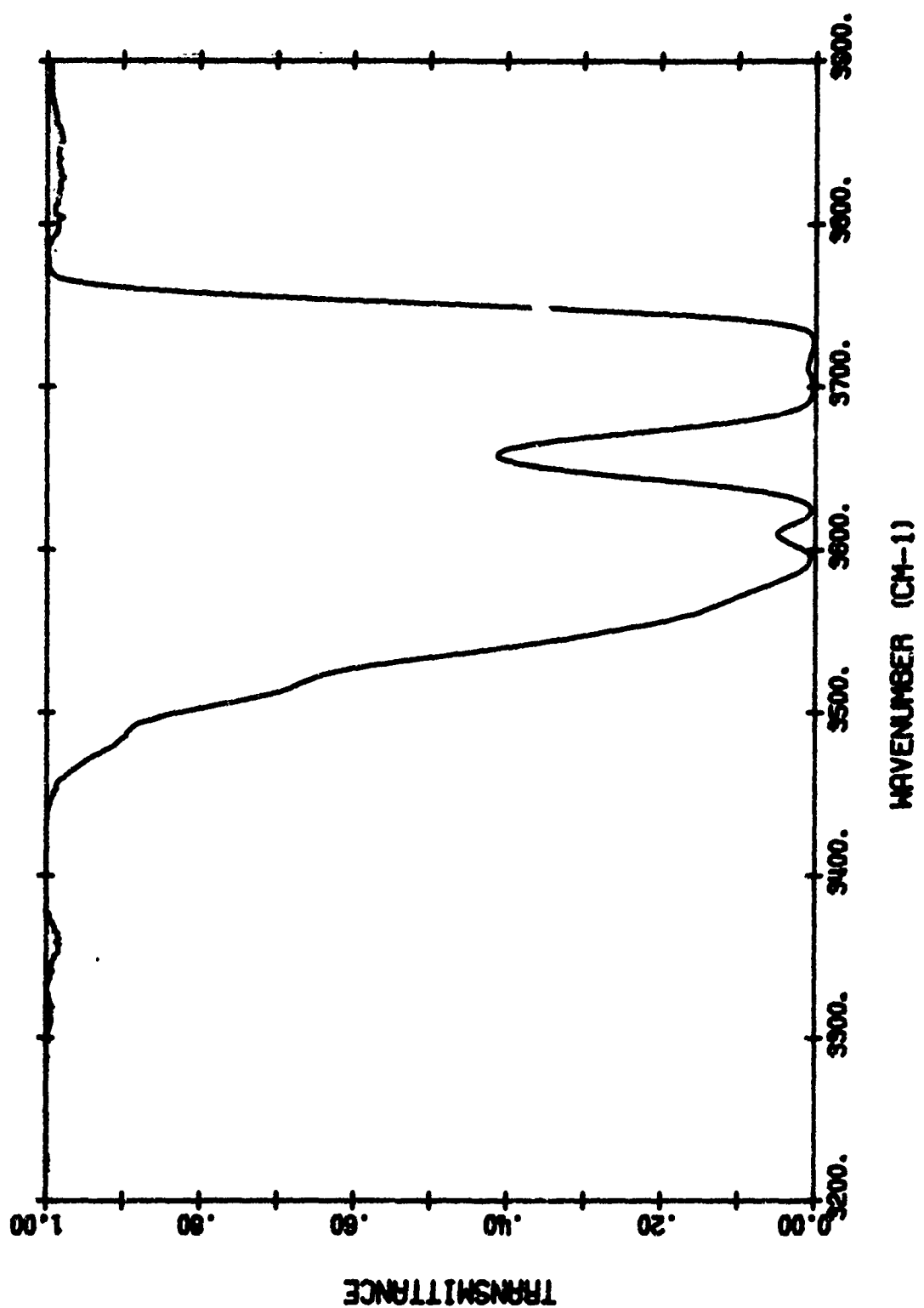


FIGURE B-2(b). MEASURED COLD CELL TRANSMITTANCE - Test 2

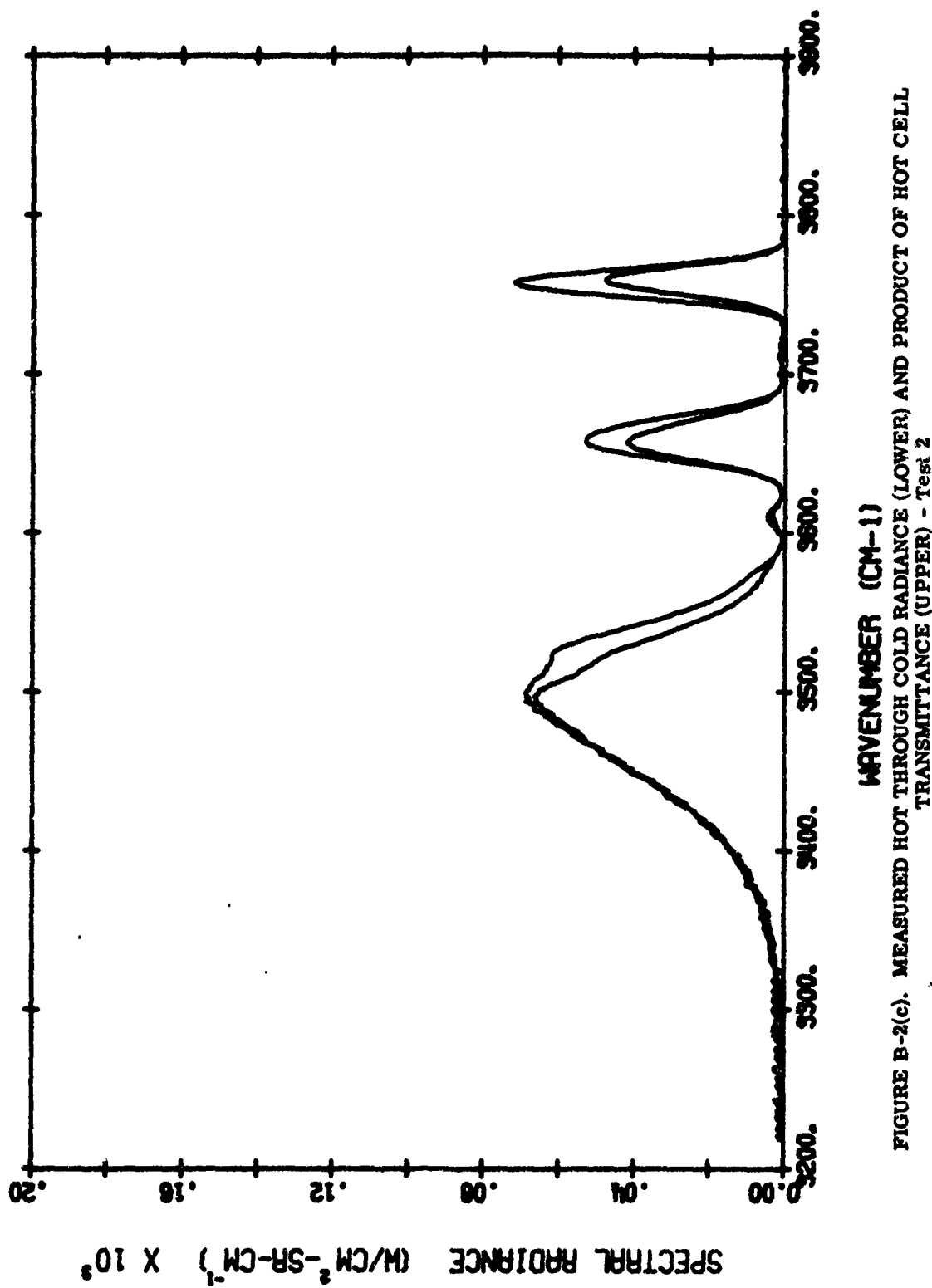


FIGURE B-2(c). MEASURED HOT THROUGH COLD RADIANCE (LOWER) AND PRODUCT OF HOT CELL TRANSMITTANCE (UPPER) - Test 2

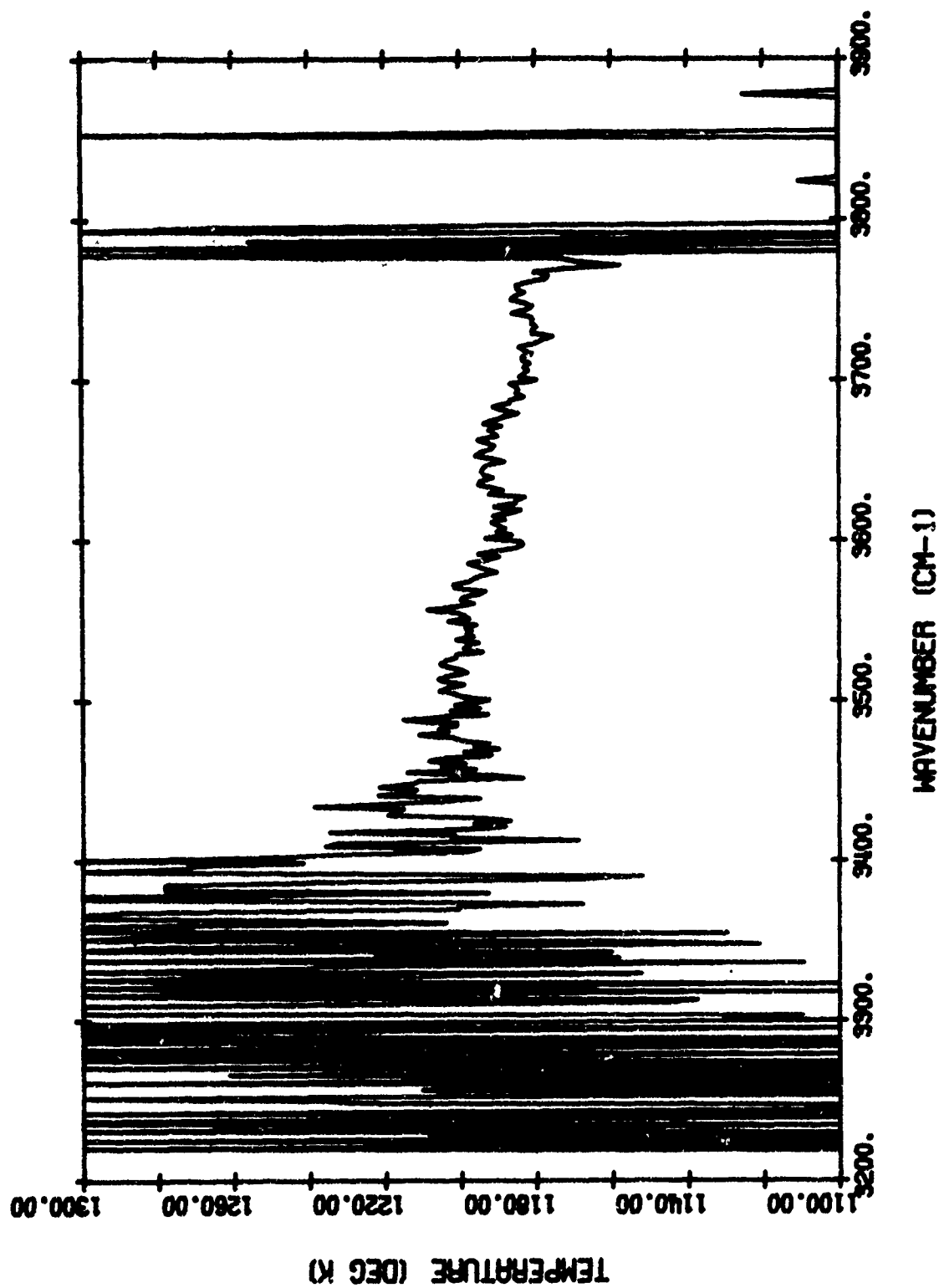


FIGURE B-2(d). MEASURED APPARENT TEMPERATURE - Test 2

TABLE B-3. TEST-3 PARAMETERS

Spectral Region	2.7 μ m	
Hot Cell	Simulated Altitude: 16 km 3.0 atm-cm CO_2	
	Total Absolute Pressure	76.0 mm
	$P_{\text{H}_2\text{O}}$	0.0 mm
	P_{CO_2}	38.0 mm
	P_{N_2}	38.0 mm
	$L = 0.6$ m	$T = 1200^{\circ}\text{K}$
Cold Cell	Simulated 10-km Path @ 15-km Altitude	
	Total Absolute Pressure	98.0 mm
	$P_{\text{H}_2\text{O}}$	0.0 mm
	P_{CO_2}	4.43 mm
	P_{N_2}	93.57 mm
	$L = 100$ m	$T = 297^{\circ}\text{K}$

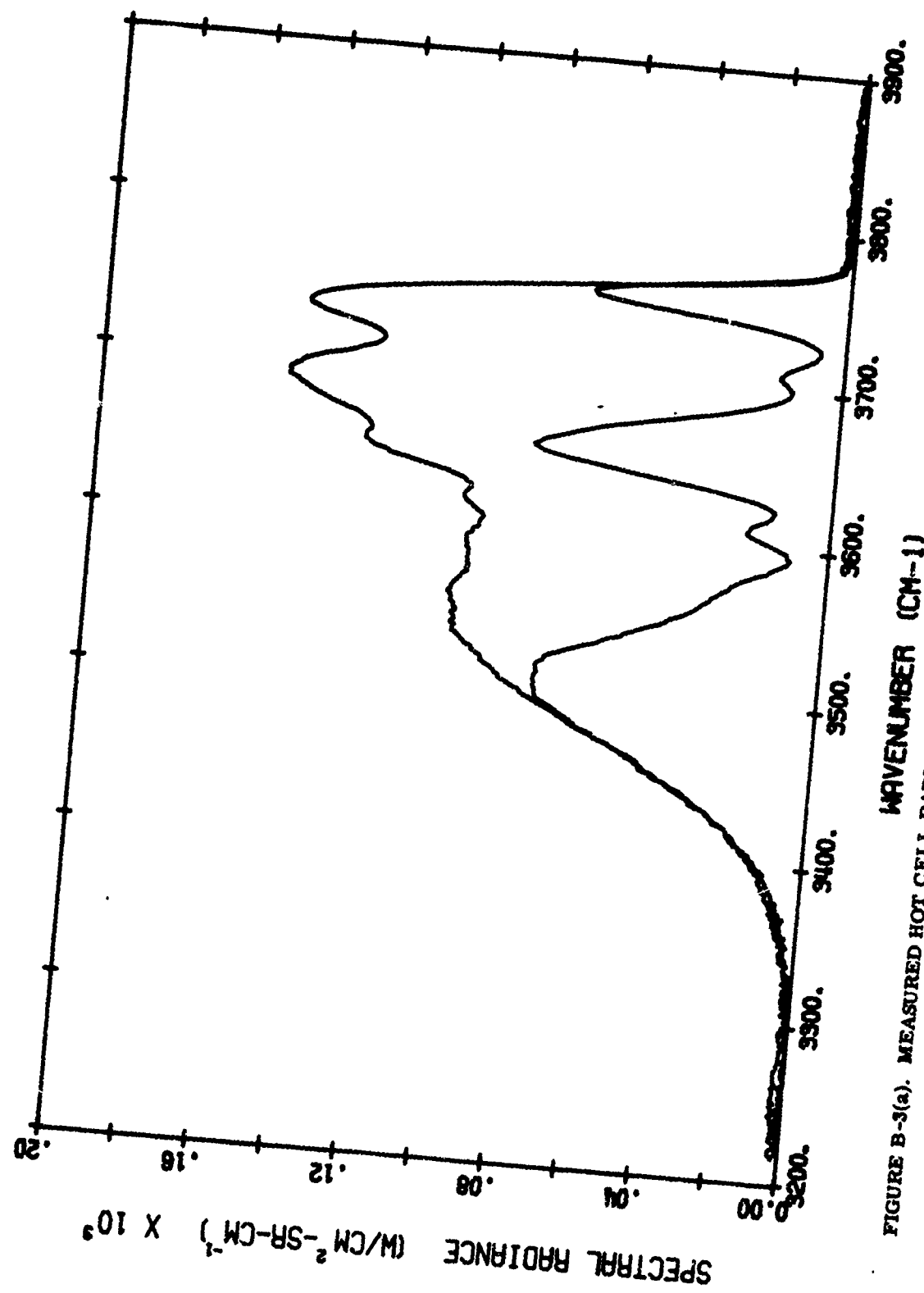


FIGURE B-3(a). MEASURED HOT CELL RADIANCE (UPPER) AND HOT-THROUGH COLD RADIANCE (LOWER)
Test 3

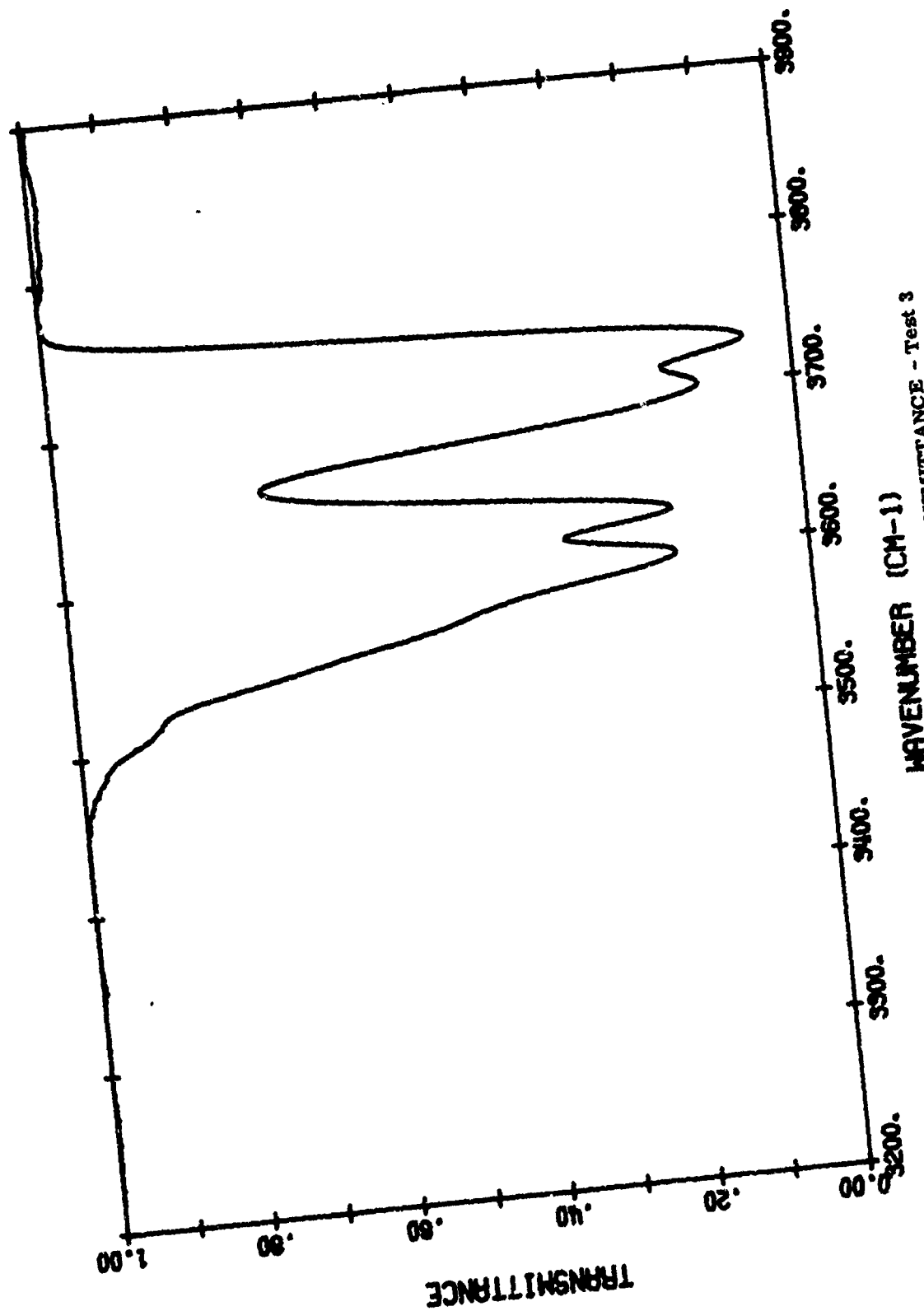


FIGURE B-3(b). MEASURED COLD CELL TRANSMITTANCE - Test 3

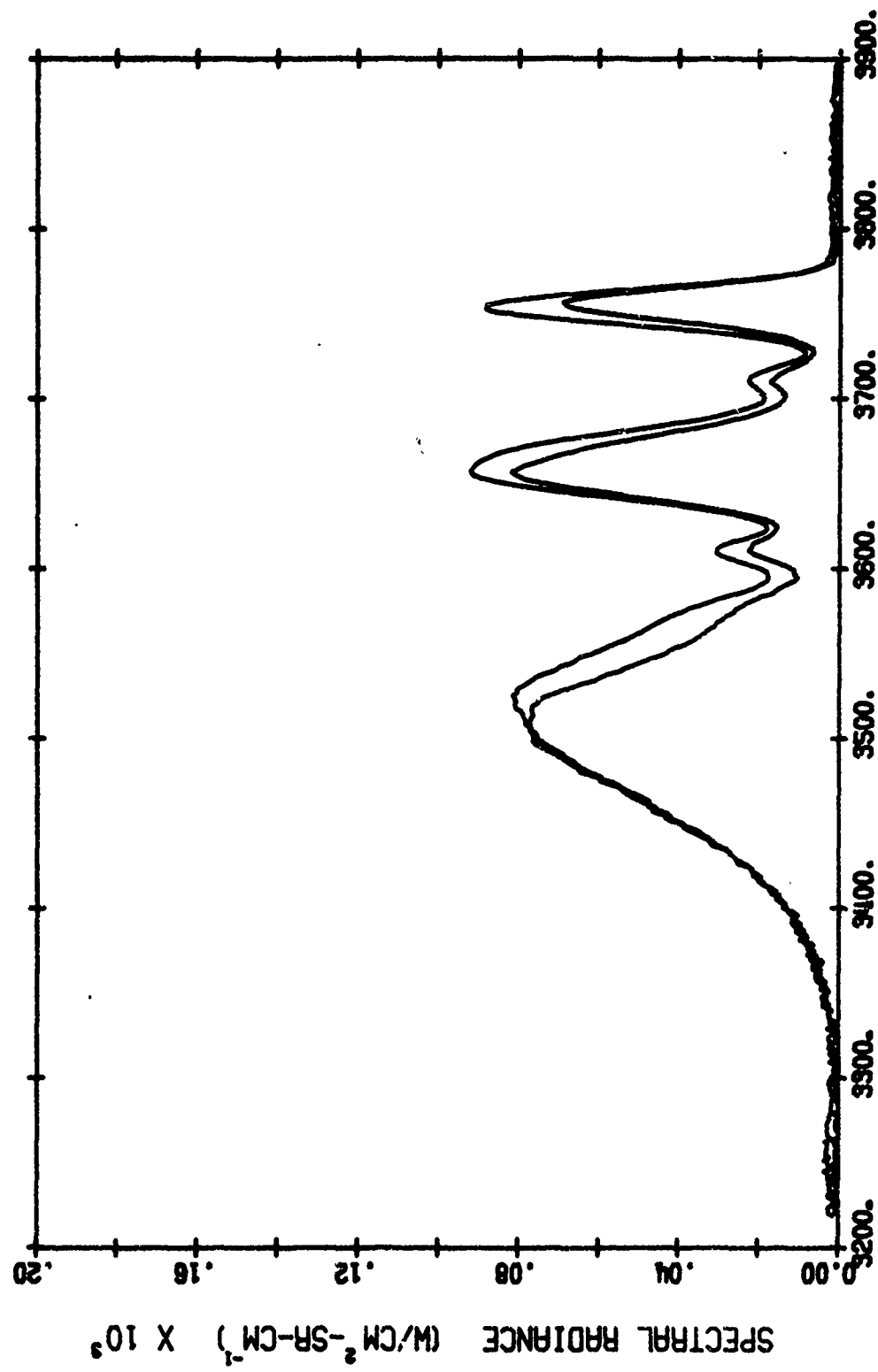


FIGURE B-3(c). MEASURED HOT THROUGH COLD RADIANCE (LOWER) AND PRODUCT OF HOT CELL RADIANCE AND COLD CELL TRANSMITTANCE (UPPER) - Test 3

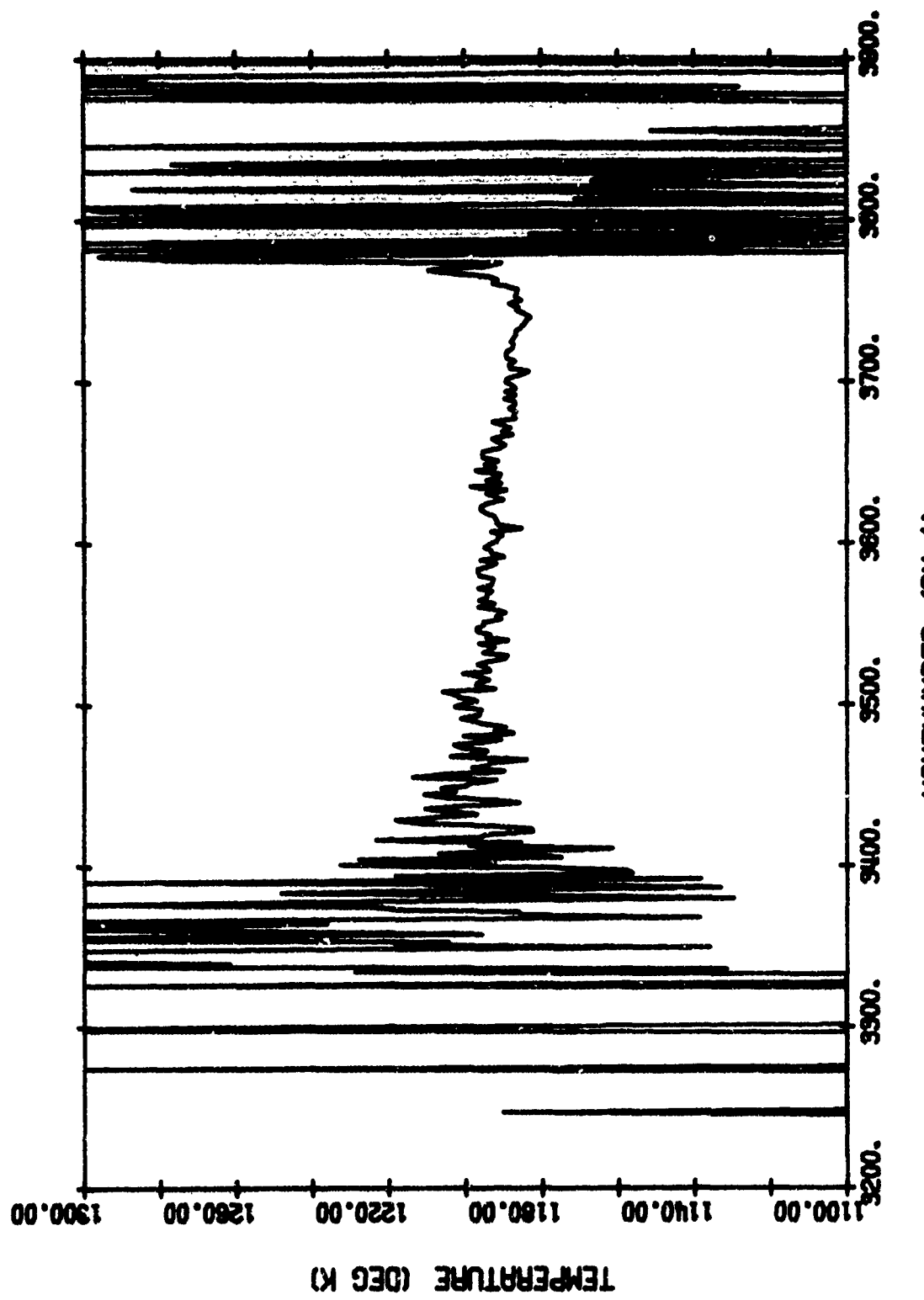


FIGURE B-3(d). MEASURED APPARENT TEMPERATURE - Test 3

TABLE B-4. TEST-5 PARAMETERS

Spectral Region	4.3 μ m	
Hot Cell	Simulated Altitude: 16 km. 0.598 atm-cm CO_2	
	Total Absolute Pressure	76.0 mm
	$P_{\text{H}_2\text{O}}$	0.0 mm
	P_{CO_2}	7.58 mm
	P_{N_2}	68.43 mm
	$L = 0.6$ m	$T = 1200^{\circ}\text{K}$
Cold Cell	Simulated 200-km Path @ 15-km Altitude	
	Total Absolute Pressure	98.0 mm
	$P_{\text{H}_2\text{O}}$	0.0 mm
	P_{CO_2}	88.63 mm
	P_{N_2}	9.37 mm
	$L = 100$ m	$T = 297^{\circ}\text{K}$

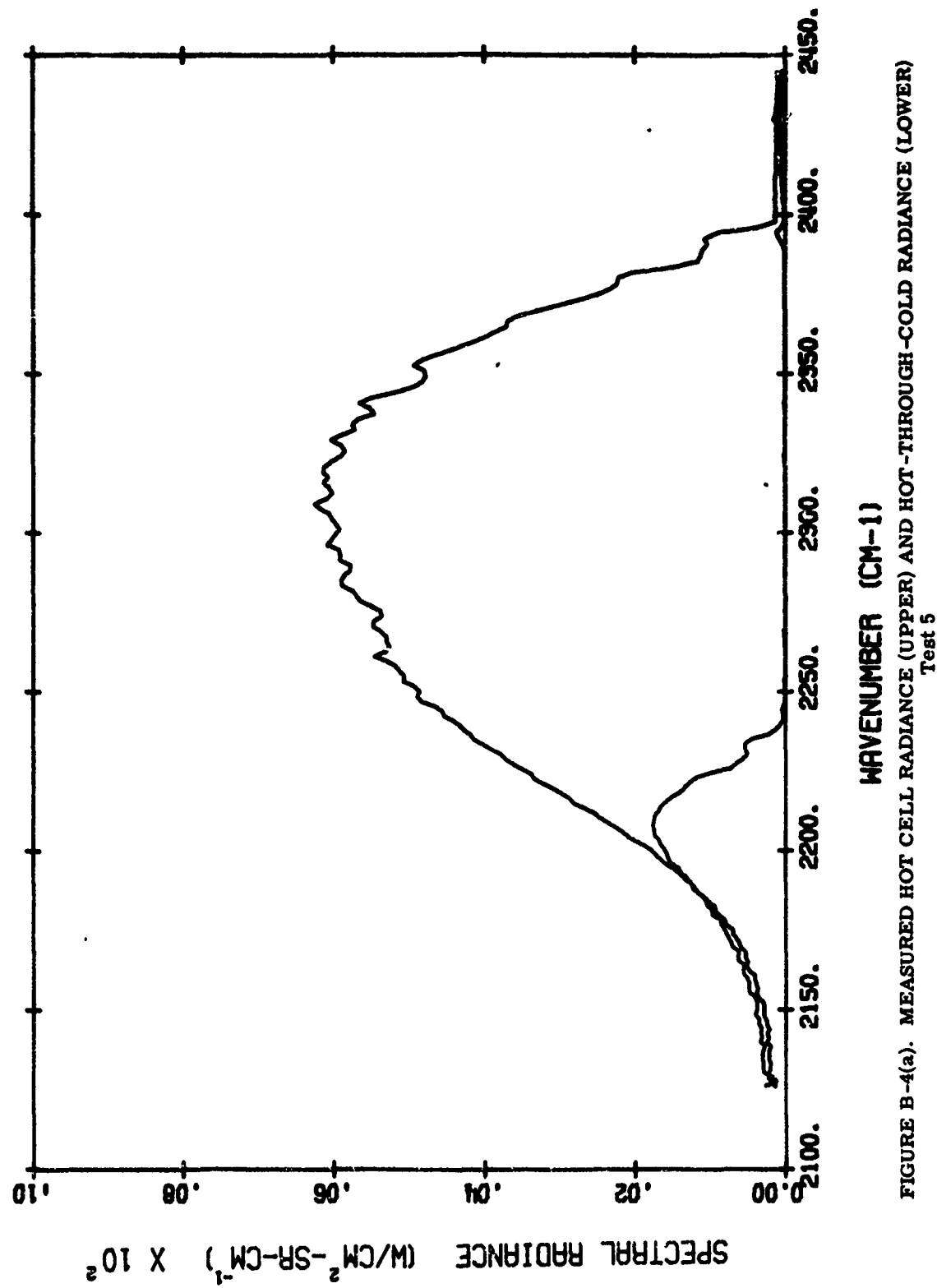


FIGURE B-4(a). MEASURED HOT CELL RADIANCE (UPPER) AND HOT-THROUGH-COLD RADIANCE (LOWER)
Test 5

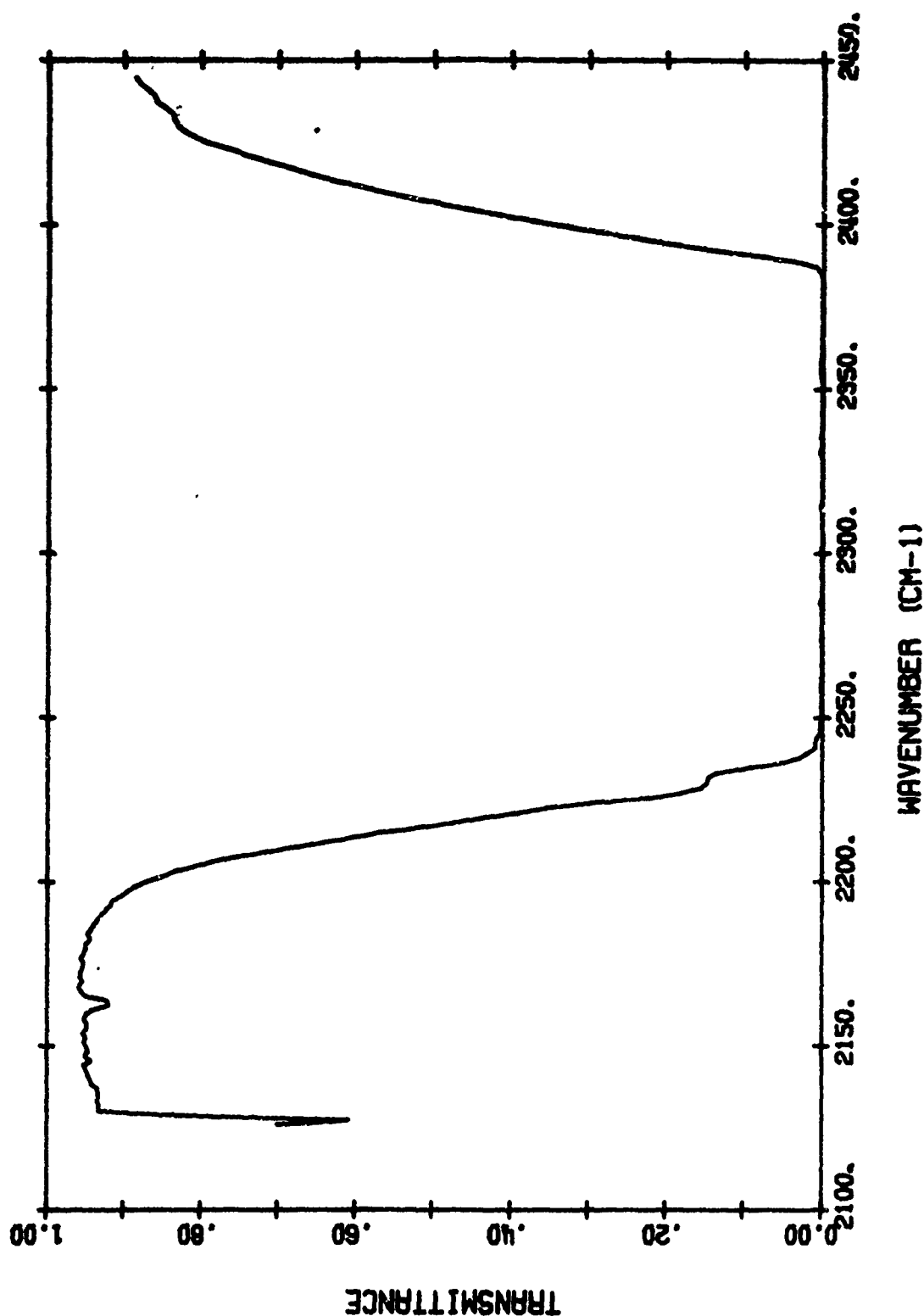


FIGURE B-4(b). MEASURED COLD CELL TRANSMITTANCE - Test 5

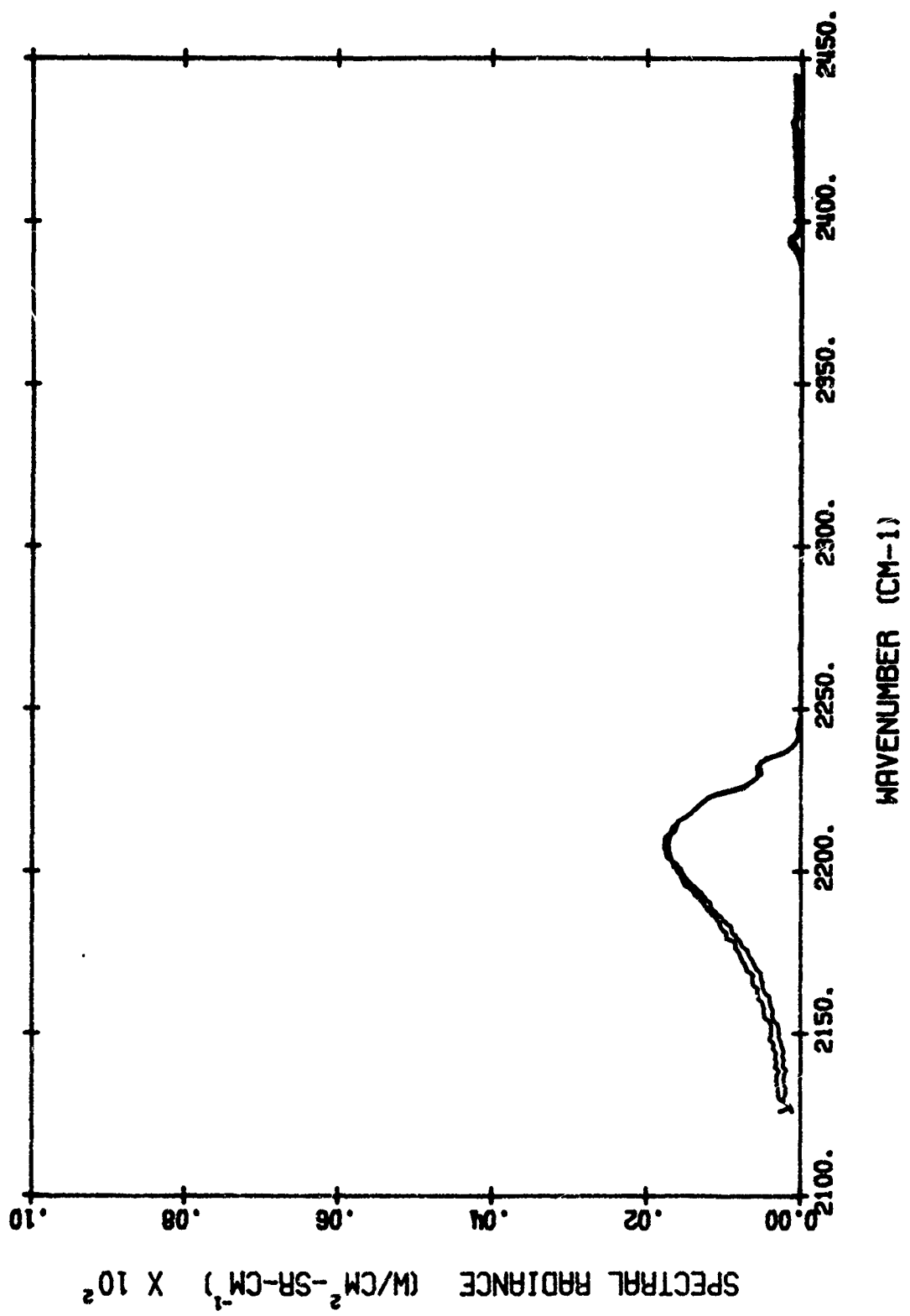


FIGURE B-4(c). MEASURED HOT THROUGH COLD RADIANCE (LOWER) AND PRODUCT OF HOT CELL RADIANCE AND COLD CELL TRANSMITTANCE (UPPER) - Test 5

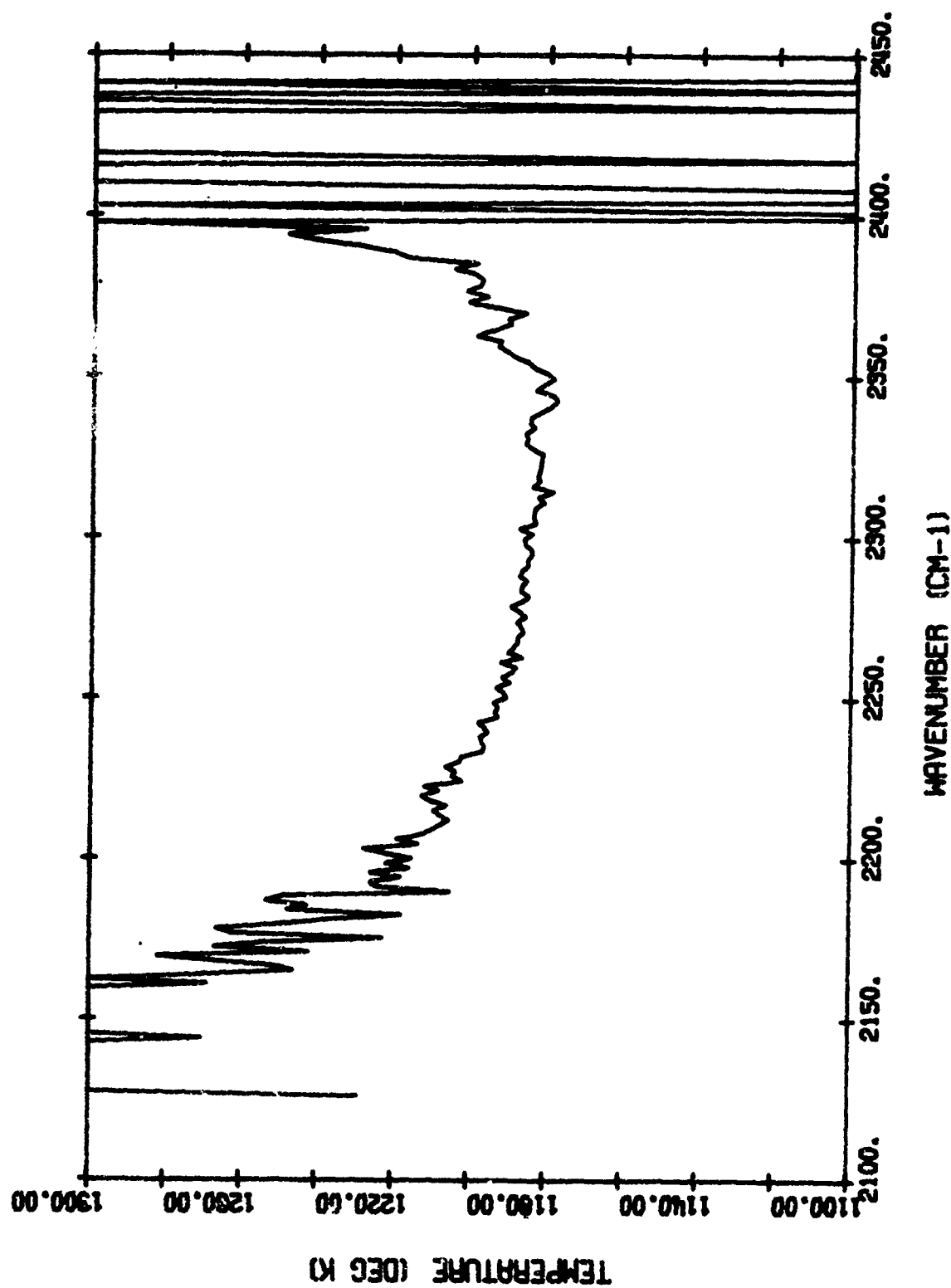


FIGURE B-4(d). MEASURED APPARENT TEMPERATURE - TEST 5

TABLE B-5. TEST-6 PARAMETERS

Spectral Region	4.3 μ m	
Hot Cell	Simulated Altitude: 16 km 0.598 atm-cm CO_2	
	Total Absolute Pressure	76.0 mm
	$P_{\text{H}_2\text{O}}$	0.0 mm
	P_{CO_2}	7.58 mm
	P_{N_2}	68.43 mm
	$L = 0.6$ m	$T = 1200^{\circ}\text{K}$
Cold Cell	Simulated 50-km Path @ 15-km Altitude	
	Total Absolute Pressure	98.0 mm
	$P_{\text{H}_2\text{O}}$	0.0 mm
	P_{CO_2}	22.15 mm
	P_{N_2}	75.85 mm
	$L = 100$ m	$T = 297^{\circ}\text{K}$

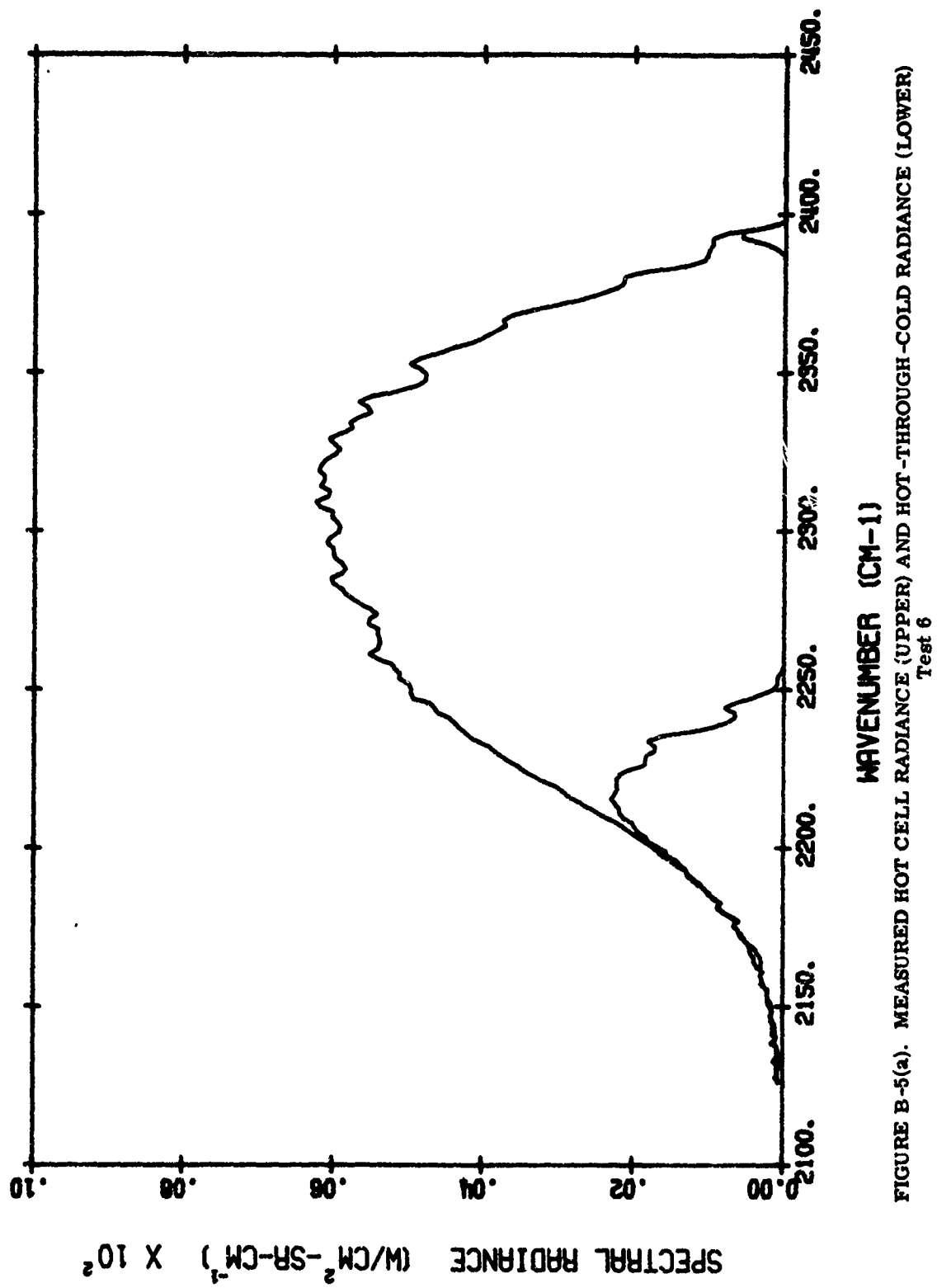


FIGURE B-5(a). MEASURED HOT CELL RADIANCE (UPPER) AND HOT-THROUGH-COLD RADIANCE (LOWER)
Test 6

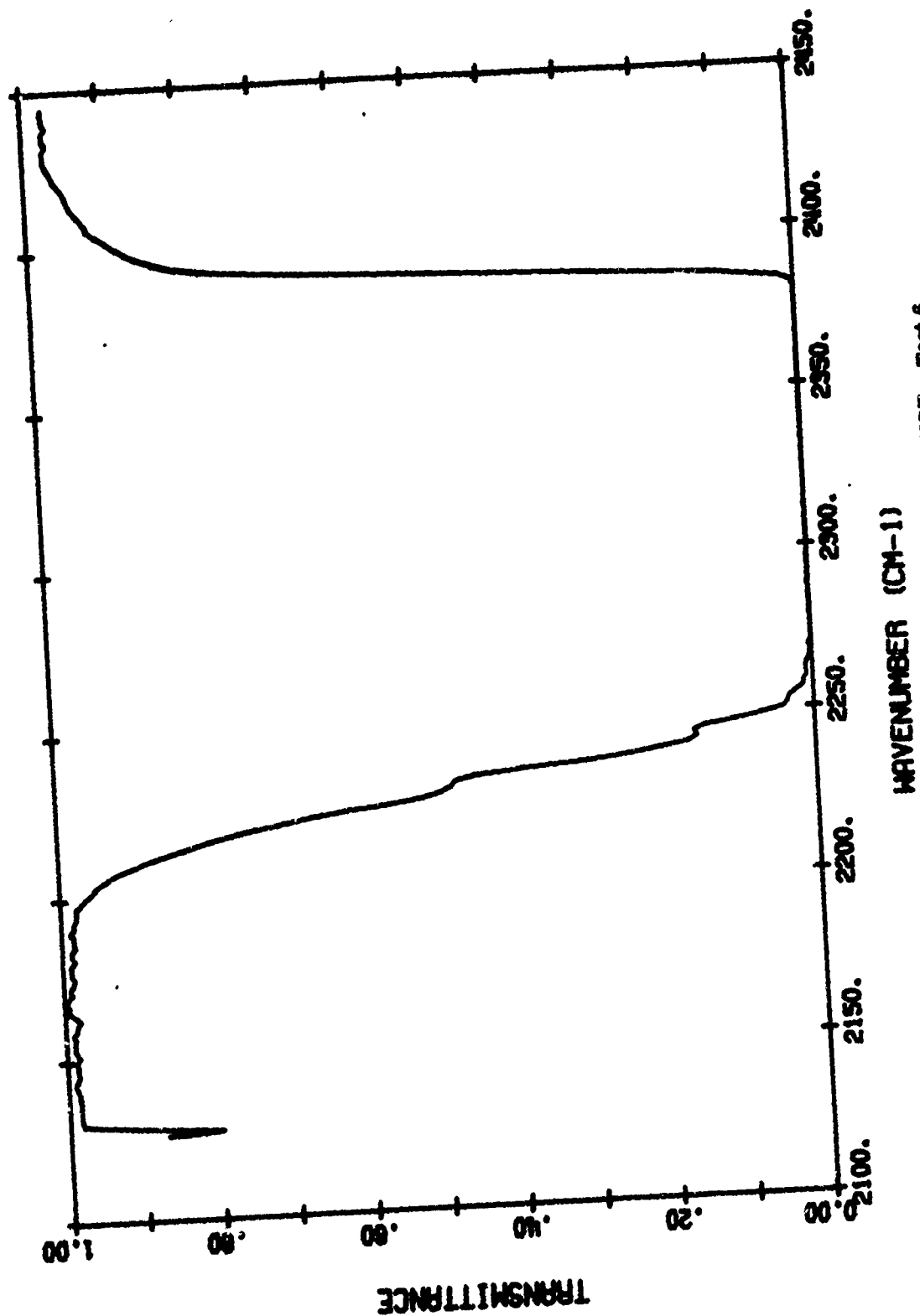


FIGURE B-5(b). MEASURED COLD CELL TRANSMITTANCE - Test 6

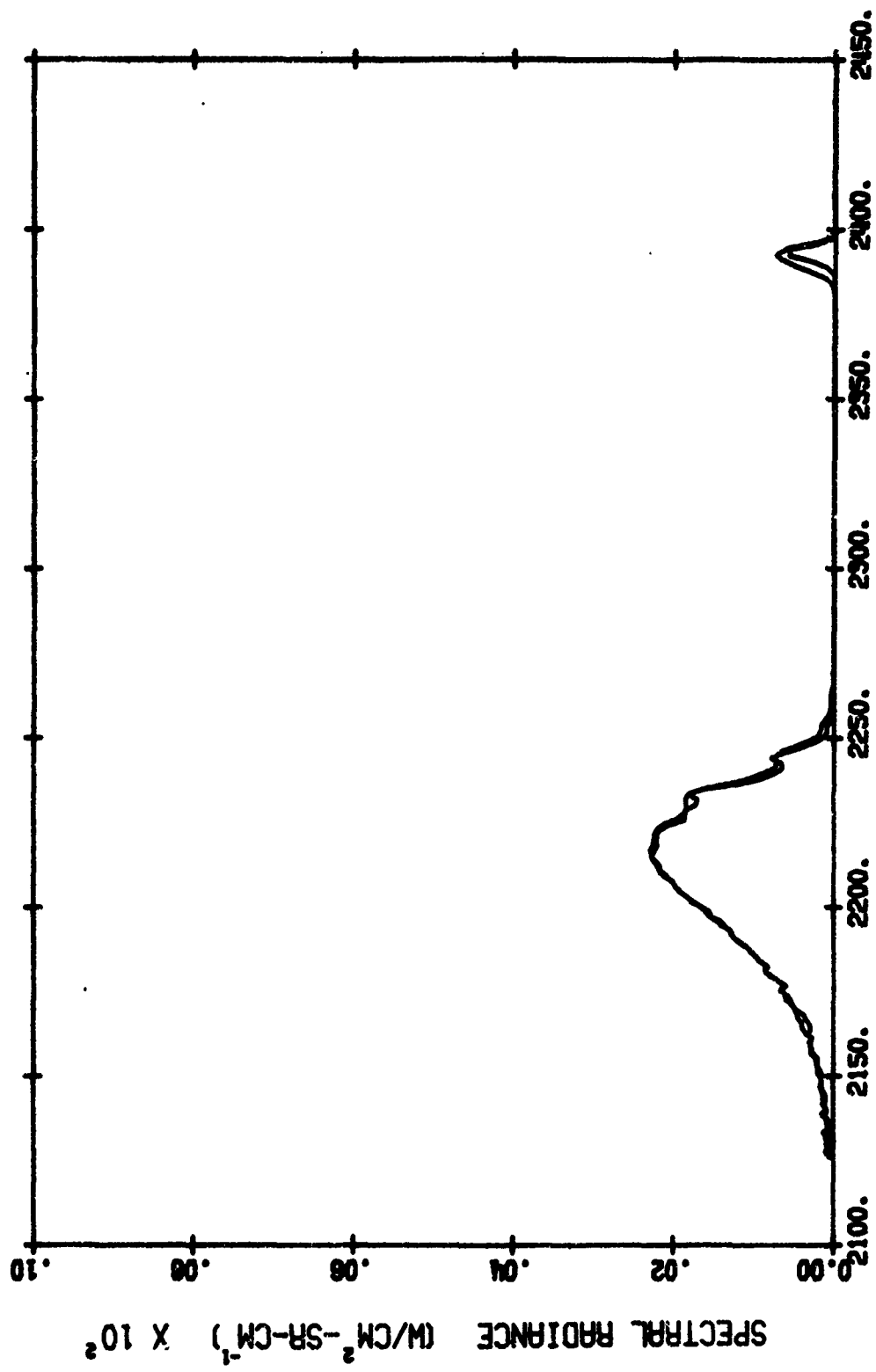


FIGURE B-5(c). MEASURED HOT THROUGH COLD RADIANCE (LOWER) AND PRODUCT OF HOT CELL RADIANCE AND COLD CELL TRANSMITTANCE (UPPER) - Test 6

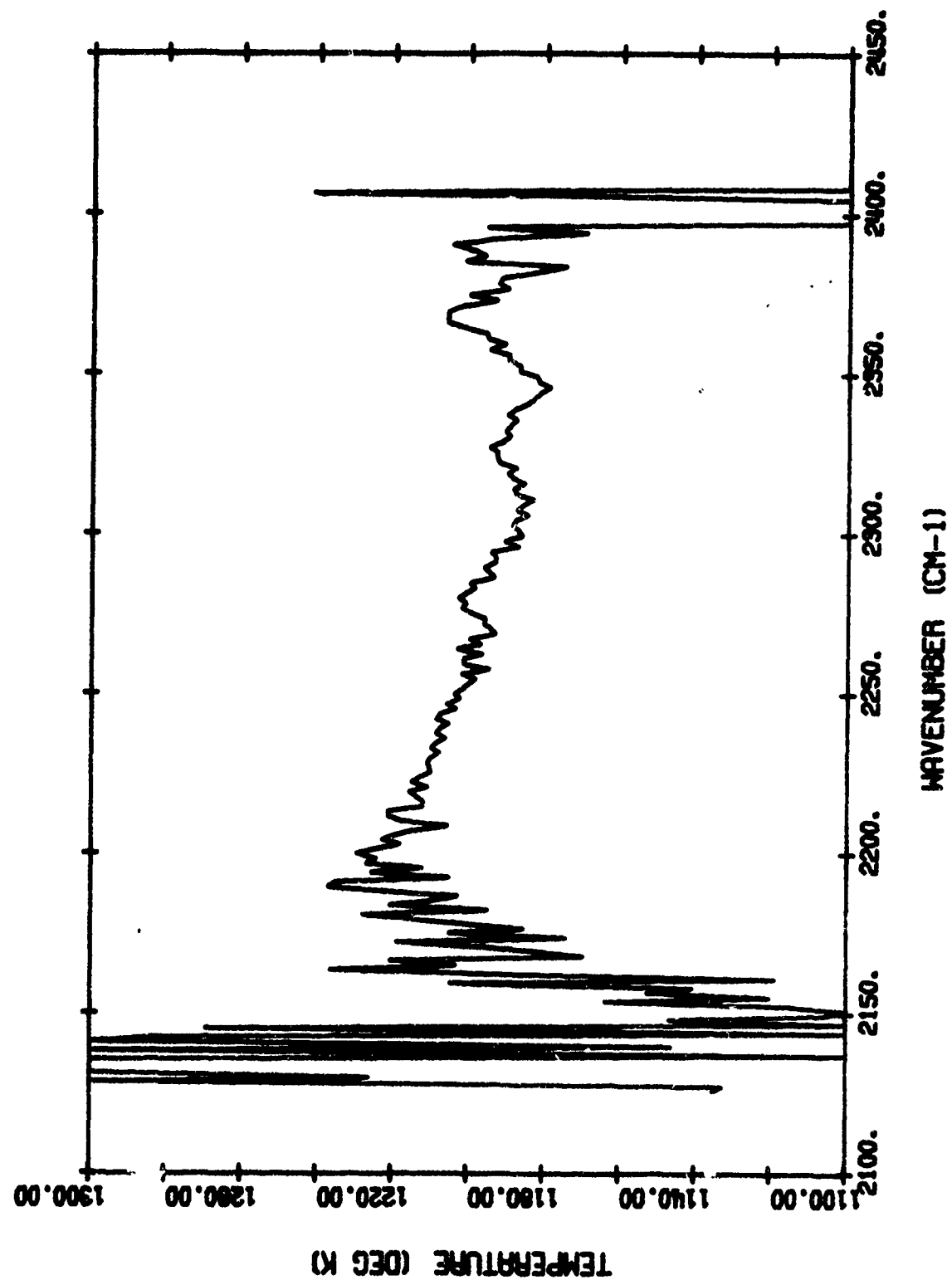


FIGURE B-5(d). MEASURED APPARENT TEMPERATURE - Test 6

TABLE B-6. TEST-7 PARAMETERS

Spectral Region	4.3 μ m	
Hot Cell	Simulated Altitude: 16 km 0.598 atm-cm CO_2	
	Total Absolute Pressure	76.0 mm
	$P_{\text{H}_2\text{O}}$	0.0 mm
	P_{CO_2}	7.58 mm
	P_{N_2}	68.43 mm
	$L = 0.6$ m	$T = 1200^{\circ}\text{K}$
Cold Cell	Simulated 10-km Path @ 15-km Altitude	
	Total Absolute Pressure	98.0 mm
	$P_{\text{H}_2\text{O}}$	0.0 mm
	P_{CO_2}	4.43 mm
	P_{N_2}	93.57 mm
	$L = 100$ m	$T = 297^{\circ}\text{K}$

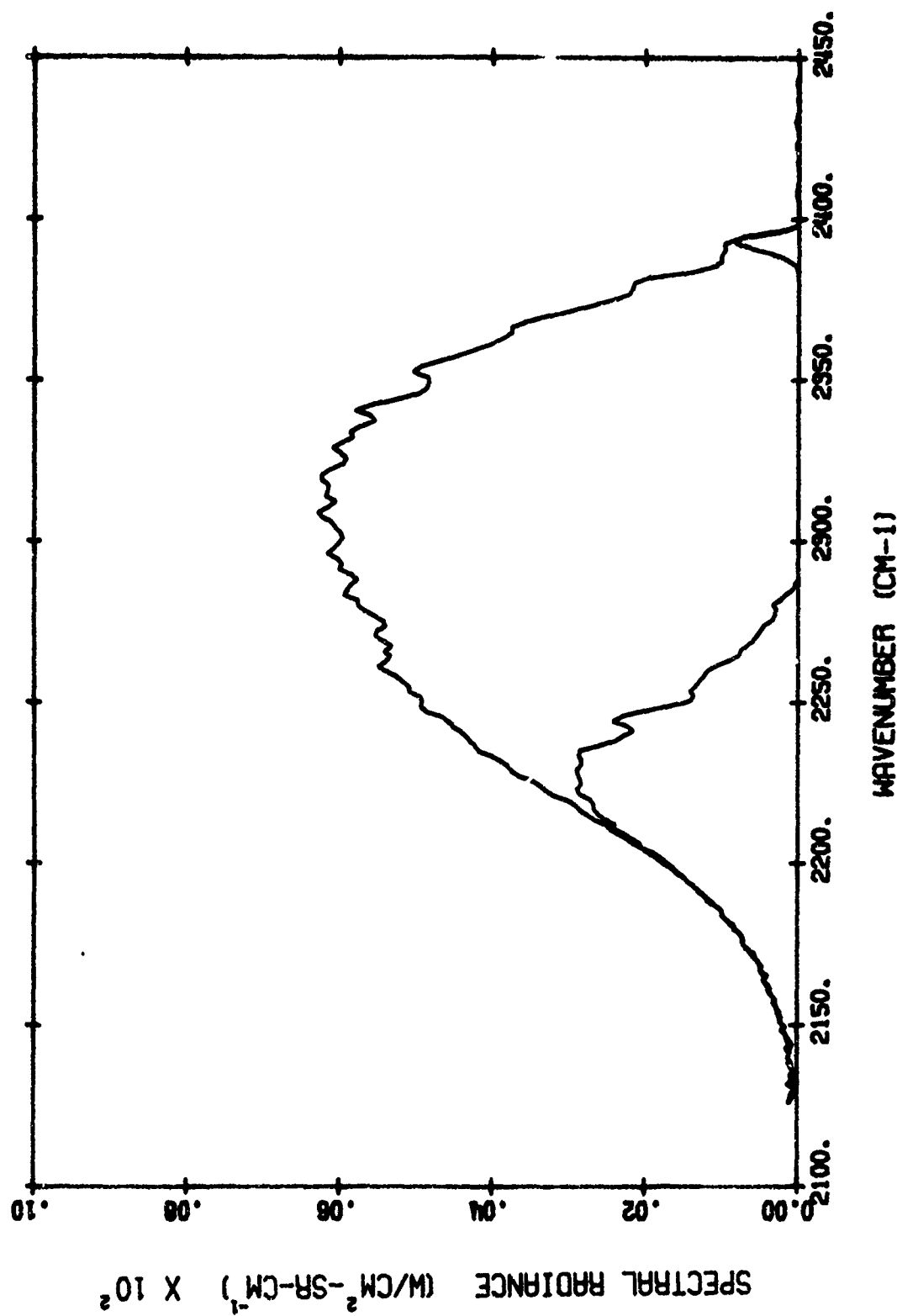


FIGURE B-6(a). MEASURED HOT CELL RADIANCE (UPPER) AND HOT-THROUGH-COLD RADIANCE (LOWER)
Test 7

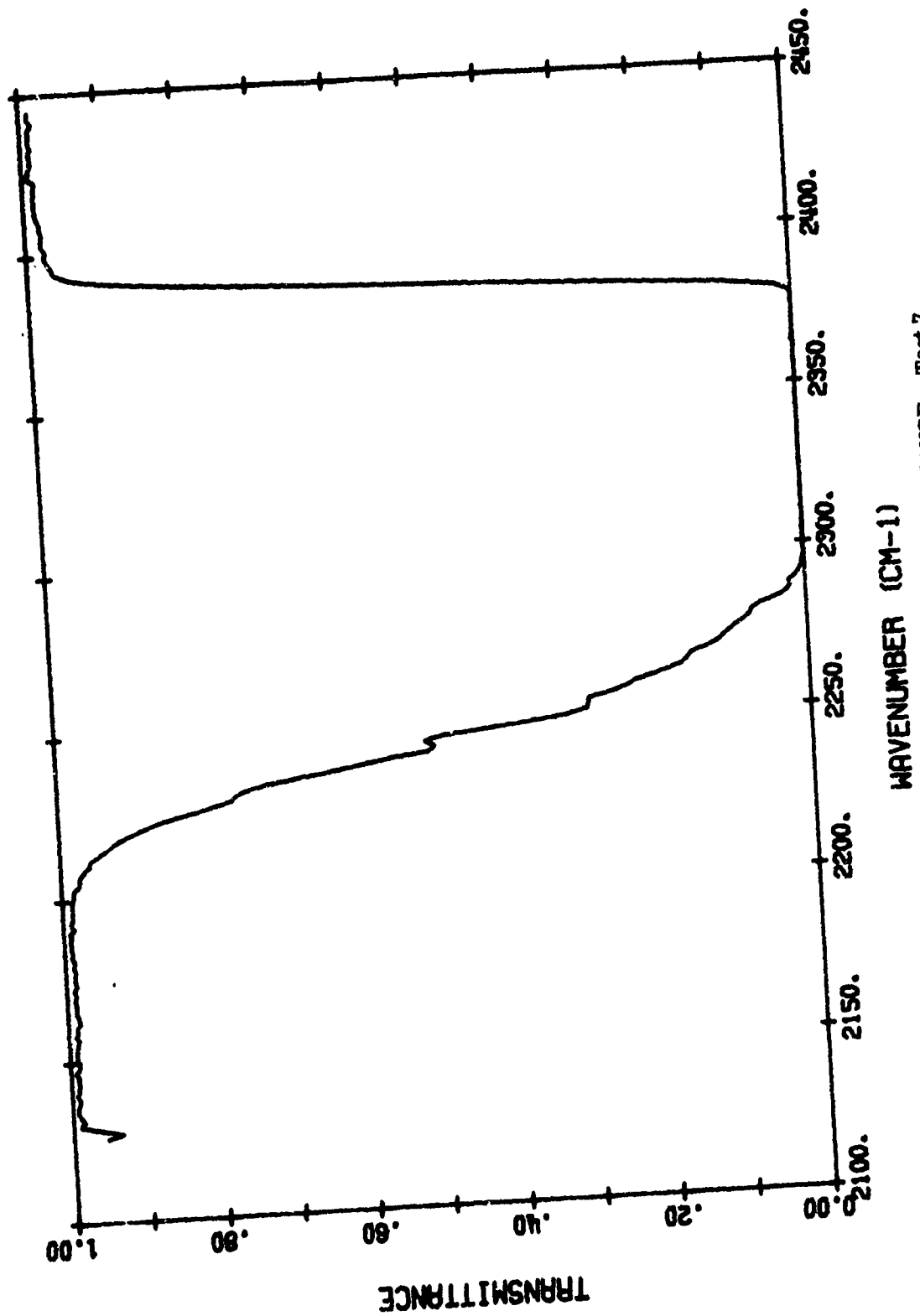


FIGURE B-6(b). MEASURED COLD CELL TRANSMITTANCE - Test 7

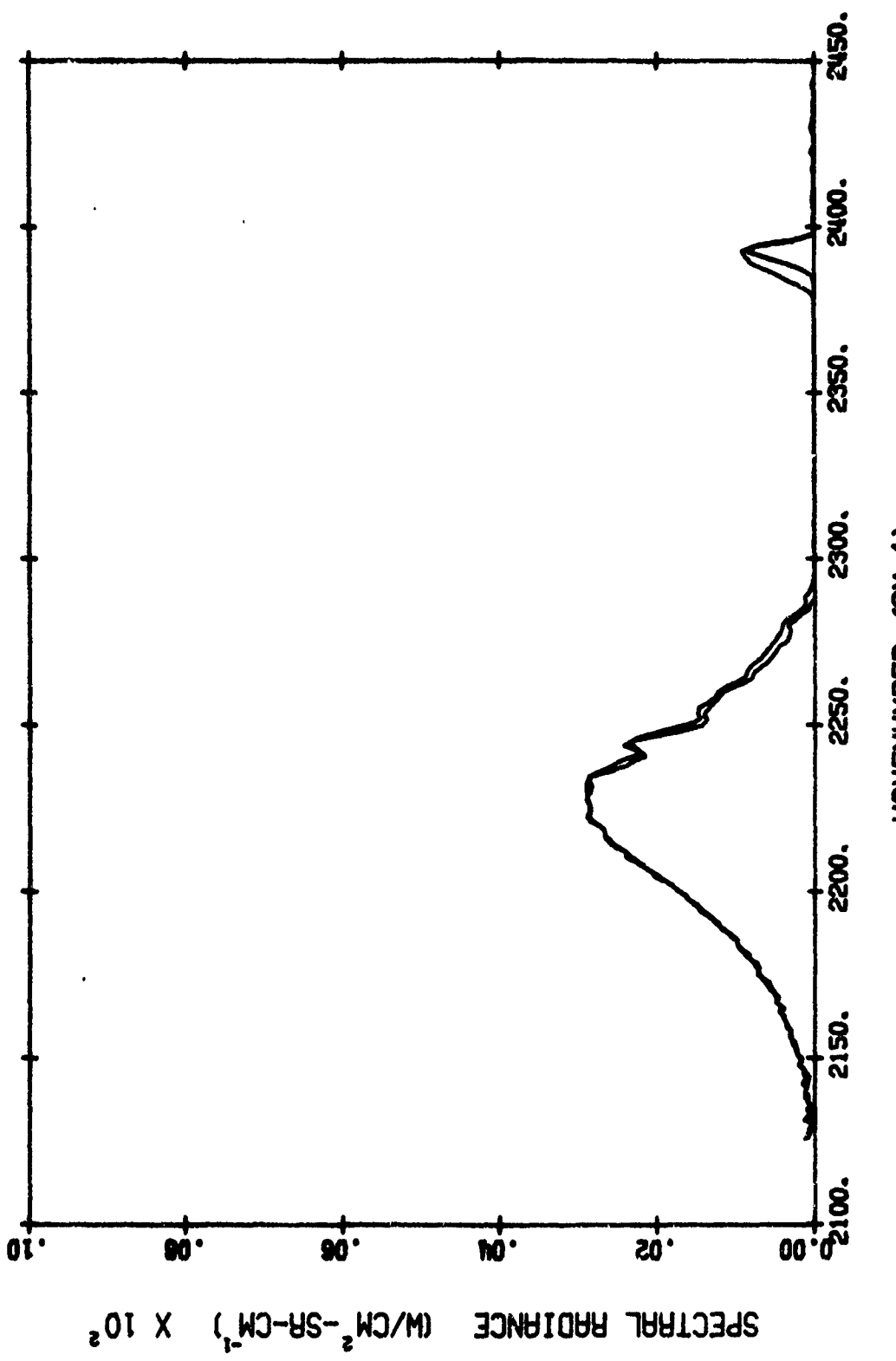


FIGURE B-8(c). MEASURED HOT THROUGH COLD RADIANCE (LOWER) AND PRODUCT OF HOT CELL RADIANCE AND COLD CELL TRANSMITTANCE (UPPER) - Test 7

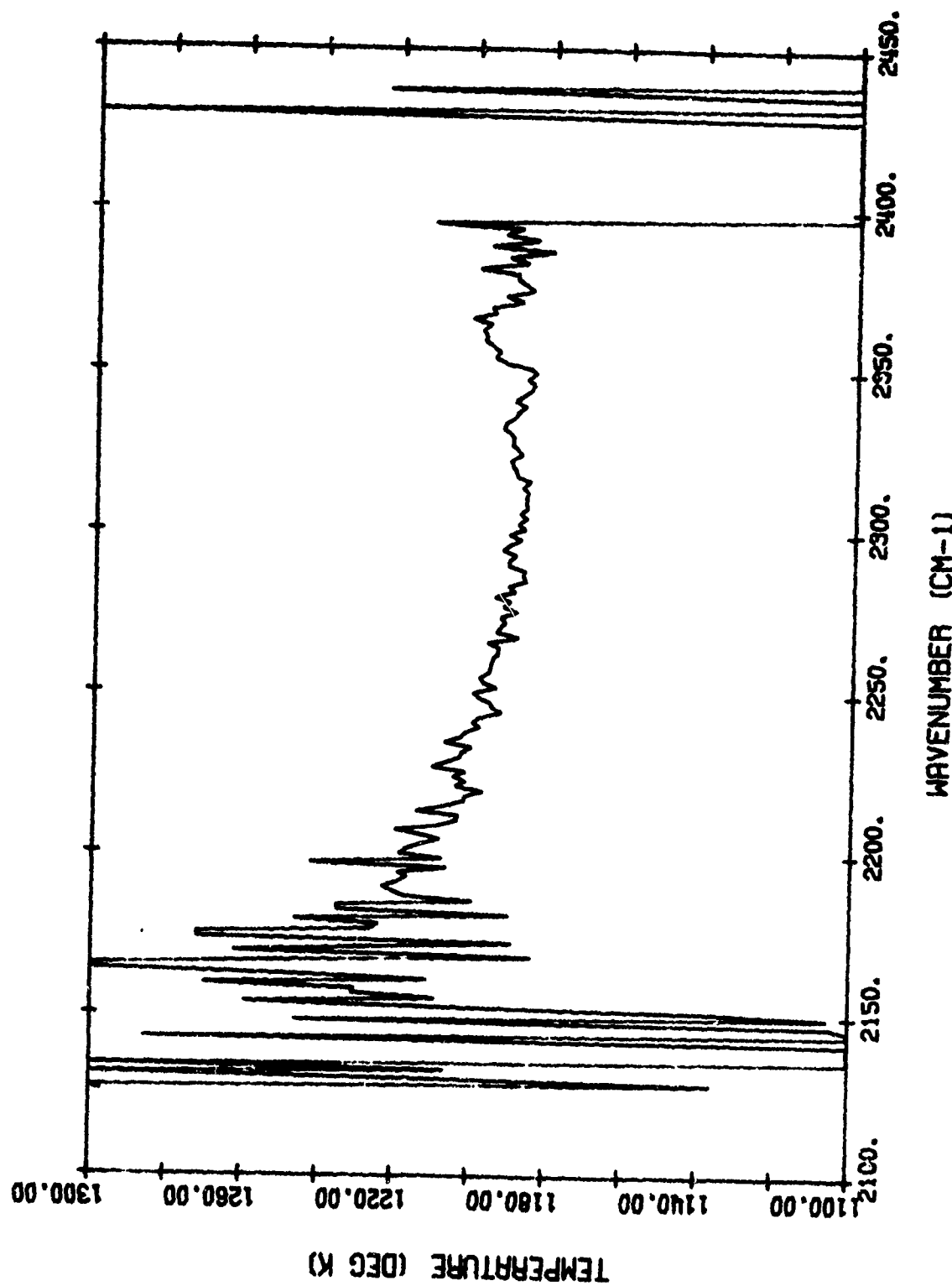


FIGURE B-6(d). MEASURED APPARENT TEMPERATURE - Test 7

TABLE B-7. TEST-8R PARAMETERS

Spectral Region	2.7 μ m	
Hot Cell	Simulated Altitude: 16 km 3.0 atm-cm H_2O	
	Total Absolute Pressure	76.7 mm
	P_{H_2O}	38.0 mm
	P_{N_2}	38.7 mm
	P_{CO_2}	0.0 mm
	$L = 0.6$ m	$T = 1215^{\circ}K$
Cold Cell	Simulated 86.0-km Path @ 18-km Altitude	
	Total Absolute Pressure	53.3 mm
	P_{H_2O}	2.28 mm
	P_{CO_2}	0.0 mm
	P_{N_2}	51.0 mm
	$L = 100$ m	$T = 296^{\circ}K$

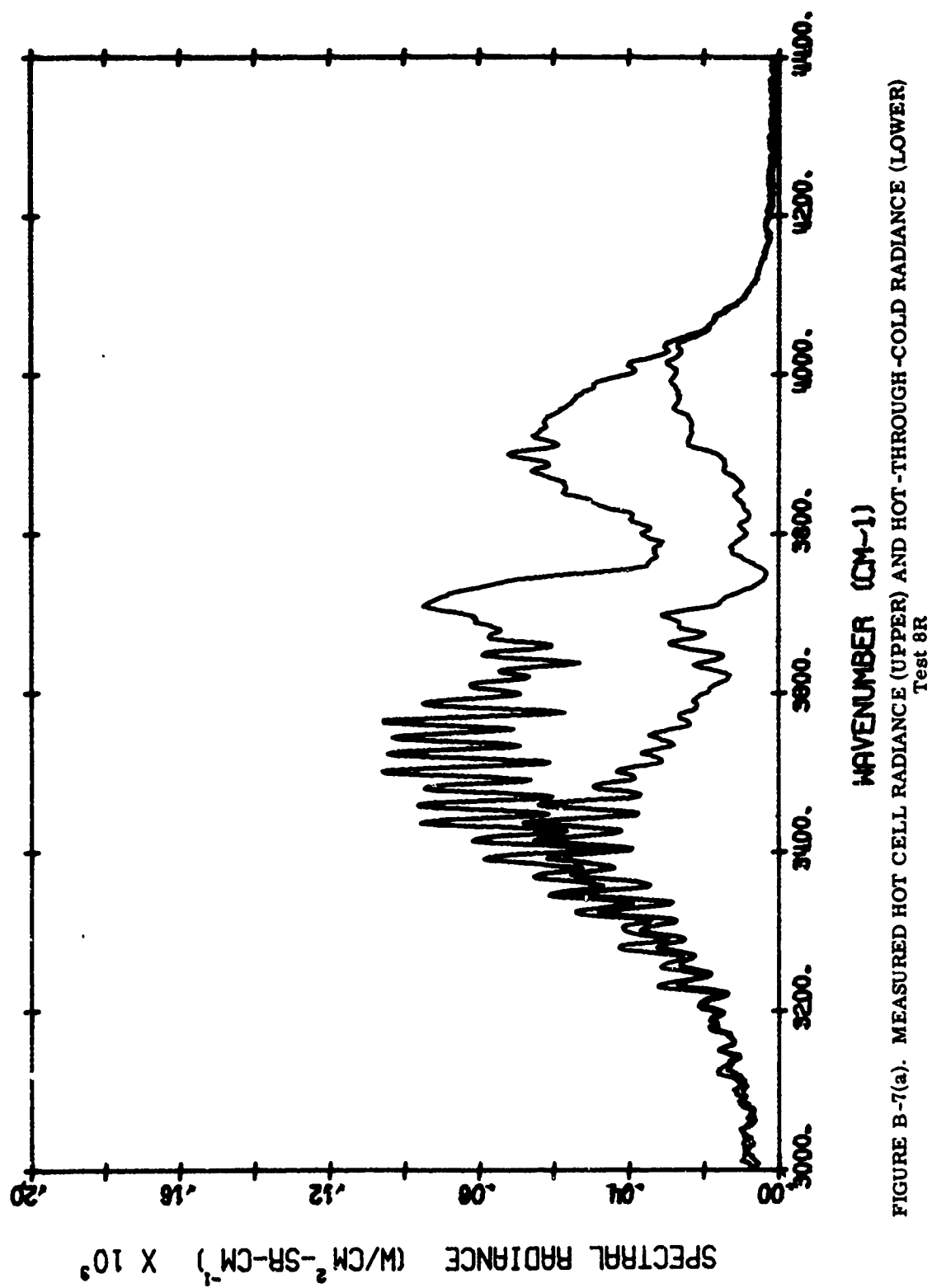


FIGURE B-7(a). MEASURED HOT CELL RADIANCE (UPPER) AND HOT-THROUGH-COLD RADIANCE (LOWER)
Test 8R

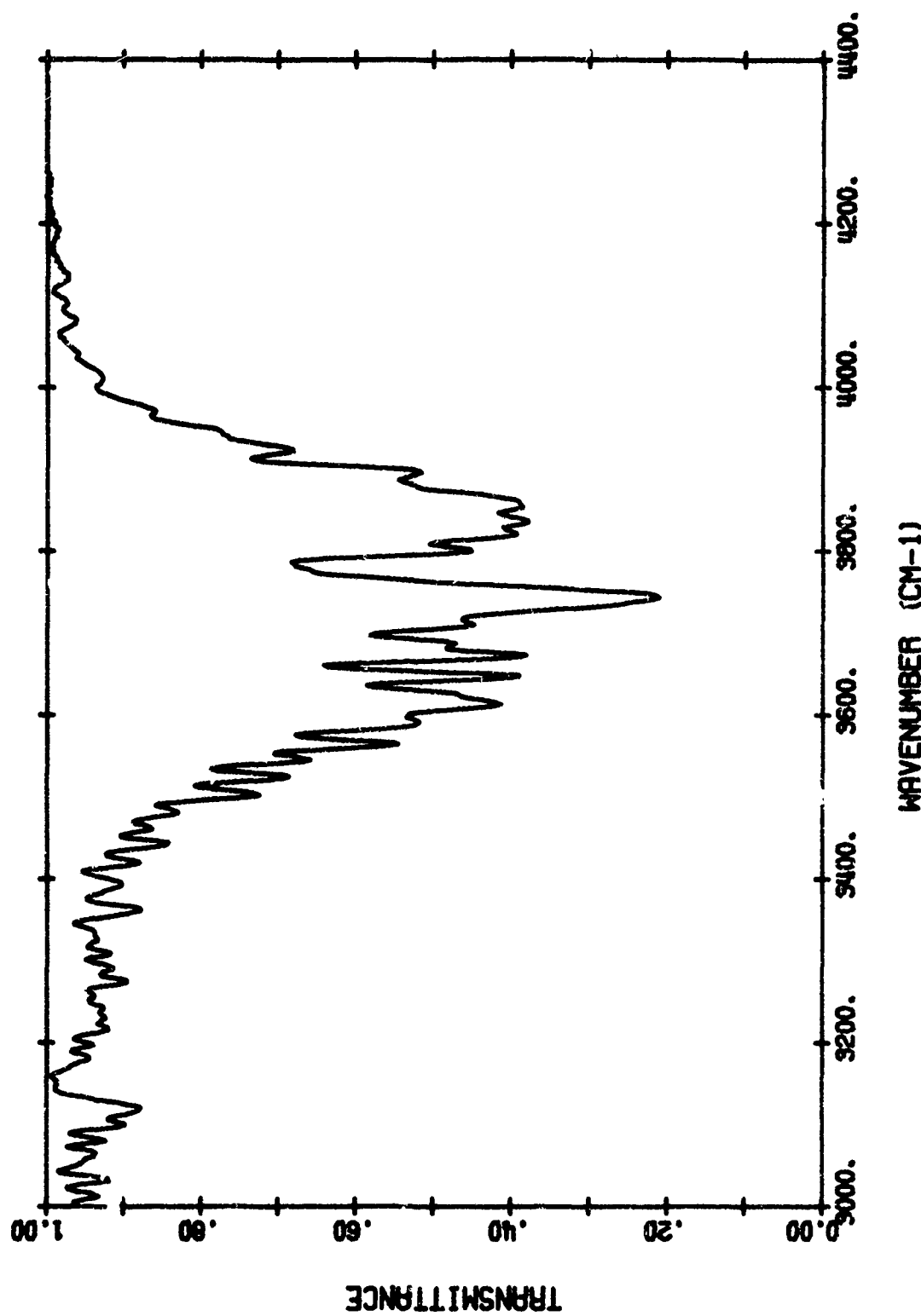


FIGURE B-7(b). MEASURED COLD CELL TRANSMITTANCE - Test 8R

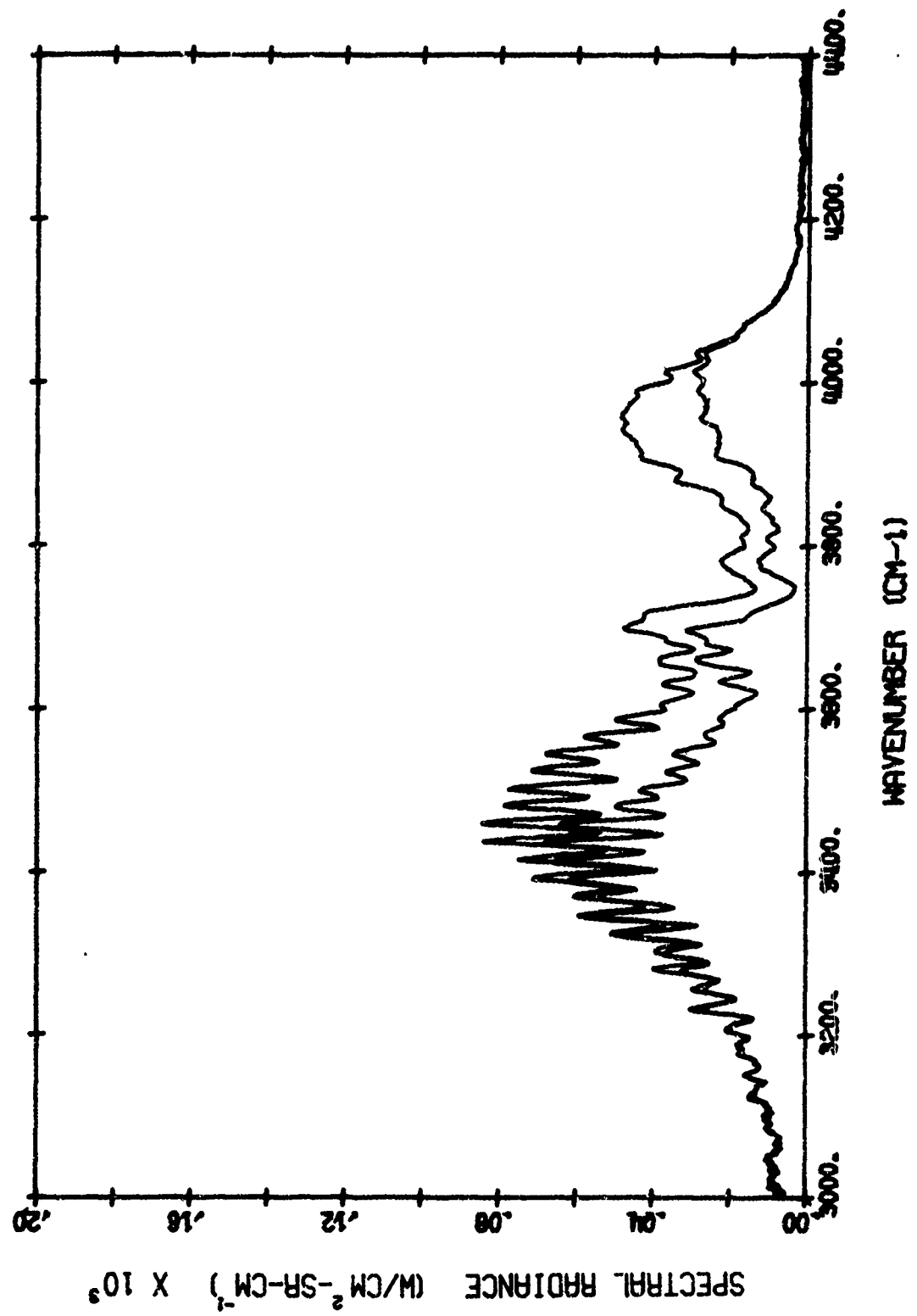


FIGURE B-7(c). MEASURED HOT THROUGH COLD RADIANCE (LOWER) AND PRODUCT OF HOT CELL RADIANCE AND COLD CELL TRANSMITTANCE (UPPER) - Test 8R

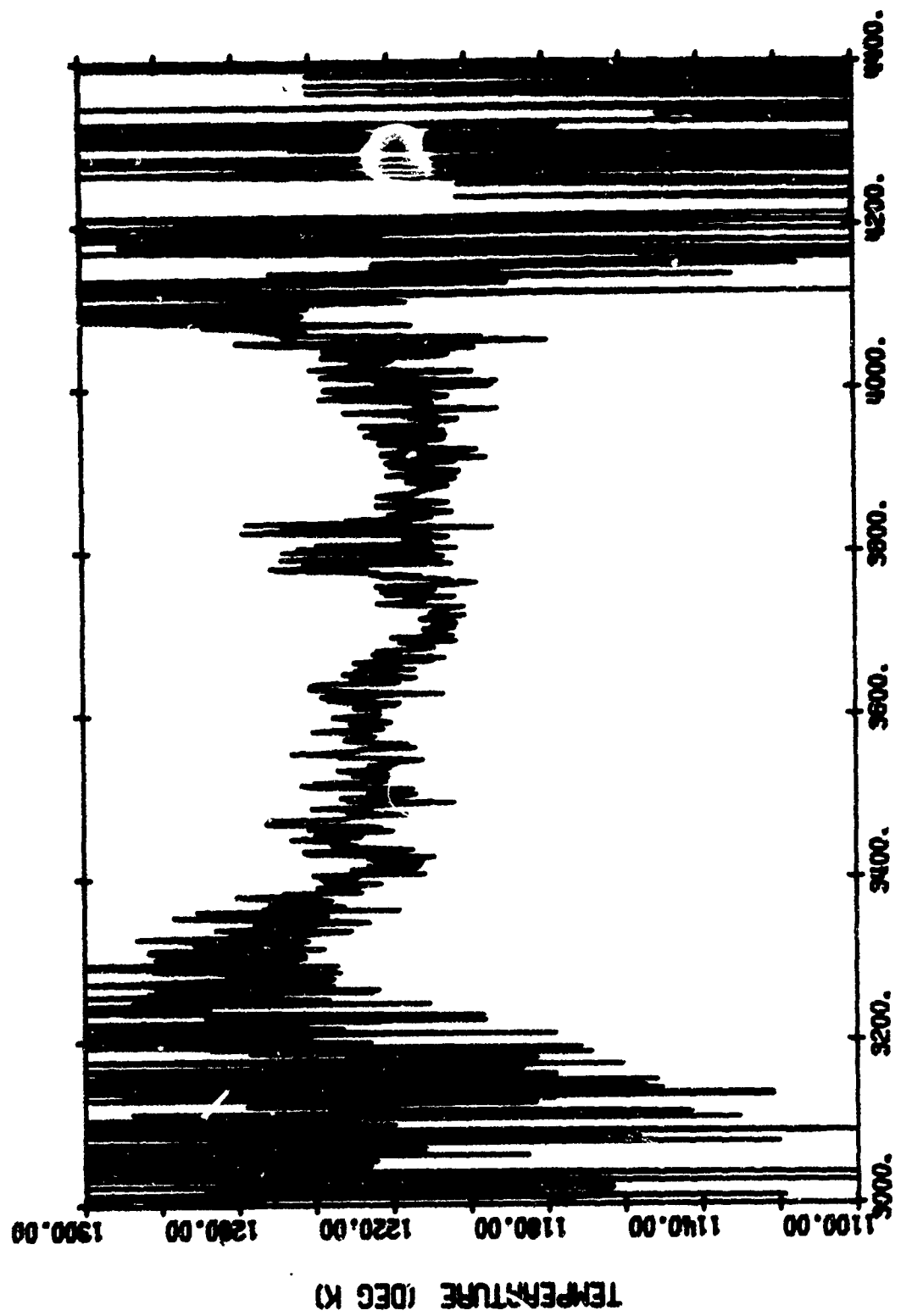
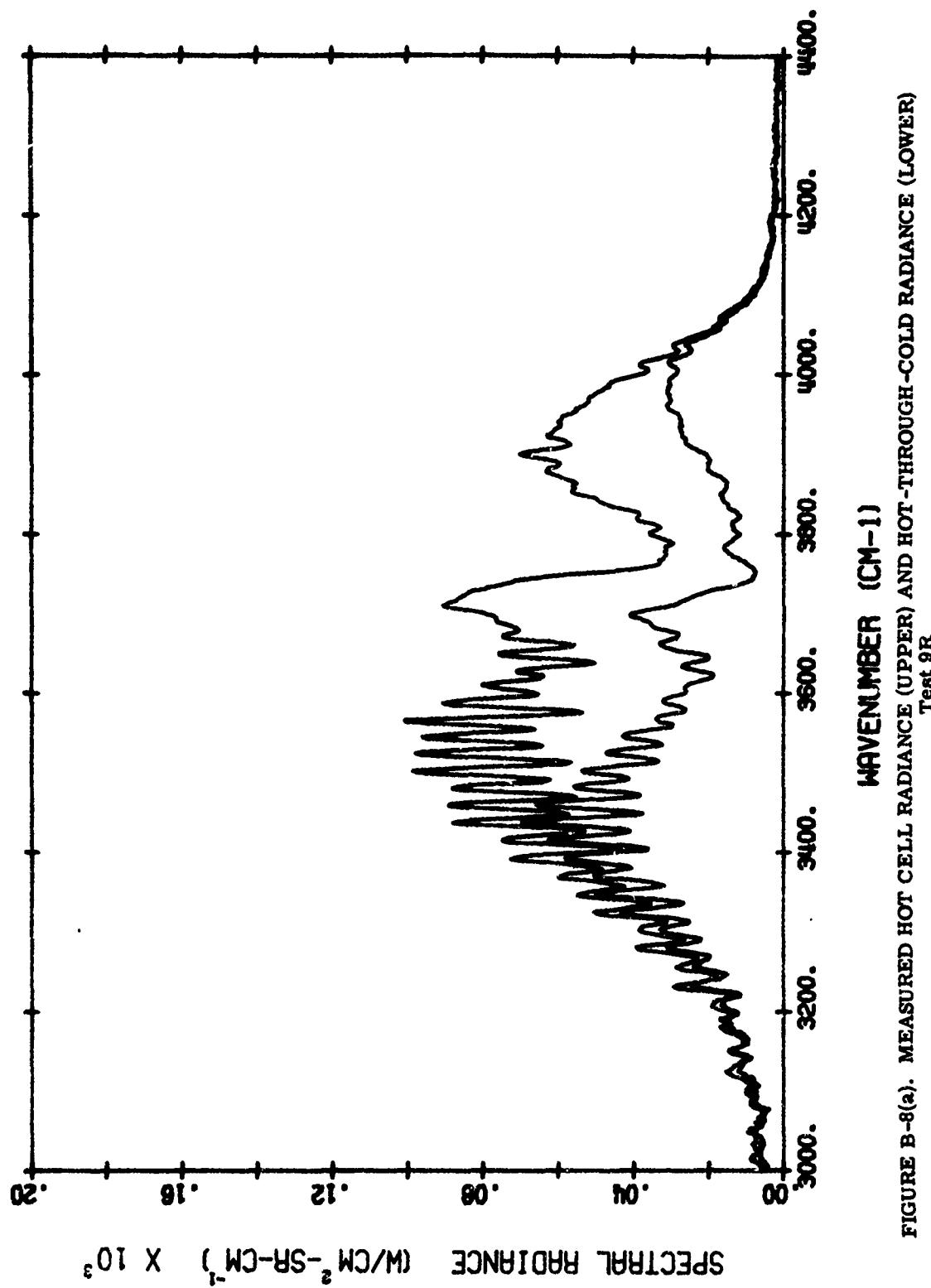


FIGURE B-7(d). MEASURED APPARENT TEMPERATURE - Test 8R

TABLE B-8. TEST-9R PARAMETERS

Spectral Region	2.7 μ m	
Hot Cell	Simulated Altitude: 16 km 3.0 atm-cm H_2O	
	Total Absolute Pressure	76.0 mm
	P_{H_2O}	38.0 mm
	P_{CO_2}	0.0 mm
	P_{N_2}	38.0 mm
	$L = 0.6$ m	$T = 1202^{\circ}K$
Cold Cell	Simulated 28.8-km Path @ 18-km Altitude	
	Total Absolute Pressure	53.2 mm
	P_{H_2O}	0.76 mm
	P_{CO_2}	0.0 mm
	P_{N_2}	52.46 mm
	$L = 100$ m	$T = 293^{\circ}K$



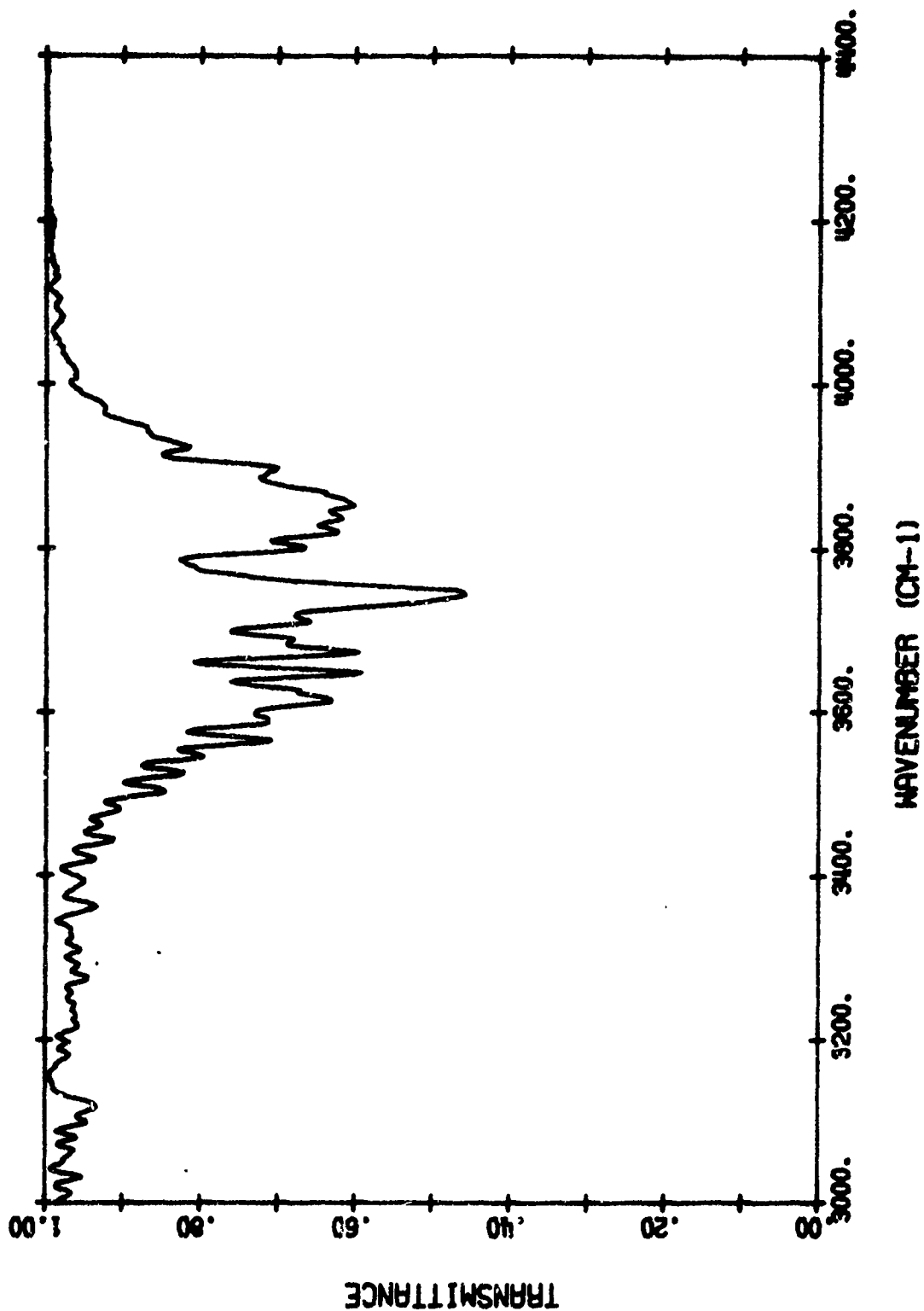


FIGURE B-8(b). MEASURED COLD CELL TRANSMITTANCE - Test 9R

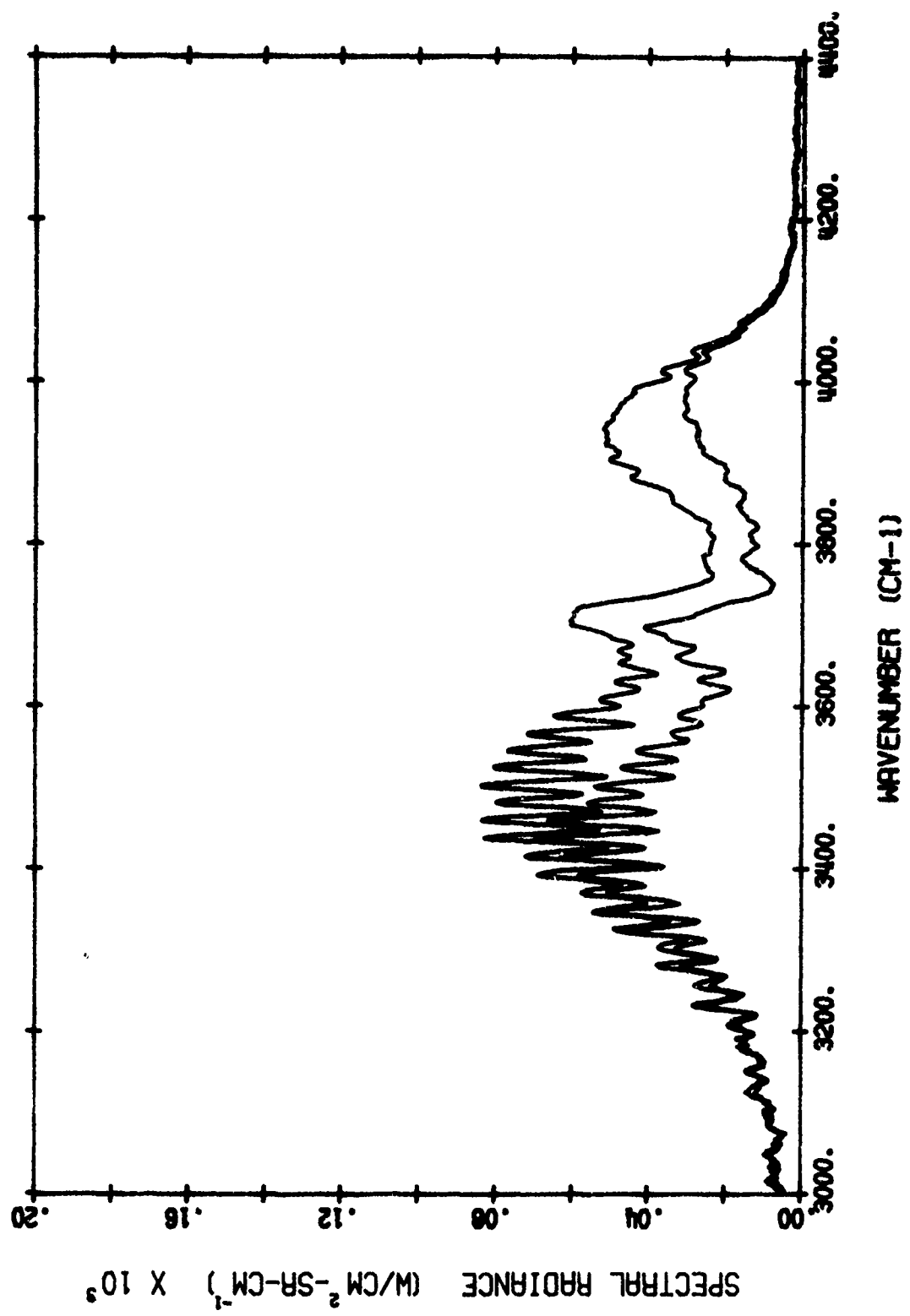


FIGURE B-8(c). MEASURED HOT THROUGH COLD RADIANCE (LOWER) AND PRODUCT OF HOT CELL RADIANCE AND COLD CELL TRANSMITTANCE (UPPER) - Test 9R

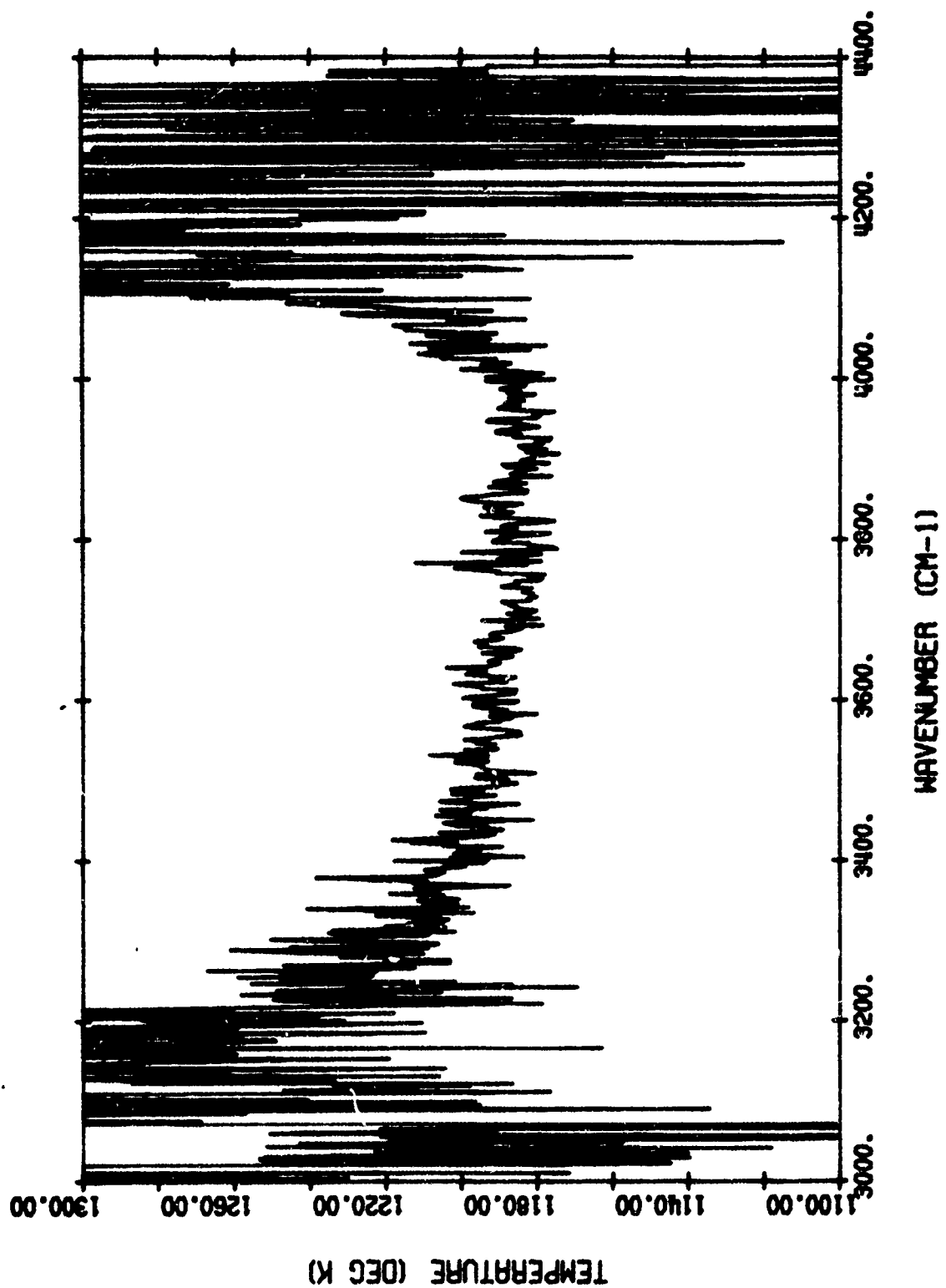


FIGURE B-8(d). MEASURED APPARENT TEMPERATURE - TEST 9R

TABLE B-9. TEST-11MK PARAMETERS

Spectral Region	2.7 μ m	
Hot Cell	Simulated Altitude: 16 km 3.0 atm-cm H_2O	
	Total Absolute Pressure	76.0 mm
	P_{H_2O}	38.0 mm
	P_{CO_2}	0.0 mm
	P_{N_2}	38.0 mm
	$L = 0.6$ m	$T = 1202^0K$
Cold Cell	Simulated 288-km Path @ 18-km Altitude	
	Total Absolute Pressure	53.2 mm
	P_{H_2O}	7.6 mm
	P_{CO_2}	0.0 mm
	P_{N_2}	45.6 mm
	$L = 100$ m	$T = 296^0K$

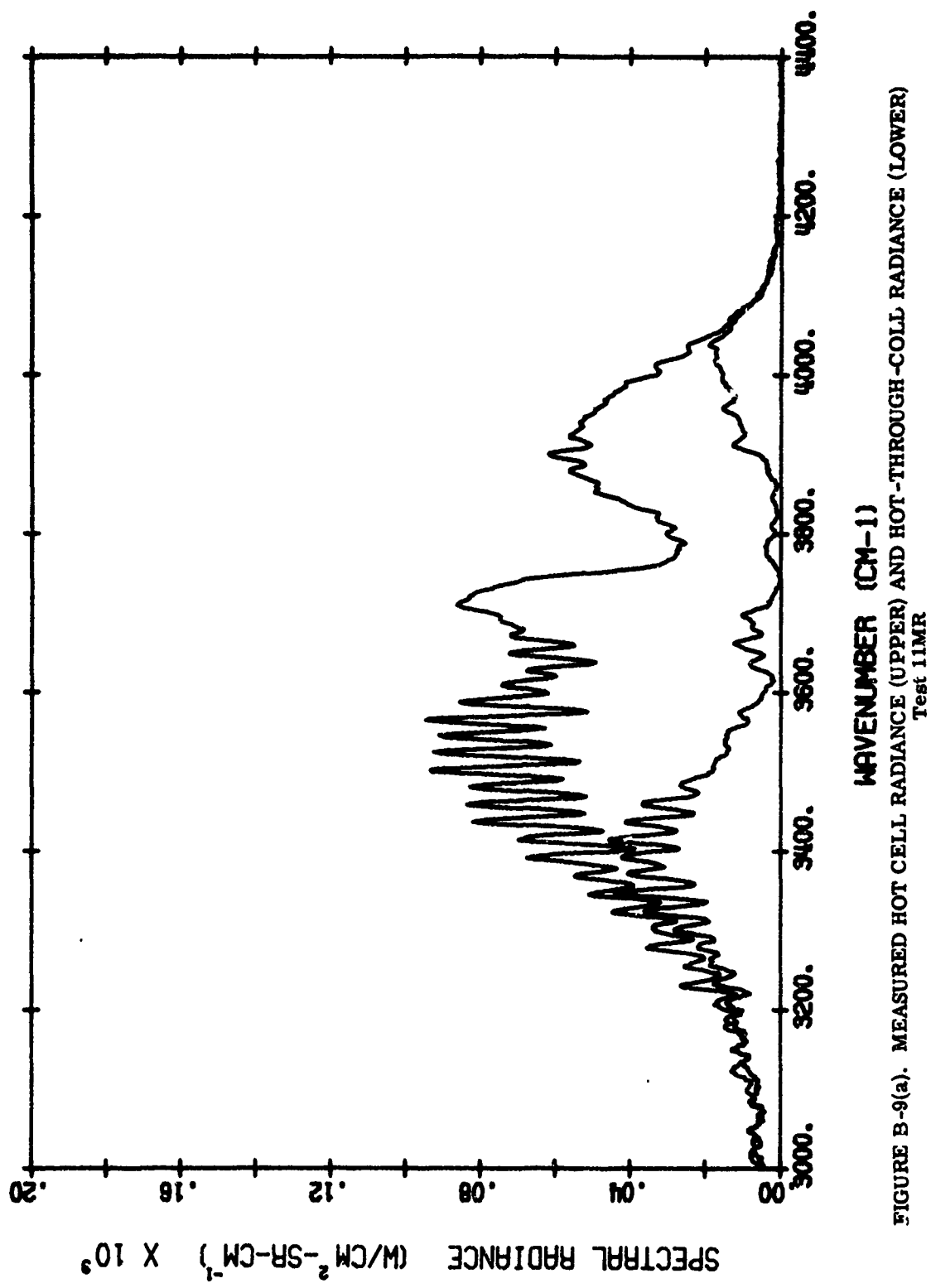


FIGURE B-9(a). MEASURED HOT CELL RADIANCE (UPPER) AND HOT-THROUGH-COLL RADIANCE (LOWER)
Test 11MR

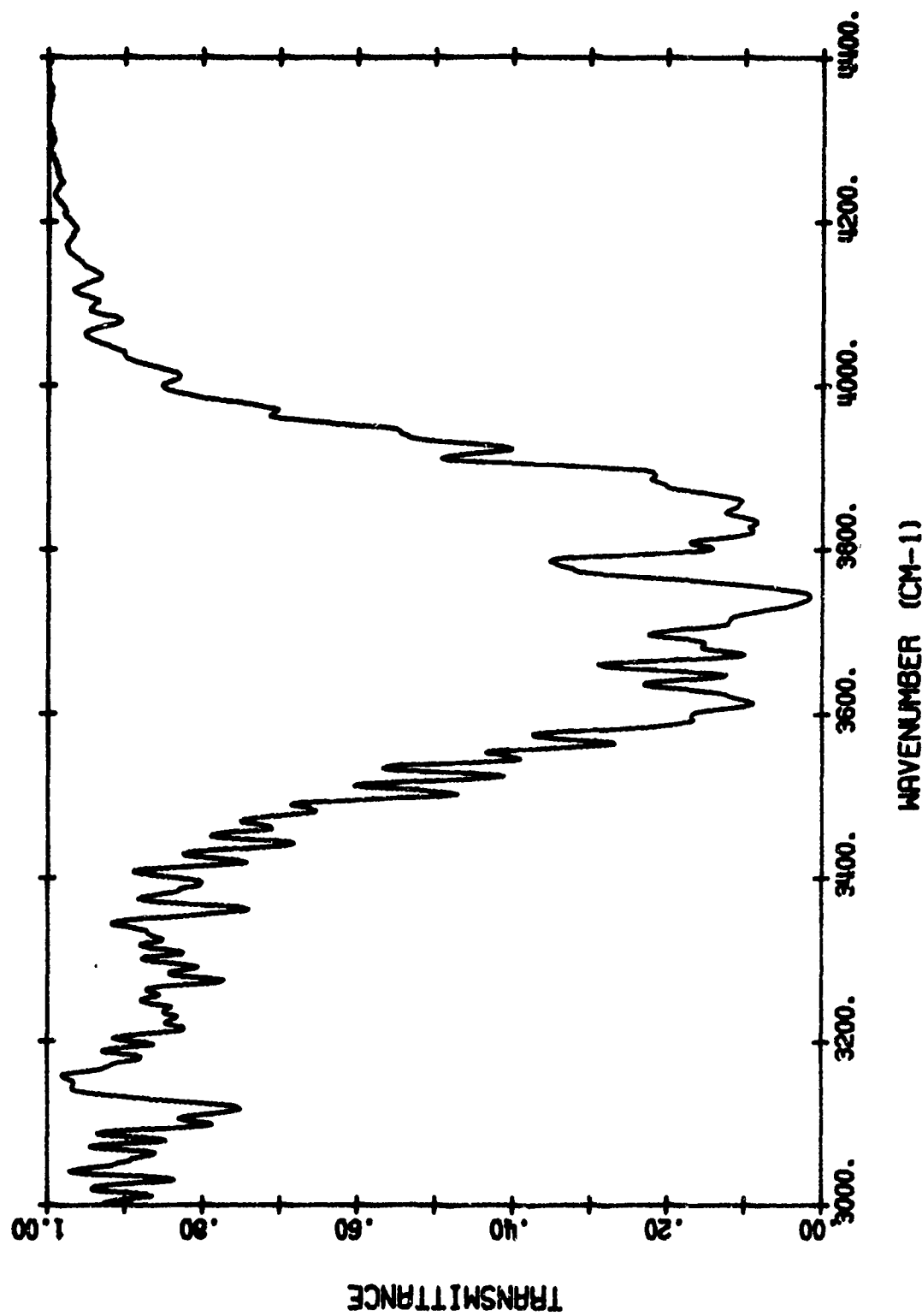


FIGURE B-9(b). MEASURED COLD CELL TRANSMITTANCE - Test 11MR

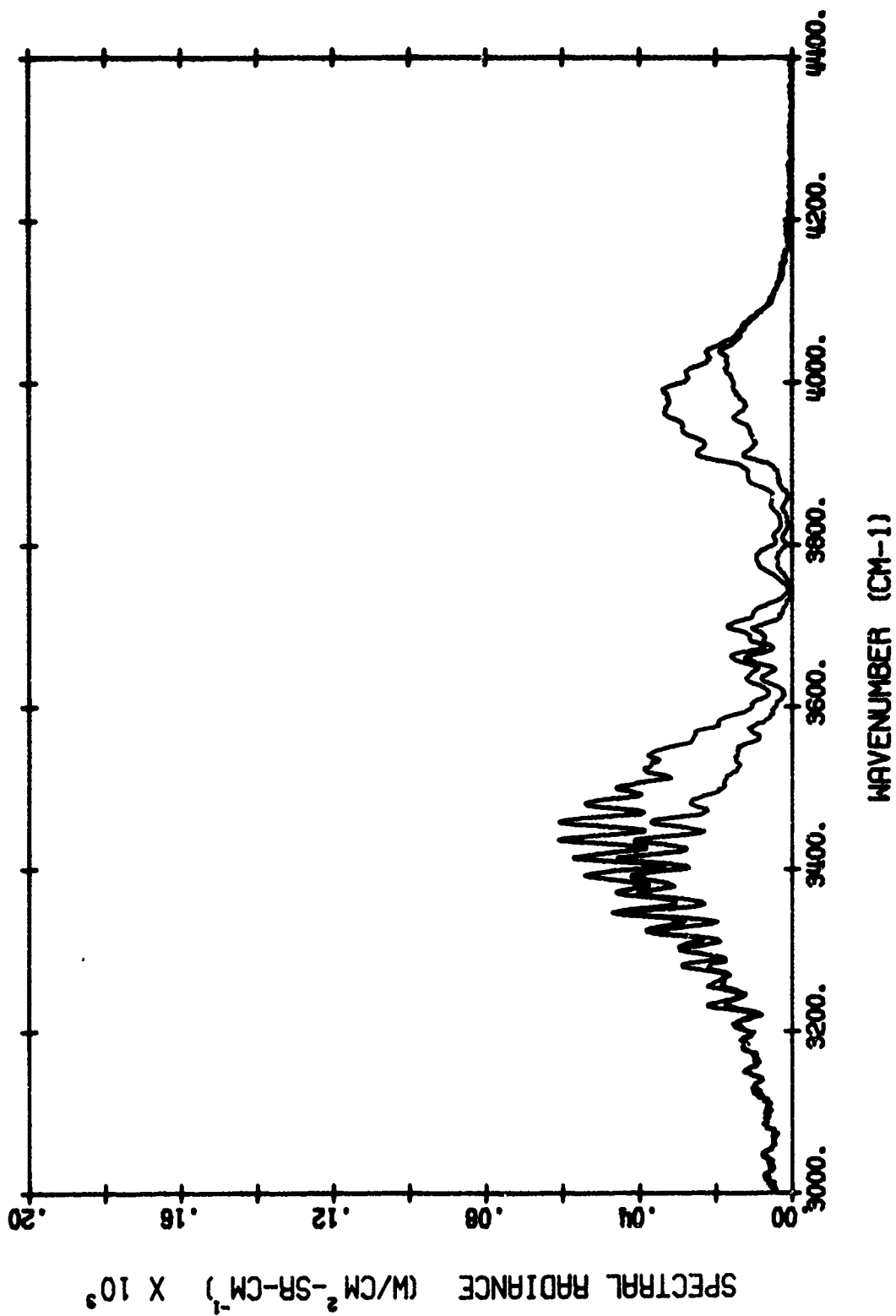


FIGURE B-9(c). MEASURED HOT THROUGH COLD RADIANCE (LOWER) AND PRODUCT OF HOT CELL RADIANCE AND COLD CELL TRANSMITTANCE (UPPER - Test 11MR

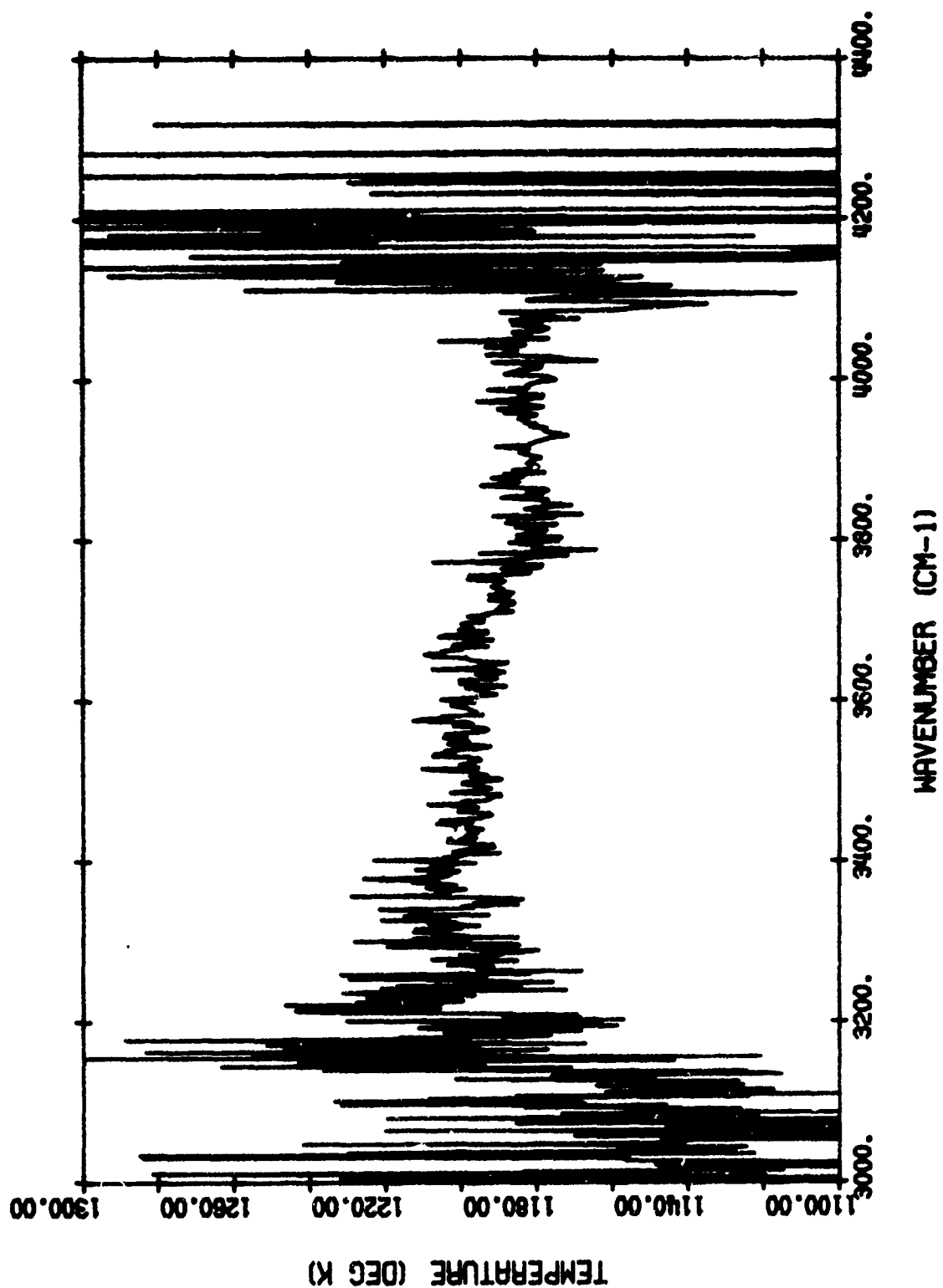
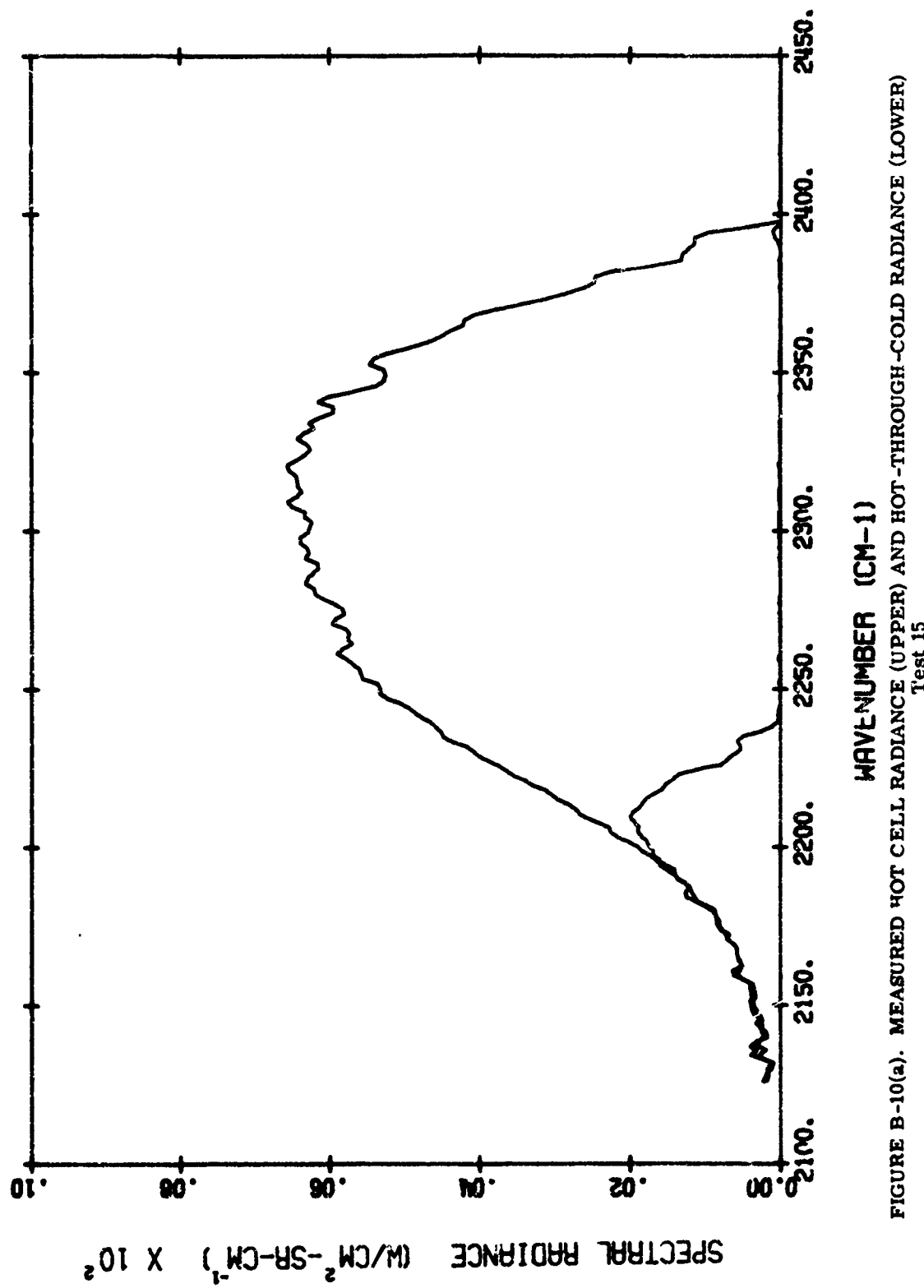


FIGURE B-9(d). MEASURED APPARENT TEMPERATURE - Test 11MR

TABLE B-10. TEST-15 PARAMETERS

Spectral Region	4.3 μ m	
Hot Cell	Simulated Amine Exhaust Mixture @ 16-km Altitude	
Total Absolute Pressure		76.0 mm
P_{H_2O}		35.26 mm
P_{CO_2}		7.58 mm
P_{CO}		1.44 mm
P_{H_2}		4.64 mm
P_{N_2}		27.09 mm
$L = 0.6$ m	$T = 1201^{\circ}\text{K}$	
Cold Cell	Simulated 200-km Path @ 15-km Altitude	
Total Absolute Pressure		98.0 mm
P_{H_2O}		8.64 mm
P_{CO_2}		88.63 mm
P_{N_2}		0.73 mm
$L = 100$ m	$T = 297^{\circ}\text{K}$	



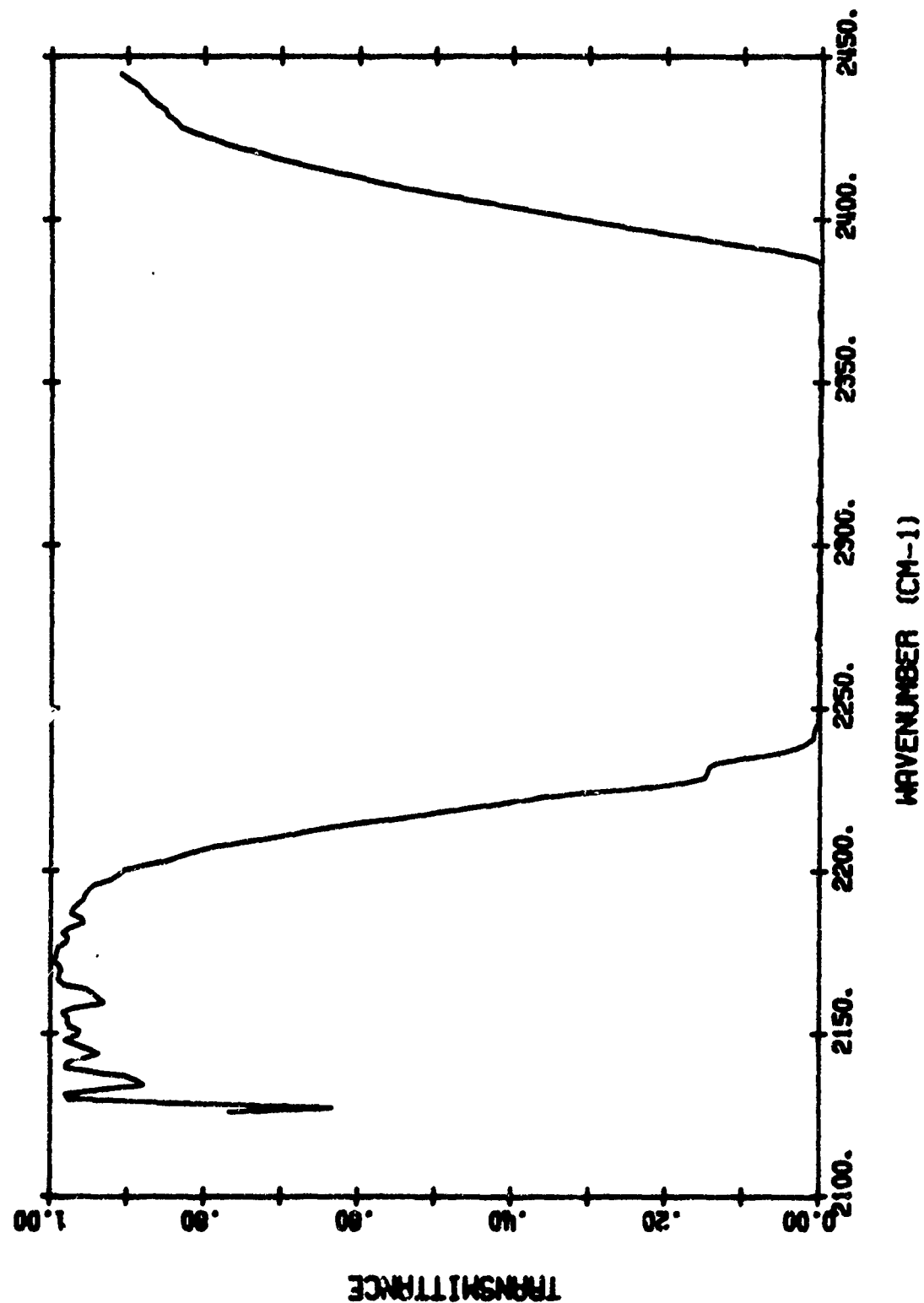


FIGURE B-10(b). MEASURED COLD CELL TRANSMITTANCE - Test 15

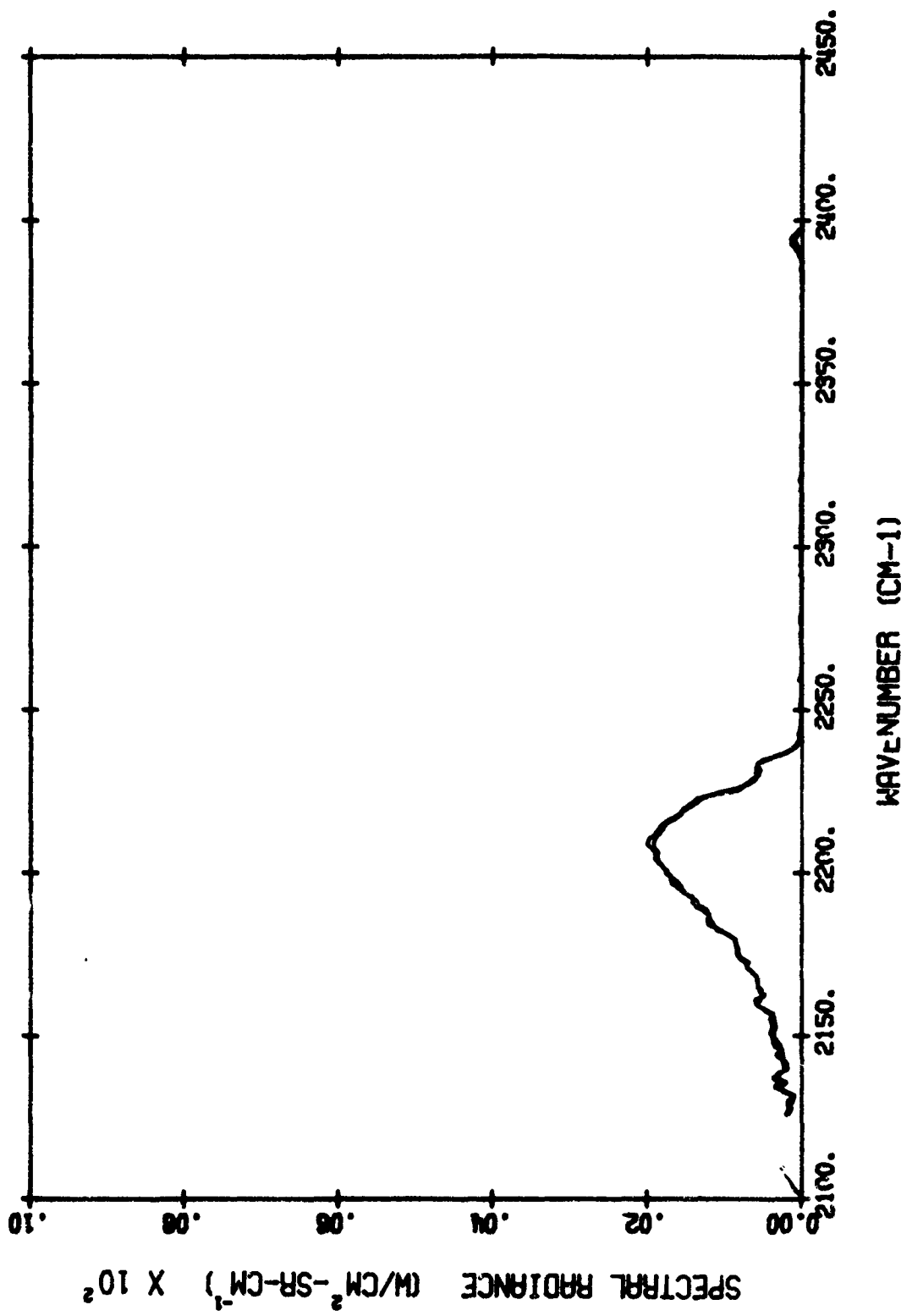


FIGURE B-10(c). MEASURED HOT THROUGH COLD RADIANCE (LOWER) AND PRODUCT OF HOT CELL RADIANCE AND COLD CELL TRANSMITTANCE (UPPER) - Test 15

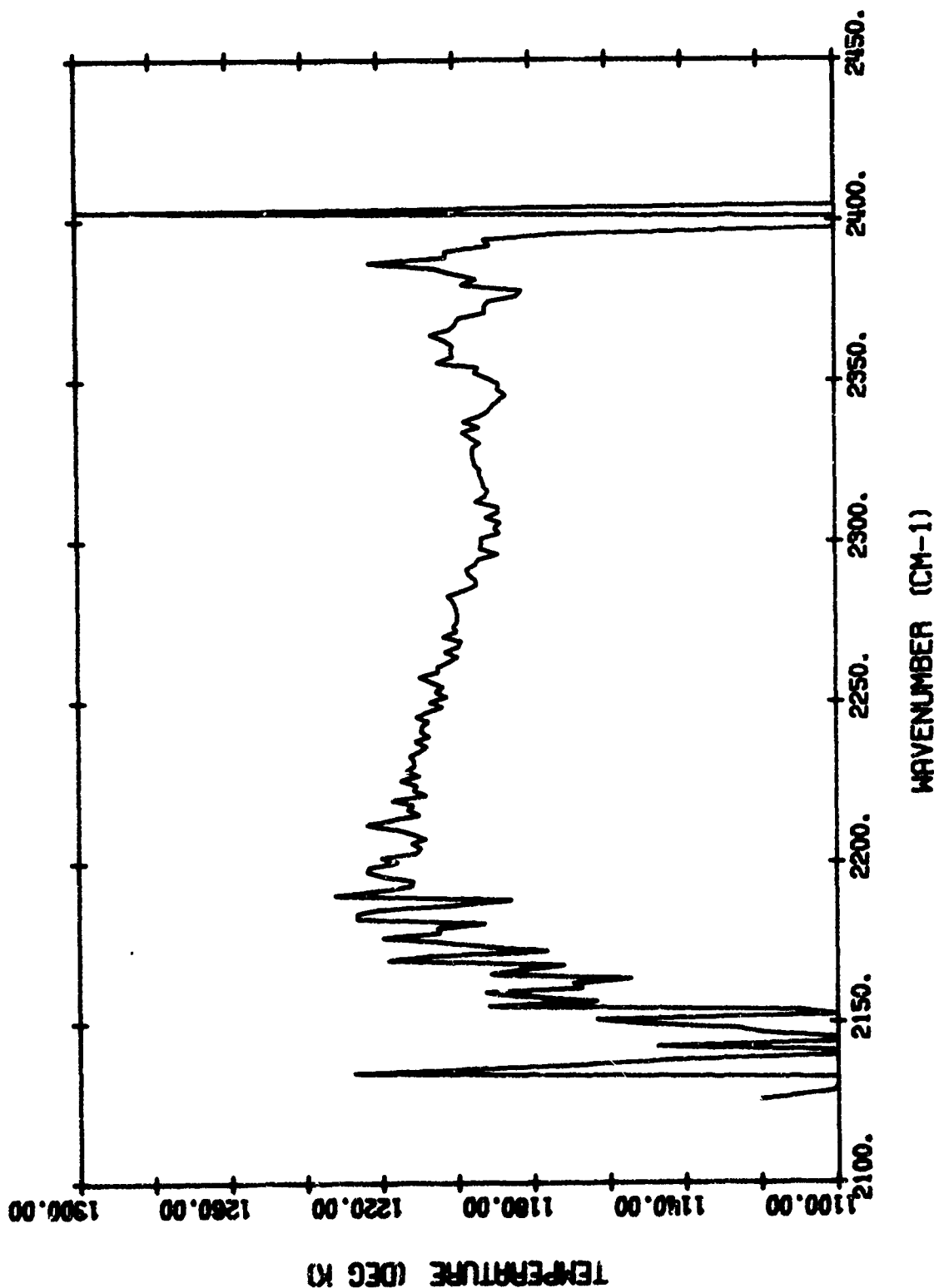
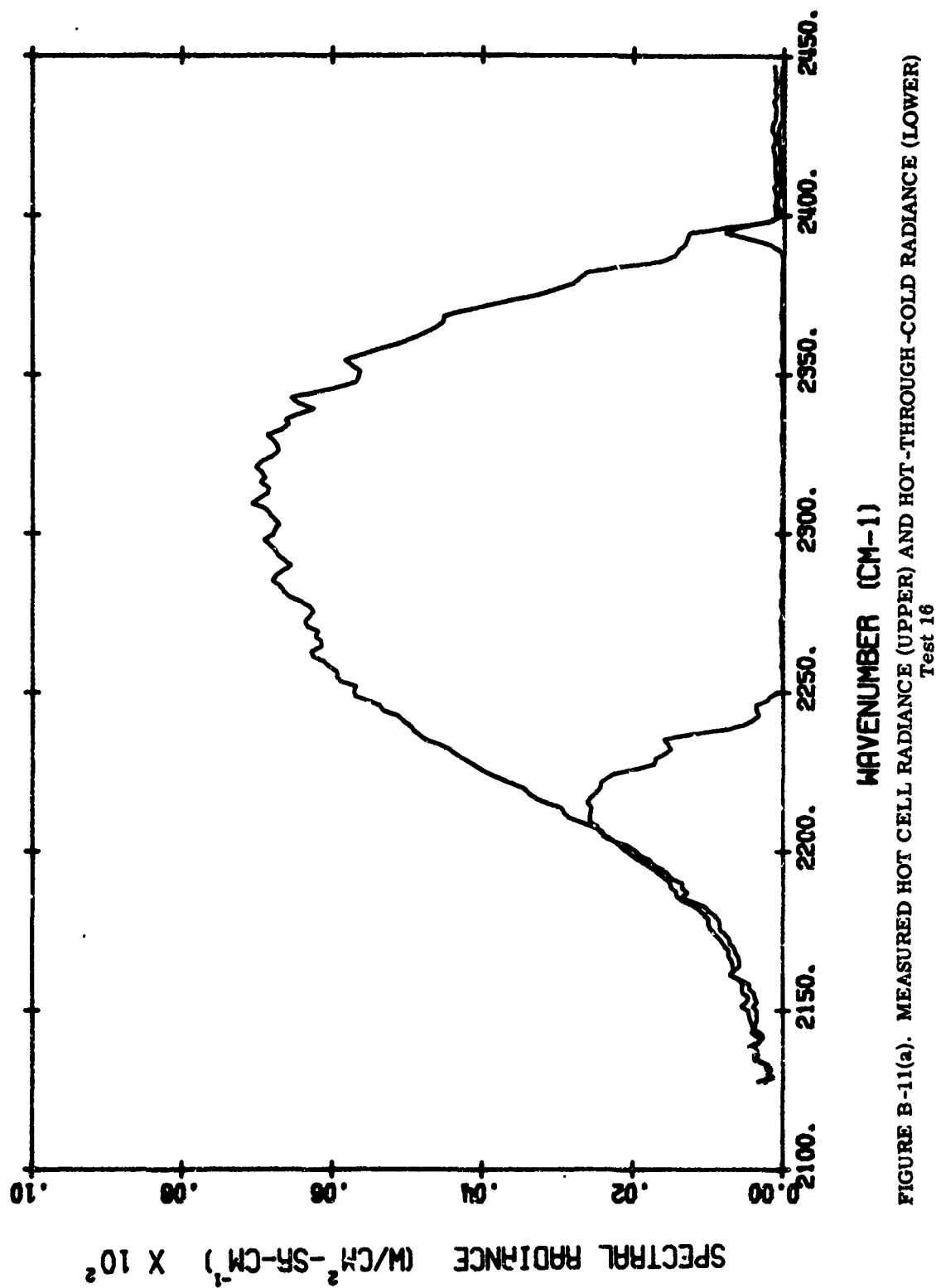


FIGURE B-10(d). MEASURED APPARENT TEMPERATURE - Test 15

TABLE B-11. TEST-16 PARAMETERS

Spectral Region		4.3 μm
Hot Cell	Simulated Amine Exhaust Mixture @ 16-km Altitude	
	Total Absolute Pressure	76.0 mm
	P_{H_2O}	35.26 mm
	P_{CO_2}	7.58 mm
	P_{CO}	1.47 mm
	P_{H_2}	4.64 mm
	P_{N_2}	27.06 mm
	$L = 0.6$ m	$T = 1200^{\circ}K$
Cold Cell	Simulated 50-km Path @ 15-km Altitude	
	Total Absolute Pressure	98.0 mm
	P_{H_2O}	2.17 mm
	P_{CO_2}	22.15 mm
	P_{N_2}	73.68 mm
	$L = 100$ m	$T = 298^{\circ}K$



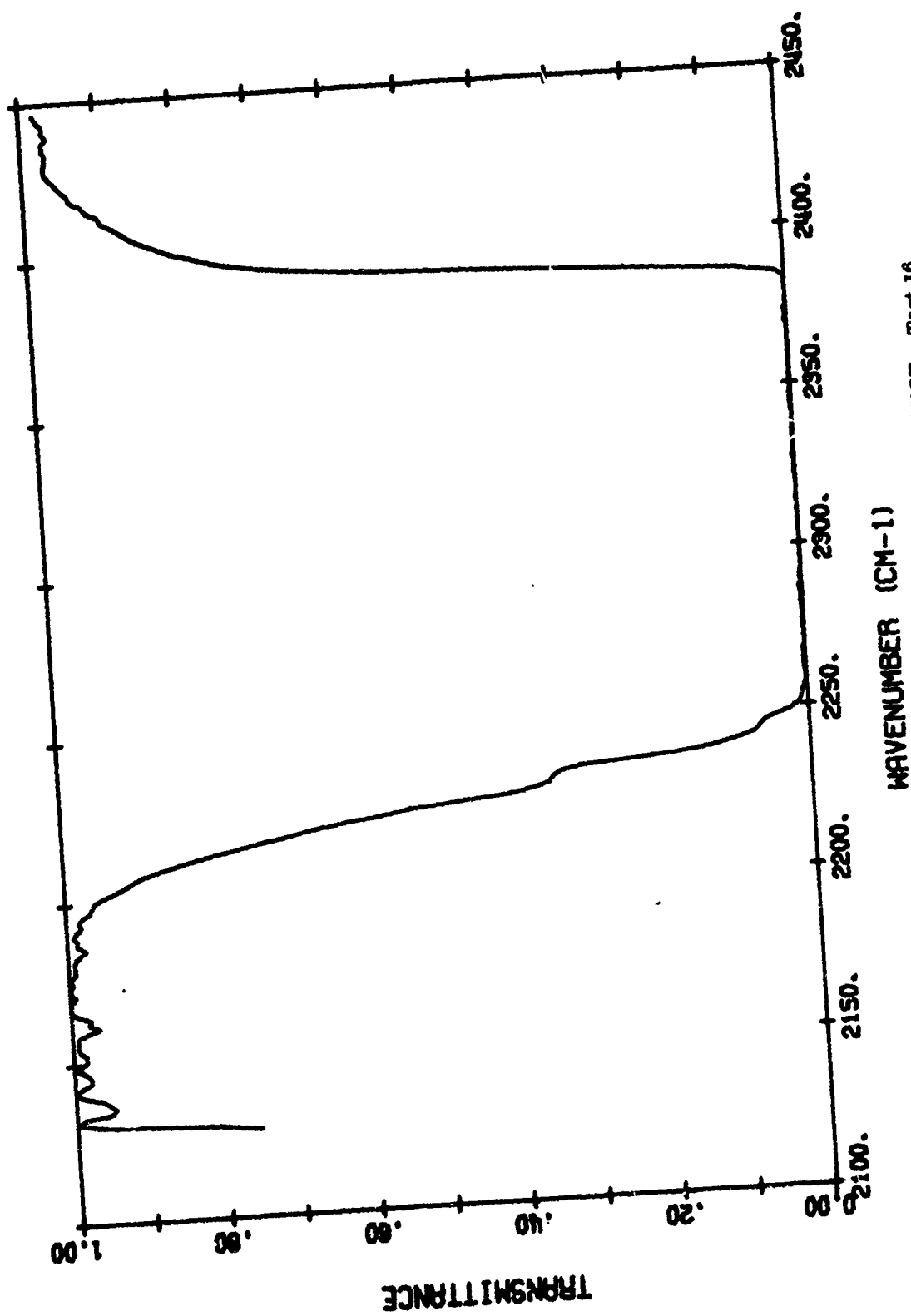


FIGURE B-11(b). MEASURED COLD CELL TRANSMITTANCE - Test 16

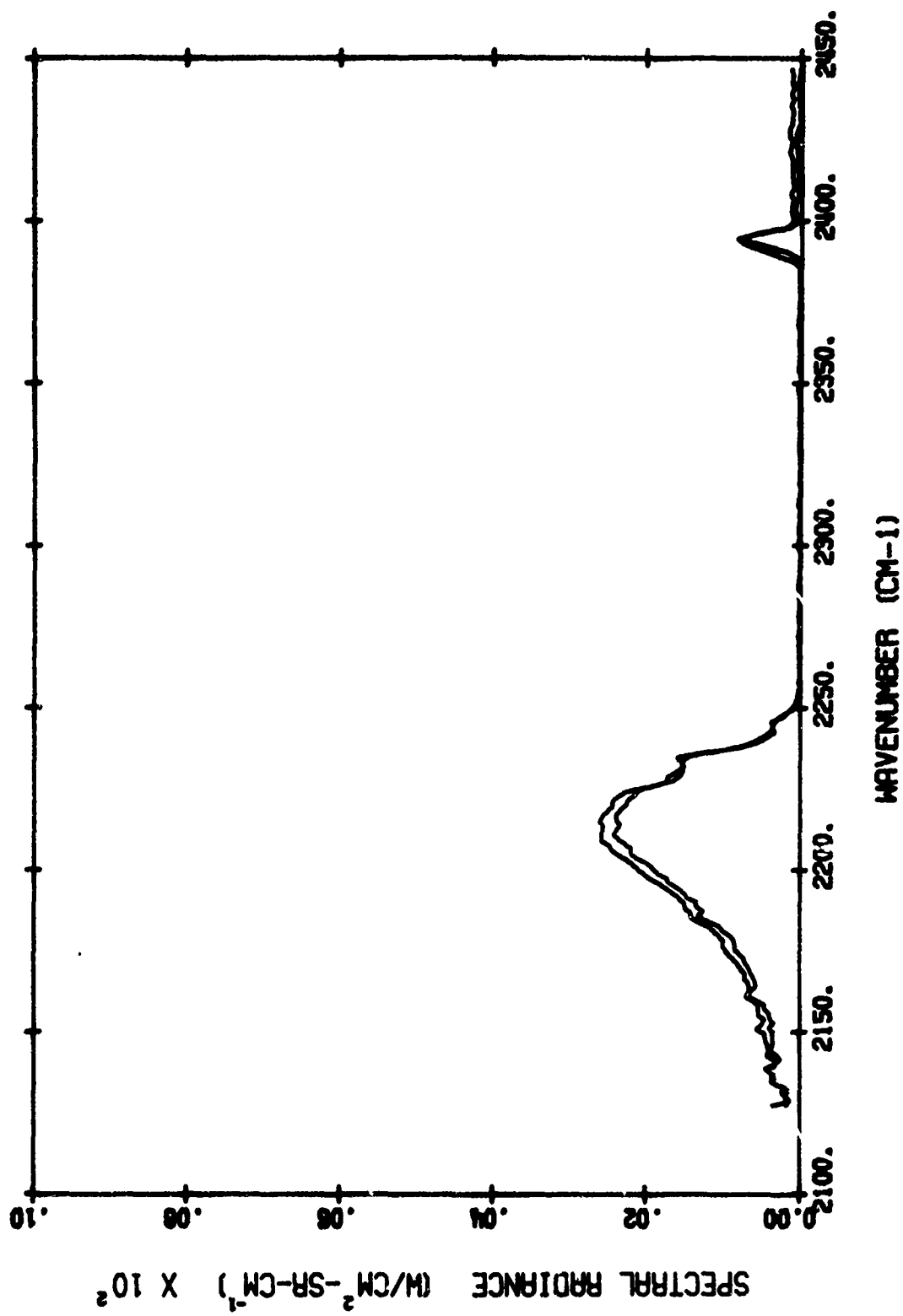


FIGURE B-11(c). MEASURED HOT THROUGH COLD RADIANCE (LOWER) AND PRODUCT OF HOT CELL RADIANCE AND COLD CELL TRANSMITTANCE (UPPER) - Test 16

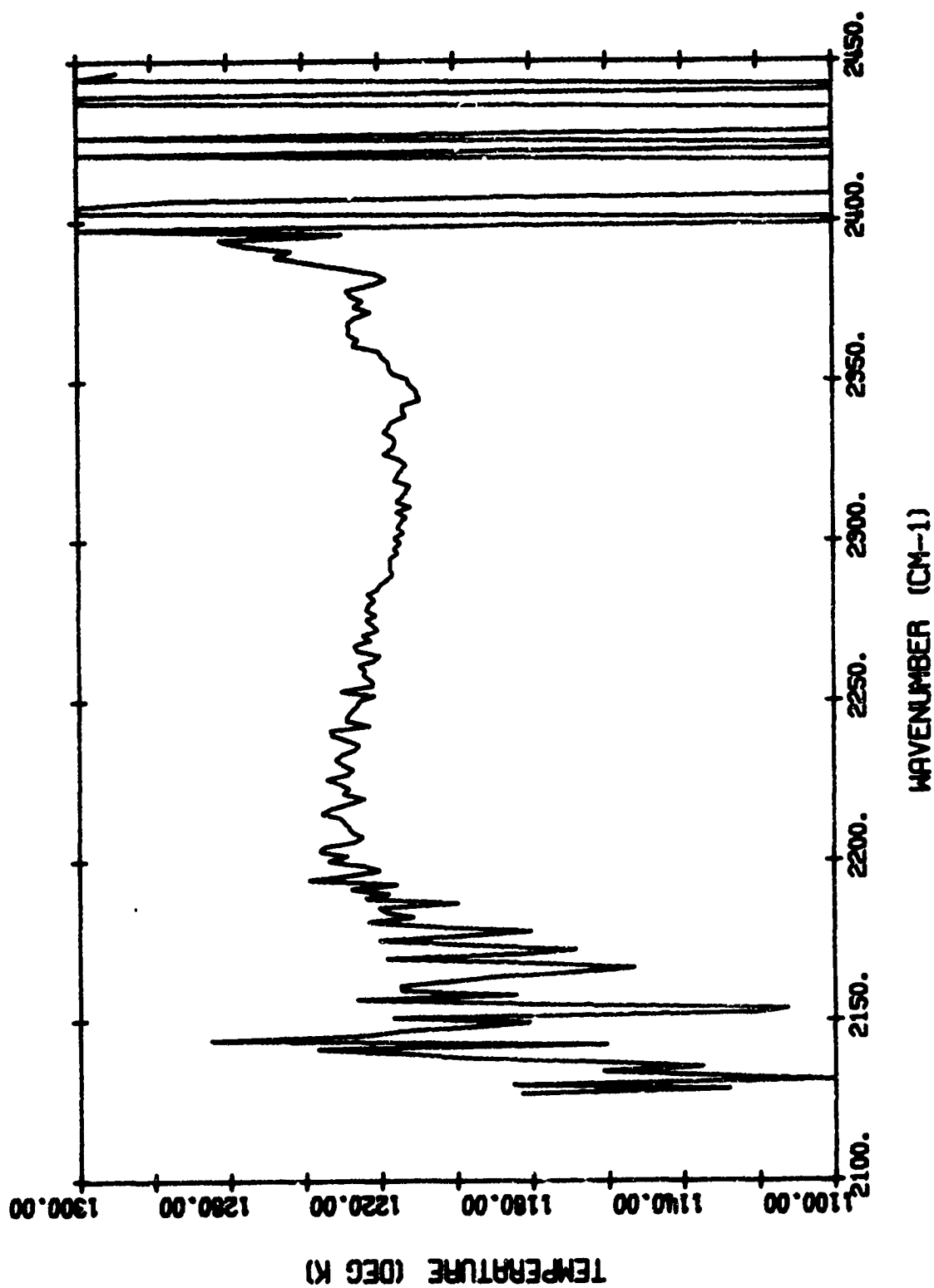


FIGURE B-11(d). MEASURED APPARENT TEMPERATURE - Test 16

TABLE B-12. TEST-17 PARAMETERS

Spectral Region	4.3 μ m	
Hot Cell	Simulated Amine Exhaust Mixture @ 16-km Altitude	
Total Absolute Pressure		76.0 mm
P_{H_2O}		35.26 mm
P_{CO_2}		7.59 mm
P_{CO}		1.47 mm
P_{H_2}		4.67 mm
P_{N_2}		27.21 mm
$L = 0.6$ mm		$T = 1202^0K$
Cold Cell	Simulated 10-km Path @ 15-km Altitude	
Total Absolute Pressure		98.0 mm
P_{H_2O}		0.43 mm
P_{CO_2}		4.43 mm
P_{N_2}		93.14 mm
$L = 100$ m		$T = 296^0K$

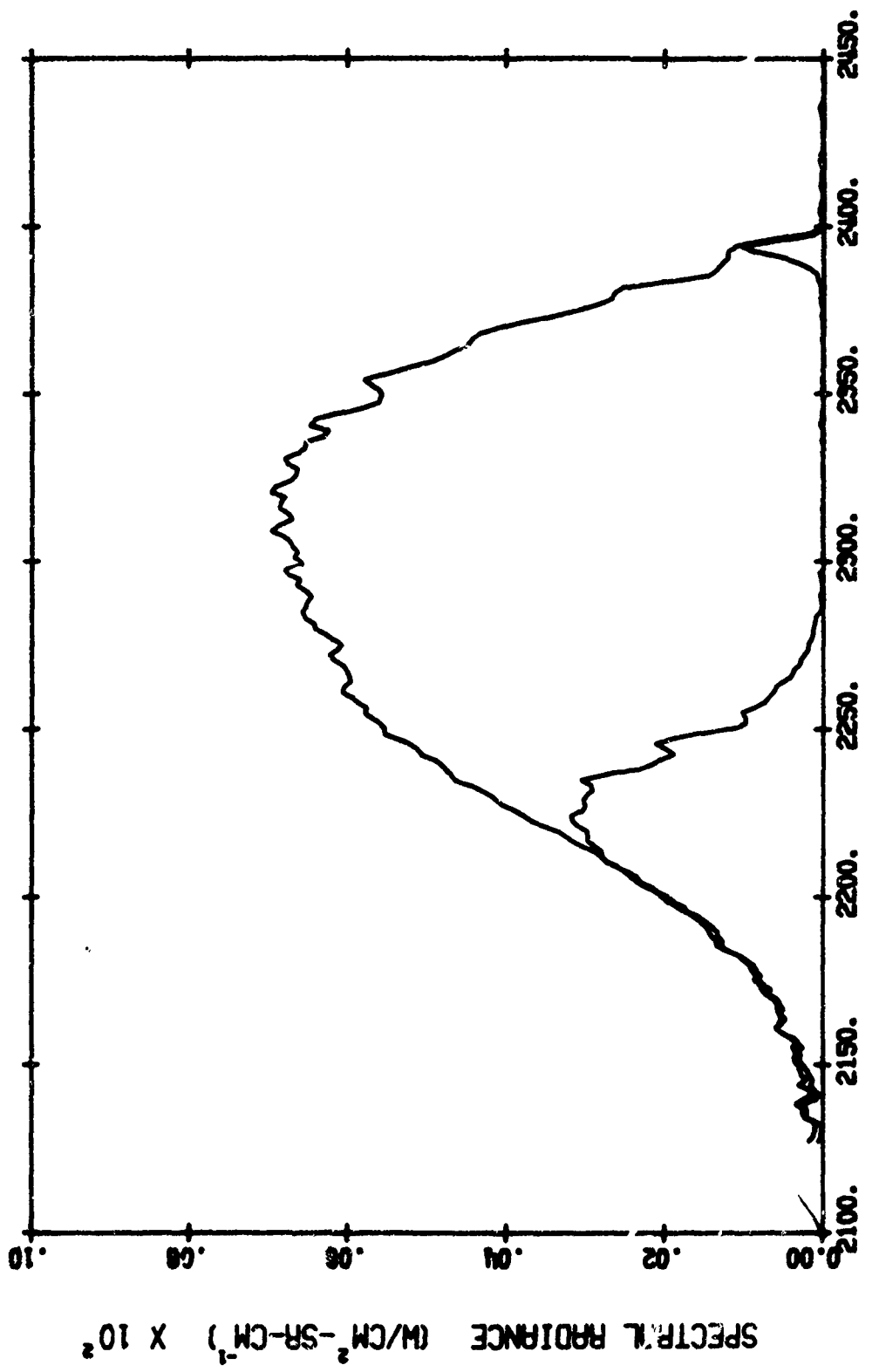


FIGURE B-12(a). MEASURED HOT CELL RADIANCE (UPPER) AND HOT-THROUGH-COLD RADIANCE (LOWER)
Test 17

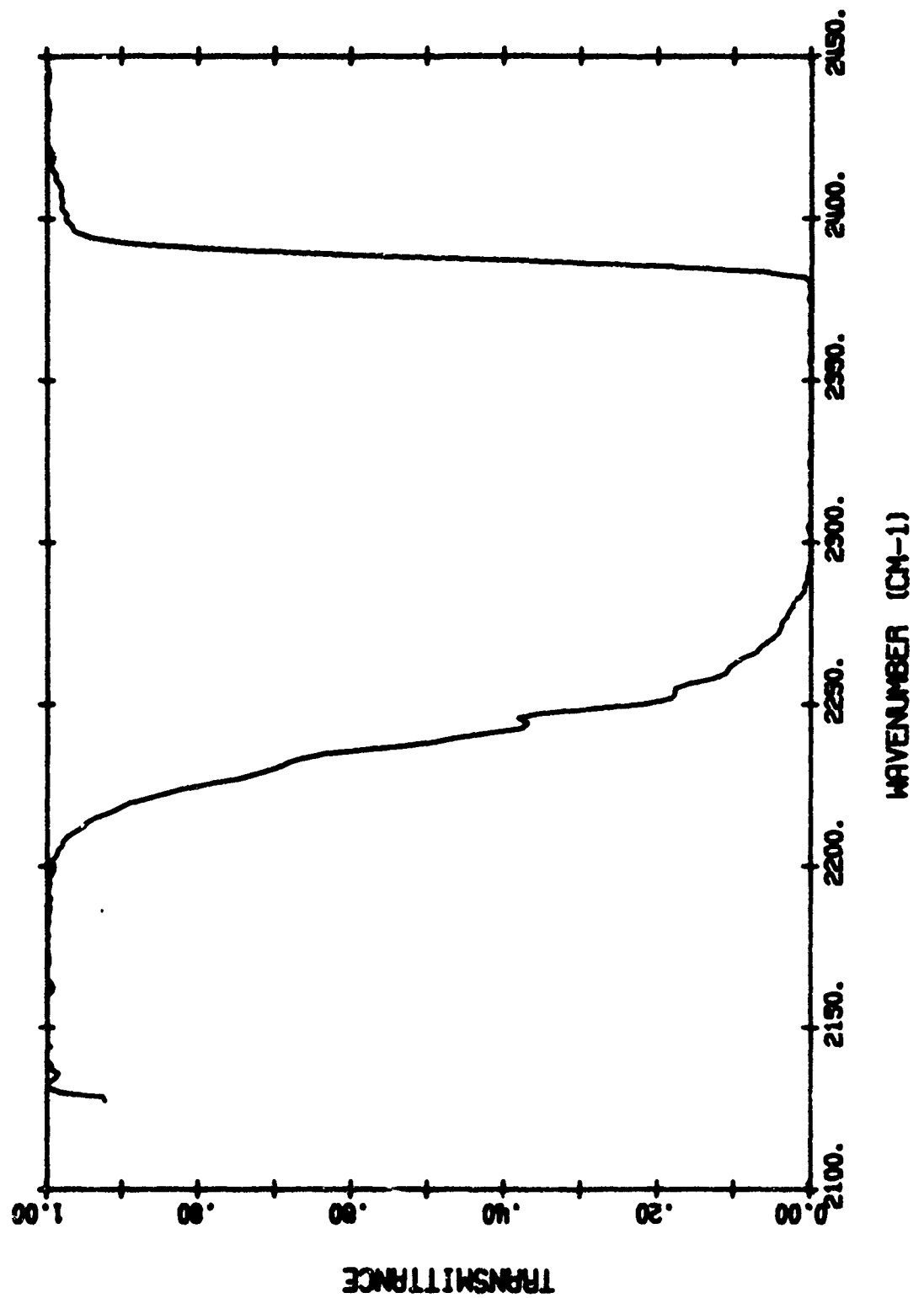


FIGURE B-12(b). MEASURED COLD CELL TRANSMITTANCE - Test 17

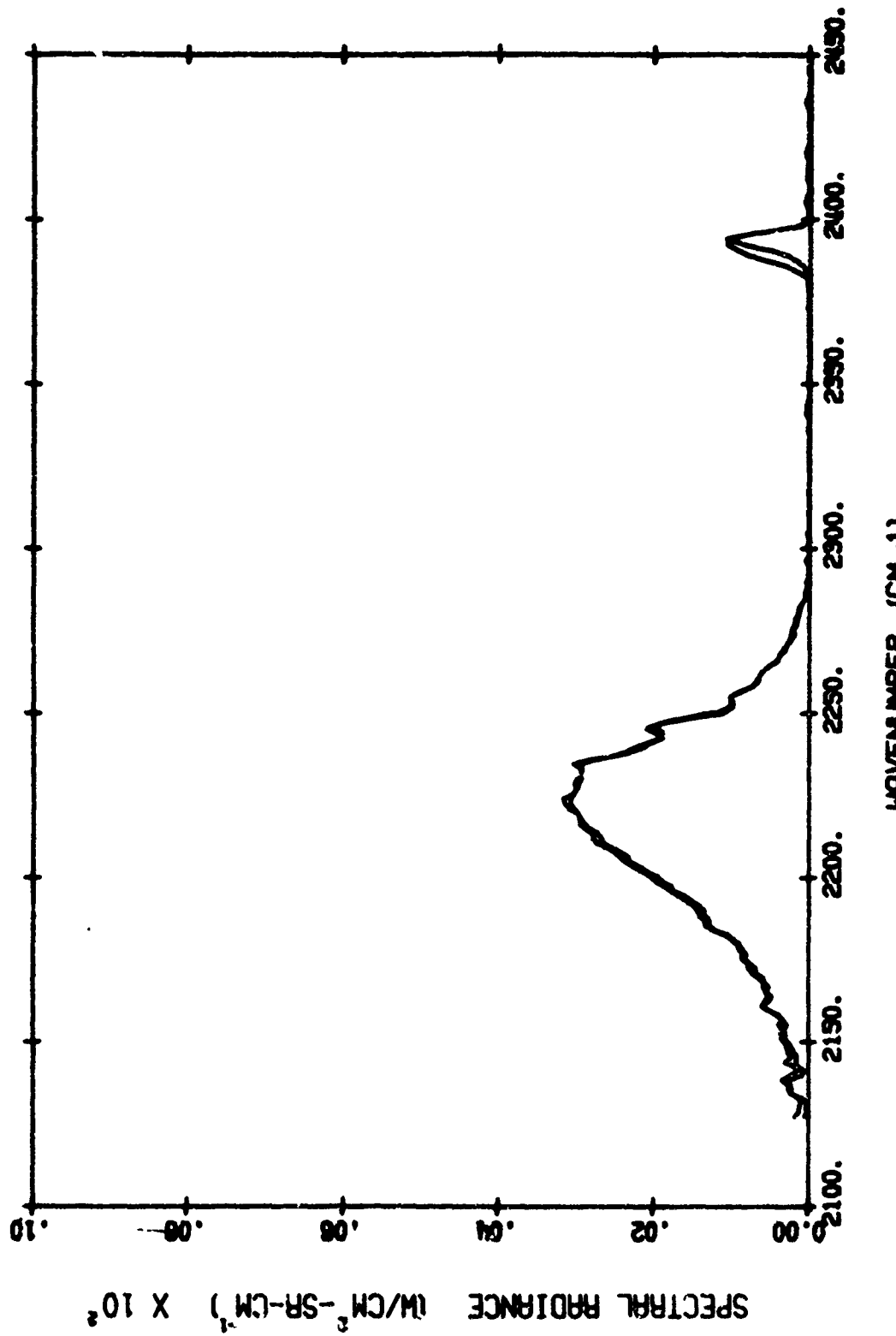


FIGURE B-12(c). MEASURED HOT THROUGH COLD RADIANCE (LOWER) AND PRODUCT OF HOT CELL RADIANCE AND COLD CELL TRANSMITTANCE (UPPER) - Test 17

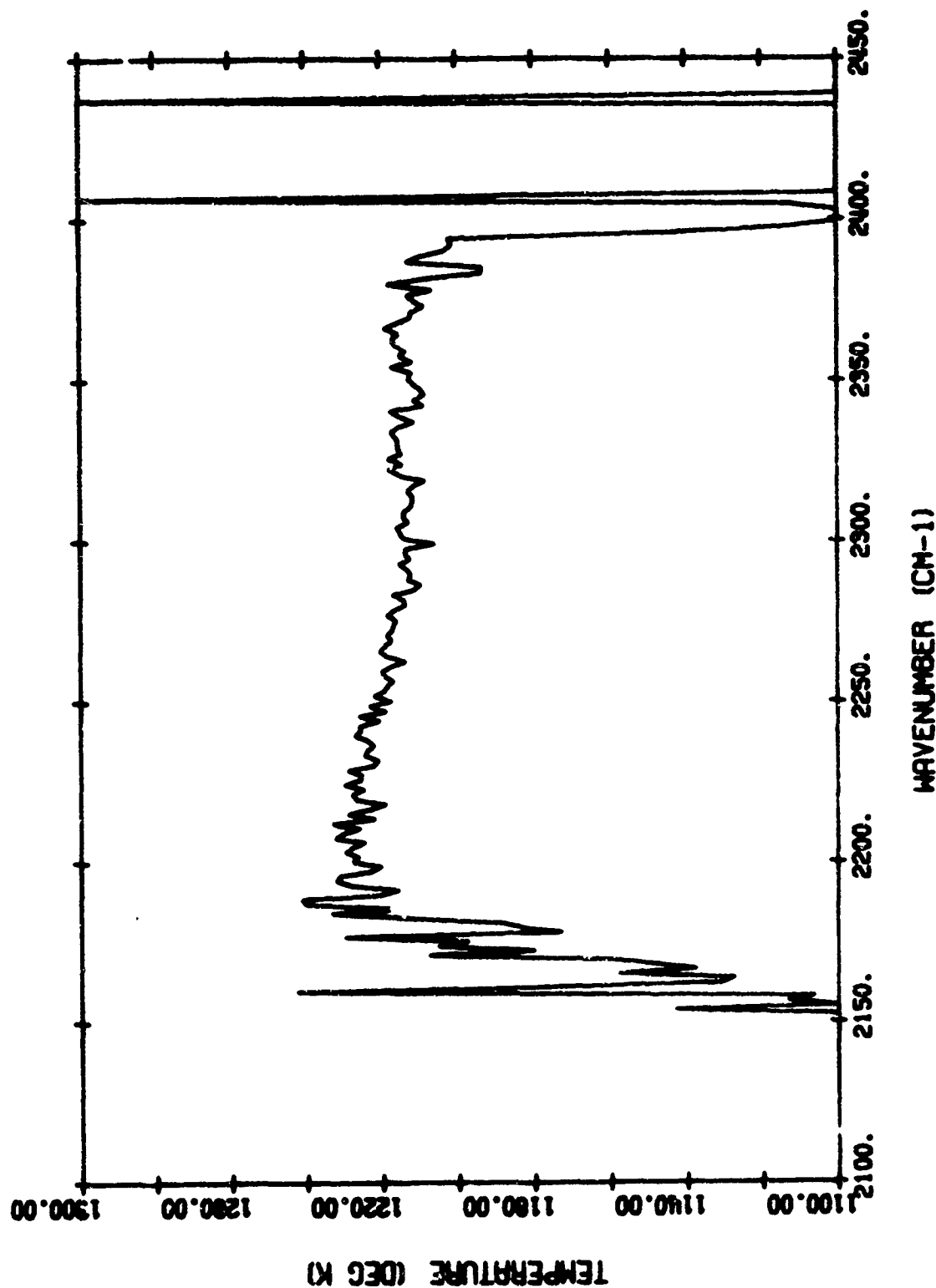


FIGURE B-12(d). MEASURED APPARENT TEMPERATURE - Test 17

TABLE B-13. TEST-18 PARAMETERS

Spectral Region	2.7 μ m	
Hot Cell	Simulated Amine Exhaust Mixture @ 16-km Altitude	
	Total Absolute Pressure	76.0 mm
	P_{H_2O}	35.26 mm
	P_{CO_2}	7.58 mm
	P_{CO}	1.47 mm
	P_{H_2}	4.62 mm
	P_{N_2}	27.06 mm
	$L = 0.6$ mm	$T = 1202^0K$
Cold Cell	Simulated 200-km Path @ 15-km Altitude	
	Total Absolute Pressure	98.0 mm
	P_{H_2O}	8.64 mm
	P_{CO_2}	88.63 mm
	P_{N_2}	0.73 mm
	$L = 100$ m	$T = 301^0K$

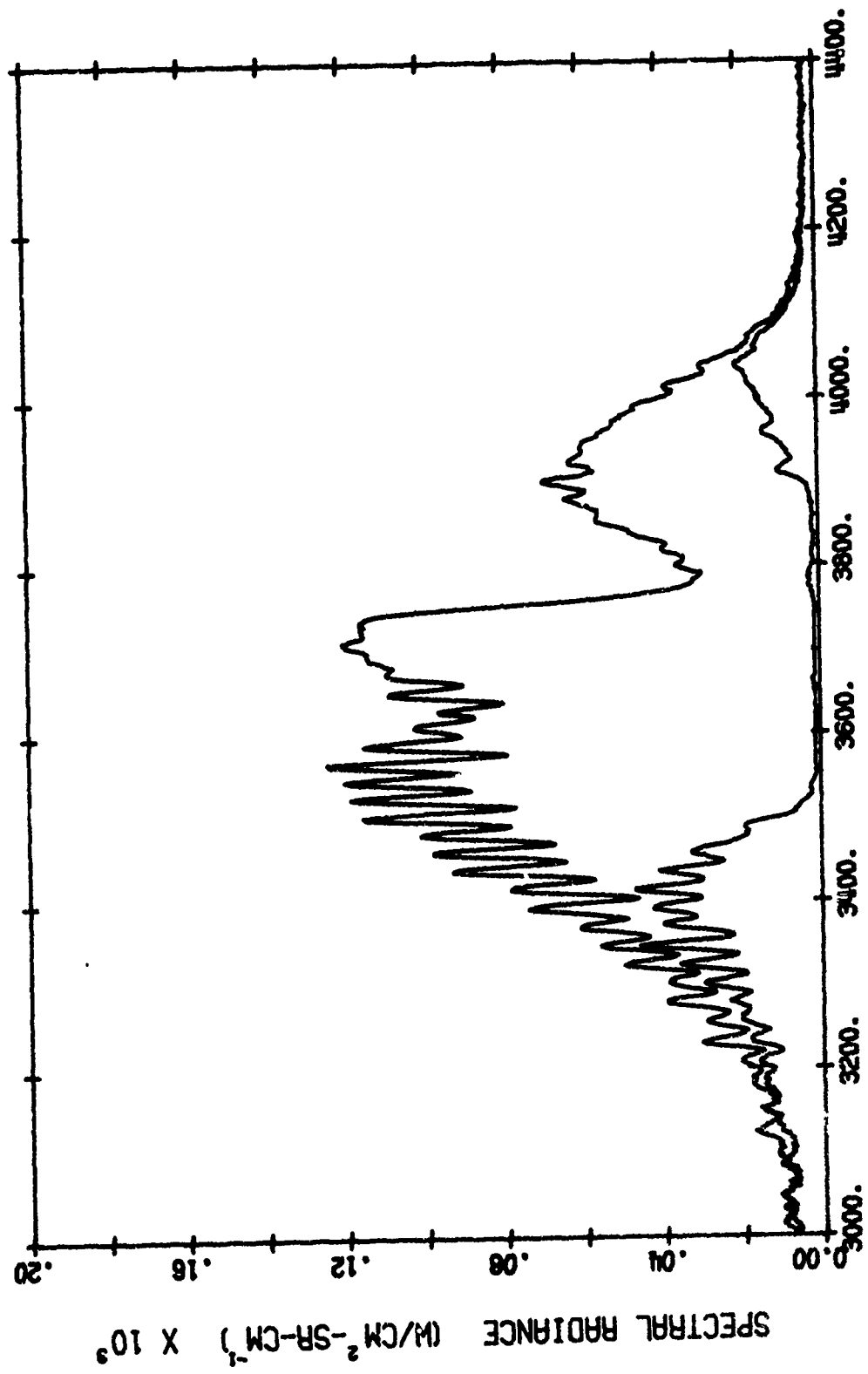


FIGURE B-13(a). MEASURED HOT CELL RADIANCE (UPPER) AND HOT-THROUGH-COLD RADIANCE (LOWER)
Test 18

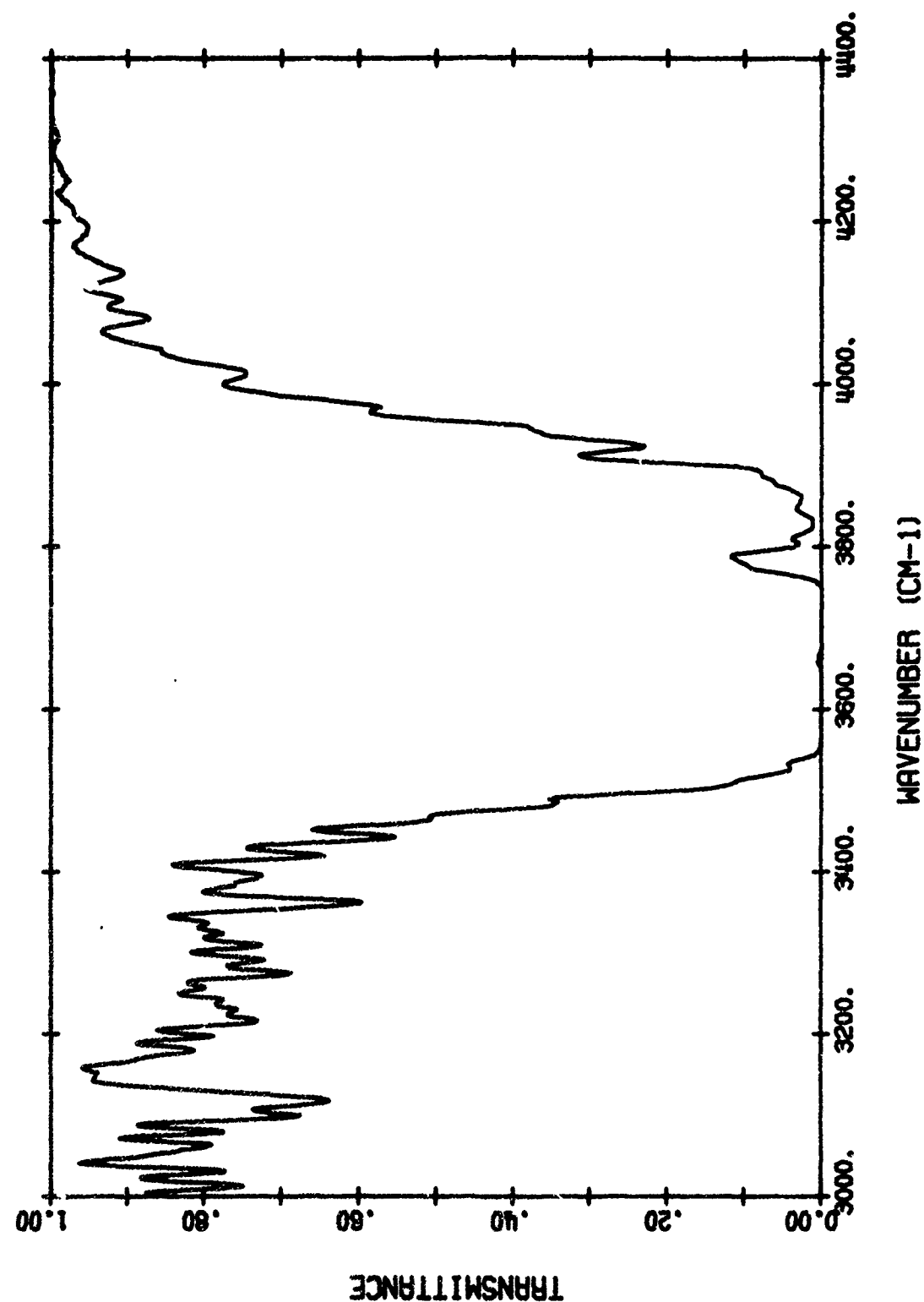


FIGURE B-13(b). MEASURED COLD CELL TRANSMITTANCE - Test 18

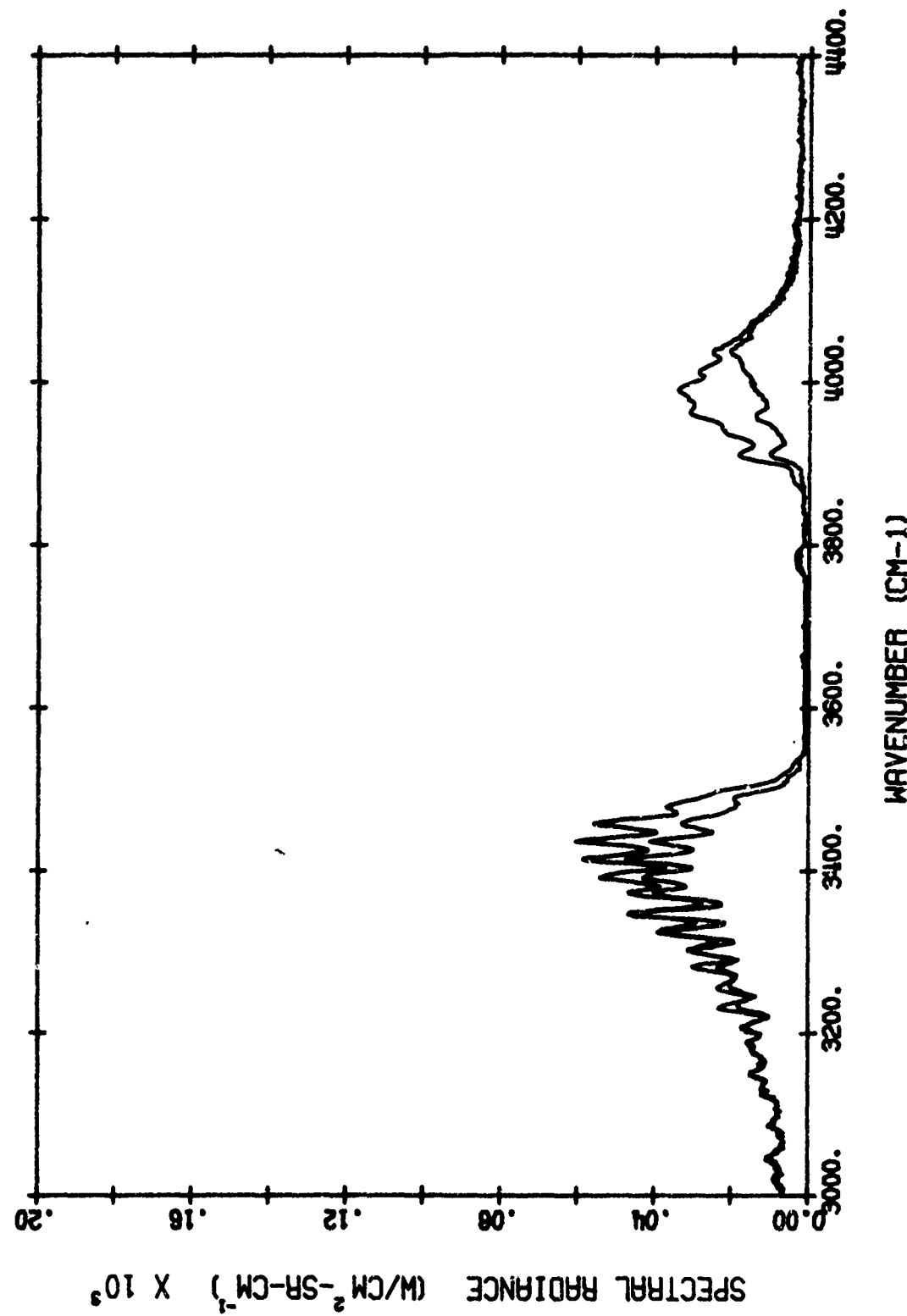


FIGURE B-13(c). MEASURED HOT THROUGH COLD RADIANCE (LOWER) AND PRODUCT OF HOT CELL RADIANCE AND COLD CELL TRANSMITTANCE (UPPER) - Test 18

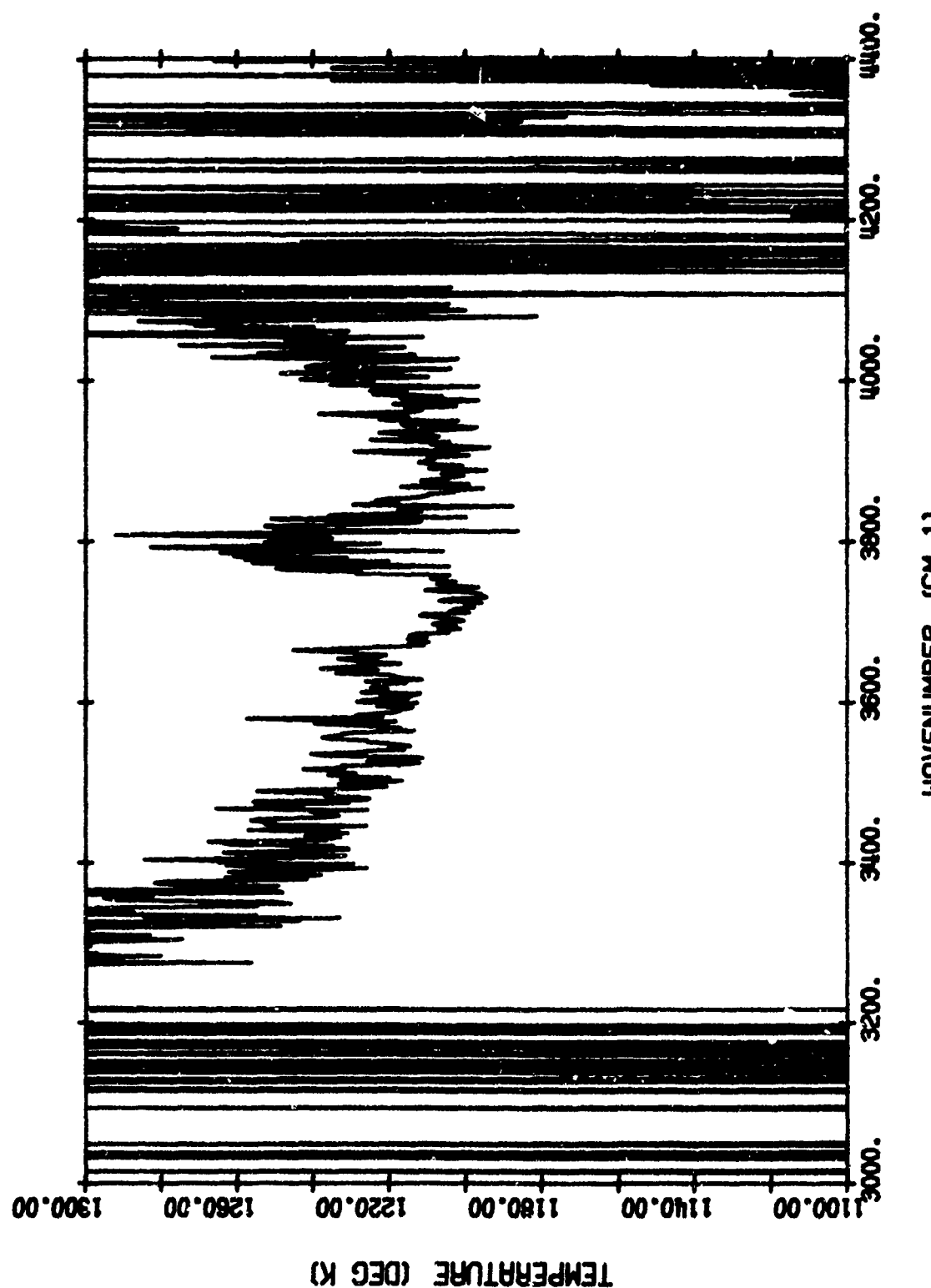


FIGURE B-13(d). MEASURED APPARENT TEMPERATURE - Test 18

TABLE B-14. TEST-19 PARAMETERS

Spectral Region	2.7 μ m	
Hot Cell	Simulated Amine Exhaust Mixture @ 16-km Altitude	
Total Absolute Pressure		76.0 mm
P_{H_2O}		35.26 mm
P_{CO_2}		7.58 mm
P_{CO}		1.47 mm
P_{H_2}		4.64 mm
P_{N_2}		27.06 mm
$L = 0.6$ m		$T = 1202^0K$
Cold Cell	Simulated 50-km Path @ 15-km Altitude	
Total Absolute Pressure		98.0 mm
P_{H_2O}		2.17 mm
P_{CO_2}		22.17 mm
P_{N_2}		73.65 mm
$L = 100$ m		$T = 301^0K$

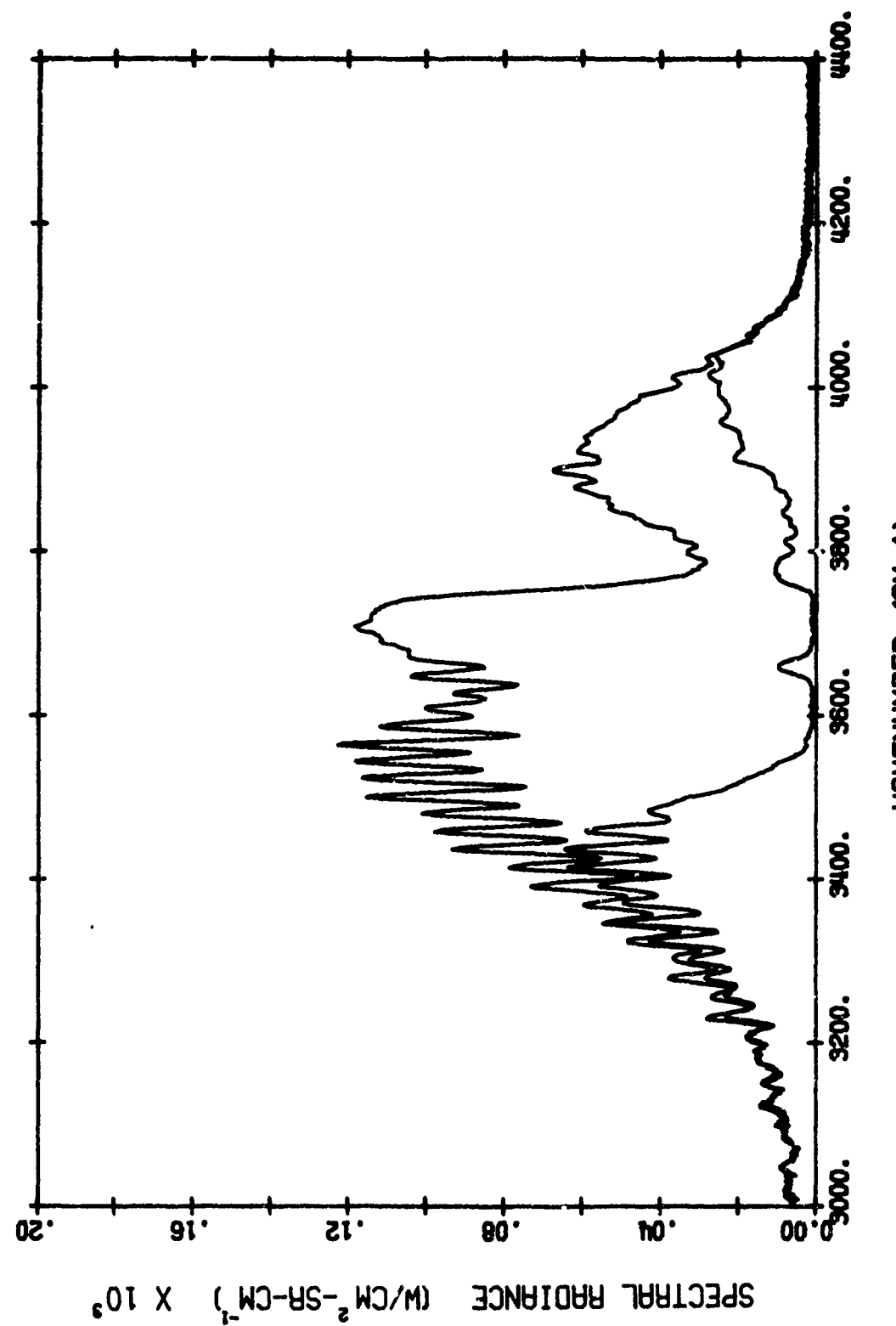


FIGURE B-14(a). MEASURED HOT CELL RADIANCE (UPPER) AND HOT-THROUGH-COLD RADIANCE (LOWER)
Test 19

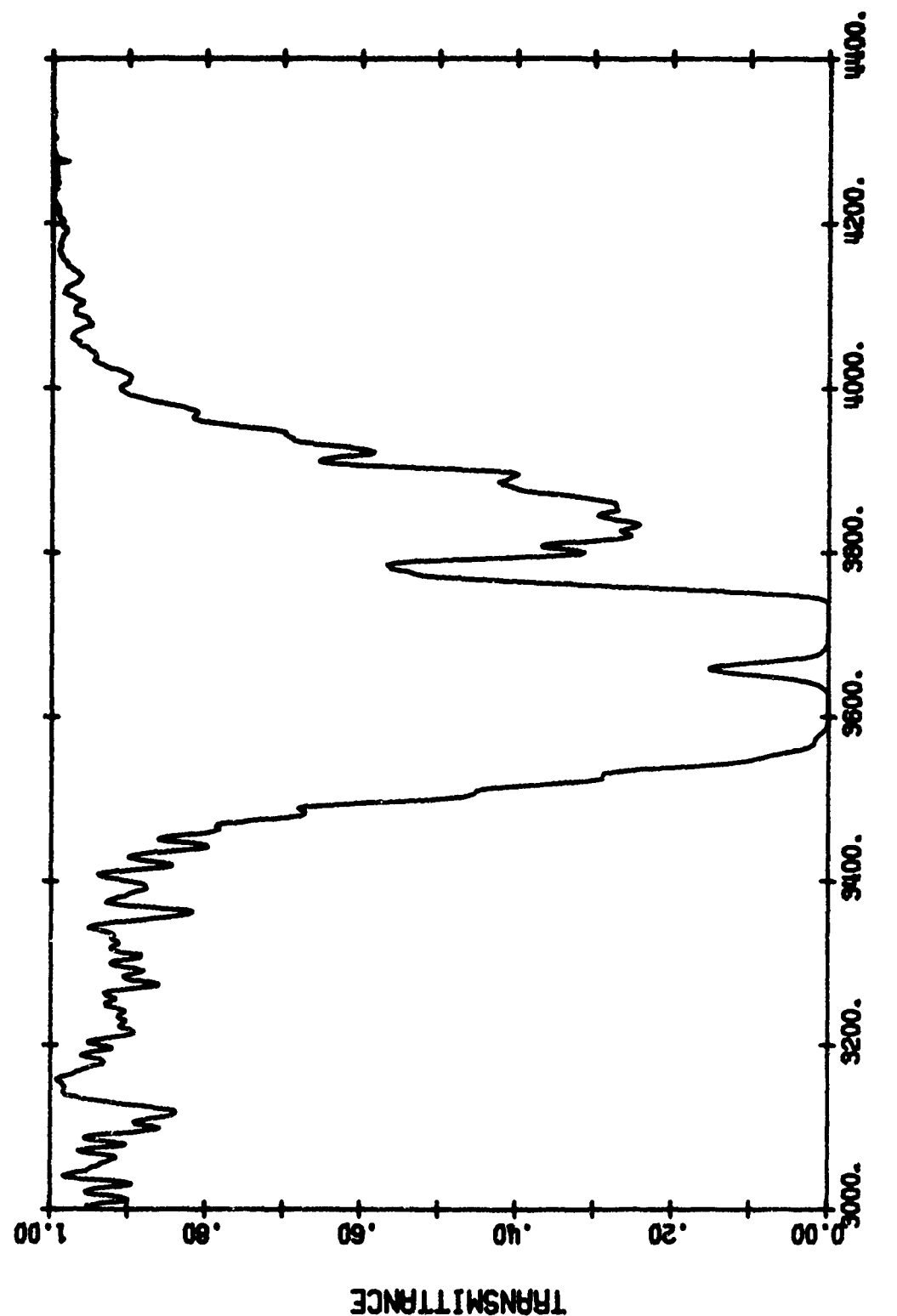


FIGURE B-14(b). MEASURED COLD CELL TRANSMITTANCE - Test 19

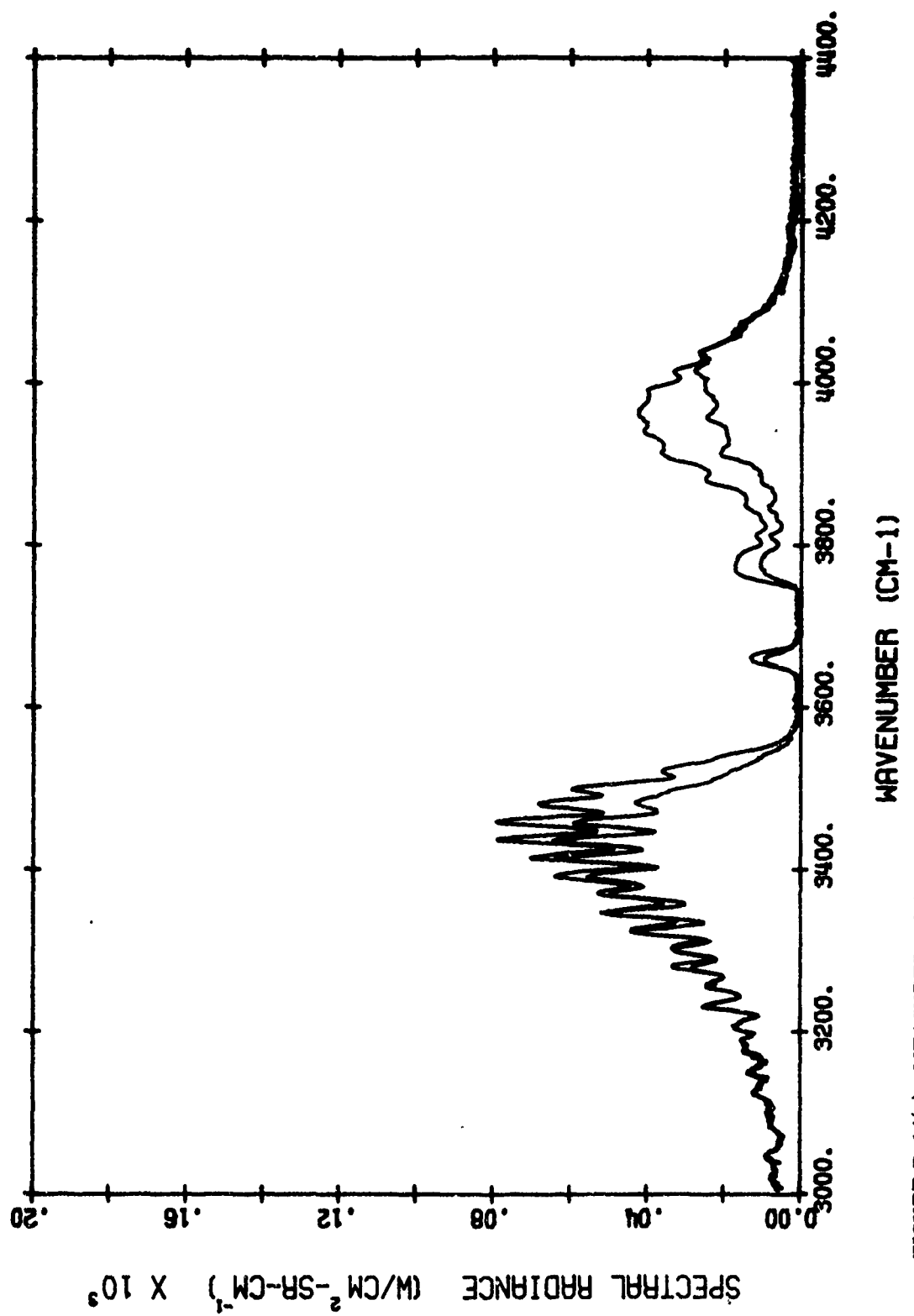


FIGURE B-14(c). MEASURED HOT THROUGH COLD RADIANCE (LOWER) AND PRODUCT OF HOT CELL RADIANCE AND COLD CELL TRANSMITTANCE (UPPER) - Test 19

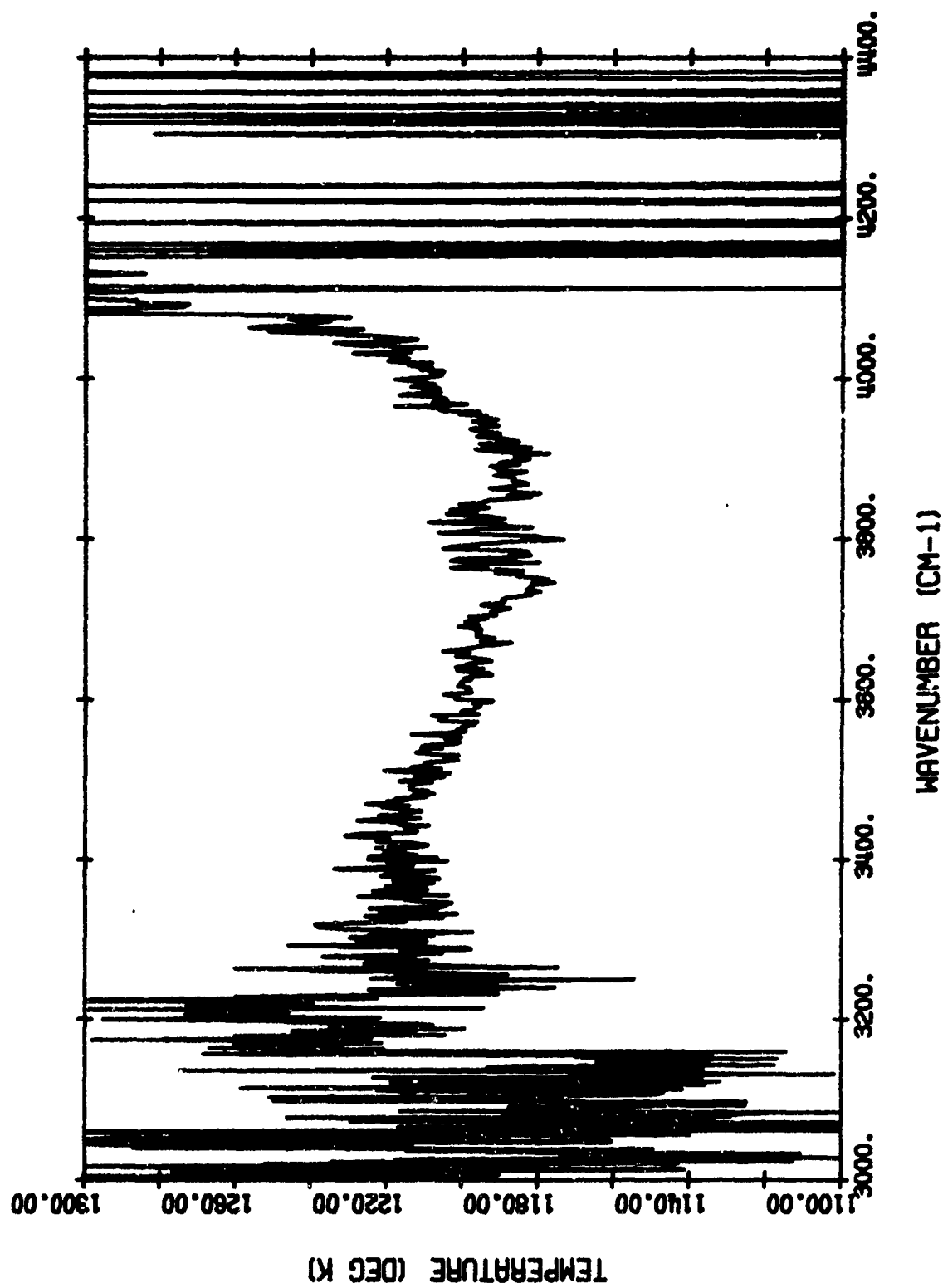


FIGURE B-14(d). MEASURED APPARENT TEMPERATURE - Test 19

WAVENUMBER (CM-1)

TABLE B-15. TEST-20 PARAMETERS

Spectral Region	2.7 μ m	
Hot Cell	Simulated Amine Exhaust Mixture @ 16-km Altitude	
Total Absolute Pressure	76.0	mm
P_{H_2O}	35.26	mm
P_{CO_2}	7.58	mm
P_{CO}	1.47	mm
P_{N_2}	27.06	mm
P_{H_2}	4.64	mm
$L = 0.6$ m	$T = 1202^{\circ}K$	
Cold Cell	Simulated 10-km Path @ 15-km Altitude	
Total Absolute Pressure	98.0	mm
P_{H_2O}	0.43	mm
P_{CO_2}	4.43	mm
P_{N_2}	93.14	mm
$L = 100$ m	$T = 297^{\circ}K$	

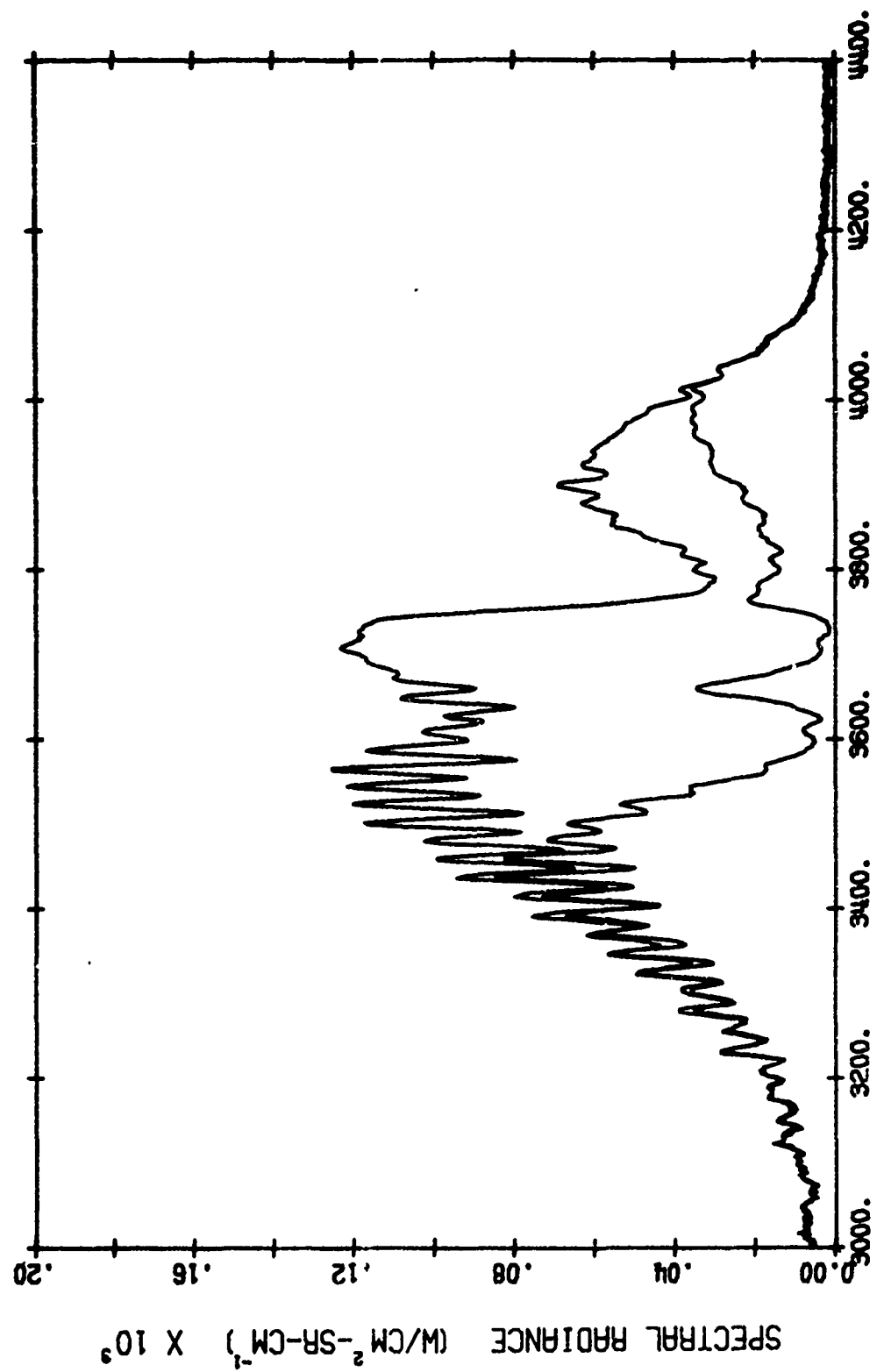


FIGURE B-15(a). MEASURED HOT CELL RADIANCE (UPPER) AND HOT-THROUGH-COLD RADIANCE (LOWER)
Test 20

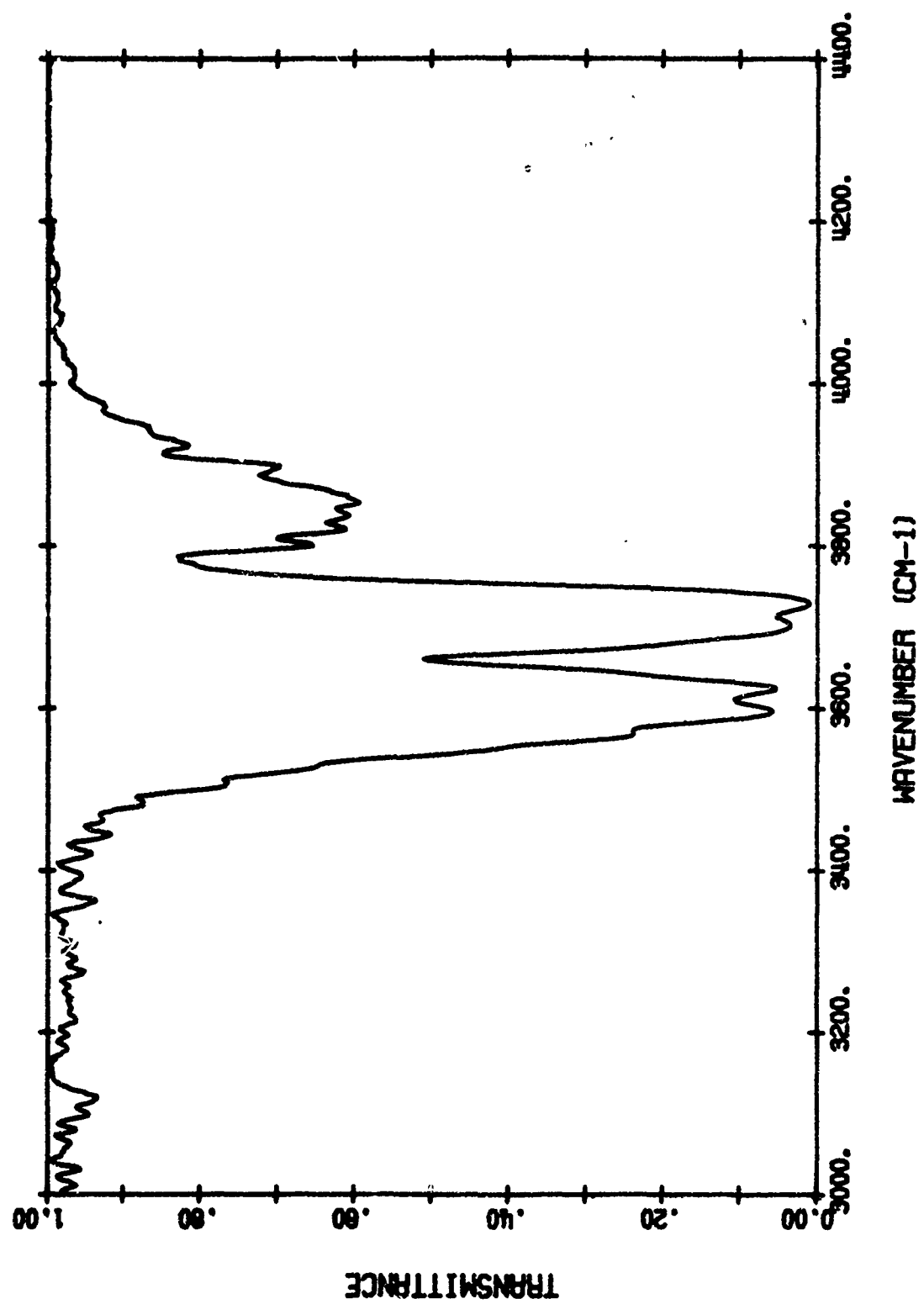


FIGURE B-15(b). MEASURED COLD CELL TRANSMITTANCE - Test 20

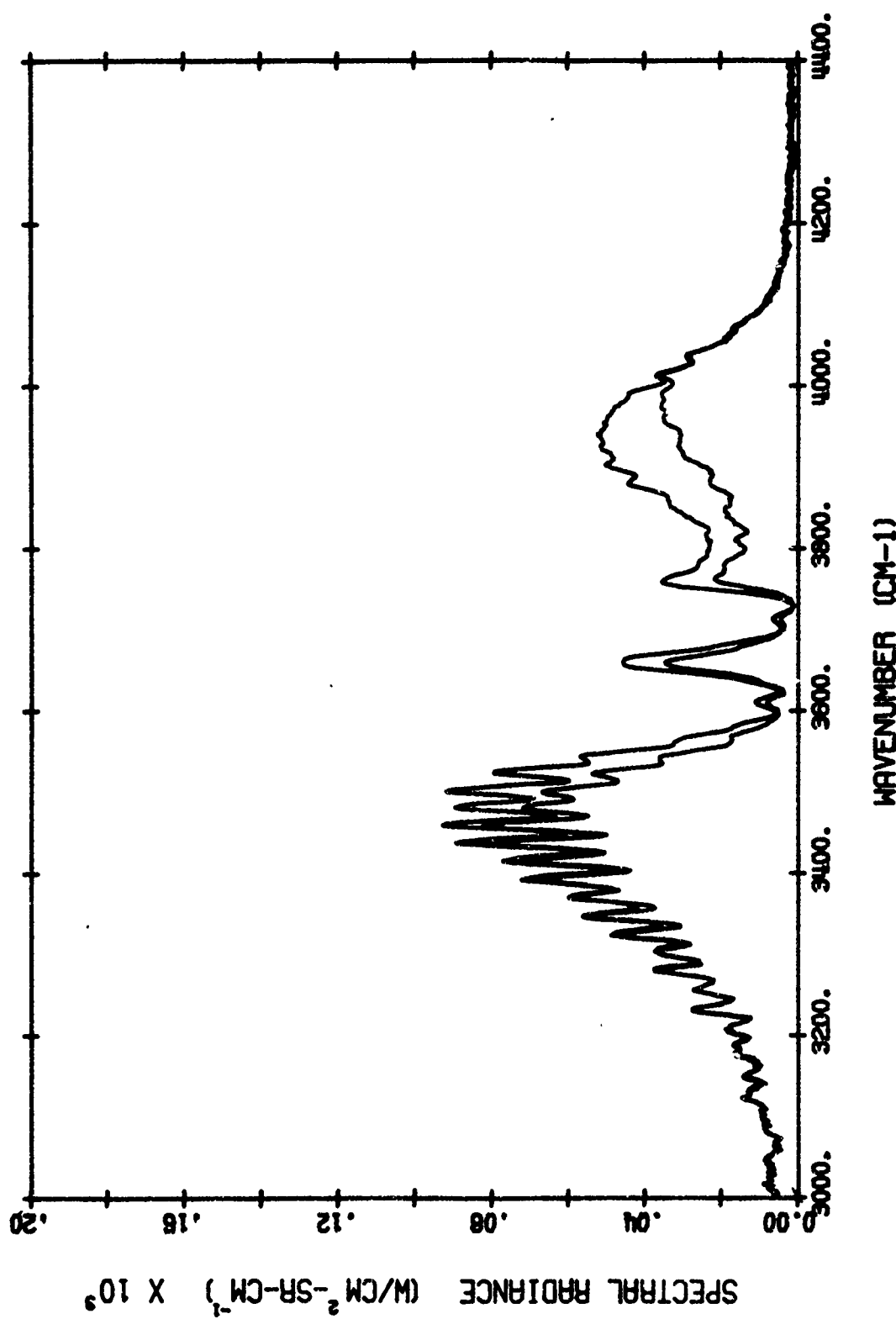


FIGURE B-15(c). MEASURED HOT THROUGH COLD RADIANCE (LOWER) AND PRODUCT OF HOT CELL RADIANCE AND COLD CELL TRANSMITTANCE (UPPER) - Test 20

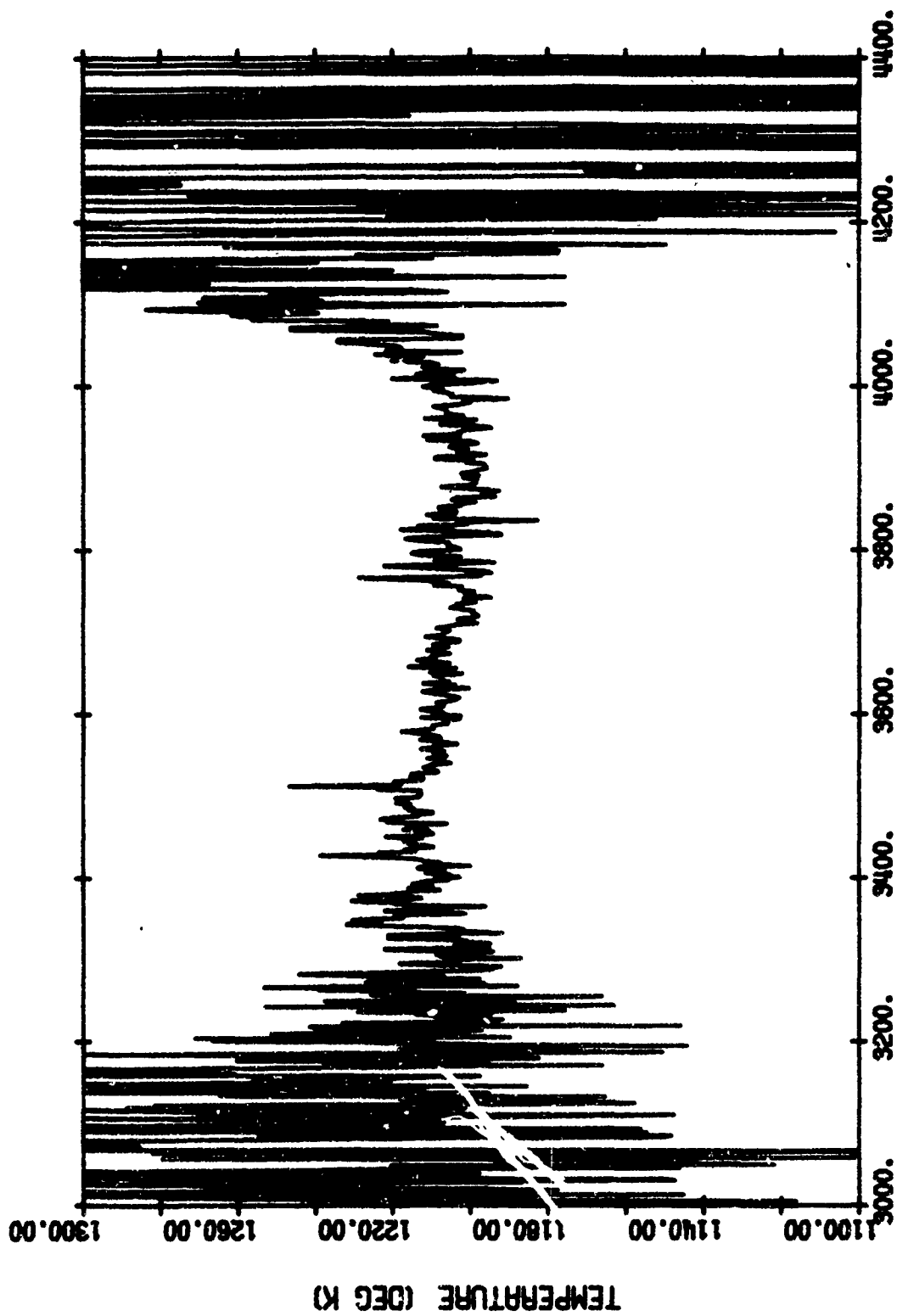


FIGURE B-15(d). MEASURED APPARENT TEMPERATURE - Test 20

WAVENUMBER (CM⁻¹)

REFERENCES

1. R. A. McClatchey, et al., AFCRL Atmospheric Absorption Line Parameters Compilation, AFCRL-TR-73-006, Air Force Cambridge Research Laboratories, Bedford, Massachusetts, January 1973.
2. R. M. Goody, Atmospheric Radiation I: Theoretical Basis, Clarendon Press, Oxford, England, 1964.
3. D. Anding, Band Model Methods for Computing Atmospheric Slant-Path Molecular Absorption, Report No. 7142-21-T, Willow Run Laboratories, Ann Arbor, Michigan, February 1967.
4. S. S. Penner, Quantitative Molecular Spectroscopy and Gas Emissivities, Addison-Wesley, Reading, Massachusetts, 1959.
5. C. B. Ludwig, et al., Handbook of Infrared Radiation from Combustion Gases, NASA-SP-3080, Scientific and Technical Information Office, NASA, Washington, District of Columbia, 1973.
6. D. E. Burch and D. A. Gryvnak, Infrared Radiation Emitted by Hot Gases and Its Transmission through Synthetic Atmospheres, Report No. U-1929, Research Laboratory, Aerotontronic Division, Ford Motor Company, Newport Beach, California, October 1962.
7. F. S. Simmons, et al., "Calculation of Radiation from Hot H_2O and CO_2 Viewed Through a Cool Intervening Atmosphere," Applied Optics, Vol. 9, p. 2792f (1970).
8. G. H. Lindquist and F. S. Simmons, "A Band Model for Very Non-Uniform Paths," JQSRT, Vol. 12, p. 807f (1972).
9. S. J. Young, Band Model Formulation for Inhomogeneous Paths, SAMSO-TR-74-255, The Aerospace Corporation, El Segundo, California, December 1974.
10. B. H. Armstrong, "Analysis of the Curtis-Godson Approximation and Radiation Transmission Through Inhomogeneous Atmospheres," Journal of the Atmospheric Sciences, Vol. 25, p. 312f (1968).
11. M. Abramovitz and I. A. Stegun, Handbook of Mathematic Functions, AMS-55, National Bureau of Standards, Washington, District of Columbia, 1964.
12. S. J. Young, Band Model Calculations of Atmospheric Transmittance for Hot Gas Line Emission Sources, SAMSO-TR-74-248, The Aerospace Corporation, El Segundo, California, December 1974.
13. G. H. Lindquist, et al., Investigations of Chemical Laser Processes, Report No. 19300-1-P, Environmental Research Institute of Michigan, Ann Arbor, Michigan, February 1973.
14. G. H. Lindquist, "High Resolution Measurements of Water Vapor Spectrum," ongoing contract on ARPA Order 2656, Environmental Research Institute of Michigan, Ann Arbor, Michigan, April 1974-August 1975.
15. A. Goldman and T. G. Kyle, "A Comparison between a Statistical Model and Line-by-Line Calculations with Application to the $9.6 \mu m$ Ozone and the $2.7 \mu m$ Water Vapor Bands," Applied Optics, Vol. 7, p. 1167f (1968).
16. C. B. Ludwig, "Measurements of the Curves-of-Growth of Hot Water Vapor," Applied Optics, Vol. 10, p. 1057f (1971).
17. I. S. Gradshteyn and I. W. Ryzhik, Table of Integrals. Series and Products, Academic Press, New York, New York, 1965.